Freie Universität Berlin (FU)
Fachbereich Geowissenschaften
Malteserstr. 74-100, 12249 Berlin

GeoForschungsZentrum (GFZ)
Helmholtz-Zentrum Potsdam
Telegrafenberg, 14473 Potsdam

GeoSim

Characterization of the subduction zone seismic cycle of the Northern Chile-Southern Peru seismic gap region: analysing and modelling GPS and InSAR data of the 2014 M_W 8.1 Iquique-Pisagua earthquake.

Dissertation
zur Erlangung des akademischen Doktorgrades
doctor rerum naturalium (Dr. rer. nat.) im Fachbereich
Geowissenschaften an der Freien Universität Berlin

vorgelegt von

Felix Hoffmann

eingereicht: 16.07.2019
verteidigt: 07.01.2020

Erstgutachter: **Prof. Dr. Onno Oncken**
Freie Universität Berlin, GeoForschungsZentrum Potsdam

Zweitgutachter: **Prof. Dr. Frederik Tilmann**
Freie Universität Berlin, GeoForschungsZentrum Potsdam

Prüfungskommission:
Vorsitzende: **Jun. Prof. Dr. Eline Le Breton,** *Freie Universität Berlin*
Prof. Dr. Frederik Tilmann, *Freie Universität Berlin, GeoForschungsZentrum Potsdam*
Prof. Dr. Onno Oncken *Freie Universität Berlin, GeoForschungsZentrum Potsdam*
Prof. Dr. Georg Kaufmann*, Freie Universität Berlin*
Dr. Sabrina Metzger, *GeoForschungsZentrum Potsdam*

This thesis is dedicated to my dear wife
Juliane and my beloved daughter Lenja.

Abstract

Modern geodetic measurements have extraordinarily broadened our knowledge about plate tectonic kinematics by providing spatially and temporally dense crustal deformation constraints. Those measurements are particularily important for understanding tectonic processes at the Earth´s subduction zones that have been generating most devastating seismic events and tsunamis since the beginning of historical records. The hazard assessment of an active convergent margin mostly relies on geologic archive data as input for the earthquake recurrence concept that can be highly improved by robust kinematic models relating in-situ ground surface measurements to plate interface slip motion.

In my thesis, I present an extensive analysis of crustal deformation variations during a subduction zone earthquake cycle in Northern Chile and hence contribute to the refinement of the subduction zone seismic cycle concept. I use GPS and InSAR measurements to constrain the purely tectonic signal and integrate a joint slip inversion model approach at the inter-, co- and postseismic stage of the mature Northern Chile-Southern Peru seismic gap. The characterization of crustal deformation is based on the case-study of the recent M_w 8.1 Iquique-Pisagua earthquake that ruptured the central part of the seismic gap on 1st April 2014. I compare interseismic ground motion rates of a dense continuous and survey-mode GPS network including a time-series of more than ten years with postseismic deformation rates two years after this megathrust event. Moreover, I generate an updated interseismic coupling map of the Northern Chilean subduction zone and present afterslip at different stages of the postseismic period. The joint inversion of InSAR data from two different satellites (Radarsat-2 and TerraSAR-X) and GPS measurements yields different coseismic slip models of the mainshock and separately of the largest aftershock two days later.

The Iquique-Pisagua earthquake ruptured a highly coupled patch of the subduction zone interface (Camarones segment). Presented coseismic slip models range at the lower magnitudinal level of published models, are less compact in their geometry and stop at the Iquique Low coupling zone at 21° S. Afterslip is also limited southwards interpreted as impediment through a seismotectonic barrier at this latitudinal range. Postseismic deformation lasts for about two years before relocking rates are equal to interseismic ground motion velocity. Causal factors for the barrier that may behaves as seismotectonic segment limitation involve crustal (forearc) strength heterogeneities, interface coupling discontinuities potentially triggered by variations in seafloor roughness and differences in the subducting plate geometry. GPS observations south of the inferred

seismotectonic barrier reveal a deformation rate increase in the second year after the earthquake. Afterslip models suggest a down-dip coupling increase as main driver for the rate increase, perhaps bringing the highly coupled southern Loa segment closer to failure. A megathrust event in Northern Chile was expected for more than thirty years based on slip deficit analysis and recurrence estimations. The fact that the Iquique-Pisagua earthquake 2014 did not rupture the entire Northern Chile- Southern Peru seismic gap like the last big event in 1877 (M_w 8.6 Iquique earthquake) is due to (1) tectonic pre-conditions that lowered the slip deficit as aseismic slow slip events and/or partial unlocking induced by seismic triggering of a foreshock sequence preceding the mainshock and (2) time-dependent, changing interface coupling conditions that may also change seismotectonic segment limitations over time. The Iquique-Pisagua event was not characteristic in the sense of the 1877 M_w 8.6 Iquique earthquake, but maybe for another smaller magnitudinal category of megathrust events that rupture more freuquently.

The Northern Chile case-studie clearly demonstrates that subduction zone earthquakes are not only dependent on the slip deficit, but also on limitations of seismotectonic segments and tectonic pre-conditions as interface coupling variations. Thus, subduction zone earthquakes do not necessarily show same rupture characteristics over time. Taken together, the results of my thesis reveal (1) the interaction between different areas undergoing stress release and stress build-up in a major seismic gap, (2) constraints for the temporal variation of coupling degree and interface slip at different stages of the seismic cycle and (3) the influence of large earthquakes at adjacent segments at a subduction zone location and inferred implications for future seismic risk assessment.

Zusammenfassung

Moderne geodätische Messmethoden ermöglichen einen tiefen Einblick in räumlich und zeitlich hochauflösende krustale Deformationsprozesse und haben damit unser Wissen um kinematische Prozesse der Plattentektonik signifikant erweitert. Die Messmethoden sind vor allem wichtig, um tektonische Prozesse an den weltweiten Subduktionszonen zu studieren, an welchen seit Beginn historischer Aufzeichnungen die verheerendsten Erdbeben und Tsunamis entstehen. Die Gefährdungsanalyse eines aktiven, konvergenten Kontinentalrandes basiert zu großen Teilen auf geologischen Archivdaten als Basis des Konzepts für das periodische Wiederauftreten von Erdbeben, welches durch die robuste kinematische Inversion krustaler Deformation auf Bewegungen auf der Platten-Störungsfläche erheblich verbessert werden kann.

In meiner Dissertation zeige ich umfangreiche Analysen krustaler Deformation und deren Variationen während eines kompletten Erdbebenzyklus in Nord-Chile und trage damit Wesentlich zur Verbesserung des Konzeptes des seismischen Subduktionszyklus bei. Ich nutze GPS und InSAR Messungen, um das tektonische Signal zu extrahieren und erstelle jeweils ein Inversionsmodell zur inter- co- und postseismischen Deformation in der tektonisch überfälligen nord-chilenischen-süd-peruanischen seismischen Lücke. Die Charakterisierung krustaler Deformation basiert auf der Fallstudie des aktuellen M_w 8.1 Iquique-Pisagua Erdbebens, welches den zentralen Teil der seismischen Lücke am 1. April 2014 brach. Ich vergleiche interseismische Bodenbewegungsraten eines dichten Netzwerkes aus kontinuierlichen und Kampagne- GPS Stationen von mehr als 10 Jahren mit postseismischen Deformationsraten von bis zu zwei Jahren nach dem Subduktionsbeben. Darüberhinaus generiere ich eine interseismische Plattenkopplungskarte der nord-chilenischen Subduktionszone und zeige Afterslip zu verschiedenen Zeiträumen der postseismischen Phase. Als Ergebnis der Inversion von InSAR-Daten zweier verschiedener Satelliten (Radarsat-2 und TerraSAR-X) mit GPS-Messungen präsentiere ich zwei verschiedene Slip-Modelle des Hauptbebens und separiert davon des größten Nachbebens zwei Tage später.

Das Iquique-Pisagua Erdbeben brach einen hochgradig gekoppelten Bereich der Störungszone der subduzierenden Platte (im Camarones Segment). Meine co-seismischen Slip-Modelle sind eher am unteren Ende der Größenordnung bereits publizierter Modelle einzuordnen, zeigen eine weniger kompakte Geometrie und stoppten im Bereich eines sehr niedrig gekoppelten Plattenareals (Iquique-Low-coupling zone) bei 21° S. Afterslip ist nach Süden begrenzt, was als seismische Barriere in dieser geographischen Breite interpretiert wird. Die Phase postseismischer Deformation dauert etwa zwei Jahre an,

bevor tektonische Bewegungsraten wieder mit den interseismischen Boden-Geschwindigkeiten vergleichbar sind. Die Entstehung einer solchen Barriere, welche möglicherweise als seismotektonische Segmentgrenze dient, geht zurück auf Festigkeitsunterschiede der Erdkruste, Kopplungs-Diskontinuitäten auf der Platten-Störungsfläche, verursacht durch Bathymetrieundulationen uund Geometrievariationen der subduzierenden Platte. GPS Messungen südlich der seismotektonischen Barriere zeigen einen Geschwindigkeitsanstieg innerhalb des zweiten Jahres nach dem Erdbeben. Afterslip-Modelle suggerieren, dass ein Anstieg der Plattenkopplung hauptverantwortlich ist für diesen Geschwindigkeitsanstieg, welcher das hochgekoppelte, südliche Loa Segment näher an einen Bruch der Platten-Störungszone bringt. Analysen eines Slip-Defizits und Abschätzungen des Erdbebenwiederkehrintervals ließen ein Subduktionsbeben in Nord-Chile seit mehr als 30 Jahren erwarten. Der Grund, dass das Iquique-Pisagua Erdbeben nicht die gesamte nordchilenische-südperuanische seismische Lücke gebrochen hat, wie es zuletzt 1877 beim M_w 8.6 Iquique-Beben geschehen ist, liegt in (1) den tektonischen Vorbedingungen und damit der Reduktion des Slip-Defizites durch ein aseismisches, langsames „stilles Erdbeben“ bzw. einer dem Hauptbeben vorangegangenen seismischen Vorschock-Sequenz, die eine partielle Platten-Entkopplung induzierte und (2) zeitlich variierende Konditionen der Kopplung an der Platten-Störungsfläche, die möglicherweise auch eine Verschiebung seismotektonischer Segmentgrenzen initiieren. Das Iquique-Pisagua Erdbeben war nicht charakteristisch in Bezug auf das M_w 8.6 Iquqiue Erdbeben von 1877, aber eventuell in Bezug auf eine andere Kategorie von kleineren Subduktionsbeben mit einer höheren Bruchfrequenz.
Diese Fallstudie aus Nord-Chile beweist, dass Subduktionsbeben nicht ausschließlich abhängig vom Slip-Defizit sind, sondern auch von seismotektonischen Segmentgrenzen und tektonischen Vorbedingungen wie Kopplungsunterschieden. Daher zeigen Subduktionsbeben nicht unbedingt die selben Bruchcharakteristika über die Zeit. Zusammengefasst zeigen die Resultate meiner Dissertation (1) die Interaktion verschiedener Plattenareale, die Stressabbau und –aufbau in einer großen seismischen Lücke erfahren, (2) zeitliche Variation des Plattenkopplungsgrades und des Slips auf der Platten-Störungszone in verschiedenen Phasen des seismischen Zyklus und (3) den Einfluss eines großen Erdbebens auf benachbarte Segmente an einer Subduktionszone und daraus abgeleitete Implikationen zur seismische Gefährdungsanalyse.

Contents

Abstract III

Zusammenfassung V

Contents VII

List of Tables X

List of Figures XI

1 Introduction 13
1.1 Subduction zone seismic cycle concept 13
1.2 Tectonic setting of the Northern Chile-Southern Peru seismic gap region and introduction of the Iquique-Pisagua earthquake 2014 16
1.2.1 Tectonic characterization of the Central Andes in Northern Chile 16
1.2.2 The Iquique-Pisagua earthquake 2014 19
1.3 Introducing modern geodetic observation techniques 20
1.3.1 Global Position System (GPS) 22
1.3.2 Interferometric Synthetic Aperture Radar (InSAR) 23
1.4 Thesis objectives, aims and outline 24

2 Processing and modelling concepts of geodetic data 28
2.1 GPS methods 28
2.1.1 GPS Basic Principles 28
2.1.2 GPS Data Processing 30
2.1.3 Time series inversion 32
2.2 InSAR methods 35
2.2.1 InSAR data processing 37
2.2.2 Interferometric Errors and Decorrelation 42
2.2.3 Quadtree subsampling and InSAR weighting 47
2.3 From ground displacement data to distributed slip models 49

3 Characterizing afterslip and ground displacement rate increase following the 2014 Iquique-Pisagua M_w 8.1 earthquake, Northern Chile 51
3.2 Impact of the 2014 earthquake on the 1877 seismic gap 51
3.2 GPS observations and model approach 54
3.2.1 GPS data processing 54
3.2.2 Extracting the tectonic GPS signal 55
3.2.3 Data time windows and model strategy 58
3.3 Interseismic period 60
3.3.1 Constraining GPS rates 60
3.3.2 Model results 62

3.4 Postseismic period 64
3.4.1 Constraining static GPS displacements 64
3.4.2 Model results 68
3.5 Discussion 71
3.5.1 Spatial correlation of afterslip and aftershocks 71
3.5.2 Seismotectonic barrier at 21° S 75
3.5.3 GPS rate change south of 21° S 76
3.6 Conclusion 79

4 Refining coseismic slip of the 2014 M_w 8.1 Iquique-Pisagua earthquake and the largest M_w 7.7 aftershock by jointly modelling InSAR and GPS data 80
4.1 Introduction 80
4.1.1 Iquique-Pisagua mainshock 80
4.1.2 Iquique-Pisagua earthquake trigger scenarios 82
4.2 Methods 84
4.2.1 InSAR processing 84
4.2.2 InSAR errors and subsampling 89
4.2.3 Methods GPS 90
4.2.4 Geodetic Modelling: joint inversion of InSAR and cGPS data 92
4.2.5 Model strategy: Extraction of coseismic slip 94
4.3 Results 96
4.3.1 Interferograms 96
4.3.2 Models 102
4.4 Discussion 111
4.4.1 Refined mainshock and aftershock coseismic slip model 111
4.4.2 Analysis of coseismic slip distribution 114
4.4.3 Tectonic pre-conditions of the Iquique-Pisagua earthquake 117
4.4.4 Temporal and longterm changes in the deformational regime of Northern Chile as a consequence of the Iquique-Pisagua earthquake 121
4.5 Conclusion 122

5 Synthesis 124
5.1 Conclusion 124
5.2 Outlook 130

Supplementary Material 131
A: Illapel Earthquake 131
A.1. Introduction and Tectonic Setting 131
A.2. Methods 133
A.2.1. InSAR data processing 133
A.2.2. GNSS processing and geodetic inversion 135
A.3. Coseismic Rupture 137
A.4. Discussion and Conclusion 138

B: Supporting Information for *Characterizing afterslip and ground displacement rate increase following the 2014 Iquique-Pisagua M_w 8.1 earthquake, Northern Chile* 140
C: Supporting Information for *Refining coseismic slip of the 2014 M_w 8.1 Iquique-Pisagua earthquake and the largest M_w 7.7 aftershock by jointly modelling InSAR and GPS data* 185

References 211

Curriculum Vitae 232

Acknowledgements 233

Eidesstattliche Erklärung 235

List of Tables

Table B.1: Residuals of cGPS time series after subtracting seasonal model 169
Table B.2: Best-fit cGPS seasonal model paramters 170
Table B.3: Mean cGPS seasonal model parameters 171
Table B.4: Absolute interseismic, horizontal GPS ground deformation rates split into three stages 172
Table B.5: Interseismic deformation rates and errors for interseismic model approach in SOAM reference frame 173
Table B.6: Interseismic deformation rates for interseismic model approach in ITRF2014 reference frame 174
Table B.7: GPS static displacements, error and visco-elastic contribution (E N U) of Period 1 in SOAM reference frame 175
Table B.8: *GPS static displacements, error and visco-elastic contribution (E N U) of Period 1 in ITRF2014 reference frame* 176
Table B.9: GPS static displacements, error and visco-elastic contribution (E N U) of Period 2 in SOAM reference frame 178
Table B.10: GPS static displacements, error and visco-elastic contribution (E N U) of Period 2 in ITRF2014 reference frame. 179
Table B.11: GPS static displacements, error and visco-elastic contribution (E N U) of Period 3 in SOAM reference frame 181
Table B.12: GPS static displacements, error and visco-elastic contribution (E N U) of Period 3 in ITRF2014 reference frame 182
Table B.13: Relocking rates (E N U) 184
Table C.1: InSAR Quad displacements (LOS) and errors for Sub-Model I 191
Table C.2: InSAR Quad displacements (LOS) and errors for Sub-Model II 193
Table C.3: InSAR Quad displacements (LOS) and errors for Sub-Model III 195
Table C.4: InSAR Quad displacements (LOS) and errors for Sub-Model V 196
Table C.5: InSAR Quad displacements (LOS) and errors for Sub-Model VI 198
Table C.6: cGPS displacements and errors (E N U) in SOAM reference frame for Sub-Model I 199
Table C.7: cGPS displacements and errors (E N U) in SOAM reference frame for Sub-Model II 200
Table C.8: cGPS displacements and errors (E N U) in SOAM reference frame for Sub-Model III 201
Table C.9: cGPS displacements and errors (E N U) in SOAM reference frame for Sub-Model V 202
Table C.10: cGPS displacements and errors (E N U) in SOAM reference frame for Sub-Model VI 203

List of Figures

Figure 1.1: Seismic cycle subduction zone concept 14
Figure 1.2: Tectonic units in Northern Chile 18
Figure 1.3: INSAR and GPS acquisition geometry 21
Figure 2.1: GPS trilateral and pseudorange principle 29
Figure 2.2: GPS processing overview 31
Figure 2.3: Different components of the GPS time series signal 32
Figure 2.4: Repeat-pass radar interferometry principle 36
Figure 2.5: INSAR processing overview 40
Figure 2.6: Interferometric error sources 43
Figure 2.7: InSAR (layered) atmospheric noise reduction 44
Figure 2.8: InSAR (turbulent) atmospheric noise estimation 46
Figure 2.9: InSAR subsampling and weighting 48
Figure 3.1: Topographic map of the Northern Chile-Southern Peru seismic gap 53
Figure 3.2: Decomposition of the cGPS time series (station CRSC) 56
Figure 3.3: Seasonal signal of the cGPS network 57
Figure 3.4: Averaged interseismic GPS model results and inferred backslip map 63
Figure 3.5: Postseismic GPS model results and inferred afterslip maps 66
Figure 3.6: Postseismic GPS ground displacement evolution 67
Figure 3.7: Aftershock distribution in comparison to afterslip on the interface 72
Figure 3.8: Comparison of different slip models and CFS change model 74
Figure 3.9: Ground deformation rate changes in the Loa segment 78
Figure 4.1: Topographic map of the Northern Chile- Southern Peru seismic gap subduction zone setting 81
Figure 4.2: Overview of InSAR image pairs and satellites 85
Figure 4.3: Varying Coherence maps dependent on InSAR processing strategy 86
Figure 4.4: Quadtree subsampling (TSX 18122011-02042014) 90
Figure 4.5: Linear ramp correction strategy (RS2 27032014-20042014) 92
Figure 4.6: Weighting ratio w = wInSAR/wcGPS 93
Figure 4.7: Model substitution overview 95
Figure 4.8: Results of wrapped and unwrapped asc. TerraSAR-X interferograms. 97
Figure 4.9: Results of wrapped and unwrapped asc. Radarsat-2 interferograms 100
Figure 4.10: Results of wrapped and unwrapped desc. Radarsat-2 interferograms ... 101
Figure 4.11: Results of Model A: coseis. largest aftershock slip model (Model II-I) .. 103
Figure 4.12: Results of Model B: coseis. mainshock slip model (Model III-IV) 106
Figure 4.13: Results of Model C: coseis. mainshock slip model (Model V-IV). 108
Figure 4.14: Results of Model D: coseis. mainshock slip model (Model VI-A-Model Period I). 110
Figure 4.15: Joint coseismic mainshock slip model overlain by cumulative aseismic slip preceding the earthquake 112

Figure 4.16: Comparison of coseismic mainshock slip models from literature..... 112
Figure 4.17: Slip model of the 15 days (17^{th} – 31^{th} March 2014) between the M_w 6.7 foreshock and the Iquique-Pisagua mainshock..... 112

Figure A.1: Locking map of the Illapel study area 132
Figure A.2: Wrapped Sentinel-1 Interferogram (14082015-17092015) 134
Figure A.3: Unwrapped and subsampled Sentinel-1 Interferogram (14082015-17092015)..... 135
Figure A.4: Optimal coseismic slip obtained by joint InSAR and GPS observation.... 137
Figure A.5: *Coseismic slip model*..... 138
Figure B.1: sGPS and cGPS availability overview..... 140
Figure B.2: cGPS time series (E N U) for selected stations..... 146
Figure B.3: sGPS time series (E N U) for selected stations...... 149
Figure B.4: Map of cGPS reference stations. 151
Figure B.5: Seasonal model correction for sGPS station PEIN (East)..... 152
Figure B.6: Geometry model set up (Pylith) for visco-elastic modelling..... 154
Figure B.7: Horizontal visco-elastic model results for different viscosities 155
Figure B.8: Vertical visco-elastic model results for different viscosities..... 156
Figure B.9: Trade-off curve between model roughness and misfit 157
Figure B.10: Temporal evolution of interseismic ground displacement 158
Figure B.11: Ground deformation transients for coastal cGPS stations 159
Figure B.12: Model weighting ratios w = wsGPS /wcGPS for afterslip models 160
Figure B.13: GPS deformation prediction for Andean sliver motion..... 161
Figure B.14: Checkerboard resolution tests for different afterslip model periods 162
Figure B.15: Horizontal GPS residuals between observed and predicted data for afterslip models 163
Figure B.16: Vertical GPS residuals between observed and predicted data for afterslip models 164
Figure B.17: Vertical GPS observations and predictions for interseismic and postseismic models 165
Figure B.18: Modelled partition of observed GPS signal split into interseismic and visco-elastic components..... 166
Figure B.19: Cumulated Afterslip model oft wo years 167
Figure B.20: Error estimation of modelled afterslip 168
Figure C.1: SAR SLC image concatenation..... 185
Figure C.2: Results of the RS2 orbit enhancment..... 189
Figure C.3: Trade-off curves between model roughness and misfit 204
Figure C.4: cGPS, InSAR and model weighting auxiliary plots for Sub-Model I 205
Figure C.5: cGPS, InSAR and model weighting auxiliary plots for Sub-Model II..... 206
Figure C.6: cGPS, InSAR and model weighting auxiliary plots for Sub-Model III.... 207
Figure C.7: cGPS, InSAR and model weighting auxiliary plots for Sub-Model IV.... 208
Figure C.8: cGPS, InSAR and model weighting auxiliary plots for Sub-Model V 209
Figure C.9: cGPS, InSAR and model weighting auxiliary plots for Sub-Model VI.... 210

1 Introduction

1.1 Subduction zone seismic cycle concept

Subduction zones generate about 90% of the Earth´s seismic moment, released by huge, devastating seismic events such as the largest ever recorded earthquakes: the M_w 9.5 Chile event in 1960 and the M_w 9.2 Alaska event in 1964 (*Pacheco and Sykes 1992*; *Lay and Bilek, 2007*). At these convergent plate boundaries, mechanically strong lithosphere descends into the asthenosphere. The seismogenic part of the subduction plate interface spans exceptionally large patches that favour slip-weakening behaviour and thus frictionally unstable deformation. The subducting plate that moves under the overriding plate at several centimetres per year, occasionally slips suddenly in devastating earthquakes (megathrust events) with an extremely short cycle of stress accumulation and release within decades to centuries (*Scholz, 1998*). The movement on the plate interface is referred to as slip that can occur rapidly during earthquakes, slowly as aseismic slip in the stage following these earthquakes, or as slow slip before earthquakes. Maximum stress is accumulated at the plate interface, where the subducting plate and the overriding plate interact by dragging, pushing and pulling forces (*Turcotte and Schubert, 2014*). These forces are induced by coupling of the two plates being constrained to a depth range of 0 up to max. 70 km controlled by certain pressure-temperature conditions and lithologies (e.g. *Oleskevich et al., 1999*). Below this depth range, thermal conditions allow stable sliding of the two plates and stress accumulation decreases to a minimum.

The joint analysis of geodetic data at different time-scales and various locations of megathrust events on Earth have led to a generalized and widely accepted model of the deformation cycle at subduction zones. This model generally corresponds to the elastic-rebound theory of the early twentieth century (*e.g. Reid, 1910*) and includes three cyclic stages: (1) linear, interseismic strain accumulation, (2) sudden coseismic stress release and (3) transient postseismic afterslip (**Figure 1.1**) (*Wang et al., 2012*).

(1) The interseismic phase is the period between two earthquakes that can last decades to centuries at subduction zones. This period is characterized by steady accumulation of elastic strain caused by frictional processes of the locked plate interface. The interface locking pattern is not distributed uniformly, but instead varies in time and space (e.g. *Aki, 1979*; *Moreno et al., 2011*). By analysing ground deformation data using the elastic

rebound theory approach (*Reid, 1910*), the current locking state and a potential slip deficit of the subduction interface can be determined. Recent studies showed that a small portion of the interseismic stress build-up by interface locking may be relaxed by viscoelastic processes of the asthenosphere and this process should be taken into account when assessing slip deficit in relation to seismic hazard (*Wang et al., 2012*; *Li et al., 2015*).

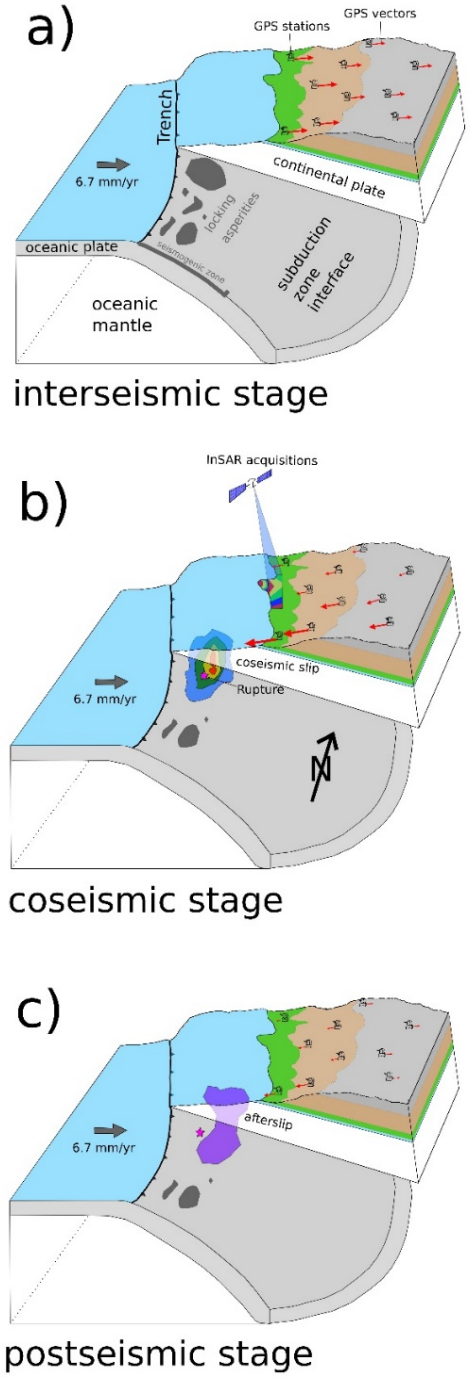

Figure 1.1: Sketch of the three stages of the seismic cycle at the Northern Chilean subduction zone setting:

a) The interseismic stage is characterized by steady strain accumulation due to the subduction of the oceanic Nazca Plate. Locking asperities (dark grey patches) are an expression of inhomogeneities on the subduction zone interface (light grey surface). The signal of onshore GPS stations (red arrows) shows inland motion, collinear to the direction of plate convergence.

b) The sudden failure of one or more locking asperities (color-coded slip at the interface) is also referred to as coseismic stage. The direction of ground motion changes to trenchward motion as inferred by GPS (red arrows) and InSAR (colored fringes at the coast) observations.

c) The postseismic stage that can last months to decades subsequently follows the coseismic stage. The area affected by the failure on the subduction plate interface (purple patch) is characterized by afterslip. Onshore GPS stations close to the trench show trenchward motion (red arrows), whereas far-field stations may have already turned to inland motion indicating relocking.

(2) The coseismic phase terminates the build-up of stress, thus the interseismic phase ends with a sudden failure of the plate coupling when a stress threshold is reached. The

release of stress lasts only seconds to minutes due to frictional instability of the fault interface (*Kanamori, 1986*). By using the fault interface geometry (pre-determined by seismic and gravitational observations) and recorded geodetic ground deformation data, the coseismic slip distribution can be modelled. The large magnitude megathrust events that are typical for subduction zones may affect the seismic stability of interface patches adjacent to the rupture hypocentre by transferring released stresses. As a consequence, large aftershocks are often observed (e.g. *Perfettini & Avouac, 2007*).

(3) The postseismic phase directly follows the coseismic phase and lasts months to years depending on the size of the main rupture. This stage is characterized by transient ground deformation decaying with time and involving various processes as afterslip (e.g. *Marone et al., 1991*), poroelastic rebound (e.g. *Peltzer et al., 1996*), viscoelastic relaxation (e.g. *Kanamori, 1973*; *Savage and Prescott, 1978*) and relocking (e.g. *Wang et al., 2012*). The separation of the recorded postseismic surface deformation signal into single components requires prior assumptions about individual spatio-temporal characteristics of each process (*Bedford et al., 2016*). Near-field postseismic data are assumed to be dominated by elasto-plastic afterslip, whereas far-field observations can show long wavelength deformation patterns that are interpreted as induced by viscoelastic mantle relaxation extending the traditional elastic rebound theory (*Kanamori, 1973*; *Wang et al., 2012*).

Concerning hazard assessment, it is very important to evaluate the current seismic cycle stage of a subduction plate interface that is known for having generated megathrust events in the past. Therefore, the seismic potential of a tectonic segment is assessed based on earthquake recurrence intervals calculated from past, instrumentally recorded seismic events and geological archive data in the subsurface as terrace data or fault offsets (e.g. *Clague and Bobrowsky, 1994*; *Mouslopoulou et al., 2011*; *Melnick et al., 2009*; *Bilham et al., 2005*). Tectonic evidence of the last earthquake, moreover provides important information of the length of a seismic cycle and the current slip deficit in a particular seismotectonic segment (e.g. *Bilham & Ambraseys, 2005*). The slip deficit is related to the locking degree of the two plates at the convergent plate boundary and can be estimated instantaneously from geodetic measurements by comparing actual ground deformation of the overriding plate with the velocity of the subducting plate. The degree of locking is described by the state of coupling of the two plates represented by a number ranging from 0 (fully uncoupled) to 1 (fully coupled). This number is related to the ratio between local sliding velocity on the fault and long-term subduction plate velocity (e.g. *Moreno et al., 2010*). If the time that has passed since the last rupture is beyond the calculated recurrence interval, it is assumed that the slip deficit has been exceeded and the segment will be identified as mature seismic gap (*McCann et al., 1979*). As a conse-

quence, this segment is considered as being at imminent risk of generating an earthquake. Those regions have reached the late stage of the interseismic phase and thus accumulate large elastic stresses along the subduction plate interface. The monitoring of mature segments provides constraints on time-dependent strain accumulation processes directly before an earthquake and moreover increases the chance of capturing co-and postseismic deformation mechanisms.

1.2 Tectonic setting of the Northern Chile-Southern Peru seismic gap region and introduction of the Iquique-Pisagua earthquake 2014

1.2.1 Tectonic characterization of the Central Andes in Northern Chile

The Andean Cordillera constitutes one of the youngest oroclines on Earth and has mainly been uplifted as a result of crustal shortening associated to rapid Nazca-South America subduction (e.g., *Isacks, 1988; Oncken et al., 2006; Oncken et al., 2012 and references therein*). Subduction of oceanic crust has been ongoing since the Jurassic with slightly varying orientations of the generally ENE-directed convergence vector (*Mpodozis and Ramos, 1989; Pardo-Casas and Molnar, 1987*). Today, the plates converge with rates of ~65- 70 mm/yr along a vector oriented ~N 75° E (e.g. *Angermann et al., 1999*; *Norabuena et al., 1999*). The subduction plate interface hosts the seismogenic zone that dips 20-30° E down to a Moho depth of about ~50 km at 20-23° S latitude (*Cahill and Isacks, 1992*; *Husen et al., 2000*; *Oncken et al., 2003*). Interseismic GPS observations reveal crustal velocity vectors that are parallel to the plate convergence (*Li et al., 2015*). These vectors indicate an east-west interseismic compressional regime that is caused by plate motion of the overriding plate while the subduction plate interface is heterogeneously locked (e.g. *Moreno et al., 2011*; *Métois et al., 2014*). Main geological structures of Northern Chile include margin-parallel faulting that reveal spatio-temporal heterogeneities from North to South and a shortening-dominated backarc (e.g. *Hoffmann-Rothe et al., 2006; Boutelier et al., 2014*).

The nearly orthogonal plate convergence between the Nazca and South American Plate has driven the formation of margin-parallel tectonic provinces in Northern Chile, including from West to East: the Coastal Cordillera referred to as outer forearc and the Central Depression, Precordillera and Western Cordiller referred to as backarc or also inner forarc (**Figure 1.2**) (e.g. *Victor et al., 2004*; *Cembrano et al., 2007*; *Allmendinger et al., 2010*).

Morphologically, the Coastal Cordillera is mainly characterized by two tectonic features: the coastal cliff that sharply breaks off towards the coastline with an elevation difference of 1000 m (*Mortimer et al., 1974*) and the Atacama fault system (AFS) in the inner part of the range. Extending about 1000 km along the Chilean coast south of 20.5° S, the AFS predominantly exhibits major north-south striking normal faults with documented neotectonic activity (e.g. *Brown et al., 1993*; *Delouis et al., 1998*). These normal faults indicate east-west directed extension and are interpreted as being caused by upper plate bending and coseismic extension of compressional earthquakes resulting in a long-term forearc uplift (*Gonzáles et al., 2003, Cembrano et al., 2007*). In contrast, moderately dipping reverse faults parallel to the convergence direction besides some minor normal faults mainly characterize the northern regions of the outer forearc between 19° and 21° S and thus indicate a predominant trench parallel shortening regime (e.g. *Allmendinger et al., 2005; Oncken et al., 2006*).

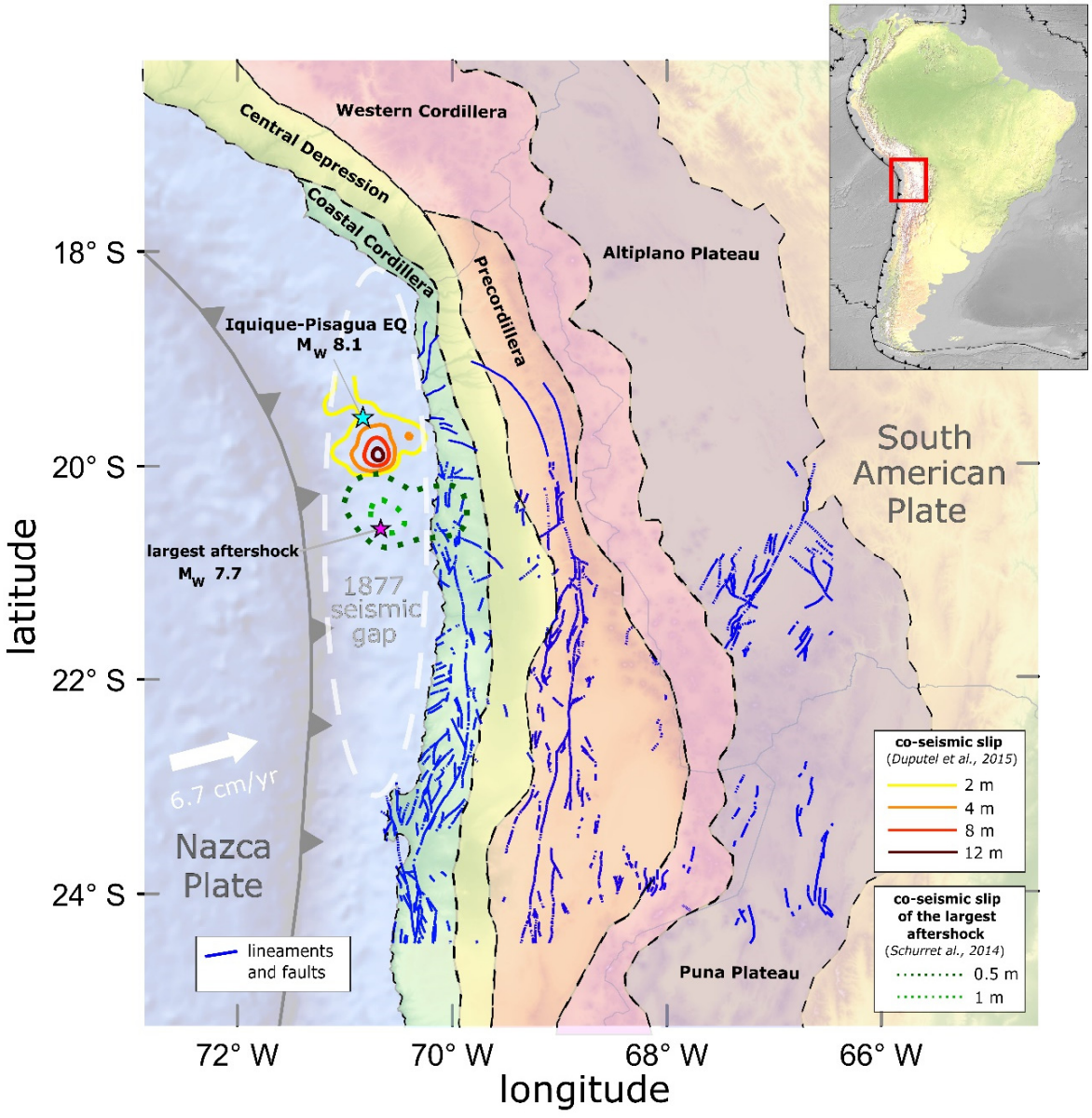

Figure 1.2: (previous page) *Overview map of the tectonic units at the Northern Chilean subduction zone setting, from East to West: Coastal Cordillera (green), Central Depression (yellow), Precordillera (orange), Western Cordillera (pink) and Altiplano-Puna Plateau (violet). Major faults and lineaments (blue) are highlighted (Reutter et al., 1994; Cembrano et al., 2007). The trench marks the border between the oceanic Nazca and the continental South American Plate. The extent of the last inferred megathrust event in this region in 1877 is marked with a white ellipse in which also color-coded coseismic contour lines of the Iquique-Pisagua mainshock (Duputel et al., 2015) and the largest aftershock (Schurr et al., 2014) are displayed.*

The inner forearc is mainly characterized by thrusting induced by neotectonic E-W shortening that is controlled by the plate convergence and moreover consistent with the tectonic regime that has initiated the uplift of the central Andes. Forming a flat surface at 1500 m elevation, the Central Depression represents remnants of a Neogene infill of rhyolitic tuff and sedimentary deposits (*Cembrano et al., 2007*). The Precordillera to the East reaches altitudes of 3500 to 4500 m mainly uplifted due to Neogene reactivation of reverse faults and west-vergent folding (*Victor et al., 2004*). A similar system of west-vergent, moderately dipping reverse faults forms the Neogene volcanic chain of the Western Cordillera that reaches peak elevations of above 6000 m and constitutes the geologic border of the Bolivian Altiplano Plateau at 4000m altitude (*Victor et al., 2004*). The spatio-temporal patterns of both, elastic deformation observed by instantaneous GPS measurements and permanent deformation documented by geological records in the inner forearc are surprisingly very consistent (e.g. *Allmendinger et al., 2005; Oncken et al., 2006*). This consistency indicates that both modes of deformation (localized upper crustal faulting and broadscale strain pattern due to megathrust locking) are controlled by the same compressional stress regime.

All introduced morphotectonic provinces (**Figure 1.2**) are orientated parallel to the meridional trend of the Andean orogen thus blocking regional moisture-bearing winds from the Eastern Lowlands. This orientation has led to extreme aridity west of the Altiplano-Puna Plateau since the Eocene to Oligocene when diachronous and spatially disparate range uplift began (e.g. *Carrapa et al., 2005; Oncken et al., 2012).* This setting emphasizes the strong climatic impact of the Andes in South America thought to also control tectonics (e.g. *Strecker et al., 2007*). Due to one of the lowest erosion rates on Earth with less than 0.2 mm/yr tectonic structures as fault scarps or surface cracks are well preserved over a time span of several millions of years in the geologic archive (e.g. *Allmendinger and Gonzáles, 2010; Bookhagen and Strecker, 2012*). The extensive surface cracks mapped in Northern Chile are assumed to reflect primarily deep seated tectonic processes rather than constituting only surface phenomena (e.g**.** *González et al.,*

2008; *Loveless et al., 2009*). Extensional cracks that form during earthquakes as a consequence of elastic rebound of the upper plate might indicate long-term rupture segments. *Loveless et al.* (*2009*) documented a regional variation of crack orientations in the central part of the Coastal Cordillera at 21° S latitude, possibly reflecting tectonic fragmentation. The deformation regime in this area is characterized by margin-parallel shortening on E-W trending faults (e.g. *González et al., 2015*). In contrast, the morphology of the coastal area around the city of Iquique is mainly controlled by N-S striking normal faults composing the northern elongation of the large Atacama Fault System (*Victor et al., 2004*; *González et al., 2003*).

A widely accepted tectonic model at the Northern Chile subduction zone comprises three plates, including a forearc sliver located between the Nazca and South American Plate (e.g. *Bevis et al., 2001*; *Chlieh et al., 2011; Métois et al., 2014*). The formation of such a forearc-sliver may be caused by active shear stresses within a margin-parallel strike-slip fault system (*Boutelier et al., 2014*; *Hoffmann-Rothe et al., 2006*).

1.2.2 The Iquique-Pisagua earthquake 2014

The convergent plate contact between the Nazca and the South American Plate west of Chile is mainly characterized by frequent megathrust events with short recurrence times of several decades in a subduction zone setting. Almost all segments south of Peru broke within the past century and large subduction earthquakes occurred 1960 in Valdivia (M_w 9.5) or more recently 2010 in Maule (M_w 8.8) (e.g. *Kanamori, 1977*; *Moreno et al., 2010*). The only segment that has not ruptured in this area since 1877 (M_w 8.6 Iquique earthquake) and is capable of generating a M_w ~9 earthquake (e.g. *Kelleher*, *1972*) is referred to as Northern Chile-Southern Peru seismic gap, located between 18- 23° S latitude. The earthquake recurrence interval in Northern Chile is estimated to be ~100 years and therefore this gap is considered to be one of the most mature seismic gaps along the South American plate boundary south of Peru, meaning that the slip-deficit of this seismotectonic segment is considered to have reached the stage of when a great earthquake is imminent (e.g. *Comte and Pardo*, *1991*).

The Iquique-Pisagua earthquake ruptured the central part of the Northern Chile- Southern Peru seismic gap (**Figure 1.2**) on 1 April 2014 at 23:46 (UTC). The mainshock is assumed to constitute a double-couple solution with a strike of ~350°, a dip of 14°, a rake of ~91°, a hypocentre location at 19.64° S, 70.82° W and a centroid depth of ~35km rupturing a planar fault of ~160 km length (*Lay et al., 2014; Hayes et al., 2014*). The mainshock nucleated at 25km depth, propagated downdip to rupture an area of in-

termediate interseismic coupling between 18.5-21° S and generated a tsunami of ~2 m height that hit the Northern Chilean coast (*Hayes et al., 2014*). The peak slip zone is thought to be rather small, extending 30 km downdip and 30 km southward from the hypocentre, but slip magnitude vary in scientific literature with values of 4.4m (*Schurr et al., 2014*), 6.5m (*Lay et al., 2014*; *Liu et al., 2015*), 7m (*Gusman et al., 2015*), 8m (*Hayes et al., 2014*) up to 10m (*Duputel et al., 2015*) southeast and downdip of the hypocentre at 30-40km depth. Similarly, the largest M_w 7.7 aftershock nucleated at shallow depth and propagated downdip in a northeasterly direction, approximately 30-40 km south of the mainshock on 3 April 2014 (*Schurr et al., 2014*). Peak slip of this aftershock is reported as being between 1.2 to 2.5m (*Schurr et al., 2014*; *Liu et al., 2015*).
The Iquique-Pisagua earthquake 2014 was preceded by three foreshock clusters, the first occurring in July 2013 (*Schurr et al., 2014*). It has been suggested that these foreshock clusters weakened a zone of intermediate coupling in the central part of the Northern Chile- Southern Peru seismic gap (*Schurr et al., 2014*; *Bürgmann et al., 2014*). Of particular interest is the series of foreshocks that preceded the mainshock for about three months and intensified after a M_w 6.7 foreshock on 16 March 2014 that occurred southwest of the mainshock epicentre. The M_w 6.7 foreshock was the reactivation of a trench-oblique upper plate reverse fault (*Gonzalez et al., 2015*). The subsequent intensified foreshock sequence propagated northwards towards the center of the later main rupture and could thus be interpreted as precursor finally triggering the main event (*Kato & Nakagawa, 2014*; *Bürgmann, 2014*). Seismically induced crustal weakening might have caused the mainshock to nucleate in the northern part of the foreshock area, continuing downdip with increasing velocity towards higher locking for the nucleation stage for about 40s before an area close to the epicenter was reactivated at the end of the main rupture (*Schurr et al., 2014*). Tectonic processes that finally led to crustal weakening and thus the main rupture are discussed in scientific literature in the context of either a possible slow slip event preceding the mainshock or a cascade of foreshocks and respective afterslips (e.g. *Yagi et al., 2014; Bedford et al., 2015*). Summing the seismic moment of the mainshock and all related aftershocks in 2014 yields a M_w of ~8.3 and thus a much smaller magnitude compared to the inferred 1877 event (e.g. *Hayes et al., 2014*; *Comte and Pardo*, *1991*).

1.3 Introducing modern geodetic observation techniques

In the last two decades, major advances in spatial and temporal resolution and accuracy from Global Positioning System (GPS) and Interferometric Synthetic Aperture Radar

(InSAR) have facilitated the improved measurements of surface deformation caused by tectonic processes (e.g. *Dixon, 1993*; *Hyndman et al., 1995*; *Bürgmann et al., 2000*). Both techniques enable the precise measurement of small-scale deformation across large areas, in line with the range of deformation produced before, during and after great earthquakes (in millimeter to centimeter scale).

These two geodetic techniques, while complimentary for tectonic analysis, give different measures of surface deformation. Using GPS, we measure the absolute position of a particular receiver on the ground in three dimensions East, North and Vertical (**Figure 1.3**). With InSAR, we measure the phase difference of points reflecting the radar wave (scatterers) on the ground between two SAR acquisitions. We then convert this phase difference to a corresponding distance change between the scatterer and the sensor by taking into account the radar wavelength. The result is a one-dimensional displacement in the line-of-sight (LOS) of the satellite (**Figure 1.3)**. A big advantage in using InSAR besides the high spatial resolution is the independence of any instruments on the ground. On the other hand, the application of InSAR requires spatially stable atmospheric conditions and limited vegetation to ensure spatial and temporal coherence between two acquisitions.

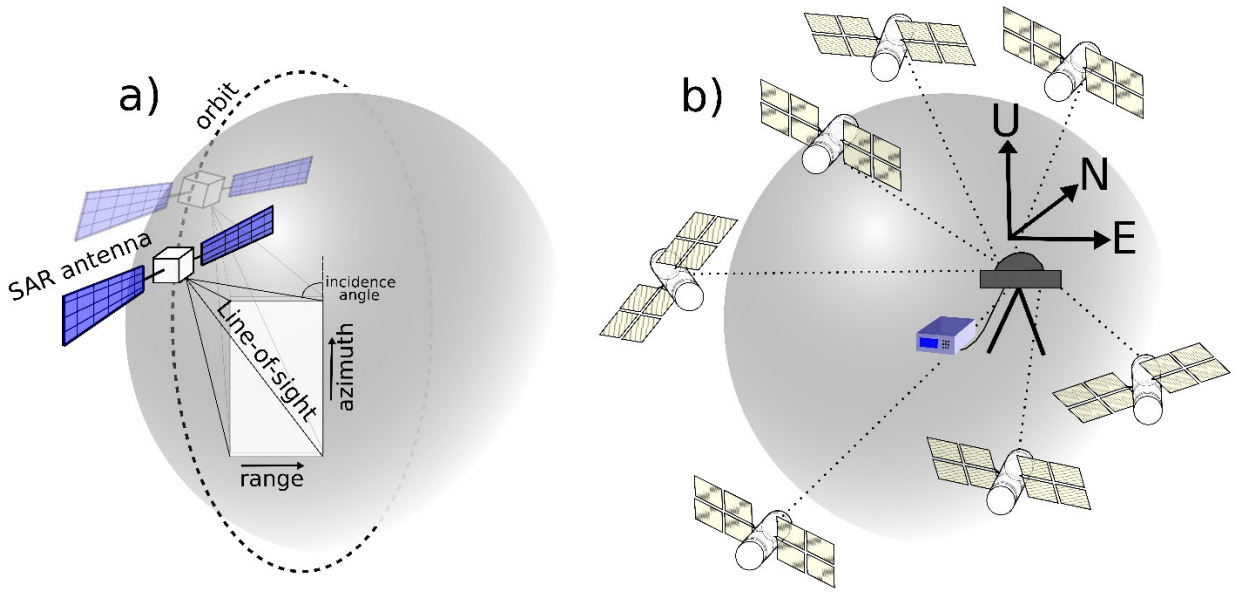

Figure 1.3: Sketch of the two geodetic technologies used in this study. a) InSAR observations combine two SAR acquisitions to yield a ground deformation in the line-of-sight of the satellite and b) GPS satellites provide East, North and Up component of a single receiver on the Earth´s ground.

1.3.1 Global Position System (GPS)

The Global Positioning System is an American satellite navigation system consisting of 24 satellites that was originally designed for military applications in the 1970s and made available for public use twenty years later (e.g. *El Rabany, 2002*). By measuring the travel time for the transmitted electromagnetic wave travelling from at least four GPS satellites to one passive receiver (antenna), this technology provides precise three-dimensional information about position and velocity. One big advantage is that the signal is independent from weather conditions and daylight.

The first documented geodetic observations on surface motions related to an earthquake were already taken at the end of the 19th century (1892 Tapanuli event, Sumatra) by means of triangulation and leveling (e.g. *Reid, 1913*; *Bonafede et al., 1992*). By the end of the last century, the development of spaceborne satellite systems extended the spectrum of geodetic technology enormously. Nowadays, improvements of GPS technology and the increased number of Global Navigation Satellite Systems (GNSS) have enabled the precise measurement of the Earth´s ground deformation at millimeter-scale-accuracy.

GPS measurements are used to characterize in detail the transient deformation before (e.g. *Vigny et al., 2009*) and after earthquakes (e.g. *Bedford et al., 2016*) as well as the abrupt coseismic stress release of large fault ruptures (e.g. *Pritchard et al., 2002*). GPS measurements have significantly improved our understanding of deformation processes at subduction zones that harbour the potential of generating the largest and most devastating earthquakes on Earth (e.g. *Lay and Bilek, 2007*). The analysis of geodetic records sheds light on subduction zone processes that were only theoretically known before, such as slow slip events (e.g. *Hirose et al., 1999*; *Miller et al., 2002*) or heterogeneous interseismic coupling at the plate interface (e.g. *Mazzotti et al., 2000*; *Moreno et al., 2011*).

In my thesis, I process and analyse GPS observations that were mainly recorded under the framework of the Integrated Plate boundary Observatory (IPOC) project (*Moreno et al., 2017*). This international monitoring project, that aims to study the seismic cycle and related deformation phenomena at the Chilean subduction zone has been operating multi-purpose geophysical measurements in Northern Chile since 2007 thus replacing the South American Geodynamic Acitivities (SAGA) project installed in 1993 (*Klotz et al., 1999*). Therefore, the project has facilitated an optimal data management and sharing policy between the cooperating institutions. Among other geophysical instrumentations, the IPOC initiative consists of a dense network of GPS stations mainly located in Chile. As one of the key partners, the GFZ Potsdam has access to all available meas-

urements. The continuous GPS data in the IPOC project is complemented spatially by a survey GPS network that is measured every one or two years. This network was installed as continuation of the SAGA project (*Klotz et al., 1999*) in the late 1990´s and consequently extended in the last two decades (*Moreno et al., 2017*).

1.3.2 Interferometric Synthetic Aperture Radar (InSAR)

Interferometric Synthetic Aperture Radar (InSAR) data are poorly resolved temporally but have a high spatial resolution. InSAR therefore complements the GPS measurements in the observation of tectonically-driven ground movements. The actual term InSAR denotes a nested acronym involving three individual technologies: radio detection and ranging (radar), Synthetic Aperture Radar (SAR) and interferometric SAR (InSAR) (*Hanssen, 2001*).

The radar technique makes use of the two-way travel time of emitted electromagnetic pulses in the millimeter to centimeter wavelength regime that are backscattered from reflecting objects (*Skolnik, 1962*). SAR extends the classical radar approach by creating an artificially long antenna that synthetically combines received pulses from a moving source (*Hanssen, 2001*). This conceptual antenna is much longer than its real aperture thus affording a tremendous increase in resolution.

With simple radar systems, it is impossible to distinguish two objects having the same distance but different angles to the instrument. The development of the interferometric approach of SAR systems has overcome this problem: the combination of two SAR images either received by repeated acquisitions or acquired by two different antennas enables the simultaneous measurement of distance and angular differences of one single object in the radar beam (*Hanssen, 2001*). The interferometric SAR approach is capable of providing distance changes of one object between two acquisitions with an accuracy in the range of fractions of the radar-wavelength simply based on Huygens´ wave front theory (*Huygens, 1690*). Since the launch of the European Remote Sensing Satellites (ERS-1 and ERS-2) operated by the European Space Agency (ESA) in 1991 and 1995, InSAR has become a widely adopted tool in the geodetic science community for measuring ground motions induced by processes such as earthquakes (*e.g. Massonnet et al., 1993; Rosen et al., 1998*), volcanoes (e.g. *Delacourt et al., 1998*; *Amelung et al., 2000*), antropogenic subsidence or uplift (e.g. *Fialko and Simons, 2000*; *Ferretti et al., 2000*) and glaciers (e.g. *Goldstein et al., 1993*; *Mohr et al., 1998*).

Nowadays, SAR data is available in many different configurations and from various satellites operating with a range of frequencies, footprint sizes and resolution modes.

However, the interferometric approach of SAR data is only possible for two images acquired with the same frequency of coherent radar beams due to an introduced frequency shift of the moving transmitter referred to as Doppler Centroid frequency (*Hanssen, 2001*). The repetition interval of acquiring the same footprint on the Earth´s surface twice in the same mode depends on the mission, but is six days in best case (Sentinel-1 a/b). Thus, for some tectonic applications the advantage of the high spatial resolution of InSAR images is counterbalanced by the relatively low temporal resolution that might often be too low for separating sudden events related to surface motions, such as earthquakes from other processes, e.g. postseismic slip.

1.4 Thesis objectives, aims and outline

This thesis aims primarily to provide insights on tectonic processes at different stages of the seismic cycle at the Northern Chilean subduction zone with a specific focus on the recent Iquique-Pisagua earthquake in 2014.

In my thesis, I combine modern high-resolution geodetic observations (cGPS, sGPS and InSAR) to analyse, model, and constrain geo-mechanical processes that are related to motions on the Northern Chilean subduction plate interface. The presented data set is exceptional in facilitating the characterization of the tectonic state in all three stages of the seismic cycle (inter-, co- and postseismic) with unprecedented detail.

The Chilean coast is part of a larger tectonic system that consists of different spatially connected convergent plate boundaries in the circum-Pacific region, also known as Ring of Fire. Large seismic events that generated devastating tsunamis in the past two decades, such as the 2004 M_w 9.0 Sumatra event (e.g. *Wang & Liu, 2006*), the 2010 Maule M_w 8.8 Chile earthquake (e.g. *Delouis et al., 2010*) or the 2011 Tohoku-Oki M_w 9.1 earthquake, Japan (e.g. *Goto et al., 2011*), are typical for these tectonically highly active subduction zones. Despite decades of research into subduction zone mechanics, including geodetic and geophysical Sub-surface measurement campaigns, it is still impossible to predict the location, timing, and magnitude of future megathrust events, and therefore their potential impact (e.g. tsunami generation). In order to better constrain earthquake characteristics and to identify seismically hazardous regions, well-recorded megathrust events must be analysed in detail. Linking crustal deformation mechanics of a megathrust region at the Northern Chilean Coast to different stages of the seismic cycle, I tackle the following open questions of subduction zones research:

1. **Do interseismic ground deformation rates give direct insights to coseismic motions, thus location and extent of future megathrust events?**
2. **What does the comparison of inter- and postseismic ground deformation in neighbouring segments of a subduction zone earthquake tell us about the risk of a future megathrust event?**
3. **Is there any evidence that megathrust events behave characteristically over multiple seismic cycles?**

The scientific focus in my thesis is on analysing the recent Iquique-Pisagua earthquake 2014. Specifically related to this event, I aim to address the following questions:

4. **Why did the entire Northern Chile- Southern Peru seismic gap not rupture during the Iquique-Pisagua event 2014?**
5. **What factors may control the coseismic slip distribution of the Iquique-Pisagua earthquakes?**
6. **How long does afterslip of the recent Iquique-Pisagua earthquake dominate over relocking in the postseismic stage?**
   and
7. **Can we improve methodological aspects for the applied geodetic measurements to yield more reliable slip inversion results?**

My thesis is organized in three chapters that address these formulated objectives and individual research issues. I mainly focus on combining various geodetic data types to perform a joint analysis on different stages of the Northern Chile seismic cycle. All chapters of my thesis combine complex spatio-temporal aspects with data related information and therefore are split into a data methods part (chapter 2), a comparison of pre- and post-seismic conditions (chapter 3) and a coseismic deformation analysis of the Iquique-Pisagua earthquake 2014 (chapter 4).

In chapter 2, I give an overview of the basic principles of the applied geodetic techniques: cGPS, sGPS and InSAR. I provide detailed explanations of data processing and (post-) processing strategies, GPS time series inversion, data correction methods and InSAR resampling algorithms in preparation for geodetic slip inversion. Here, I present all methods applied to extract the purely tectonically induced ground deformation signal in my data and present a kinematic (slip) model for all stages of the Northern Chilean seismic cycle.

In chapter 3, I focus mainly on deformation related to the postseismic stage of the Iquique-Pisagua earthquake by analysing and modelling two years of afterslip. Three consecutive slip models show the spatio-temporal evolution of afterslip jointly inverted from sGPS and cGPS data. I also compare interseismic deformation rates of the southern part of the former Northern Chile- Southern Peru seismic gap region with rates observed within two years after the main event. This chapter presents a unique data analysis of the postseismic stress-transfer on a potential seismotectonic border, involving (1) plate interface afterslip, (2) viscoelastic mantle relaxation and (3) re-locking of the plate interface.

In chapter 4, I analyse the coseismic ground deformation of the Iquique-Pisagua earthquake by jointly inverting high-resolution InSAR data with cGPS observations to separately refine the slip distribution of the mainshock on 1st April and its largest aftershock that occurred two days later. I present three independent coseismic mainshock slip models and one aftershock slip model from different data sources and compare geometries, magnitudes, and locations with previously published models (e.g. *Schurr et al., 2014*; *Duputel et al., 2015*). The coseismic slip models allow direct conclusions to be drawn on the location and magnitude of the released slip deficit in the seismic gap. Moreover, I discuss local tectonic and seismic (pre-)conditions that may have strongly influenced coseismic slip distribution.

The auxiliary material provides relevant data additions, such as GPS and InSAR ground motion data tables and time series plots, and presents the reasoning behind preferred model parameterizations. Moreover, I present an analysis on the M_w 8.2 Illapel earthquake 2016 and demonstrate that my methods and algorithms may be successfully applied to other subduction zones events.

Chapter 3 concerning the joint slip inversion of sGPS and cGPS data at the Northern Chilean subduction zone has been published in:

Hoffmann , F., S. Metzger, M. Moreno, Z. Deng, C. Sippl, F. Ortega-Culaciati , and O. Oncken (2018), Characterizing Afterslip and Ground Displacement Rate Increase Following the 2014 Iquique-Pisagua M_w 8.1 Earthquake, Northern Chile, Journal of Geophysical Research: Solid Earth, Volume 123, Issue 5, p.4171-4192, doi: 10.1002/2017JB014970.

A similar approach of jointly inverting geodetic data to produce a high-resolution coseismic slip model of a subduction zone earthquake (the M_w 8.2 Illapel megathrust in Central Chile) is performed in a manuscript, in which I contributed as co-author (see A: Illapel Earthquake in Supplementary Material):

Tilmann, F., Y. Zhang, M. Moreno, J. Saul, F. Eckelmann, M. Palo, Z. Deng, A.Y. Babeyko, K. Chen, J.C. Baez, B. Schurr, R. Wang, and T. Dahm (2016): The 2015 Illapel earthquake, central Chile: a type case for a characteristic earthquake? - Geophysical Research Letters, 43, 2, pp. 574—583, doi: 10.1002/2015GL066963.

I want to highlight all contributions to the mentioned publications and my thesis that were not explicitly performed by myself. In Hoffmann et al. (2018) (chapter 3), the visco-elastic model geometry and viscous signal contributions are generated and calculated by Marcos Moreno and Sabrina Metzger. The daily positions of the raw GPS data were processed by Zhiguo Deng, who also provided Figure 2.1. The seismic catalogue applied in chapter 3 was calculated and provided by Christian Sippl (*Sippl et al., 2018*).

For the publication Tilmann et al., (2016), I calculated the Sentinel-1 interferogram and contributed in the joint GPS and InSAR kinematic model, whereas all other parts in the manuscript were performed and generated by other co-authors.

2 Processing and modelling concepts of geodetic data

2.1 GPS methods

The spatial wavelength of a tectonic surface displacement signal related to a subduction zone setting is in the order of at least tens of kilometers (*Kanamori, 1977*). GPS measurements recording tectonically-driven ground deformation are either taken as continuous (cGPS) or repeated measurements of survey points (sGPS) that are operated within extended geodetic networks of several tens to hundreds of stations. An increasing number of GPS networks have been established at tectonically active regions within the last two decades, improving the spatial resolution of the single point measurements for tectonic applications (e.g. *Klotz et al., 1999*; *Vigny et al., 2005*; *Ozawa, 2011; Moreno et al., 2017*). These geodetic networks are designed to monitor the entire seismic cycle especially at subduction zones and have successfully captured a range of seismic cycle deformation mechanics. All giant megathrust events since the early 2000s have been recorded by dense GPS networks: the 2004 Sumatra-Andaman M_w 9.3 earthquake, Indonesia (e.g. *Vigny et al. 2005*), the 2010 Maule M_w 8.8 earthquake, Chile (e.g. *Moreno et al., 2010*) and the 2011 Tohoku-Oki M_w 9.1 earthquake, Japan (e.g. *Ozawa, 2011*).

In my thesis, I present GPS data from a dense network of more than 150 continuous and survey-mode GPS stations. In total, the observations cover an interval of seventeen years from 1999 to 2016, thus including different stages of the seismic cycle at the Northern Chile-Southern Peru seismic gap region. I differentiate between the late interseismic linear deformation, the abrupt drop of co-seismic surface motion and about two years of transient postseismic deformation after the Iquique-Pisagua earthquake on 1st of April 2014. Differences in GPS operation mode as well as the distinct observation intervals of the entire seismic cycle require careful handling of data recorded in each interval. This chapter provides the basis of GPS processing strategies and explains data post-processing for applying GPS observations in my models.

2.1.1 GPS Basic Principles

Extracting raw measurements from GPS satellites is a very complex subject that is beyond the scope of this study. But as some GPS post-processing techniques require a sufficient level of prior-knowledge, a short summary of the basic concepts of GPS is

implemented here. The basic principle can be explained by the classical trilateration approach involving distance measurements from points at known coordinates. For that, a minimum of three GPS satellites that constitute three distinct distance ranges of transmitted electromagnetic waves to the Earth´s ground plus one additional satellite for the fourth dimension (the time) are required. The trilateration principle in its simplest form incorporates three spheres whose radii are determined by the distance between the satellite (center) and a receiver located anywhere on the sphere. The distance (radius of the sphere) can be calculated by simply measuring the transmitting-receiving time between the GPS satellite in space and antenna on the Earth´s ground assuming speed of light of the electromagnetic wave. With three satellites, the location of the receiver is equal to the intersecting point of all three spheres (**Figure 2.1 a**).

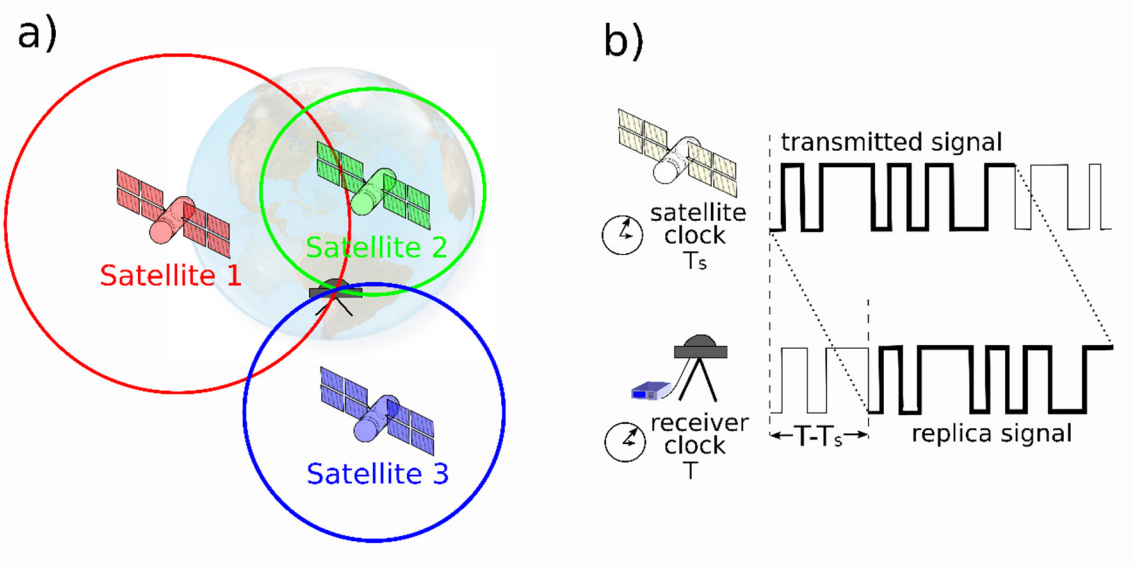

Figure 2.1: a) Simplified 2-d-trilateration principle: the intersection point of three circles whose radii are determined by the distance between satellite and receiver constitutes the location (latitude, longitude and height) of the receiver. b) Signals are compared via autocorrelation functions between the transmitted GPS signal from the satellite and the replica of this signal generated in the receiver. The time difference (T - Ts) between transmission (Ts) and reception time (T) of the GPS signal can be converted into a distance (or pseudorange). For compensating clock errors, this classical approach is extended by a fourth distance measurement that uniquely determine the location of a receiver.

The exact position of a GPS satellite is computed via the Ephemeris Algorithm (e.g. *Leick et al., 2015*) using encoded orbit parameters that are transmitted to receivers. Atomic clocks, on-board the satellite and in the receivers on the ground, measure the exact transmission and reception times of the signal. The distance between satellite and

receiver is referred to as pseudorange, computed as the multiplication of the time difference (transmitting-receiving) and the speed of light (*Blewitt, 1997*). Clock errors that arise by measuring this time difference introduce a fourth unknown to the trilateral problem. Thus, a minimum of four pseudorange measurements are required to uniquely determine the position of a receiver.

The orbit constellation of all GPS satellites includes 24 sensors that are distributed in six orbital planes. This constellation theoretically ensures coverage from a minimum of four satellites simultaneously at most locations on Earth (*Kaplan & Hegarty, 2005*). In practice, terrain elevation, signal scattering and anthropogenic obstacles often impede the GPS signal. The fundamental frequency of the transmitted signal is 10.23 Mhz. Separately multiplying this frequency by integers 154 and 120 yields the L1 and L2 carrier signals, which are additionally encoded with an algorithm that is unique to each satellite (C/A code for L1 and P code for L2). By simultaneously generating an electronic replica of this GPS signal, receivers on the ground use autocorrelation techniques to compare the received signal and to calculate time differences (*Kaplan & Hegarty, 2005*) (**Figure 2.1 b)**. The technique to reduce receiver clock bias is referred to as double differencing, whereby two satellite signals are received separately by distinct receivers (*Blewitt, 1997*). In general, a network of GPS receivers including a set of double differences improves the accuracy, although the double differenced data are characterized by a linear dependency. Introducing a common reference station for a set of double differences overcomes this problem and the number of linearly independent observations is: (number of satellites - 1) multiplied with (number of receivers - 1).

2.1.2 GPS Data Processing

All GPS were pre-processed using the Earth Parameter and Orbit System software EPOS and finally provided as 24 h solutions (**Figure 2.2**) (*Gendt et al., 2013*; *Deng et al., 2016*). In a first processing step, all GPS stations are processed in precise point positioning (PPP) model using specific GPS satellite clock and orbit products (*Deng et al., 2016*). Satellite and ground antenna phase center offsets and phase center variations were calibrated using International Global Navigation Satellite System service files (IGS08, *Schmid et al., 2007*). Ocean tide loading correction was implemented using the Finite Element Solution tide model (FES2004, *Lyard et al., 2006*). The combination of the Global Pressure and Temperature model (GPT2) and the Vienna Mapping Function provided an a priori Zenith Hydrostatic Delay (*Saastamoinen, 1973*). The Zenith Total Delay was estimated using an elevation cut-off angle of 7° and random-walk parameters

for every hour (*Gendt et al., 2013*). After outlier removal, the single station PPP coordinate results have an accuracy of ~1-2 cm. The second step applies these PPP solutions in a network processing algorithm. As the total number of GPS stations in South America exceeds 800 stations, about 250 stations were processed at once in several sub-network approaches. For each sub-network, 56 densely distributed IGS stations were included (**Figure B.4**). In the network approach, all stations are weighted equally and no station position is fixed which corresponds to a free network solution for the final coordinates. The datum of the coordinate solution is defined by the used satellite orbit and clock in the International Terrestrial Reference Frame ITRF2008. Finally, the network solutions are aligned to the IGS 2nd reprocessing combined daily coordinate product in ITRF2014 (*Rebischung et al., 2015*; *Altamimi et al., 2016*) to reduce the impact of datum effect. The coordinate results from the network solution have an accuracy of a few millimeters.

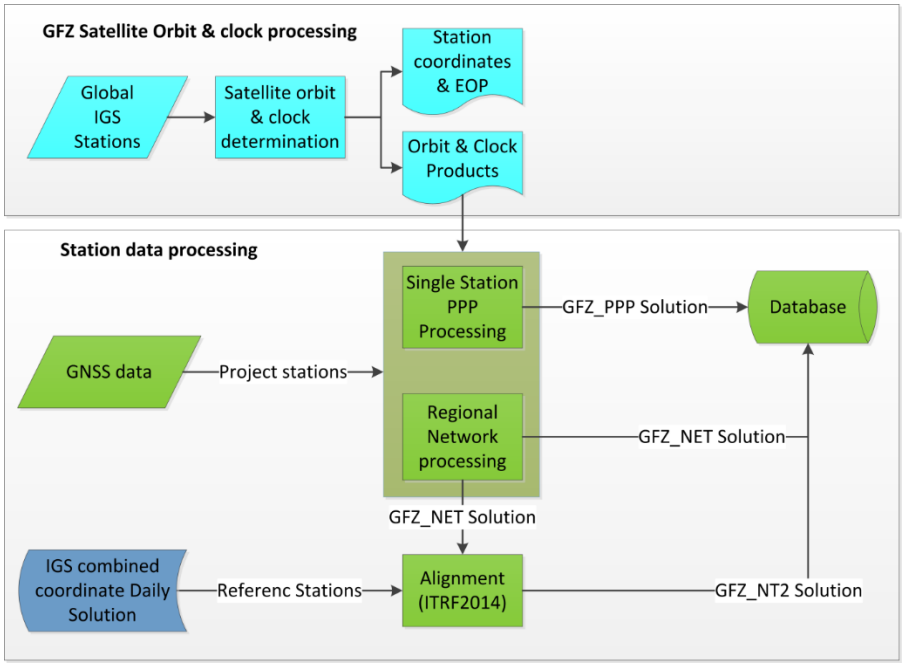

Figure 2.2: Schematic processing overview of GPS data in a network approach using EPOS software at GFZ (German Research Center for Geosciences). All GPS data are first processed in a precise point positioning (PPP) model including specific GPS clock and orbit products and Earth Orientation Parameters (EOP) and improved via a network approach (GFZ-NET) in a second processing step including reference stations. Those solutions are aligned to the ITRF2014 (Figure from Zhiguo Deng).

The non-deformational rotation of South America is not accounted for in the ITRF2014 model. Thus, I applied an Euler Pole rotation (21.44° S, 125.18° W, 0.12° Myr^{-1}, *Moreno et al., 2011*) for all GPS observations to align the velocity field relative to the stable

South American Plate (SOAM) compatible to the NNR-Nuvel-1A model (*DeMets et al.*, *1994*). Examples of the cGPS (**Figure B.2**) and sGPS (**Figure B.3**) time series are provided in the auxiliary material.

2.1.3 Time series inversion

In general, the GPS signal is assumed to consist of a combination of various ground motion components, some of which are to tectonic processes (**Figure 2.3**). To extract only tectonically-driven components from the total signal, a trajectory model can be applied that usually includes five different trends: an interseismic constant velocity trend, two distinct kinds of step functions (instantaneous jumps), a postseismic logarithmic transient and annual oscillations (*Bevis and Brown*, *2014*):

$$\delta_{\mathrm{GPS}}(t) = \delta_{\mathrm{interseismic}}(t) + \delta_{\mathrm{coseismic}}(t) + \delta_{\mathrm{AntennaOffset}}(t) + \delta_{\mathrm{postseismic}}(t) + \delta_{\mathrm{seasonal}}(t). \quad (2.1)$$

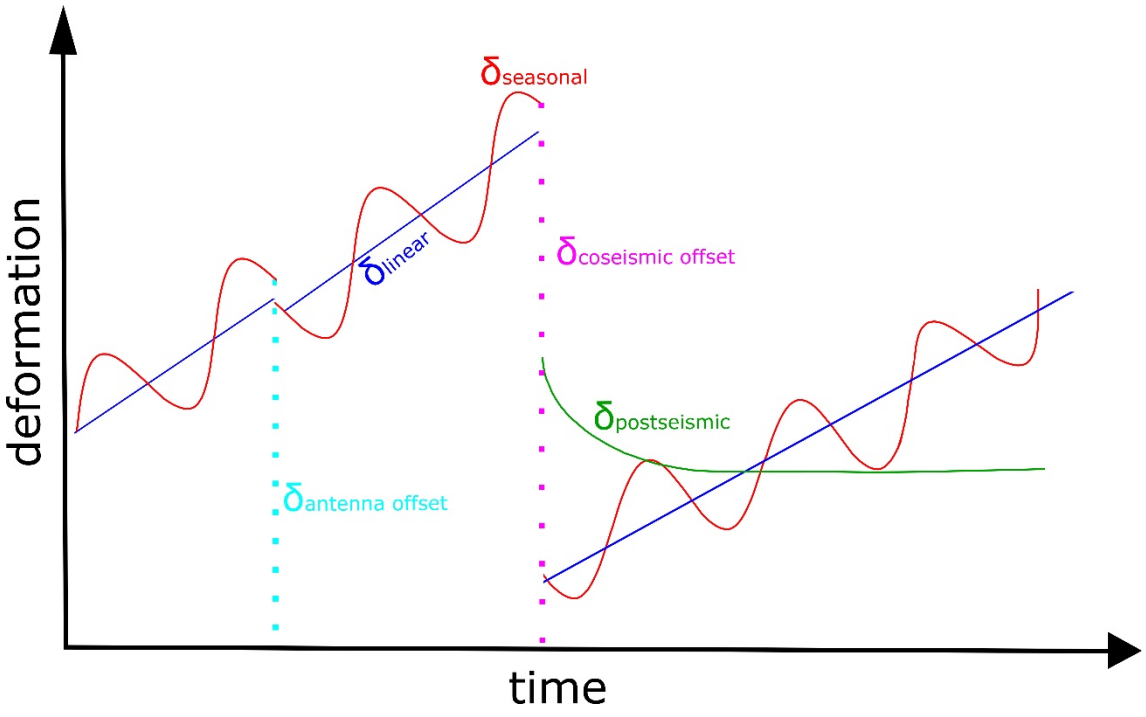

Figure 2.3: Different signal components of the cGPS time series: the (interseismic) linear trend δ_{linear} (blue), two sources of signal offsets $\delta_{antenna\ offset}$ (azure) and $\delta_{coseismic\ offsets}$ (purple), the seasonal trend $\delta_{seasonal}$ (red) and the postseismic decay $\delta_{postseismic}$ (green).

Each of the three GPS directions (East, North and Up) is treated as an individual trajectory. The simplest component of the time series assumes a constant velocity for the

ground movement. The underlying assumption for this linear relation is the uniformity of the plate velocity in all stages of the seismic cycle (*Wang et al., 2012*). Each station is described by a linear dependency of its actual position with its velocity term B, the reference position A and the pre-defined reference time t_r:

$$\delta_{\text{linear}}(t) = A + B \cdot (t - t_r). \qquad (2.2)$$

The continuous time series is occasionally interjected by discontinuities, or so called jumps. These jumps in the time series can easily be recognized as instantaneous shifts in the displacement component and can arise from real surface movements by earthquake generated coseismic displacements or as manifestations of changes in the GPS hardware *(Bevis and Brown, 2014*). Such step features in the time series, in absence of an earthquake, are artificial discontinuities that must be accounted for. The mathematical approach to model velocity drops is to apply a Heaviside function H(t), where a number of earthquake jumps n_{eq} with amplitude C_{eq} occur at coseismic times t_{eq} or respectively a number of antenna offsets n_{ao} with amplitude D_{ao} occur at times t_{ao}

$$\mathrm{H}(t) = \begin{cases} 0 & t < 0 \\ 1 & t > 0 \end{cases}, \qquad (2.3)$$

$$\delta_{\text{coseismic}}(t) = \sum_{eq=1}^{n_{eq}} C_{eq} \cdot H\left(t - t_{eq}\right), \qquad (2.4)$$

$$\delta_{\text{Antenna Offset}}(t) = \sum_{ao=1}^{n_{ao}} D_{ao} \cdot H(t - t_{ao}). \qquad (2.5)$$

One major challenge in GPS time series inversion is to distinguish antenna offsets from tectonically-driven coseismic jumps. In section 3.3.2, I describe in detail how I separate both signal contributions for my GPS time series. However, the lack of a logarithmic transient usually following earthquakes above a certain magnitude is one criteria for determining artificial jumps. These so called postseismic transients are characterized by a fast, non-linear decay of ground velocities with the fastest accelerations in a GPS time series immediately after a coseismic displacement. The rate of velocity change is highly dependent on the magnitude of the earthquake. The postseismic decay may constitute the most complex contribution to the GPS time series due to the superposition of at least three main processes – afterslip, poroelastic rebound and viscoelastic relaxation (*Wang et al., 2012*). The latter two mechanisms usually require complicated numerical models, whereas afterslip can be mathematically reproduced using a simple logarithmic formula that is derived from rate-and-state friction models (*Marone et al., 1991*). When aiming

to invert station trajectories, rather than focussing on resolving the complex mechanisms taking place after an earthquake, *Bevis & Brown* (*2014*) showed that it might be sufficient to simply use afterslip models to account for the total postseismic transient motion:

$$\delta_{\text{postseismic}}(t) = \sum_{p=1}^{n_p} E_p \cdot log\left(1 + \frac{t-t_{eq}}{T}\right), \quad (2.6)$$

where n_p is the number of logarithmic transients based on the number of detected earthquakes.

Another very prominent feature in the GPS signal is a quasi-constant sinusoidal annual trend. These oscillations are widely attributed to actual surface motions as elastic response to seasonal changes in loads imposed upon the crust and associated with the water-cycle (e.g. *Heki, 2001*; *Van Dam et al., 2001*). The mathematical approach for approximating those oscillations in the GPS time series is a Fourier series (*Dong et al., 2002*):

$$\delta_{\text{seasonal}}(t) = F_1 \cdot sin(2\pi \cdot t) + F_2 \cdot cos(2\pi \cdot t) + F_3 \cdot sin(4\pi \cdot t) + F_4 \cdot cos(4\pi \cdot t). \quad (2.7)$$

The sum of equations 2.2-2.7 constitute the trajectory model used in this study. For each cGPS station, the time series is inverted component-wise using a least-squares approach. The main purpose of inverting the time series is to account for the non-tectonic contributions to the GPS signal – the antenna offsets and the seasonal loading. The GPS observations can mathematically be described with:

$$d = G \cdot m\,, \quad (2.8)$$

where *d* represent the data, *m* the model parameters (A – F) and *G* the matrix of Greens functions (*Menke, 2012*). The Greens functions matrix describes a transfer operation that relates the individual signal contributions of equations 2.2-2.7 to the total GPS signal. The basic concept of time series inversion is to resolve equation 2.8 for the model parameters A, B, C_{eq}, D_{ao}, E_p and $F_{1\text{-}4}$ using the linearized equation:

$$m = (G^T \cdot G)^{-1} \cdot G^T \cdot d. \quad (2.9)$$

By applying the respective model parameters to equations 2.2-2.7, I derive a model for each individual signal contribution and am able to substract the antenna offsets and the

seasonal oscillations from the signal. Results of the inversion are provided in the auxiliary material (**Figure B.2**). Moreover, a more detailed analysis of extracting GPS rates and corrections of sGPS data using model parameters A – F as well as the time series split strategy is given in section 3.3.2.

Time series outlier detection and removal is based on error statistics. First, all measurements above the 99.5th percentile of the average position error are removed for the East, North and Up component. Second, after time series inversion, I used a moving window approach with a window size of 50 observation points on data residuals to remove measurements that differ more than three times the standard deviation of each window.

2.2 InSAR methods

This chapter gives an overview of InSAR principles by introducing applied acquisition geometries of the satellites, providing a generalized processing strategy and explaining possible error sources. In general, the synthetic aperture radar works similar to a single static radar, whereby information in range direction can be converted to distance to the sensor at certain azimuth times. This conversion is based on the pulse return times to the radar antenna. The detection of radar waves is related to Hertz´s experiments from the end of the nineteenth century (*Hertz, 1894*), but military applications since the 1930´s and subsequent space exploration since the 1960´s have boosted the evolution of this technology (*Curlander and McDonough, 1991*). The general concept of exploiting the radar´s phase information to discriminate two objects that reflect the antenna pulses is contributed to the work of Carl Wiley in the early 1950´s (Wiley, 1954). A major problem of a single radar image is that two points P and R that have the exact same distance to the antenna (slant range), but that are displaced horizontally in ground range cannot be distinguished (**Figure 2.4**). This geometric problem is solved by applying SAR interferometry that provides two observations of both points in slightly different geometry. The along-track flight direction of a SAR satellite is referred to as azimuth, whereas the direction perpendicular to the azimuth is the range. A SAR-satellite acquires images at an oblique line-of-sight (mostly right-looking) and has two different orbit directions: from south towards north (ascending) or vice versa (descending). The interferometric approach of SAR data is only possible for two images acquired with the same frequency of coherent radar beams due to an introduced frequency shift of the moving transmitter referred to as Doppler Centroid frequency (*Hanssen, 2001*). The repetition interval of acquiring the same footprint on the Earth´s surface twice in the same mode depends on the mission, but is six days in best case (Sentinel-1 a/b).

Using the orbit differences (baseline) of the two SAR acquisitions, positions of the two points P and R (**Figure 2.4**) can be derived by applying simple trigonometric formulas. Moreover, assuming a coherent system, the phase difference of the backscattered electromagnetic wave between both acquisitions only depends on the difference in range. In other words, position changes in the line-of-sight of the satellite of one ground scatter point at two SAR images can be measured as fraction of the signal wavelength. The InSAR signal contains different contributions and is highly influenced by the (side-) looking geometry of the satellite acquisitions as well as disturbances along the path of the electromagnetic wave through the atmosphere (**Figure 2.4**). In my thesis, I apply the differential two-pass interferometry (two SAR images at different dates) using an Shuttle Radar Topography Mission (SRTM-2, *Farr et al., 2007*) Digital Elevation Model (DEM) with a resolution of 90 m to extract the ground motion differences associated to the Iquique-Pisagua earthquake 2014. Due to the acquisition geometry and the path of the electromagnetic wave through the tropo- and atmosphere, the InSAR signal has various phase contributions. Similar to the case of the GPS signal, not all of these contributions will be related to actual surface motion and need to be analysed and corrected for if aiming to extract the deformation related signal.

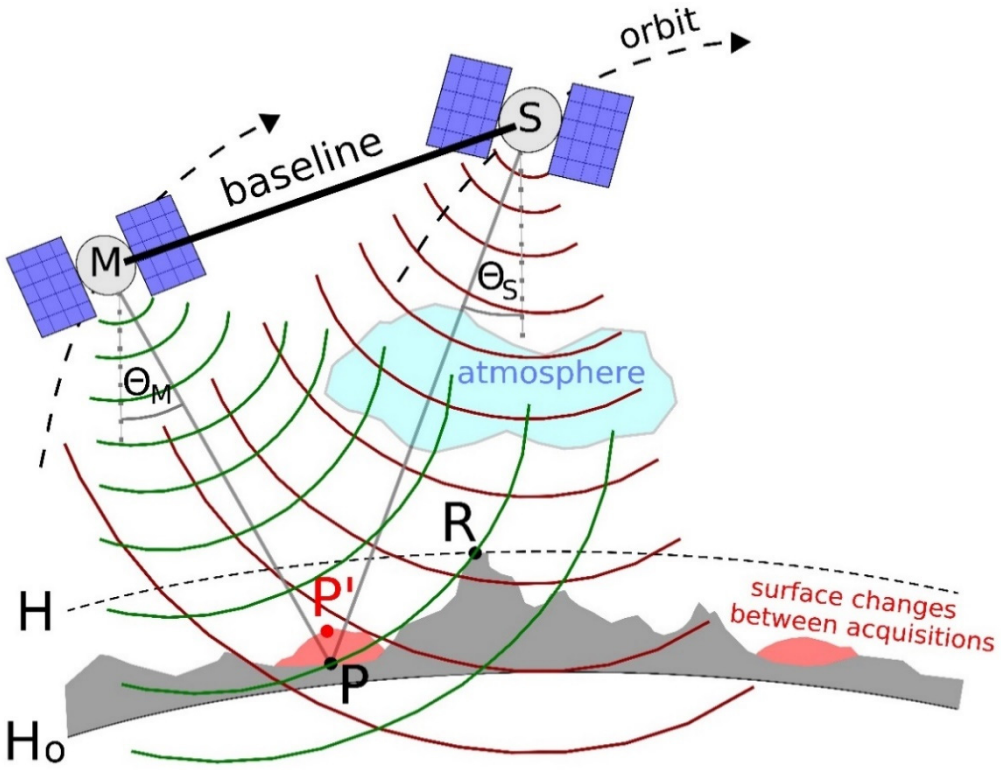

Figure 2.4: Configuration of the repeat-pass radar interferometry with master (M) and slave (S) acquisition. The coloured arcs represent electromagnetic wavefronts from the master (green) and slave (red) satellite. Points P and R have the same range distance to the master satellite (M), but cannot be resolved in a single SAR image as both would

appear in one resolution cell. The interferometric approach enables the separation of both points by a difference in look angle $\Delta\Theta$ (Θ_M-Θ_S). The distance between M and S orbit is referred to as baseline. The interferometric phase contains different contributions, i.a. the flat Earth phase defined by the reference surface H_0, the topographic phase determined by the topographic height H above the reference surface, the deformational phase defined by changes of the Earth´s ground between two acquisitions (P and P'), the orbital phase derived from the difference in satellite orbits M and S, the atmospheric phase representing the difference of water vapour content along the path of the electromagnetic wave through the atmosphere and noise contributions.

Here, I present InSAR data from the TerraSAR-X (TSX) and Radarsat-2 (RS2) satellites. A total of 28 RS2 scenes in Multi-look fine beam mode that were finally concatenated to seven SLC images were received in the course of the SOAR-EU data proposal *#16660 Monitoring the crustal deformation cycle in the Chilean subduction zone data.* The multi-looked fine beam mode is characterized by a resolution of 2.7 x 2.9 m in range and azimuth and a single tile footprint size of 50 x 50 km. For TSX, I received fifteen scenes in StripMap mode from the scientific collaboration partner DLR that were finally concatenated to five SLC images. In the StripMap mode, a continuous pulse sequence illuminates the ground swath while the antenna beam is stable in azimuth and range. This mode is characterized by a resolution of 1.2 x 3.3 m in range and azimuth and a single tile footprint size of 30 x 50 km in width and length.

The nomenclature of single interferograms is consistent in my thesis by first stating the name of the satellite followed by the dates of the master and the slave SLC image: TSX/RS2 date_master-date_slave, e.g. *RS2 01072011-04042014*)

2.2.1 InSAR data processing

In this sub-chapter, I will introduce the common processing steps for SAR interferometry (e.g. *Massonnet and Feigl, 1998*; *Rosen et al., 2000*; *Hanssen 2001*). Each interferogram is unique, thus introduces individual processing challenges that may arise by co-registration problems, atmospheric decorrelation, phase-elevation dependencies or orbital inaccuracies. A more detailed analysis of processing TerraSAR-X and Radarsat-2 scenes in particular and applied post-processing steps is given in section 4.2.1.

Spaceborne SAR antennas transmit radar wave pulses towards the Earth´s surface in a side-looking geometry to recapture fractions of the transmitted electromagnetic wave, while other parts are refracted or reflected off the travel path. The recaptured radar wave is a superposition of the reflections from different objects (scatterers) on the ground that first need to be sorted by arrival times as an equivalent to distances between the

reflector and the satellite. This signal can be converted into a Single Look Complex image (SLC) which has become the standard exchange format for raw SAR data (**Figure 2.5 a,b**). The size of a single pixel of the SLC corresponds to the resolution cell size which is the minimum area on the ground resolvable with the radar satellite based on instrument specifications. Each pixel p yields a complex value:

$$p = a \cdot e^{i\varphi}, \tag{2.10}$$

with φ as the mean phase of the electromagnetic wave of all scatterers in that pixel and a as their combined amplitude (backscatter value). One requirement for calculating the phase difference of a certain point on the ground between two acquisitions is that the phase information of this point is located at the same position in both SLC images. Tiny geometric differences in the orbit of the satellite at each acquisition cause small time shifts of the reflections of the same point on the ground and thus slightly different positions in each SLC image. Therefore, the geometry of two SAR images needs to be matched to realise the radar coordinates of all reflections before forming the interferogram. This process is called co-registration and is performed at sub-pixel domain. The common co-registration approach includes an offset calculation based on the local spatial correlation function for small image patches. Polynomial functions for range and azimuth are calculated for refining those offsets and used to resample the slave SLC to the reference (master) SLC image. The acquisition dates of the images indicate the master-slave classification - the earlier acquired image is defined as the master SLC. To reduce the noise level of the final interferogram, a so-called multi-looking is applied, which is the resampling of pixels to a lower resolution. The resampling factors are applied individually for range and azimuth direction and chosen based on the best balance of resolution and signal-to-noise-ratio as well as to generate square pixels (*Massonett and Feigl, 1998*). The azimuth and range spectra of the two SLC images differ in their Doppler centroids and therefore need to be filtered in a way that only common spectral parts are included, which is referred to as common band filtering. With the complex multiplication of all pixels p of the two co-registered and multi-looked SAR images, the interferogram can then be formed:

$$p_1 \cdot p_2^* = a_1 \cdot a_2 \cdot e^{i(\varphi_1 - \varphi_2)} = a \cdot e^{i\Delta\varphi}, \tag{2.11}$$

with $\Delta\varphi$ as the interferometric phase. The phase differences are expressed modulo 2π ranging from $-\pi$ to $+\pi$ and thus appear as phase cycles or so-called fringes in the interferogram as they are wrapped (**Figure 2.5 c**).

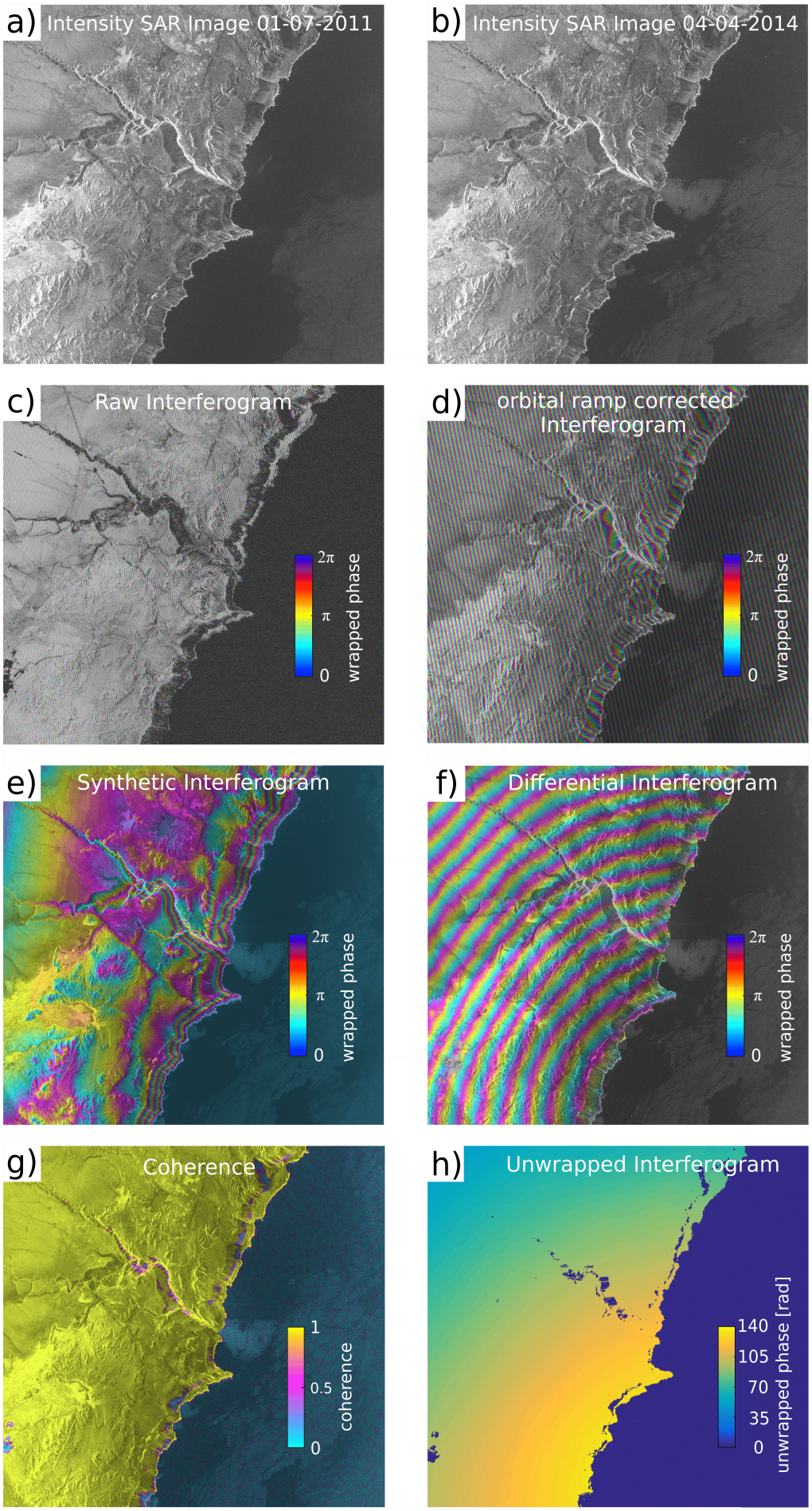
a)
Intensity SAR Image 01-07-2011
b)
Intensity SAR Image 04-04-2014
c)
Raw Interferogram
2π
π
0
wrapped phase
d)
orbital ramp corrected Interferogram
2π
π
0
wrapped phase
e)
Synthetic Interferogram
2π
π
0
wrapped phase
f)
Differential Interferogram
2π
π
0
wrapped phase
g)
Coherence
1
0.5
0
coherence
h)
Unwrapped Interferogram
140
105
70
35
0
unwrapped phase [rad]

*Figure 2.5: (*previous page*) Results of the InSAR processing chain in radar coordinates (RS2 01072011-04042014) with a) SAR intensity image as master input (01-07-2011, multi-looked with 5 x 10 looks in range and azimuth) b) SAR Intensity image as slave input already co-registered (04-04-2014, multi-looked 5 x 10), c) raw interferogram as complex multiplication of all pixels from a) and b), d) orbital ramp corrected interferogram, e) synthetic topographic phase generated from DEM (SRTM-2) and orbit information, f) differential interferogram derived by subtracting the synthetic interferogram from the flattened interferogram, g) coherence as indication for decorrelation of pixels h) unwrapped interferogram with ground motion in LOS direction.*

This wrapped interferometric phase now contains different signal fractions that might not all be related to tectonically driven ground motion, but instead appear as manifestations of different signal characteristics due to the acquisition geometry of the image and as sources of phase noise. The interferometric phase $\Delta\varphi$ thus contains:

$$\Delta\varphi = -2\pi \cdot c + \Delta\varphi_{orb} + \Delta\varphi_{flat} + \Delta\varphi_{topo} + \Delta\varphi_{defo} + \Delta\varphi_{atmo} + \Delta\varphi_{noise}. \quad (2.12)$$

The first term $-2\pi \cdot c$ is an expression for the InSAR phase ambiguity expressed as fractions of a full wavelength cycle c, thus the absolute distance from satellite to scatter. $\Delta\varphi_{defo}$ as the surface deformation is the main important phase contribution that I want to extract from equation 2.12. All other contributions have to be compensated for in the processing. The different orbit geometries of the two SAR acquisitions introduce phase gradients across the interferogram. The orbital state vectors jointly provided together with the raw SAR data include instant position and velocity information of the satellite. Using this sensor orbit information, the orbital phase $\Delta\varphi_{Orb}$ can be subtracted (**Figure 2.5 d**). To remove the effect of a curved Earth on the interferogram, a so-called flattening has to be applied. Interferometric flattening consists of removing the phase component $\Delta\varphi_{flat}$ that is caused by variations of the range distance across the image. A basic assumption for this operation is that the Earth's surface can be approximated by a curved reference ellipsoid. In this way, a fringe rate across the interferogram can be computed taking into account incidence angle, perpendicular baseline and slant range distance and the interferogram is flattened (*Rosen et al., 2000*). When aiming to process differential interferograms containing ground displacement information only, the topographic phase contribution $\Delta\varphi_{topo}$ needs to be accounted for. From the flattened interferogram, the topographic phase is subtracted by simulating topographic heights that are extracted from a digital elevation model (DEM). For that purpose, a synthetic interferogram in radar coordinates is generated using terrain height information extracted from

the DEM (**Figure 2.5 e**). The remaining differential interferometric phase $\Delta\varphi_{diff}$ is then (**Figure 2.5 f**):

$$\Delta\varphi_{diff} = \Delta\varphi - \Delta\varphi_{orb} - \Delta\varphi_{topo} - \Delta\varphi_{flat}. \qquad (2.13)$$

The quality of the differential interferogram is mainly determined by the accuracy of the orbit information as well as the DEM. To prepare the differential, wrapped interferogram for phase unwrapping, the coherence (**Figure 2.5 g**) as a quality characteristic is calculated using a sliding window approach from the cross-product of master and slave images. The coherence value ranges from 0 to 1, thus from no matching to perfect matching of geometry (from total to no decorrelation) in two intensity images. Pixels below a pre-defined threshold are not taken into account for the later phase unwrapping because they are assumed to more likely contain discontinuities (the coherence map is an estimate for robust and non-robust unwrapping areas). This threshold is defined case-specifically and can e.g. be smaller for an expected long-wavelength tectonic signal compared to small scale anthropogenic surface changes.

Finally, the remaining wrapped interferometric phase that is given modulo 2π in the differential interferogram must be unwrapped by calculating the correct integer number of phase cycles to each phase measurement via a path-dependent integration to yield absolute surface deformation (**Figure 2.5 h**). To avoid unwrapping errors caused by so-called residuals, the interferogram can be adaptively filtered applying filtering functions in a moving window approach that are based on local fringe spectrum (*Goldstein and Werner, 1998*). A residual (or inconsistency) in the differential interferogram is a location, where the cumulative phase differences of pixels along a closed integration path is not equal to zero. Inconsistencies exist as antagonistic pairs and result in unwrapping errors, thus misinterpretations of the real ground deformation. Other filtering concepts than adaptive filters to avoid these errors include 2-d band-pass filtering or additional multi-looking of the complex interferogram.

Unwrapping is the path-dependent, two-dimensional, pixelwise integration over coherent phase cycles incorporating the smoothness criterion: phase changes from one pixel to another should not exceed half a cycle (*Chen and Zebker, 2001*). This processing step may introduce errors as phase jumps above the smoothness criterion due to isolated phase information. These phase jumps need to be masked out or corrected individually, otherwise they distort the surface displacement information. A commonly used unwrapping algorithm that is applied in this thesis is the Minimum Cost Flow (MCF) technique. This global optimization approach involves masking, adaptive thinning, and

patch processing to find the minimum cost solution of an objective function (e.g. *Constatini et al., 1999*). Another unwrapping algorithm is the branch-cut method (*Rosen et al., 1994*).

The unwrapped phase ϕ can then be converted into a LOS-displacement Ω by using the relation that half the radar wavelength λ corresponds to one fringe cycle 2π, because of the two-way travel-path of the wave:

$$\Omega = -\frac{\phi}{2\pi} \cdot \frac{\lambda}{2}. \qquad (2.14)$$

Finally, the radar coordinates of the unwrapped interferogram are converted into geocoordinates in a process step called georeferencing. This coordinate transformation is determined pixel by pixel using the DEM and satellite sensor information as the relation between radar- and geocoordinates is distorted across the interferogram due to topography.

2.2.2 Interferometric Errors and Decorrelation

InSAR data errors arise from different sources and processing steps due to the complexity of the SAR image generation from the backscattered electromagnetic wave to the image superposition. The quantification and extraction of those errors, included in the phase terms φ_{atmo} and φ_{noise} of equation 2.12, is not trivial. Here, I introduce common error sources of SAR interferograms that occurred in one or more of my interferograms and may influence the resulting ground deformation if not compensated for. A first error source results from thermal anomalies in the the radar antenna and the transmitting/receiving procedure of the electromagnetic wave. Usually this error is very small and can be neglected. Another error source results from the acquisition geometry of the radar instrument that can cause topography-related errors in the SAR images, especially in regions with high elevation gradients as the region of interest in Northern Chile. The so called foreshortening arises if the antenna receives reflections from a mountain flank facing towards the sensor very close in time and slopes that are oriented towards the LOS appear compressed (**Figure 2.6 a**). If both the mountain slope and the incidence angle of the LOS are steep, the mountaintops even appear superimposed, thus closer than their flanks in the SLC. This toppled geometry is called layover (**Figure 2.6 b**). Those geometric errors are masked out for processing and can generally be identified using an external DEM. Incorrect representations of the satellite orbit geometry will also cause an error that introduces ramps, if the orbital phase (φ_{orb}) is not fully compen-

sated for (**Figure 2.6 c**). Another data error source that is particularly important in the single-interferometry approach emerges from the wave path through the Earth's atmosphere (φ_{atmo}). Atmospheric water vapour changes the speed of the electromagnetic wave, thus data errors correlate spatially with tropospheric humidity at the time of observation (e.g. *Hanssen 2001*; *Tarayre and Massonnet, 1996*). Those data errors are the consequence of a difference of atmospheric water vapour concentration between two SAR acquisitions (*Zebker et al., 1997*; *Delacourt et al., 1998*).

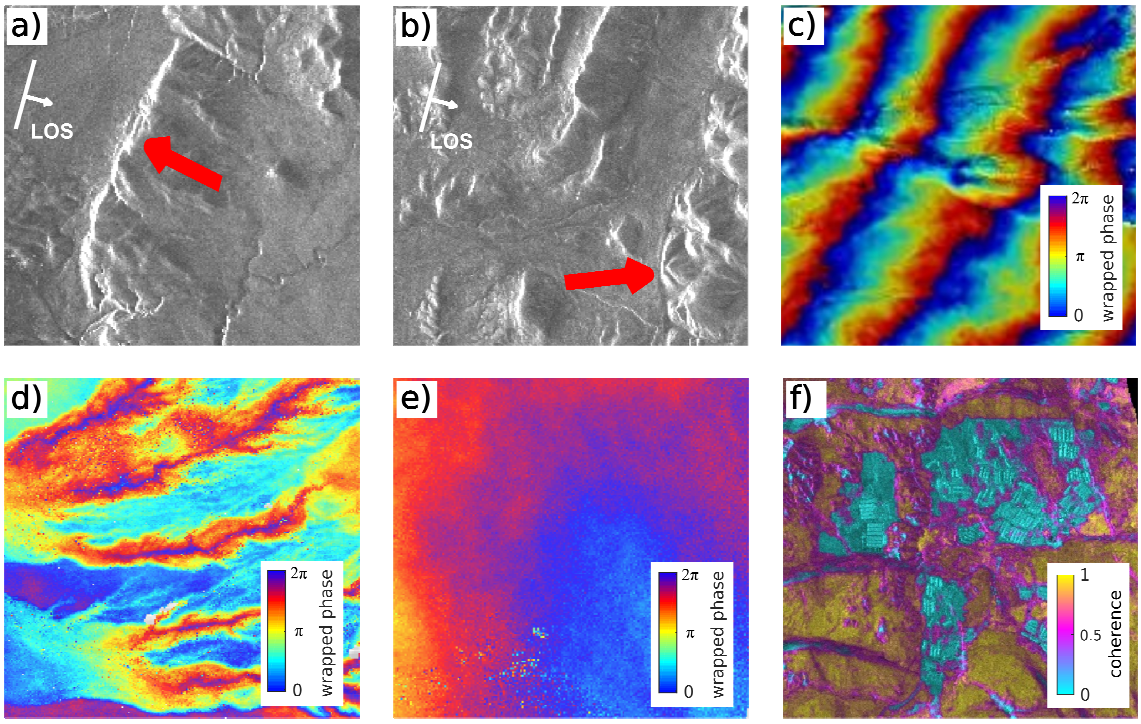

Figure 2.6: Interferometric error sources: a) foreshortening (red arrow) and b) layover (red arrow), both in the intensity image of TSX 18122011-02042014, c) orbital ramps (RS2 27032014-20042014), d) layered tropospheric error, e) turbulent atmospheric error in the wrapped interferogram RS2 04042014-15062014 and f) decorrelation in the coherence image that may cause unwrapping errors (RS2 01072011-04042014).

The atmospheric phase φ_{atmo} is difficult to distinguish from deformation, topography or orbital errors due to its spatial correlation with the differences in the atmospheric state between two acquisitions. However, two main sources of atmospheric data errors are generally distinguished: (1) errors that correlate with the topographic height as a consequence of the layered troposhere (e.g. *Delacourt et al. 1998; Hanssen 2001; Cavalié et al. 2007*) (**Figure 2.6 d**) and (2) errors that emerge due to turbulent atmospheric mass movements with strongly varying water vapour concentrations (wet delay) causing spatial and temporal signal delay heterogeneities (*Hanssen, 2001*) (**Figure 2.6 e**). All error types can cause decorrelation in the interferogram, thus areas where no deformation can be extracted (**Figure 2.6 f).**

The turbulent atmosphere is hard to compensate for as it requires a detailed analysis of tropospheric conditions at the exact time of observation. I remove those errors from the data by identifying high phase gradients at regions with a steep topographic gradient and crop the interferogram in those regions (**Figure 2.7**). The layered tropospheric error source can be approximated by using atmospheric models and a linear signal-elevation inversion approach (*Cavalié et al., 2007*). The linear inversion approach is similar to equation 2.9, where in this case G is the Greens function matrix containing DEM height information, d is a vector with the phase information $\Delta\varphi$ and m is the model vector containing the model parameters b0 (phase constant) and b1 (phase slope) based on a simple linear trend. The phase data are then corrected ($\Delta\varphi_{atm\_cor}$) by applying:

$$\Delta\varphi_{atm\_cor} = \Delta\varphi - (b0 + b1 \cdot height). \qquad (2.15)$$

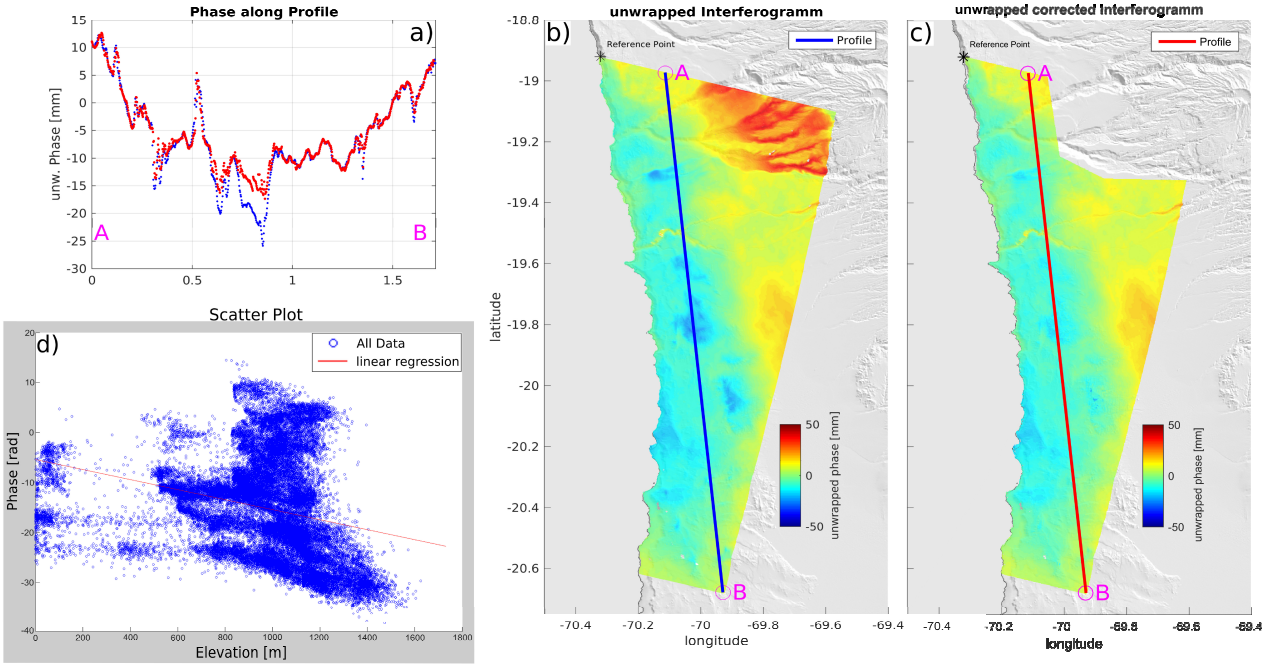

Figure 2.7: Effect of the linear inversion as correction for the layered atmospheric error. a) Uncorrected (blue) and corrected (red) interferometric phase along a N-S profile highlighted in the unwrapped interferogram RS2 04042014-15062014 (b)), c) corrected unwrapped interferogram using linear relation in the scatter plot of the phase vs. topographic height with the regression line in red (d)).

The drawback of this approach is that contributions of the tectonic deformation signal may be cut in the case of a correlation of deformation with topography. In my case, indeed, the maximum deformation signal is expected at coastal regions and decreases gradually landwards, thus towards higher altitudes. For that reason, I define non-deforming or least-deforming areas of the interferogram that are located in the far-field

of the deformation source and estimate a simple linear relationship between interferometric phase and topography in those areas. This relationship is then applied to the entire interferogram in a linear inversion approach (**Figure 2.7**).

The refraction and dispersion of radar waves caused by charged particles in the ionosphere is also a signal-path dependent error source that may influence the interferometric phase. This effect becomes stronger for larger signal wavelengths and is negligible for X- and C-band data (*Xu et al., 2004*). A processing-related error source for interferometry is aliasing, introduced by frequency spectrum doubling due to the complex multiplication in the time domain (convolution in the frequency domain). The interferogram generation thus induces spectral contributions above the Nyquist frequency as the interferogram frequency spectrum is twice as wide as that of the single SLC. I prevent aliasing by doubling SLC samples and applying an azimuth and range oversampling of two.

The interferometric data error is an expression for the quality of the data set and is used to calculate the weights (section 2.2.3) in my model approach. To account for the quality of InSAR data, the errors have to be quantified, which is not a trivial and standard processing step. As explained above, one of the main contributors to interferometric signal errors is induced by atmospheric phase delays. The turbulent atmosphere error can be expressed as correlated random functions and the water vapour concentration as main driver of phase delays follows power laws (*Hanssen, 2001*). Implying similar characteristics for total phase delay as well as a quasi-stationary and isotropic data error within the interferogram, the variance and covariance fully describe the data error, expressed as $\Delta\varphi_{atmo}$ and $\Delta\varphi_{noise}$ in equation 2.12. For the interferometric error estimation, I chose an area that is non-deforming (**Figure 2.8 a**) and calculate sample semivariograms and covariograms to estimate the data error variance and co-variance (*Sudhaus & Jonsson, 2009*). In case of co-seismic interferograms that show comprehensive deformation throughout the footprint, I defined an area with the largest distance to the deformation source. In non-deforming areas, spatially uncorrelated decorrelation is characterized by the variance, whereas spatially correlated atmospheric errors are specified by the covariogram. I generate the semi- and co-variogram by randomly sampling point pairs at different directions and with varying distances h in the non-deforming area of the interferogram (**Figure 2.8 a**). Variances and covariances of each point pair are calculated and classified in distance bins h_c (of 0.2°):

$$\text{Semi-variogram:}\quad S(h_c) = \frac{1}{2 \cdot N} \cdot \sum_{i=1}^{N} [\Omega(q_i) - \Omega(r_i)]^2 \,, \qquad (2.16)$$

$$\text{Covariogram:}\quad Co(h_c) = \frac{1}{2 \cdot N} \cdot \sum_{i=1}^{N} \Omega(q_i) - \Omega(r_i), \qquad (2.17)$$

with the number of point pairs N at locations qi and ri with LOS-displacement Ω. At longer point distances, the variogram values saturate forming a sill (**Figure 2.8 b**). I estimate the variance of the correlated data error based on the level of this sill (*Chilés & Delfiner, 1999*). A continuous covariance function is finally retrieved by fitting the sample covariogram with an exponential decay (**Figure 2.8 c**).

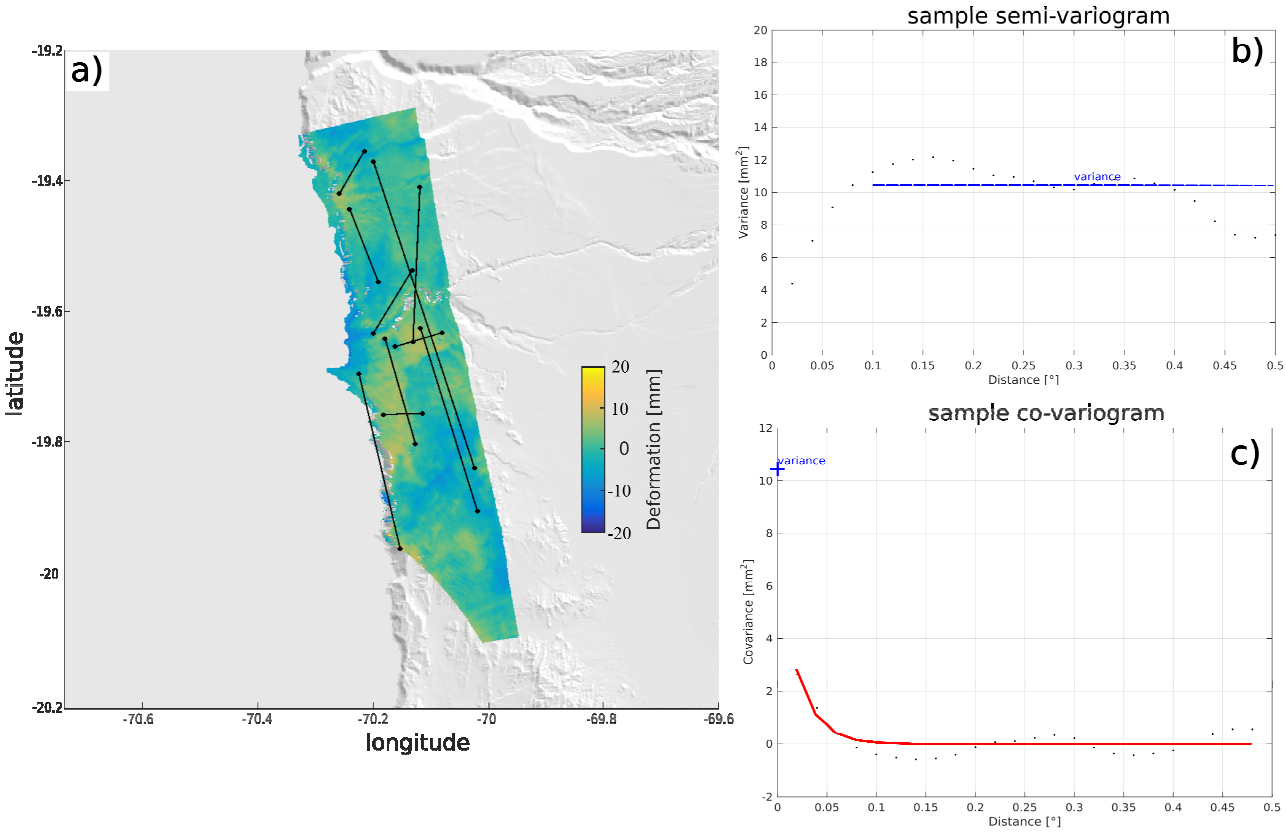

Figure 2.8: Estimation of the InSAR data error in TSX 02042014-18062014 caused by atmospheric noise with a) random point pair sampling (black dots and lines) in the non-deforming part of the interferogram (southern part was cropped) at different distances and random directions, b) sample semi-variogram of the interferogram in distance bins of 0.02° (black dots) and estimated variance (blue line), and c) sample-covariogram (black dots) with the variance (blue cross) as starting point of the fitted covariance function (red line).

One crucial requirement for stable interferometry between two SAR acquisitions is the conservation of the average phase information within a resolution cell. If this criterion is not matched, the InSAR resolution cell will decorrelate and no ground deformation can be extracted. The correlation is an expression for the magnitude of coherence of the pixels or in other words the difference in scatter characteristics of one pixel between two acquisitions (**Figure 2.5 g**). Decorrelated pixels may cause unwrapping errors, thus potentially distort extracted ground deformation and have to be identified and masked out. One reason for decorrelation is a changing acquisition geometry between two im-

ages (**Figure 2.6 f**), e.g. through different satellite orbits or by different incidence angles and is referred to as geometric decorrelation (*Gatelli et al., 1994*). Phase differences also arise, if the reflection characteristics of the pixel change due to physical changes of the Earth´s ground, e.g. through mass movements, snow cover or vegetation which is referred to as temporal decorrelation (*Zebker and Villasenor 1992*; *Hanssen 2001*). Another reason for interferometric decorrelation may be a rapid ground deformation, whereby the phase information becomes ambiguous for the phase unwrapping as the phase shift between two pixels exceeds half the radar wavelength (*Hanssen 2001*). This usually happens at epicentre locations of onshore earthquakes, but does not appear in the near-field deformation area of the Iquique-Pisagua earthquake with an epicenter located more 50 km offshore. A difference in the center frequency of the azimuth spectrum (Doppler centroid frequency) between two acquisitions causes the Doppler Centroid decorrelation. However, a high correlation value for a pixel in the interferogram means higher accuracy and also reliability of remaining phase contributions. Masking out pixels below a coherence threshold is one strategy for noise reduction. Another strategy is adaptive filtering that reduces phase jumps by smoothing pixels.

2.2.3 Quadtree subsampling and InSAR weighting

The full-resolution interferogram consists of an enormous amount of scatterers with redundant information, which requires huge computational effort for the modelling of InSAR and GPS data. Therefore, data reduction is important to efficiently model my data. Since the ground deformation of subduction zone earthquakes usually varies smoothly, I can subsample my interferometric data without losing important phase information. For this purpose, I used the Quadtree subsampling approach (*Jónsson et al., 2002*). This subsampling algorithm combines a number of interferometric data points to squared areas. The size of one square and the total number of subsampled cells is based on an arbitrary variance threshold and may differ across the interferogram. That means squares are usually smaller in areas of larger phase gradients preserving small-scale phase changes. For most of my interferograms, I decided to define an equal size of all Quadtree squares, as the observed phase gradient is rather smooth. An exception is the TSX 02042014-15062014 interferogram including the coseismic deformation of the largest aftershock that is characterized by a spatially extremely dense ground motion change (**Table C.2**). The variance threshold, thus the number of total subsampled cells was adapted to the number of independent GPS measurements (number of stations times three directions E N U). The total number of Quads ranges between 130 to 196. The phase information as well as the location of a Quadtree square is given by the mean

interferometric phase respectively location of all combined pixels in one cell. The big advantage of the Quadtree approach is that the algorithm averages over pixels instead of reducing data based on the spatial domain which may distort data error statistics (*Delouis et al., 2002*).

For my model approach (more details in section 4.2.5), each Quadtree square is handled as data point, thus requires a weight. The weighting of InSAR data is based on the idea of reducing the influence of data points that have a larger error compared to others. I calculate a data error variance-covariance matrix from the data error covariance functions (section 2.2.2, **Figure 2.8**). The diagonal of the variance-covariance matrix gives the variance (var) for each subsampled cell. The final InSAR weights W are then estimated from the cell variances as an estimate for the error:

$$W = \sqrt{var^{-1}}. \qquad (2.18)$$

Applying error statistics on the Quadtree-subsampled data, I also average the variances and covariances of all pixels in one square so that the error as the square root of the variance is reduced compared to the full-resolution variance. The error is dependent on the size of the square, which means that smaller subsampled cells have a higher variance hence a lower weight. This is compensated by their higher quantity compared to large cells. In this way, I ensure that the overall InSAR weight is balanced and not influenced by the number of subsampled cells, but instead by the variance estimate (**Figure 2.9**).

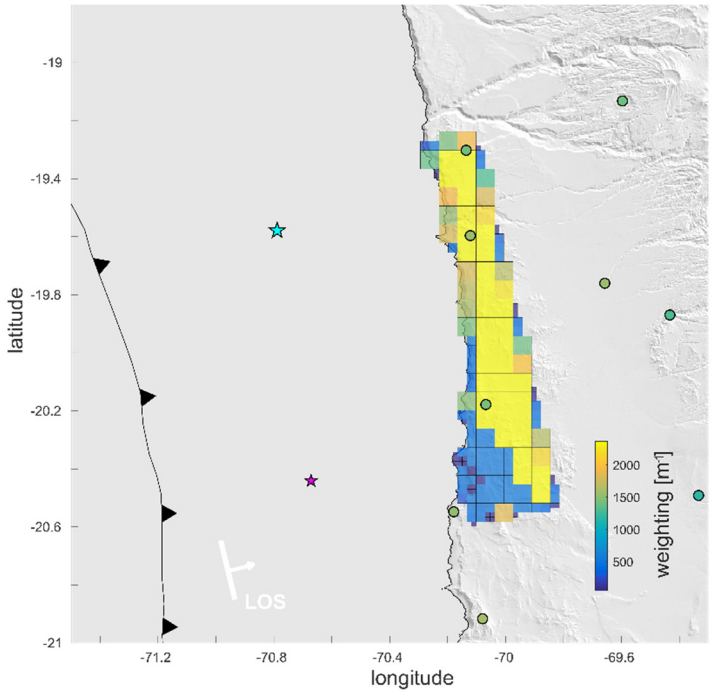

Figure 2.9: InSAR Quadtree subsampling for TSX 02042014-15062014 and weights of InSAR cells (squares) and GPS measurements (dots). Stars mark mainshock (turquoise) and largest aftershock (magenta) epicenter location.

2.3 From ground displacement data to distributed slip models

In this chapter, I introduce the general elastic modelling strategy for the inversion of geodetic data to produce kinematic models of all three stages of the seismic cycle. The case-specific adaptions for my kinematic models of the corresponding stage will be given in the sub-chapters 3.3 (interseismic), 3.4 (postseismic) and 4.2.5 (coseismic).

First of all, I invert the geodetic data received from GPS- and InSAR measurements to model subduction fault interface motion using dislocation in an elastic half-space approach (*Okada, 1992)*. Therein, the linear relation between the surface movements and slip on the plate interface is described via Greens Functions. My model geometry assumes uniform slip and model parameters include along strike- and dip-slip dislocations only. All other parameters, such as fault dimension, location, and orientation of the subduction interface are pre-defined by the SLAB1.0 subduction zone model (*Hayes et al., 2012*). This commonly used geometry model of the Chilean subduction interface (e.g. *Li et al., 2015*; *Bedford et al., 2013*) is well determined by seismic records as the majority of earthquakes occur in the seismogenic zone, where the subducting and overriding plate interact with each other.

The inversion is realized with a linear least-squares approach that allows for data weighting and regularization of fault patches (e.g. *Moreno et al., 2009*). In its simplest mathematical form the linear least-squares approach can be formulated as:

$$(G \cdot m) + e = d, \tag{2.19}$$

where G is the matrix of Greens functions, m is the model vector as slip on fault patches, e is the data error vector and d is the vector containing all GPS and InSAR ground deformation data. The least-squares approach solves equation 2.19 by minimizing the cost function:

$$C = \|d - (G \cdot m)\|^2. \tag{2.20}$$

The relative weights of each data measurement are expressed as the inverse of the data error. When aiming to invert for the slip m, equation 2.19 can be reformulated as (*Menke, 2012*):

$$m = (G^T \cdot G)^{-1} \cdot G^T \cdot d. \tag{2.21}$$

Motion on fault patches is not only modelled as slip in the co- and postseismic stage, but also as interseismic plate-interface locking. Using the backslip assumption (*Savage, 1983*), I model locking as fault patch dislocation opposite to the coseismic slip direction and thus define backslip to be negative. This assumption enables slip to occur in each

direction for all my kinematic models and thus allow relocking at any time. To regularize the inversion, I applied a Laplacian operator that minimizes slip variations of neighbouring patches based on a smoothing parameter that is determined on the trade-off between model misfit and slip roughness. The slip inversion (equation 2.21) is done with the MATLAB routine ‘lsqlin’ based on a subspace trust-region-reflective algorithm (Co*leman and Li, 1996*).

3 Characterizing afterslip and ground displacement rate increase following the 2014 Iquique-Pisagua M_w 8.1 earthquake, Northern Chile

This chapter has been published as: *Hoffmann , F., S. Metzger, M. Moreno, Z. Deng, C. Sippl, F. Ortega-Culaciati , and O. Oncken (2018), Characterizing Afterslip and Ground Displacement Rate Increase Following the 2014 Iquique-Pisagua M_w 8.1 Earthquake, Northern Chile, Journal of Geophysical Research: Solid Earth, Volume 123, Issue 5, p.4171-4192, doi: 10.1002/2017JB014970.*

3.1 Impact of the 2014 earthquake on the 1877 seismic gap

The convergent plate boundary of western South America is characterized by megathrust events with short recurrence intervals. Almost all segments south of Peru broke within the last century and generated large subduction earthquakes such as the 1960 Valdivia M_w 9.5 earthquake (*Kanamori*, *1977*) or the 2010 Maule M_w 8.8 earthquake (e.g. *Moreno et al., 2010*). The segment between 18- 23° S latitude, known as Northern Chile-Southern Peru seismic gap, has not ruptured since 1877 (M_w 8.6 Iquique earthquake), but is capable of generating a M_w ~9 earthquake (e.g. *Kelleher*, *1972*) (**Figure 3.1**). With an estimated recurrence interval of ~100 years (*Comte and Pardo*, *1991*) and two recent earthquakes in the adjoining segments, namely the 1995 Antofagasta M_w 8.1 event in the south (*Ruegg et al.*, *1996*) and the 2001 Arequipa M_w 8.3 event in the north (*Ruegg et al., 2001*), this gap was considered to be the most mature seismic gap along the South American plate boundary south of Peru. Despite the occurrence of several smaller earthquakes in the area during the last century (*Comte & Pardo, 1991*; *Engdahl & Villaseñor, 2002*) and the 2007 Tocopilla M_w 7.8 event (e.g. *Motagh et al.*, *2010*), the slip deficit remained nearly unchanged and recent geodetic studies report high plate coupling rates (e.g. *Métois et al., 2013; Li et al., 2015*). A megathrust event leading to a closure of the seismic gap has been expected for more than thirty years (e.g. *Kelleher, 1972; Nishenko, 1985*). For this reason, the region has been particularly well monitored for more than two decades already: first by the South American Geodynamic Activities (SAGA) project that started in 1993 (e.g. *Klotz et al., 1999*; *Klotz et al., 2001*) and the International Associated Laboratories (LIA) “Montessus de Ballore” project in the 1990´s (*Chlieh et al., 2004*; *Métois et al., 2013*). Since 2007 the area has constantly

been monitored by the Integrated Plate Boundary Observatory Chile (IPOC), an international effort to measure ground deformation with multi-purpose instrumentation (*Moreno et al., 2017*) extended with UNAVCO data (*Simons et al., 2010*). In 2014 and 2015, I took part in two measurement campaigns for sGPS data in Northern Chile, hence contributing to the enormous IPOC data archive (*Moreno et al., 2017*). Those two campaigns aimed to observe the late interseismic stage of the Northern Chile- Southern Peru seismic gap region and the postseismic deformation of the Iquique-Pisagua earthquake 2014. During the campaigns, I remeasured existing points by installing mobile GPS antennas for a time span of 36 to 48 consecutive hours. The antennas were installed and levelled to already existing basements on the ground.

On 1st April 2014, the Iquique-Pisagua M_w 8.1 megathrust event with a rupture length of about 100 km broke the plate interface in the central-northern part of the gap close to the town of Pisagua (e.g. *Schurr et al., 2014*; *Ruiz et al., 2014*). The mainshock nucleated in a zone of intermediate interseismic coupling and initially ruptured down-dip towards a patch of higher coupling (*Schurr et al., 2014; Hayes et al., 2014*). Aftershocks are concentrated at the southern edge of the rupture zone (*Meng et al., 2015*) with the largest one being a M_w 7.7 event that occurred two days after and 100 km SSE of the main event *(Duputel et al., 2015*). Both events led to a cumulative failure of the plate interface of about 200 km length, which reflects only a partial release of the slip deficit accumulated since 1877 (*Schurr et al.*, 2014).

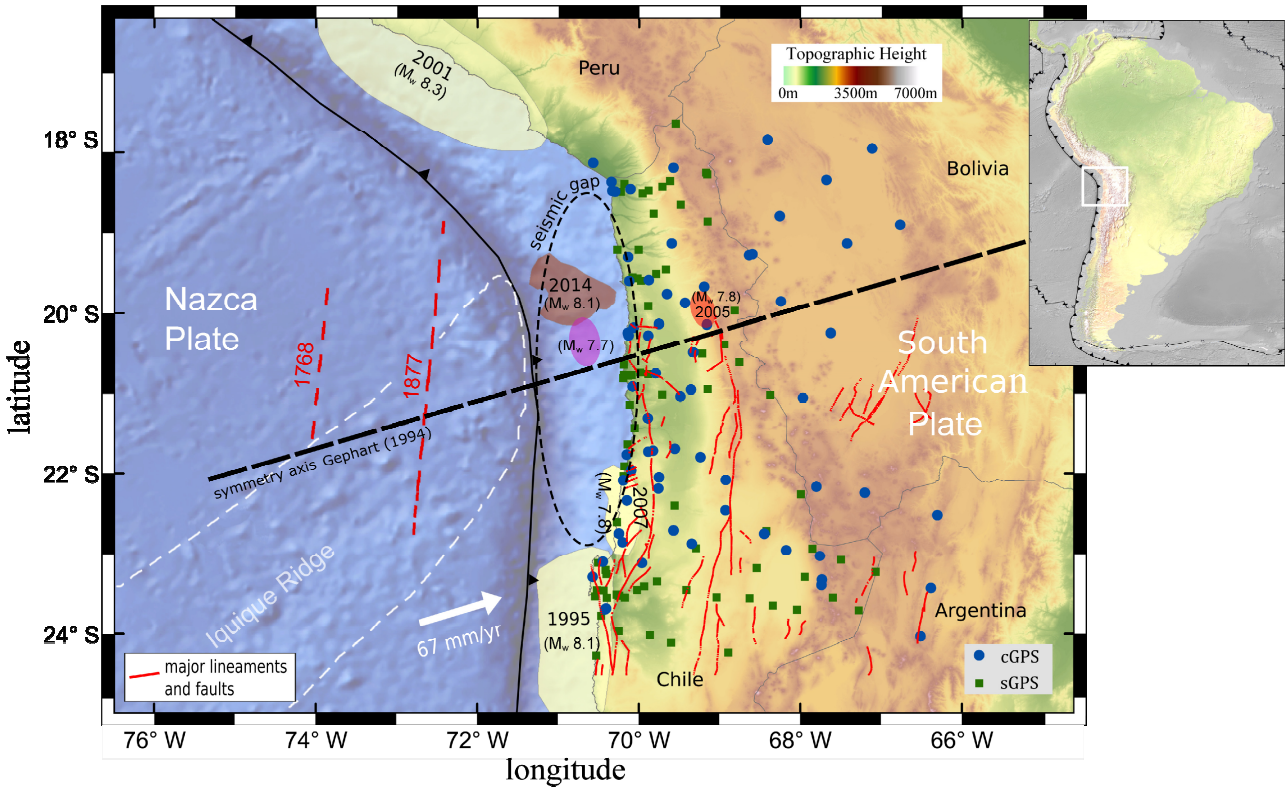

*Figure 3.1: (*previous page*) Topographic and geographic map of the Northern Chile-Southern Peru seismic gap region. Its relative location on the South American continent is shown in the inset. Rupture zones of past relevant earthquakes are indicated as shaded areas (source: USGS): the 1995 Antofagasta, the 2001 Arequipa and the 2007 Tocopilla event (yellow), the 2005 Tarapacá event (orange), the–2014 Iquique-Pisagua event (red) including its largest aftershock (magenta). The Northern Chile- Southern Peru Seismic gap is highlighted with a dashed ellipse. Inferred along-strike extents of the two last megathrust events in the gap area are indicated with dashed red lines (Comte & Pardo, 1991). The blue circles (continuous GPS stations, cGPS) and green squares (survey-mode GPS stations, sGPS) mark the location of GPS stations used in this study. The Iquique Ridge is marked as dashed white line (Geersen et al., 2015).Major geologic faults and lineaments are highlighted in red (Reutter et al., 1994). The topographic symmetry axis of the Andes is indicated as black dashed line (Gephart, 1994).*

In this study, we present new Global Positioning System (GPS) data acquired before and after the Iquique-Pisagua earthquake. From the acquired time series, we extract inter- and postseismic deformation rates to analyse the temporal and spatial evolution of deformation following the earthquake. We further investigate deformation rate changes on the unbroken southern segment of the seismic gap. Interpreting surface displacements is one of the key elements in understanding the behaviour of subduction zones. After a large earthquake, lithospheric stress is released in three principal processes: (1) continued slip of the fault referred to as afterslip (e.g. *Marone et al., 1991*; *Perfettini et al., 2010*), (2) poroelastic rebound due to pore fluid pressure changes (e.g. *Peltzer et al., 1998*; *Jónsson et al., 2003*), and (3) visco-elastic relaxation of the mantle (e.g. *Nur & Mavko, 1974*; *Wang et al., 2012*), while the fault simultaneously relocks during the postseismic stage. These postseismic processes may take place simultaneously and vary in duration between months to decades depending on the magnitude of the event as well as on the rheology of the deformed material and/or the frictional properties of the slipping interface. In our analysis, we assume afterslip to be the driving mechanism controlling early postseismic deformation, although we recognize that other processes may contribute to the GPS derived surface displacements. Of particular interest to us is the assessment of slip behaviour in the postseismic stage across different tectonic segments, especially towards the southern edge of the pre-2014 seismic gap. The rupture zone of the Iquique-Pisagua event only covers less than one third of the 1877 rupture as inferred by *Comte and Pardo (1991*). This means that the southern segment of the Northern Chile-Southern Peru seismic gap now has accumulated a slip deficit for more than 140 years (**Figure 3.1**). For the regional earthquake hazard assessment, it is important to understand, how the 2014 earthquake affects this segment of the gap. Thanks to the

dense spatial coverage of GPS observations in Northern Chile (**Figure 3.1**), we can characterize regional crustal deformation in great detail. In order to evaluate spatial and temporal changes in plate coupling, we compare GPS rates before and after the Iquique-Pisagua event on the northern and southern part of the 1877 seismic gap. We first isolate tectonic GPS rates from non-tectonic contributions (section 3.3.2), then use a combination of elastic and visco-elastic slip models to analyse the interseismic and post-seismic stage of the Iquique-Pisagua earthquake (section 3.3 and 3.4), discuss the interpretation of the model results (section 3.5) and finally draw conclusions (section 3.6).

3.2 GPS observations and model approach

3.2.1 GPS data processing

The geodetic instrumentation of the IPOC (*Moreno et al., 2017*) and LIA network (*Chlieh et al., 2004; Métois et al., 2013*) include GPS sites that are operated continuously (cGPS) and in survey-mode (sGPS), the latter of which are also referred to as campaign GPS sites. We include data from 75 cGPS stations and 77 sGPS sites covering a latitudinal range of 17-24° S from the coast to 450 km inland (**Figure 3.1**). The sGPS sites are not strictly measured periodically, but at least once every three years for at least 48 consecutive hours, thus delivering less accurate positioning than the cGPS stations. But since the sGPS time series extend further back in time compared to the cGPS time series, they are most helpful to estimate interseismic rates prior to the 2014 Iquique-Pisagua earthquake (**Figure B.1**).

All GPS data are organized in units of 24 h periods and were processed using the Earth Parameter and Orbit System software (EPOS) (*Deng et al., 2016*). We calibrated the positions using absolute antenna phase centres provided by the International Global Navigation Satellite System Service (IGS) (*Schmid et al., 2007*) and compensated tidal effects using the Finite Element Solution tide model (FES2004) (*Lyard, et al., 2006*). We estimated station coordinates and tropospheric wet zenith delays using random-walk parameters for every hour (*Gendt et al., 2013*). Finally, we estimated coordinates in network mode and aligned them to the IGS combined coordinate product reducing the impact of the Earth rotation parameter (*Rebischung et al., 2015*). The GPS processing results are compatible with the International Terrestrial Reference Frame ITRF2014 (*Altamimi et al., 2016*), which is based on a kinematic model without taking into account the non-deformational rotation of South America. We compute our final horizontal velocity field relative to the stable South American Plate by applying an Euler Pole

rotation (21.44° S, 125.18° W, 0.12° Myr^{-1}, *Moreno et al., 2011*) comparable to the NNR-Nuvel-1A model (*DeMets et al., 1994*). Examples of cGPS (**Figure B.2**) and sGPS (**Figure B.3**) time series and more details of GPS data processing (**Text B.1** and **Figure 2.2**) and reference frame realization (**Figure B.4**) are provided in the auxiliary material.

3.2.2 Extracting the tectonic GPS signal

Our GPS time series cover a time interval of more than a decade (1999-2016 for sGPS and 2003-2016 for cGPS; **Figure B.1**) and include a variety of tectonic and other signals occurring at the convergent plate boundary. We excluded three months of data preceding the Iquique-Pisagua event 2014 from our time series as they were affected by preseismic transients (*Bedford et al., 2015*) (see also section 3.1). The recorded ground displacements are the sum of tectonic, atmospheric, instrumental and other signal contributions, like interseismic shortening, coseismic displacements, instrumental failure (e.g. antenna replacements), postseismic transients, seasonal oscillations:

$$\delta_{\mathrm{GPS}}(t) = \delta_{\mathrm{interseismic}}(t) + \delta_{\mathrm{coseismic}}(t) + \delta_{\mathrm{AntennaOffset}}(t) + \delta_{\mathrm{postseismic}}(t) + \delta_{\mathrm{seasonal}}(t). \quad (3.1)$$

Following the approach of *Metzger et al.* (*2013*) and *Bevis & Brown* (*2014*), we simulate these signal types in our GPS displacement time series with (**Figure 3.2**):

$$\delta_{\mathrm{GPS}}(t) = [\mathrm{A}+\mathrm{B}\cdot(t-t_r)] + \left[\sum_{\mathrm{eq}=1}^{n_{\mathrm{eq}}} C_{\mathrm{eq}}\cdot H\left(t-t_{\mathrm{eq}}\right)\right] + \left[\sum_{\mathrm{ao}=1}^{n_{\mathrm{ao}}} D_{\mathrm{ao}}\cdot H(t-t_{\mathrm{ao}})\right] + \left[\sum_{\mathrm{p}=1}^{n_p} E_p\cdot\log\left(1+\frac{t-t_{\mathrm{eq}}}{T}\right)\right] + [F_1\cdot\sin(2\pi\cdot t)+\mathrm{F}_2\cdot\cos(2\pi\cdot t)+F_3\cdot\sin(4\pi\cdot t)+\mathrm{F}_4\cdot\cos(4\pi\cdot t)]. \quad (3.2)$$

The constant *A* corrects the time series for any initial offset and the linear term *B* represents a constant plate velocity in each stage of the seismic cycle (*Wang et al., 2012*) with respect to a pre-defined reference time t_r. Discontinuities can arise either from coseismic displacements or antenna offsets. The mathematical approach to model such data offsets is a Heaviside function H(t), where n_{eq} earthquakes (or n_{ao} antenna offsets, respectively) induce a step with amplitude C_{eq} (D_{ao}) at times t_{eq} (t_{ao}). The challenge is to distinguish artificial steps in the displacement function from earthquake induced ground

motion. Postseismic relaxation observed after large earthquakes is represented by a logarithmic transient E_p with a non-linear parameter T. *Bevis and Brown* (2014) showed that the logarithm is nearly insensitive to T, hence this component can be linearized by setting T equal to one year. The most rapid deformation within the first weeks after the earthquake might not be perfectly represented by this simplification (**Figure 3.2 b**). However, we demonstrate in section 3.3.1 that the linear term is most important for our velocity analysis. The last term in equation 3.2 represents an elastic loading response of the crust to seasonal changes in the water cycle (e.g. *Heki, 2001*; *Van Dam et al., 2001*). We apply a Fourier series for terms F_1 to F_4 that represent two annual and two semi-annual terms (*Dong et al., 2002*).

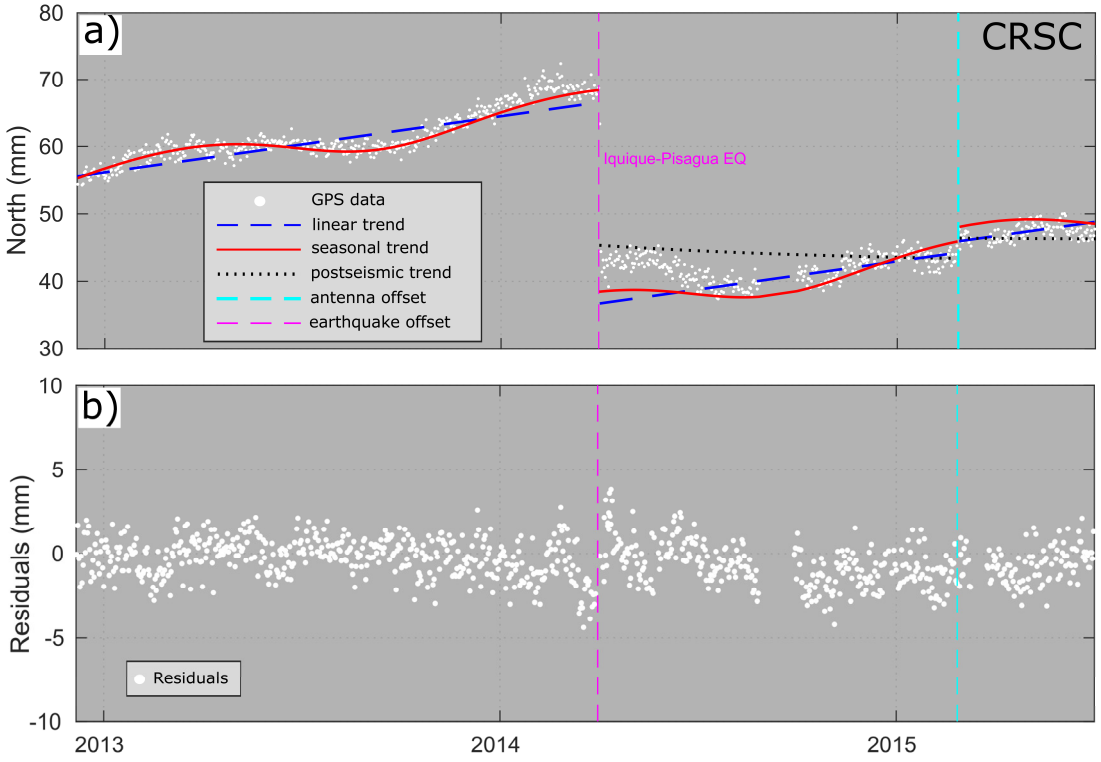

Figure 3.2: a) Time series of station CRSC (see Figure 6 for location) and its decomposition into various model trajectories highlighted in different colors. b) The model residuals of a) (based on equation 2.2).

To estimate all parameters mentioned above and to exclude irrelevant signal contributions (instrumental offsets and seasonal loading) from further analysis, we modelled the cGPS time series component-wise using a least-squares inversion (**Figure 3.2**). To exclude co- and postseismic signals related to other events than the 2014 Iquique-Pisagua earthquake, we developed a semi-automated earthquake selection procedure that extracts relevant earthquakes from the US National Earthquake Information Center (NEIC) catalogue. We used a distance-magnitude filter to identify all events that could po-

tentially have affected our GPS time series, i.e. that occurred within a radius of 20 to 2500 km and with an incremental magnitude of 5 to 8.

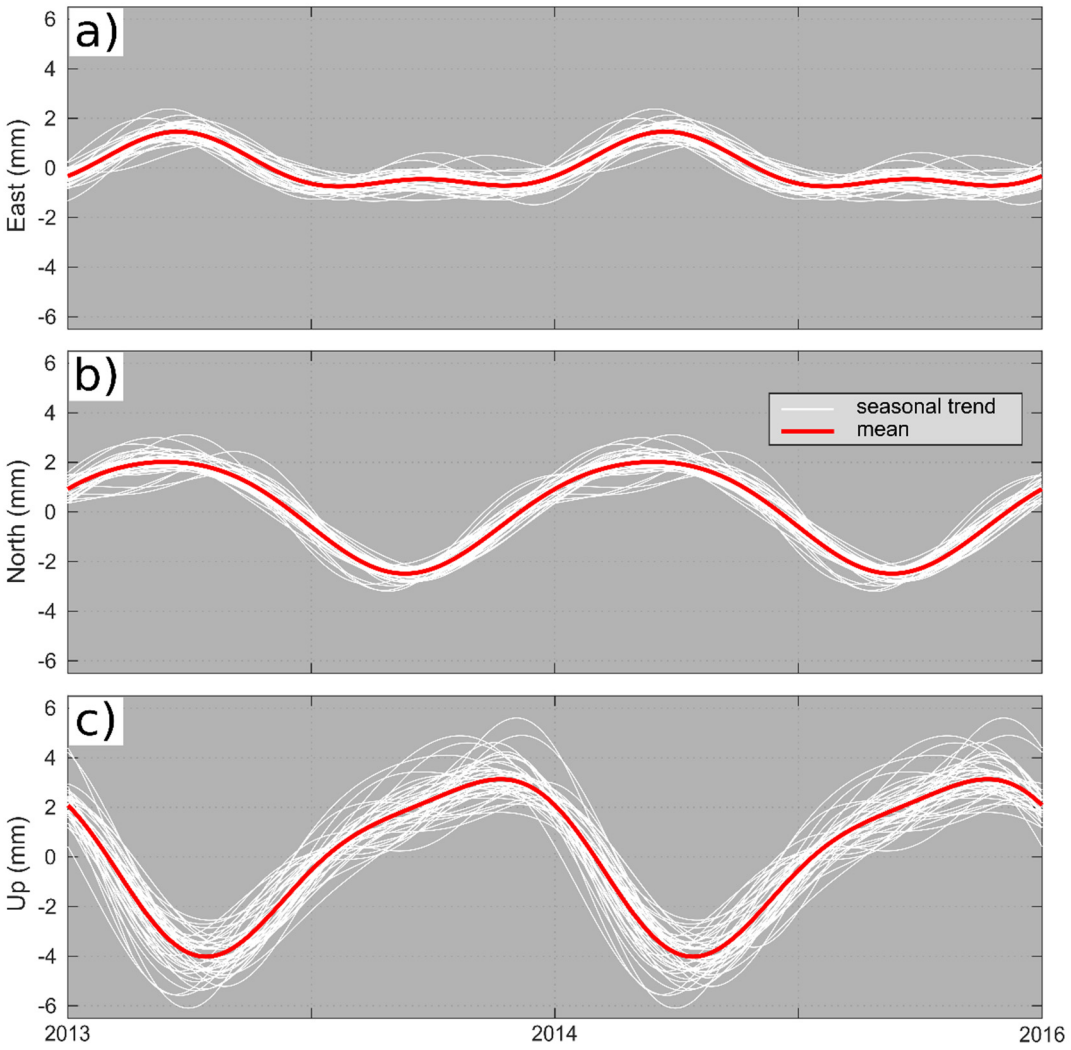

*Figure 3.3: Modelled seasonal signal on the a) East, b) North and c) Up components of 50 cGPS stations. Stations with significant data gaps (**Figure B.1 b**) were excluded from the analysis.*

All remaining offsets in the time series were then visually checked and manually classified as antenna offsets. The average rms (root mean square)-error of all stations is 1.2 mm for the East, 1.0 mm for the North and 2.0 for the vertical component; stationwise, it ranges from 0.9 mm (LVRA) to 1.9 mm (PCAL) in the East component, 0.8 mm (ANT2) to 2.4 mm (PICN) in the North component and 1.5 mm (MCLA) to 2.7 mm (UTAR) in the vertical component (**Table B.1**). The residuals of the time series inversion are close to zero, thus indicate that our approach in equation 3.2 seems reasonable for approximating the observed GPS ground motion signal (**Figure B.2**). We then subtracted the non-tectonic signal contributions, the seasonal trend and the antenna offsets,

from the time series for each station individually (**Figure B.2**). We further find that the seasonal changes are surprisingly consistent over the whole cGPS network (**Figure 3.3**). The East component contains a clear bi-annual signal with one peak in February/March and a second lower peak in September, whereas the north component exhibits a clear annual signal with a peak in February/March and a low in September. The vertical component also exhibits a one-peak annual trend, in which the highs and lows are shifted in respect to horizontal components to October/November (peak) and May/June (low). The campaign GPS data have a much lower temporal resolution and have been collected irregularly and in different seasons (**Figure B.3**). Thus, the extraction of the tectonic signal is more challenging here. We used the seasonal parameters estimated from the cGPS data to correct the campaign data and applied a seasonal model derived from the mean of each parameter F_1 to F_4 in equation 3.2 (**Table B.2, B.3** and **Figure B.5**).

3.2.3 Data time windows and model strategy

In order to better understand the different stages of the Northern Chile seismic cycle, we split the GPS data into an interseismic part prior to and a postseismic part after the 2014 Iquique-Pisagua earthquake. The interseismic interval is covered by three to eight GPS campaigns between 1999 until end of 2013 and by continuous GPS observations spanning a time interval from 2003 until end of 2013 (data from 2014 was cut due to observed GPS transients, see also section 3.3.1) (**Figure B.1**). The postseismic interval contains another two to three campaign GPS surveys, covering a time period of three weeks after the mainshock until April 2016, and daily solutions from 3 April, 2014 to April 2016. To not contaminate the afterslip analysis with the largest aftershock occurring on 3 April, we excluded the cGPS solutions of the first two days after the mainshock. To analyse the temporal evolution of the postseismic response to the earthquake, we further subdivided the postseismic part into three periods that best match the timing of the campaign GPS surveys (**Figure B.1 a**). The intervals comprise days 2-16, days 17-334 and days 335-717 after the mainshock and are henceforth called Period 1, 2 and 3, respectively.

We invert the observed GPS surface displacements for estimating slip (respectively backslip) on the subduction interface using elastic and visco-elastic half-space models (*Okada, 1992*). For the interseismic model, we assume elastic deformation (*Okada, 1992*) to be the dominant driver (e.g. *Chlieh et al., 2011*; *Métois et al., 2016*). For the postseismic models of Periods 1-3, we combine the elastic afterslip model with visco-elastic mantle relaxation using the PyLith software (*Aagaard et al., 2013*). In the visco-elastic finite element modelling (FEM) approach, we use four different material blocks

to discriminate between an elastic crust and lithospheric mantle and a visco-elastic asthenospheric mantle (**Text B.2**, **Figure B.6**). The model geometry of the subducting slab is based on the SLAB1.0 model (*Hayes et al., 2012*) and the elastic-visco-elastic boundary is based on the model of *Tassara & Echaurrens (2012)*. We fixed the Young's modulus to 100, 120 and 160 GPa for the continental crust, oceanic crust, and mantle layers, respectively (*Li et al., 2015*), and use the linear Maxwell rheology in the visco-elastic body. The Poisson's ratio is set to 0.265 and 0.30 for the continental and oceanic crust (*Christensen, 1996*).

In general, Maxwell viscosity is preferably applied for long-term viscosity estimates, whereas Burgers viscosity resolves short-term rheologic transients typical for the early postseismic stage (e.g. *Trubienko et al., 2013; Li et al., 2015*). We decided to use Maxwell rheology to reduce complexity and computational cost. When using pre-determined time windows like here, the effective viscosity is defined as the best-fitting Maxwell viscosity (*Li et al., 2017*). This approach has been successfully applied for GPS data in Chile before (*Bedford et al., 2016; Li et al., 2017*), but we cannot exclude the possibility that this simplification creates artefacts in our slip models as discussed in section 3.5. To simulate the viscous response to coseismic stress perturbation, we used the slip model of *Schurr et al.* (*2014*) and estimated the visco-elastic deformation in the respective model Periods 1-3 (**Tables B.7, B.9 and B.11**). We tested different values of the Maxwell viscosity of the continental mantle and kept all other parameters constant, including the oceanic mantle viscosity, which we fixed to 10^{20} Pa s (*Hu et al., 2004; Moreno et al., 2013*; *Li et al., 2015*). Continental viscosity was varied between 10^{18} Pa s (highly viscous) and 10^{20} Pa s (nearly elastic) in our tests and was finally constrained to 2×10^{19} Pa s, based on the best data-fit (rms, see examples for Period 2 in **Figure B.7** and **B.8**). Using these fixed viscosities, we removed the predicted visco-elastic signal component from our GPS observations in advance and thus account for the viscous mantle relaxation. In a second step, we subtracted the interseismic loading component from each postseismic period to invert for the afterslip signal only (more details can be found in section 3.4.1).

The elastic model geometry of the plate interface slip is also based on the SLAB1.0 subduction zone model (*Hayes et al., 2012*), from which we utilized the region from 17.5 to 26° S latitude. Slip is modelled as along strike and up-dip dislocations on 1016 triangular fault patches with an average area of 170 km^2 and constrained to a maximum depth of 65 km, assumed to represent the Moho depth (*Husen et al., 2000*; *Chlieh et al., 2011*). We invert Green's functions describing slip at depth on the interface geometry to best fit the observed GPS displacements in a least-squares approach (*Okada*, 1992). We do not constrain the rake, thus allow backslip to occur. For regularization of the inver-

sion, we applied a Laplacian operator, making the solution more stable while minimizing slip variations of neighbouring patches based on an input smoothing weight. The strength of the regularization is determined by considering the trade-off between misfit and slip roughness (**Figure B.9**). In the interseismic backslip model, three additional model parameters describe an Euler pole that accounts for the motion of the Central Andean sliver (*Bevis et al., 2001*). The sliver motion is collinear to the plate convergence and causes back-arc shortening in the Subandeans (*Chlieh et al., 2011*)**.** This model modification allows to better describe the abnormally high interseismic GPS rates (with respect to the overall convergence rate in Northern Chile) that cannot be explained by an elastic response of the plate interface alone (e.g. *Métois et al., 2014*; *Métois et al., 2013)*. The Green´s functions are inverted with the MATLAB routine 'lsqlin', a subspace trust-region-reflective algorithm based on the interior-reflective Newton method (Co*leman and Li, 1996*). To avoid physically unreasonable slip rates and additionally improve model resolution, we apply constraints for minimum slip (*Du et al., 1992*) based on the constant plate velocity of 67 mm/yr (*Angermann et al., 1999*). The respective minimum slip for inter- and postseismic models corresponds to the "negative" backslip rates of -61 mm/yr that would equal to a locked (fully coupled) interface dipping 25-30° (e.g. *Husen et al., 2000*).

3.3 Interseismic period

3.3.1 Constraining GPS rates

The interseismic ground displacements in our GPS network were affected by two major earthquakes in Northern Chile (**Figure B.10**): the 2005 Tarapacá Mw 7.8 earthquake (*Delouis & Legrand*, *2007*; *Ruiz et al,* 2014) and the 2007 Tocopilla Mw 7.8 earthquake (*Motagh et al., 2010; Weiss et al.*, *2016*). We therefore excluded all data between November 2007 and January 2008, when GPS rates were dominated by afterslip from the Tocopilla event (e.g. *Delouis et al., 2009*) and data in May and June 2005 due to the Tarapacá event. We further excluded all GPS data in the three months before the Iquique-Pisagua main rupture on 1 April, 2014, where clear transient signals appear in the time series (**Figure B.11**). These distinct features reflect either a slow slip event preceding the mainshock (e.g. *Yagi et al., 2014*; *Ruiz et al., 2014*) or represent a surface expression of precursors of seismic slip (e.g. *Schurr et al., 2014*; *Bedford et al., 2015*). We split the interseismic GPS data into three parts to investigate on rate differences in the interseismic stage: (A) a pre-Tarapacá interval with data before June 2005, (B) a time

interval between the Tarapacá and the Tocopilla event from July 2005 until October 2007 and (C) a post-Tocopilla interval with all data from February 2008 until end of December 2013.

In all three parts of the time series, we removed data points with a position error above the 99.5th percentile and/or each point whose position differs from its neighbour by more than three times the standard deviation of the first derivative of the time series. For each of the three interseismic subsets of continuous time series longer than one year, we estimate the interseismic rate by extracting the linear trend from the signal as explained in section 3.2.2. From the sGPS data, we derived the interseismic rates using linear regression. The rate differences of the 1d-horizontal velocities between the pre-Tarapacá (A) , the inter-earthquake (B) and post-Tocopilla (C) periods do not exceed 5 mm/yr (**Table B.4**)**.** We use the mean of all three periods, equally weighted as interseismic velocity for further analysis. The resulting velocity may not fully account for interseismic transients observed in the epicentre regions of the Tarapacá and Tocopilla events (e.g. *Weiss et al., 2016*). Uncertainties of the resulting cGPS rate model parameters are calculated from the mean instrumental error in each model interval. Given the low number of observations, calculating campaign GPS errors is more challenging. Following *Geirsson et al. (2006),* we correct the rms fit by the number of model parameters (two in the linear case) and normalize it by the full length of the time series.

The resulting interseismic rates (**Table B.5, B.6**) were corrected for the Andean sliver motion (see section 3.2.2 and 3.3.2) (**Figure 3.4 a**). They exhibit a consistent ENE-motion that is collinear to the plate convergence over the entire area of interest in Northern Chile, even in the far-field of the network. The interseismic observations are characterized by a gradual rate decrease of about 7 mm per 100 km from coastal stations to stations on the Andean Plateau. Maximum horizontal GPS velocities of up to 35.3+/-3.1 mm/yr (station MEJS) occur at coastal stations at the southern edge of our GPS network at a minimum distance of ~80 km to the trench, whereas minimal horizontal GPS velocities of 14.1+/-5.2 mm/yr (PAJA) occur on the Andean Plateau at a longitude of about 67° W and ~490 km distance to the trench (**Figure 3.4 a**). The rates also exhibit a north-nouth gradient from coastal stations close to the border to Peru that show significantly slower GPS rates of 20.3+/-1.2 mm/yr (LYAR) to coastal stations in the south like the afore mentioned station MEJS. The vertical GPS data (**Figure 3.4 b**) exhibit uplift for most of the coastal stations with a maximum of 9.0+/-1.4 mm/yr (PB05) at sGPS stations near Mejillones peninsula at 23° S latitude and a maximum of 5.9+/-2.1 mm/yr (PSGA) at cGPS stations close to the epicentre of the Iquique-Pisagua earthquake 2014. Further inland, the vertical displacements show a more inhomogeneous deformation pattern with subsidence rates of less than 2 mm/yr south of 22° S.

3.3.2 Model results

The weights for the model approach of 50 cGPS and 51 sGPS stations are defined as the square of the inverse error. Given the inhomogeneous distribution of cGPS and sGPS stations, we additionally tested different weighting ratios $w = w_{sGPS}/w_{cGPS}$ between campaign and continuous data by performing a least rms-error analysis (*Cavalié et al., 2013*). A weighting ratio of w=2.5 generates the best data fit (**Figure B.12 a**). Based on a similar approach, we increased the uncertainty (i.e. decreased the weights) of our vertical GPS components by a factor of five for cGPS and a factor of ten for sGPS data (**Figure B.12 b**). The different weighting is necessary as in general, GPS data are more sensitive to horizontal motion and the vertical instrumental error might be underrepresented, especially for episodic GPS data acquisitions. Our interseismic backslip model locates the Euler pole representing the motion of the Andean sliver in central Ecuador (1.20° S, 77.31° W +0.30° Myr^{-1}). Amplitudes and azimuths of the resulting sliver motion are in agreement with *Métois et al.* (*2013*; 54.5° S, 37.5° W, -0.15° Myr^{-1}), whose model was based on a different station network (**Figure B.13**). However, the Euler pole of *Métois et al.* (*2013*) is located to the south of Chile, thus opposite of our pole, suggesting smaller sliver motion southwards, where the active Eastern front is lacking. In our case, the sliver rotation would be anticlockwise with a main NNE-component of ground motion, which is in agreement with the preferred convergence direction in Northern Chile. The shortening of the Andean sliver accounts for 12-14 mm/yr of the measured ground motion, which is consistent with other studies (e.g. *Brooks et al., 2011*; *Métois et al., 2013*). This rate corresponds to about 19% of the total convergence rate, that hence has to be reduced from 67 mm/yr (*Angermann et al., 1999*) to 54 mm/yr in Northern Chile for modelling if only data from the Chilean forearc is considered (**Figure 3.4 a**). The backslip model yields an estimate for the degree of coupling of the plate interface in the decade before the Iquique-Pisagua earthquake. The coupling degree can easily be inferred from the slip rate: the higher the rate of backslip, the higher the degree of coupling. Coupling maps (e.g. *Li et al., 2015*; *Métois et al., 2016*) are given in ratios between 0 and 1, with 0 referring to freely slipping fault patches and implying that the interface moves with the full rate of the subducting Nazca Plate (54 mm/yr after removal of 13 mm/yr of sliver motion). Slip is generally considered as interface motion towards the trench and assumed to be positive. Therefore, backslip is directed away from the trench and assumed to be negative (*Savage, 1983*). Similar to previous plate interface coupling studies in Northern Chile (e.g. *Chlieh et al., 2011*; *Li et al., 2015*; *Métois et al., 2016*), our interseismic backslip model demonstrates a heterogeneous coupling distribution ranging from almost free slipping to full coupling of the plates

with rates of up to 61 mm/yr effectively realistic (**Figure 3.4 c**). The backslip pattern in Northern Chile exhibits several highly coupled patches with rates >50 mm/yr along the Chilean coastline at an intermediate depth of 30 to 40 km. These patches are separated from each other by low coupling areas of backslip rates less than 30 mm/yr.

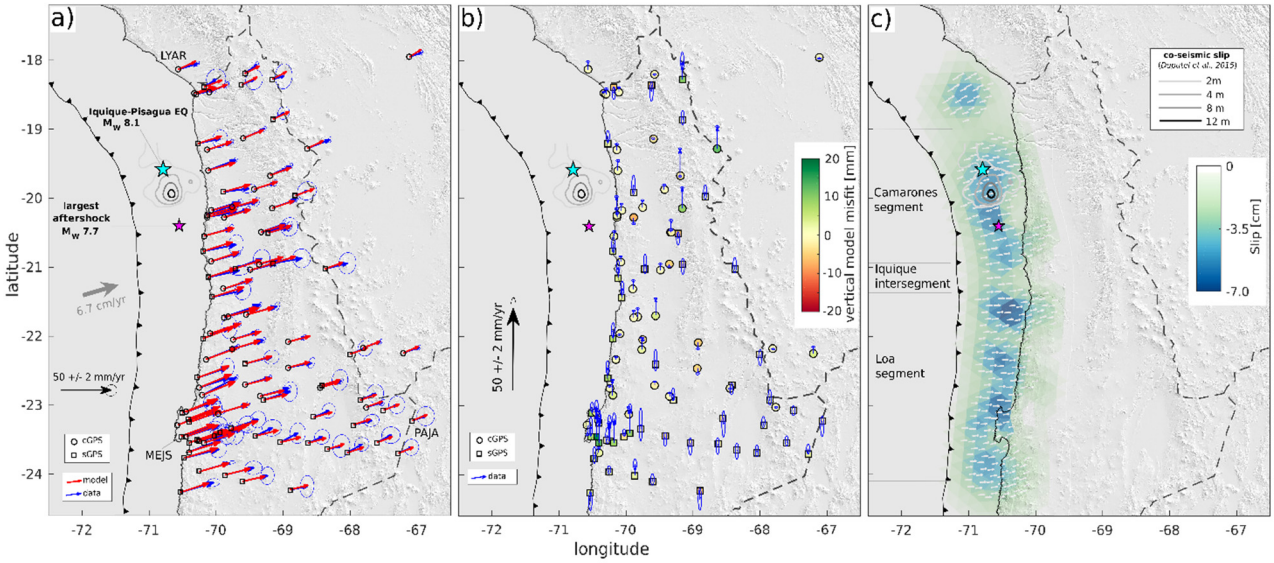

Figure 3.4: a) Modelled (red) and observed (blue) GPS displacements with 1-sigma uncertainties plotted in a stable South America reference frame, b) corresponding vertical GPS observations (blue) with corresponding misfit indicated in colors (data minus model) and c) modelled interseismic backslip on triangular fault patches on the subduction interface (white arrows indicate rake). Other features represent the coast line (solid line), the fault trench (solid line with triangles), political boundaries (dashed lines) and the coseismic slip model and aftershock location (Duputel et al., 2015). Inferred segment boundaries are marked with grey lines following the nomenclature of Métois et al. (2016).

Most prominently, the central segment between 19.3-21° S latitude referred to as the Camarones segment (**Figure 3.4 c**), where the Iquique-Pisagua earthquake ruptured, is clearly separated by lowly coupled zones to the north and south. The low coupling corridor at 21° S is referred to as Iquique low coupling zone (or Iquique interseismic segment) and was confirmed by others with slightly different extents (e.g. *Li et al., 2015*; *Métois et al., 2016*). Our interseismic backslip model generally compares well to previous coupling maps that detect highest coupling rates at a depth range of 20-40 km (e.g. *Chlieh et al., 2011*; *Béjar-Pizarro et al., 2013*; *Li et al., 2015*; *Métois et al., 2016*). But in contrast to these maps, our results show very low backslip rates at shallower depths <15 km, which could be explained by a lack of sensitivity in this depth range. For sensitivity analysis, we perform a checkerboard test, in which we generate rectangular slip and backslip patches of size ~80x80 km in a checkerboard pattern of +/- 1 m slip on our

interface geometry. This interface slip is forward modelled to yield ground deformation for our GPS network and inverted again. Inversion results can then be compared to the checkerboard geometry. The interseismic model is generally well resolved south of 19° S and in a depth range below 20 km, and is less sensitive for the very north of our study area and the shallow interface parts (**Figure B.14 b**). Overall, we fit the GPS observations very well with a rms-misfit of only 1.8 mm/yr in horizontal direction (**Figure B.15 a**) and 1.7 mm/yr in vertical direction (**Figure B.16 a**)**.** In the north of the GPS network, the Euler rotation seems somewhat overpredicted, which causes a slightly underpredicted backslip rate. Our model fit the vertical data generally well, with a few exceptions at sGPS coastal stations to the south (**Figure 3.4 b** and **B.17 a**)**.**

3.4 Postseismic period

3.4.1 Constraining static GPS displacements

We used the Euler pole obtained from the interseismic model (section 3.3.2) to correct the postseismic data for a sliver motion. Unlike for the estimation of interseismic rates, where we extracted linear rates, we extracted static displacements for the three consecutive intervals, Periods 1–3, directly from the GPS time series (**Tables B.7-B.12**). Outlier detection and calculation of individual uncertainties for cGPS in the postseismic stage is the same as in section 3.3.1. For sGPS data, we increased the instrumental error by adding the overall rms-position-error of all (usually 3-5) daily solutions of one campaign. To further account for the instrument set-up error, we lowered the relative weights for sGPS data with respect to cGPS data in the inversion (details in section 3.4.2). From the postseismic static displacements, we subtracted the visco-elastic response signal determined by the independent viscous model (section 3.2.3) in all three periods to account for the postseismic mantle relaxation (**Tables B.7, B.9, B.11 and Figure B.18**). We still allow backslip to occur to assess possible rate changes on the interface in adjoining segments of the ruptured Camarones segment. Additionally, we subtracted the interseismic backslip rates, assuming temporal consistency (**Table B.13**) to account for relocking and extract the afterslip signal. For non-active stations before 2014, we predicted an average relocking velocity based on our interseismic slip model (**Figure 3.4 c**).
In Period 1 (days 2-16), stations north of 21° S exhibit trenchward (WSW) motion of up to 46.0+/-1.2 mm ~80 km SE of the max. slip (station CGTC, **Figure 3.5 a, Table B.7**). This motion is oriented opposite to the interseismic ground displacement direction prior to the event. Stations south of 21° S remain unaffected by this early postseismic motion

and continue to move in plate convergence direction (2.3+/-1.2 mm, PB03). The latitudinal displacement gradient is not symmetric around the peak slip region at 20° S: from there, the displacement decrease is ~14 mm within the first 100 km northward, whereas the decrease is faster, ~18 mm within the first 100 km, southward (**Figure 3.5 a**). The vertical GPS data (**Figure 3.5 d**) exhibit subsidence of all stations, with a maximum of 25.4+/-2.3 mm (PSGA) at stations that are located close to the aftershock epicentre.

In Period 2 (days 17-334), the displacement pattern slightly changes and the maximum trenchward displacement has shifted about 50 km away from the coast reaching 58.9+/-2.2 mm at cGPS station PB11 (**Figure 3.5 b, Table B.9**). The asymmetric surface deformation pattern becomes more prominent, with a displacement decrease of ~34 mm northward and a decrease of ~46 mm southward within the first 100 km (**Figure 3.5 b**). Moreover, the abrupt displacement sign change of stations from north to south of 21° S is more obvious. GPS station PB01 is the southernmost station that moves towards the rupture zone (11.8+/-1.3 mm), whereas GPS station PB02, located only ~40 km south of PB01, moves opposite (16.7+/-1.3 mm) before the relocking signal is subtracted. All stations south of 21° S move collinear with the plate convergence vector with a maximum of 28.9+/-2.0 mm at station LIVE which nearly corresponds to its interseismic rate of 31.7+/-5.5 mm/a. The vertical GPS data (**Figure 3.5 e**) close to the main rupture exhibit subsidence of up to 23.9+/-2.6 mm (PSGA), whereas stations towards the south of the epicentre region show uplift of 33.0+/-2.8 mm (PRO2). This spatial sign change may represent the hinge line of postseismic uplift to subsidence at a latitudinal range of ~21-22° S. In general, the vertical displacement pattern seems more coherent for cGPS than sGPS observations. Uplift rates of sGPS data towards the south may be systematically overestimated compared to cGPS rates.

During Period 3 (days 335-717), most of the stations north of 21° S have significantly reduced their trenchward motion and relocking dominates over the afterslip component of the signal, e.g. the cGPS station (PSGA) closest to the mainshock exhibits a displacement of 5.0+/-3.7 mm towards ENE before subtracting relocking (**Figure 3.5 c**, **Table B.11**). Stations south of 20.5° S feature ENE displacement that increases southwards from 15.4+/-2.2 mm (AEDA) to 35.8+/-1.4 mm (LIVE) before subtracting relocking velocity (**Figure 3.5 c**). The vertical GPS data (**Figure 3.5 f**) is relatively inhomogeneous. Coastal stations close to the main rupture still mostly exhibit subsidence with a maximum of -19.3+/-6.1 mm (PSGA), whereas few stations south of 21° S (8.5+/-2.2, PB03) and in Bolivia (3.7+/-1.7, BMWS) experience uplift. The sGPS rates seem less coherent with generally higher subsidence rates towards the south (-10.3+/-3.0 mm, PRO3) compared to cGPS rates (-6.6+/-3.1 mm, JRGN).

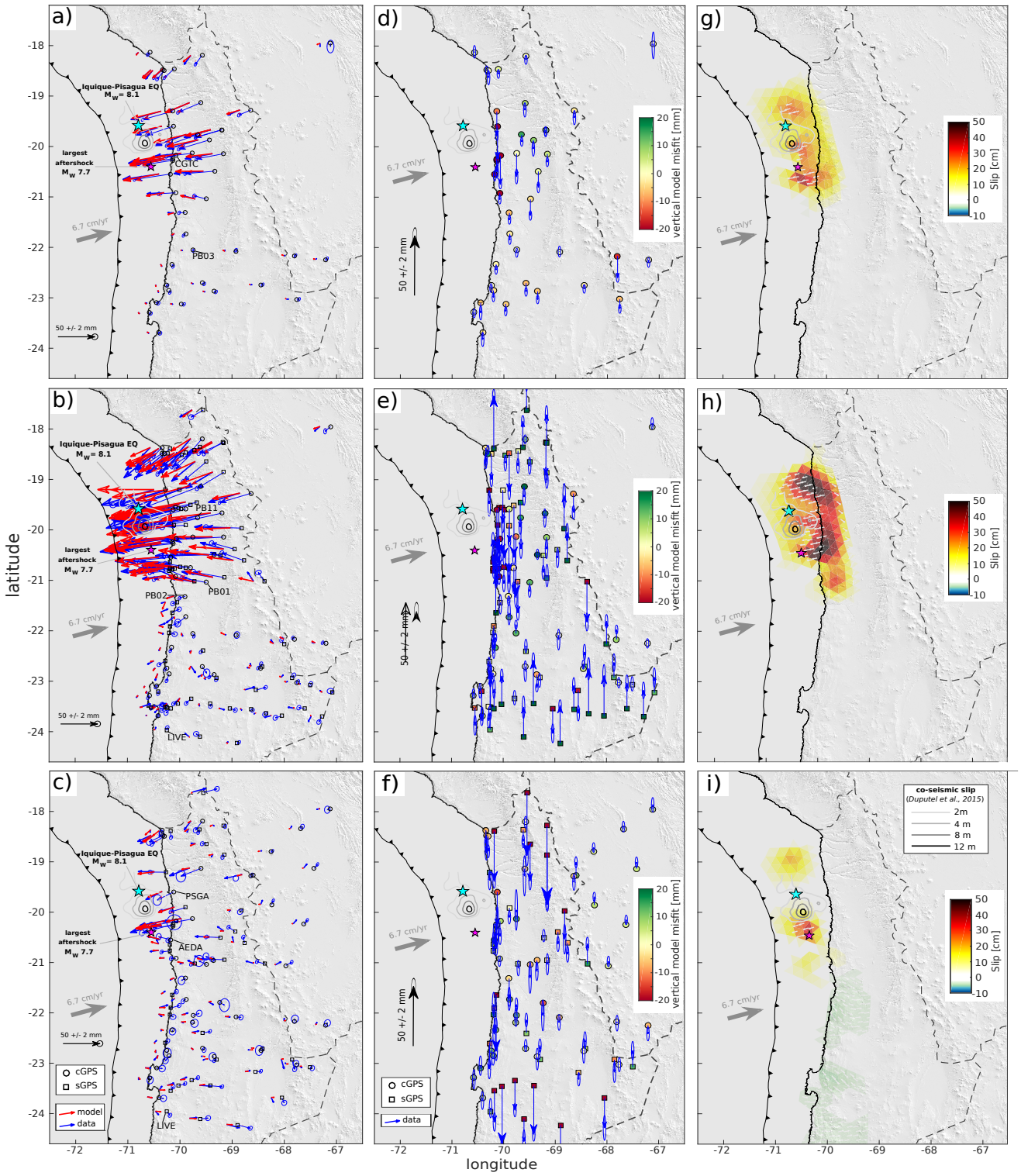

Figure 3.5: a)-c) Predicted displacements (red) and GPS observations (blue) with 1-sigma uncertainties, after subtracting the relocking signal (average interseismic rate) and the visco-elastic response for a) 2-16 days (Period 1), b) 17-334 days (Period 2) and c) 335–717 days (Period 3) after the mainshock. d)-f) Vertical GPS observations (blue) and color-coded model residuals for postseismic Periods 1-3. g)–i) Predicted postseismic afterslip on the plate interface during the corresponding postseismic Periods 1-3. For other features see Figure 3.4.

If we analyse the temporal evolution of displacement by using a moving-window of 30 days, we illustrate for how long each GPS station was affected by the Iquique-Pisagua earthquake (**Figure 3.6**). As reported before, stations south of 21° S seem not at all affected by the mainshock. Stations south of PB01 have an eastward trend collinear with the plate convergence over all investigated periods. But just 40 km north, at 21° S, the adjacent stations CRSC, CLLA and PB01 are clearly affected by co- and postseismic response to the mainshock (**Figure 3.6**).

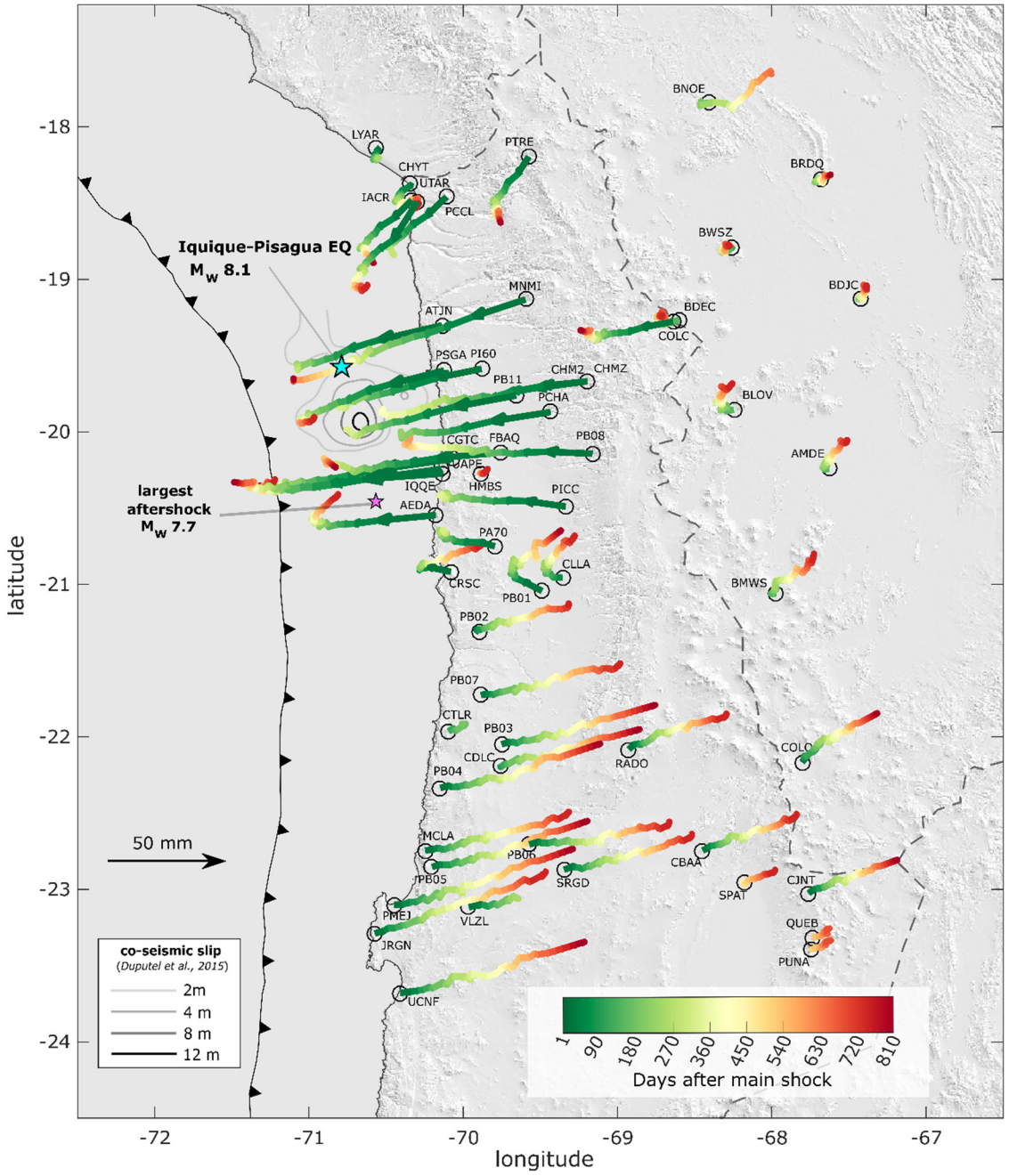

Figure 3.6: Postseismic ground displacement color-coded by days after the mainshock (sampled every 30 days). For other features see Figure 3.4.

The majority of GPS stations north of 21° S turn their sense of motion from trenchward to landward after about one year, thus slowly converge to interseismic relocking. This turnover of ground displacement motion back to interseismic relocking with surface motion collinear to the plate convergence vector is almost completed after two years. After April 2016, westward-directed motion induced by afterslip is dominated by eastward-directed motion induced by relocking and we assume interface afterslip to become negligible with less than 5 cm/yr two years after the Iquique-Pisagua event.

3.4.2 Model results

The slip models of the different postseismic stages yield a more detailed picture of the temporal evolution of afterslip (**Figure 3.5 g-i**). For the postseismic models, we first calculated the data weights based on GPS uncertainties and then introduced the weighting factor $w = w_{sGPS}/w_{cGPS}$ (**Figure B.12 a**), similar as for the interseismic model (section 3.2). Period 1 only contains cGPS data (42 stations), but for Period 2 (38 cGPS and 64 sGPS stations, w=2.0) and Period 3 (33 cGPS and 43 sGPS stations, w=1.5), we defined different relative weights to account for a difference in spatial distribution of cGPS and sGPS stations. Similar to the postseismic modelling approach, we increased the uncertainty of the vertical GPS component by a factor of five for cGPS and ten for sGPS data to more realistically represent the vertical data error (**Figure B.12 c-d**).
While subtracting averaged interseismic rates from postseismic data before inverting for postseismic slip, we assume that the relocking rate s remain constant before and after the Iquique-Pisagua event 2014. This may lead to an overestimation of afterslip rates and also the visco-elastic relaxation component of the signal, if interseismic loading signal does not resemble prevailing backslip during the postseismic period.
In Period 1, afterslip with a magnitude of 15-25 cm surrounds the rupture area of the Iquique-Pisagua earthquake down-dip at ~30-35 km depth (**Figure 3.5 g**). Maximum slip of up to 38 cm occurs 50 km south of the mainshock at ~30 km depth, near the epicentre of the largest aftershock. In a latitudinal range of 20.7-21° S, our model indicates a transition from highest slip rates to backslip-dominated interface motion. We think that this pattern is caused by the sharp latitudinal sign change of displacement and might be linked to a seismotectonic barrier at 21° S. This sharp transition moreover suggests that stations south of this zone are not affected by afterslip (**Figure 3.5 g**).
In Period 2, afterslip occurs down-dip of the main rupture at 30-50 km depth, surrounding the hypocentre and reaching peak values of 51 cm (**Figure 3.5 h)**. One peak slip patch is located 50 km south of the epicentre, again at the location of the largest aftershock, and a second high afterslip patch appears 40-50 km to the north of the main rup-

ture at ~35-40 km depth. The up-dip area of our slip model exhibits significantly less slip, only 10 to 20 cm. The geometry of afterslip extent during the first year after the earthquake is surprisingly similar to the afterslip pattern of the first two weeks, except for the larger magnitudes. Afterslip in Period 2 involves deeper parts of the interface and is shifted ~20 km northwards compared to Period 1 as visible at the aftershock peak slip. A relatively sharp transition from slip to backslip-dominated interface motion is again detected at 20.7-21° S. At this latitude, slip extends about ~40 km further south underneath the Chilean coast, thus at relatively poorly resolved, deeper parts of the interface. No difference to interseismic interface motion can be observed south of this latitudinal range as inferred by a lack of slip/backslip southwards.

In Period 3, afterslip has significantly decreased and converges to zero in the centre of the inferred rupture zone of the Iquique-Pisagua mainshock (**Figure 3.5 i**). This reflects the transition from an afterslip-dominated stress regime to relocking as described by *Wang et al. (2012*). One isolated afterslip patch is located ~50 km north of the epicentre with 10-15 cm slip. Surprisingly, peak slip occurs consistently at the area of the largest aftershock 50 km south of the mainshock, with slip of 35 cm in Period 3. The spatial transition from afterslip at the Camarones segment to interseismic relocking at the southern Loa segment becomes more diffuse in Period 3, but is shifted northwards compared to Period 2 (nomenclature from *Métois et al., 2016*). Most prominently, south of 21° S, we observe increasing backslip rates in an interface depth range of 40-60 km. After having subtracted averaged interseismic loading rates from our observations, we expect interface slip in adjoining seismotectonic segments that are not affected by afterslip to be close to zero. In contrast, backslip rates up to -2.5 cm south of 21° S indicate a coupling increase of the subduction interface in the second year after the megathrust event. Peak backslip rates are located at 45-50 km depth underneath Mejillones peninsula at ~23° S.

Overall, a cumulative peak afterslip of 89 +1.2/-0.4 cm is observed within the first two years after the Iquique-Pisagua earthquake, occurring between 30 and 45 km depth and embracing the rupture area down-dip (**Figure B.19**). We estimated the error of the maximum slip using a simplified Monte-Carlo approach calculating the standard deviation of 50 inversions in which we added normally distributed noise to the GPS data (**Figure B.20**). A sharp transition between afterslip to the north and backslip (increased interseismic coupling) to the south is observed in a latitudinal range of 21-21.5° S. Most interestingly, the pattern complements the high backslip pattern observed in the interseismic phase at these latitudes (**Figure 4c**).

The model resolution based on our checkerboard approach (section 3.3.2) for all three periods is generally good (**Figure B.14 c-d**). An exception is the southern part of Period

1, where we have rather poor resolution south of 23° S mainly due to the lack of GPS stations there as we only use cGPS data. But the expected afterslip area south of the mainshock epicentre, towards the largest aftershock, is well resolved below a depth of ~15 km. However, potential shallow afterslip above 15 km might not be resolvable with our model geometry.

The postseismic models fit the horizontal data of all three stages reasonably with a rms-residual of 1.7 mm (Period 1), 4.2 mm (Period 2) and 2.4 mm (Period 3) (**Figure B.15 b-d**). The strongest horizontal misfit is observed in Period 2 at coastal stations close to the main rupture and to the north. Further tests have shown that misfit cannot be significantly improved by changing model parameters (i.e. depth constraints or smoothing value). The overall direction of deviation is towards the south, implying a northward shifted model slip. One reason for the northward shift of slip could be the unfavourable spatial resolution of our model geometry that is poorly resolved at shallow parts of the interface as well as north of 19° S due to a lack of Peruvian GPS stations. Thus, potential shallow afterslip may be shifted deeper and northward to better fit the observations. A more physical explanation for the deviation could involve rheologic inhomogeneity in the crust, which are not taken into account in our simple half-space model. The relatively high misfit and systematic underprediction of the southward displacement in Period 2 may be a consequence of our simplified model rheology. To better fit the data, a more complex geometry involving a three-dimensional model set-up may be needed (e.g. *Li et al., 2015*; *Klein et al., 2016*). Another cause for local (point-wise) misfit of the GPS vectors as e.g. observed for stations VIRI or COLC in Period 3 could be upper crustal faulting, as has been observed in many parts of Northern Chile and Bolivia (e.g. *Lamb*, *2000*; *Allmendinger & González*, *2010*). *González et al. (2015*) even argued that the Iquique-Pisagua mainshock could have been triggered by a reactivated trench-oblique upper plate reverse fault (the M_w 6.7 foreshock on March 16th, 2014). However, we do not observe a spatially coherent, long-wavelength misfit pattern in the far-field as potentially caused by viscous relaxation (*Wang et al., 2012*)**.** Thus, we believe that our model predictions for the visco-elastic component represent the amount of mantle relaxation contributing to the measured postseismic ground deformation signal well.

The vertical displacement predications generally fit the data worse than the horizontal predictions and exhibit a rms-residual of 3.5 mm (Period 1), 5.2 mm (Period 2) and 2.0 mm (Period 3) (**Figure B.16 b-d**). The model clearly fails to properly predict the highly complex vertical displacement and, again, a three dimensional model would probably improve the fit, e.g. by including a complex crustal structure that accounts for features like local low-viscosity channels (e.g. *Klein et al., 2016*) (**Figure 3.5 d-f and B.18 b-d**). Another reason for the poorly vertical fit is the relatively large data uncertainty of

the vertical data, particularly for episodic measurements that can be explained by the acquisition geometry allowing more sensitivity to horizontal measurements. Another systematic overrepresentation of vertical data is apparent close to the rupture area of the mainshock, whereas the up-component towards the south is clearly underrepresented. Nevertheless, our model is capable of resolving the hinge line between postseismic uplift and subsidence at coastal stations between 20-21° S in Period 1 and 2. In Period 3, this hinge line may has shifted offshore.

3.5 Discussion

3.5.1 Spatial correlation of afterslip and aftershocks

The afterslip pattern of the Iquique-Pisagua earthquake is comparable with the postseismic deformation of other megathrust events of the last decade. Similar to the 2005 Nias M_w 8.7 Sumatra event (*Hsu et al., 2006*) or the 2010 Maule M_w 8.8 Chile earthquake (*Bedford et al., 2013*), afterslip surrounds the region of maximum coseismic slip, and occurs mostly in the down-dip area of the rupture (**Figure 3.5 g-i**). To shed light on this and better understand the relation between afterslip and aftershocks, we analysed the location of aftershocks of the first year after the earthquake. For this we utilized a recently compiled seismicity catalogue from the IPOC permanent station network that covers the years 2007-2014 (*Sippl & Schurr, 2017, Sippl et al., 2018*). The catalogue contains a total of 101k events and has good spatial coverage of the Northern Chile-Southern Peru seismic gap, with a completeness magnitude of 2.7-2.9. Events were detected using the multi-step procedure of phase picking and relocation outlined in *Sippl et al.* (*2013*), the last step of which is double-difference relocation using event pair cross-correlations (*Sippl et al., 2018*).

In the first two weeks after the Iquique-Pisagua mainshock, modelled peak afterslip occurs north and southeast of the rupture area (**Figure 3.5 g**), near the epicentre of the large aftershock, where interseismic backslip (coupling) is highest (**Figure 3.4 c**). This suggests that in the first few days after the mainshock, afterslip neutralizes incomplete coseismic stress drop, as it was also reported after the 2010 Maule earthquake (*Bedford et al., 2013*). In the same period, aftershocks mostly occur in the rupture area. The distribution of aftershocks in the first days following the mainshock may thus be controlled by the redistribution of stress during the coseismic phase (**Figure 3.7 a**) (e.g. *King et al., 1994*).

The early stage of afterslip is characterized by the presence of both, normal and thrust

faulting earthquakes, but after two weeks only thrust mechanisms dominate in the aftershock sequence**.** This may reflect a minor temporal change of the compressional axis of about 6° and pre-megathrust stress conditions were restored a few weeks later (*Cesca et al., 2016*). Aftershock locations in the first year after the mainshock until the end of 2014 seem to flank the highest coseismic rupture areas (slip above 8 m), but also border the regions of high afterslip (**Figure 3.7 b**).

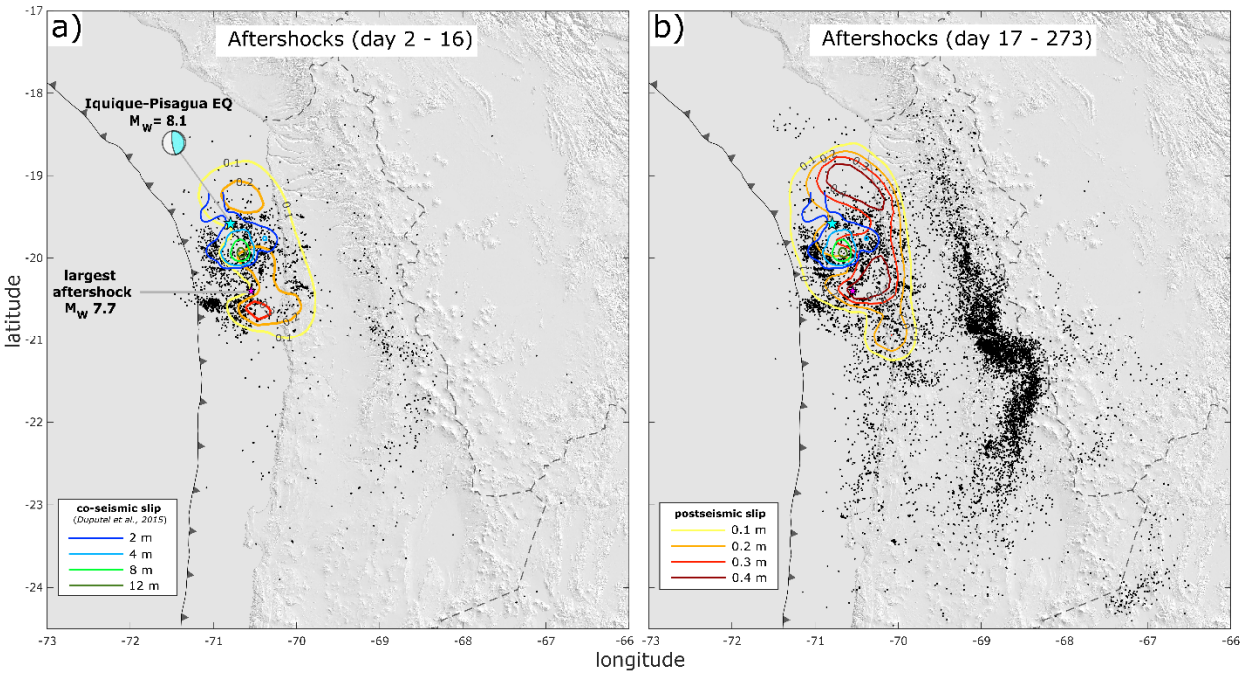

Figure 3.7: Aftershock distribution (Sippl & Schurr, 2017) during a) Period 1 and b) Period 2 in comparison to coseismic slip (blue/green isolines) and modelled afterslip (yellow/red isolines) in the respective intervals. Each coseismic slip represents an increment of 2 m, each afterslip contour an increment of 0.1 m. Note that in b) only aftershocks until the end of 2014 are included. For other features see Figure 3.4.

In a band-like geometry, aftershocks separate the northern peak afterslip patch from the southern one. Modelled afterslip mostly occurs deeper than ~35 km and reaches the assumed transition zone from (brittle) crust to the hydrated mantle wedge (e.g. *Bloch et al., 2014*). Given the clear spatial correlation between peak afterslip and the absence of aftershocks in Period 2 (**Figure 3.7 b**), we infer that postseismic stress release is mostly transferred from aseismic (rate-strenghtening) peak afterslip areas to adjacent intermediate afterslip regions close to the coseismic rupture zone. The up-dip area exhibits relatively low afterslip, which agrees with the observation of the low degree of interseismic coupling in the shallower parts of the interface, where slip deficit is assumed to be almost zero (*Li et al., 2015*). This possibly indicates interseismic creep on the up-dip portion of the plate interface. On the other hand, our checkerboard tests (**Figure B.14**) show that the shallow parts of the interface are poorly resolved, and the

relatively intense up-dip seismic activity indicates rate-weakening behaviour. North of 19° S, the seismicity in the down-dip high afterslip area decays rapidly (**Figure 3.7 b**). Thus, the aseismic area in the north seems to release stress while creeping, which potentially reflects a transient increase of pore fluid pressure (*Kodaira et al.*, *2004*). Moreover, this region spatially correlates with low coupling in shallow to intermediate crustal depths of 10-30 km (**Figure 3.4 c**), probably indicating the border to another seismotectonic segment (*Métois et al., 2013*; *Li et al., 2015*). This could also explain the relatively low GPS displacement rates north of 19° S in the interseismic (**Figure 3.4 a**) and postseismic period (**Figure 3.5 g-i**) that are probably caused by a lowly coupled segment to the north that is separated from the Camarones segment where the mainshock ruptured. Moreover, the distance to the trench increases towards the north, which also contributes to a slowing-down of the GPS velocities there.

However, south of 21° S, the high-afterslip zone also exhibits a significant decrease of seismicity. The rupture area of the mainshock terminates near a low coupling zone (Iquique intersegment, *Métois et al., 2013*) at 20° S (*Duputel et al*., *2015*; *Schurr et al., 2014*; *Ruiz et al., 2014*), but afterslip extends further south across to 21° S, probably due to the effects of the large aftershock (**Figure 3.8 a**). Low coupling zones are assumed to behave in a rate-strengthening way, increasing their frictional strength, thus decreasing the likelihood of slip propagation (e.g. *Scholz, 1998*). But the afterslip also affects this interseismically low coupled zone and terminates abruptly at ~21.2° S (**Figure 3.8 a**), where the seismicity likewise decreases sharply. Similar to above, the coupling differences may reflect a seismotectonic barrier.

In Period 2, a N-S oriented, left-stepping, band-like structure of seismicity becomes more prominent at 80-120 km depth and 250-300 km east of the trench (**Figure 3.7 b**) and is most densely populated between 20°-22.5° S. The spatial extent of this band correlates neither with the shallow seismicity described above nor with the co- or postseismic plate interface slip. The occurrence of this intermediate-depth seismicity is most likely caused by the metamorphic dehydration of the oceanic lithosphere effecting hydraulic embrittlement due to the release of fluids (*Rietbrock & Waldhauser, 2004*; *Yoon et al., 2009; Bloch et al*., *2014*). The observed kink in the seismic band spatially correlates with the southern limit of the afterslip zone at 21° S. South of the kink, the dehydration-related seismicity occurs slightly deeper, probably reflecting heterogeneity in the subducting oceanic plate (e.g. *Geersen et al., 2015*) or crustal rheology. We additionally generated a simple Coulomb Failure Stress Change (ΔCFS) model based on our visco-elastic model geometry and the coseismic shear (σ_s) and normal stress (σ_n) changes on the interface with $\mu = 0.1$ as the coefficient of friction (*Lamb, 2006*):

$$\Delta CFS = \sigma_s - \sigma_n \cdot \mu. \quad (3.3)$$

In our model, positive ΔCFS outlines the main rupture area up- and down-dip (**Figure 3.8 b**), indicating that those interface regions were brought closer to failure and are more prone to aftershocks during the postseismic stage. For the up-dip part, where we lack model resolution, aftershock locations are in good spatial agreement with positive ΔCFS. For the down-dip area, aftershocks ocurr in both, positively and negatively loaded ΔCFS regions. The negative ΔCFS of up to -4 MPa spatially coincides with the high coseismic slip regions of the rupture area of the Iquique-Pisagua mainshock, where significantly fewer aftershocks occur. The largest aftershock is located at the southern edge of the negative ΔCFS region. This may be associated to pre-mainshock stress conditions and potentially reflects interseismic stress build-up preceding the mainshock, e.g. due to the foreshock on 16 March 2014 (e.g. *González et al., 2015*).

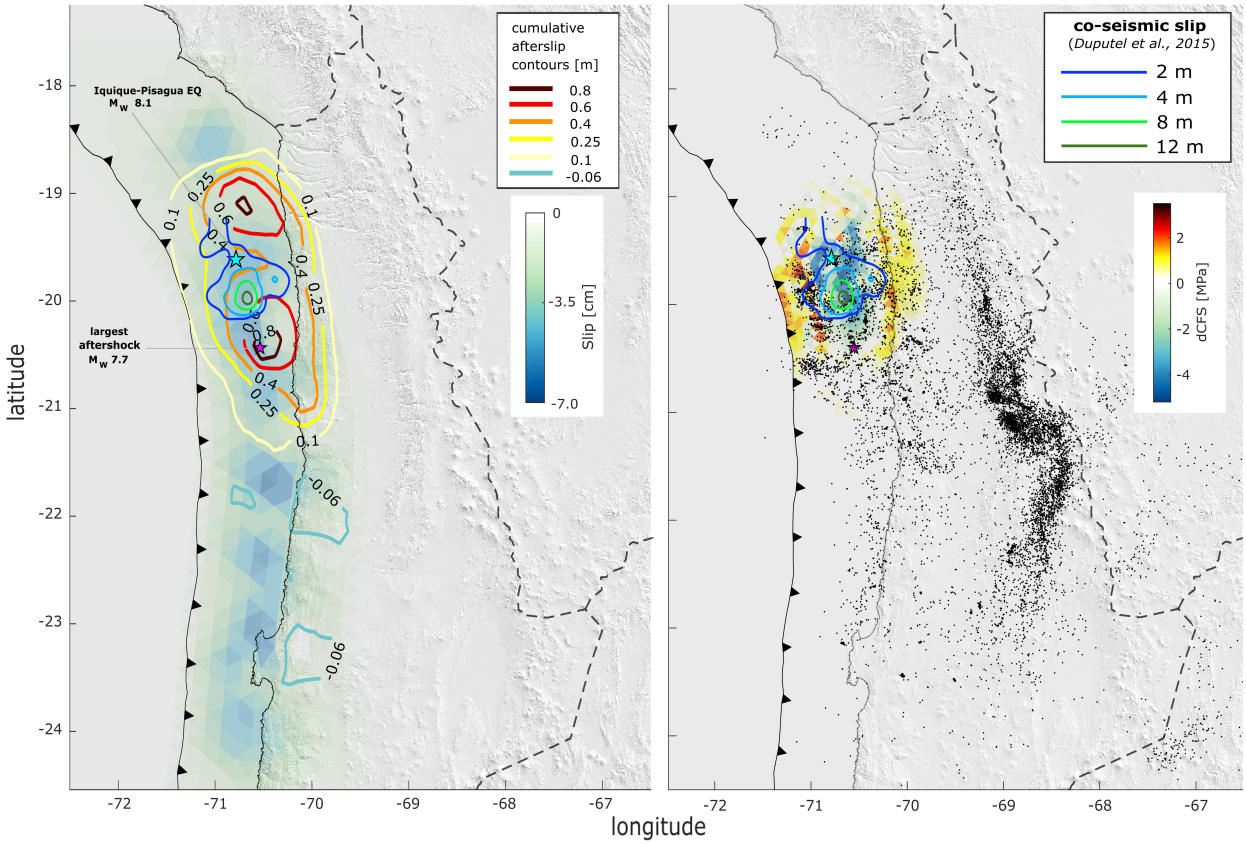

Figure 3.8: a) Comparison of interseismic backslip, coseismic slip (Duputel et al., 2015) and cumulative afterslip (see also Figure B.19). b) Comparison of coseismic slip, estimated Coulomb Failure Stress Changes based on slip model of Schurr et al. (2014) and aftershocks from April to December 2014 (Sippl & Schurr, 2017). For other features see Figure 3.4.

3.5.2 Seismotectonic barrier at 21° S

In all our observations, we find that the region at 21° S acts as a barrier or apparent discontinuity of physical properties. Throughout the whole investigated period, the GPS stations south of 21° S move permanently in the interseismic ENE direction, indicating that the plate interface remains strongly coupled (**Figure 3.4 a, 3.5 a-c, 3.8 a**). In the postseismic stage, we observe sharp GPS rate changes near 21° S that coincide with the southern termination of the narrow, low-coupled zone (Iquique low coupling zone) (**Figure 3.8 a**) (*Métois et al., 2016*). Afterslip intrudes into this possibly rate-strengthening zone south of 21° S, which we interpret as postseismic stress transfer into a very heterogeneous subduction interface (e.g. *Kaneko et al., 2010*; *Marone et al., 1991*) at the border to a region undergoing stress build-up (south of 21° S). This transition zone also shows peak seismicity at the upper plate both before and after the 2014 earthquake (*Meng et al., 2015*) (**Figure 3.7 b**) and potentially indicates a seismotectonic barrier, which is less coupled with respect to adjacent segments. The barrier may thus be a consequence of mechanical variations in the coupling between the interface and the upper plate. *Geersen et al. (2015*) attribute the heterogeneous coupling to seamounts on the subducting plate that prevented the Iquique-Pisagua rupture to migrate southwards. According to them, the so-called Iquique Ridge at 19.5-21° S (**Figure 3.1**) favours aseismic conditions with smaller earthquakes and creep rather than large ruptures due to extensive fracturing at the plate boundary (*Wang & Bilek, 2011*; *Geersen et al., 2015*). Another explanation for the presence of the barrier could be a postulated abrupt change of slab dip at ~21° S, interpreted as slab bending in recent studies (*e.g. León-Ríos et al., 2016*). In the numerical model of *Kaneko et al.* (*2010*), two rate-weakening zones were separated by a narrow rate-strengthening block. This is comparable to the tectonic setting of our study, where two highly coupled zones are separated by the narrow Iquique low coupling zone at 21° S (**Figure 3.8 a**). Whenever one of the rate-weakening zones ruptured individually in this experiment, stress was transferred to the opposite zone that, in turn, was brought closer to failure than expected from the original recurrence interval (*Kaneko et al., 2010*). These results focus our attention to the southern Loa segment at 21-23° S.

However, the origin of the seismotectonic barrier might also be related to the upper plate rather than to the plate interface. *Loveless et al.* (*2009*) reported that the preferred orientation of surface cracks north and south of 21° S changes from NNW to NE, indicating two distinct stress regimes in the upper crust. This zone is also the southern limit of E-W trending faults (**Figure 3.1**) responsible for along-strike shortening of the Coastal Cordillera (*Allmendinger et al., 2005*; *Allmendinger & González*, *2010*). These

authors have related this kinematic observation to the location of the symmetry axis of the Andean orocline (*Gephart*, *1994*) (**Figure 3.1**) as well as of the Benioff Zone. This finding is also supported by numerical analysis and analogue simulation in *Boutelier & Oncken* (*2010*) and *Boutelier et al.* (*2014*), both of which suggest that bending in conjunction with specific plate interface properties has a key role in the kinematic response. The seismotectonic barrier correlates spatially with the boundary between a strongly faulted upper plate domain in the North and an unfaulted upper plate in the South (*Allmendinger and Gonzáles, 2010*). From these observations together with the observed sharp gradient in surface motion, we additionally speculate that there could be an associated strength change of the forearc crust.

The seismotectonic barrier at 21° S potentially prevented the Northern Chile-Southern Peru seismic gap region to rupture in a single event as in the 1877 Iquique M_w 8.6 earthquake (e.g. *Comte and Pardo, 1991*). Although there is also some discord about the actual size of the 1877 event in scientific literature (*Métois et al., 2013*), this earthquake was certainly larger than the 2014 event and either extended the barrier, or the barrier was only formed in the post- and interseismic stage following the 1877 event. The 2014 earthquake could only partially release the slip deficit accumulated since 1877 (*Métois et al.*, *2013; Schurr et al.*, *2014*). Consequently, for further analysis the seismic gap region should be split into two parts separated by the seismotectonic barrier at 21° S. Moreover, our results suggest that the seismotectonic behaviour may be more strongly affected by upper plate strength variations along the Chilean margin than previously surmised.

3.5.3 GPS rate change south of 21° S

GPS rates south of 21° S reflect the crustal response to the occurrence of the 2014 earthquake at this unbroken adjacent segment. Here, we find a significant rate change of up to 10 mm/yr over different postseismic periods after the Iquique-Pisagua earthquake. To illustrate this, we extracted the linear trend from the time series of Periods 2 and 3 as described in section 3.2.2, and calculated the rate changes with respect to the interseismic rates observed before the earthquake (**Figure 3.9**). In the first year after the mainshock, stations south of 21° S latitude experienced a rate decrease compared to the pre-earthquake rates, whereas in the second year those stations (consistently sGPS and cGPS) show a rate increase (**Figure 3.9**). This rate increase may not be dependent on the distance between station and trench as maximum acceleration is observed at inland stations at distances of 130 to 170 km away from the trench and not at coastal stations that are closer to the trench. We interpret this change of behaviour between the first and

the second year following the Iquique-Pisagua earthquake as response to decreasing afterslip rates and the dominant effect of interseismic deformation at the southern Loa segment. Hence, the rate decrease in the first year could be explained by the interaction of (1) far-field afterslip on the interface and (2) visco-elastic relaxation. Both mechanisms cause GPS stations to move towards the rupture zone, opposite to the ongoing interseismic coupling locking (*Wang et al.*, *2012*; *Bedford et al., 2016*)**.** Therefore, the observed rate decrease in the first year could be the consequence of relaxation processes. This confirms that the visco-elastic relaxation decays fast, being more dominant in the first year after the event. But what causes the rate increase in the second year after the earthquake, which is comparable to what was reported from adjoining segments of the 2003 Tokachi-Oki M_w 8.0, Japan earthquake (*Heki & Mitsui, 2013*)? One explanation may be given by recent studies of *Melnick et al. (2017*) and *Klein et al. (2016)* that documented GPS rate increase after the 2010 Maule earthquake at the adjacent unbroken segments. Likewise, we propose that the observed rate increase south of 21° S can be an effect of continental-scale, visco-elastic mantle relaxation (*Klein et al., 2016*) that induces an increase of fault shear stresses more than 200 km away from the rupture zone. The increase of interseismic rates can also be mechanically related to the elastic flexural bending response of both plate segments to the uncoupling after a large earthquake in one of the segments. This uncoupling may increase the interseismic stress accumulation at adjacent clamped (locked) segments (*Melnick et al., 2017*). Our models confirm these temporal variations of interseismic rate after a large earthquake and suggest a significant increase in backslip rate of up to 10 mm/yr (**Figure 3.9**) and thus increased interface coupling in the second year after the earthquake (**Figure 3.5 i**). The observation that maximum rate increase occurs not at coastal stations, but 40 to 80 km inland potentially reflects down-dip changes of interface coupling deeper than 40 km at the down-dip limit of the seismogenic zone. Similar to the potential triggering of the 2015 Illapel M_w 8.2 earthquake (*Tilmann et al., 2016*) by the 2010 Maule M_w 8.8 event as bimodal megathrust occurrence (*Melnick et al*., *2017*; *Klein et al., 2016*), we suggest that the Iquique-Pisagua event can bring the Loa segment closer to failure due to increased shear stress at the down-dip limitation of the fault.

Another, more speculative hypothesis locates the source of surface displacement rate increase to the upper crust, particularly if we assume that our elastic models somewhat overestimate the coupling degree. This would be the case, if we underestimate the visco-elastic relaxation or the interseismic loading prior to the earthquake. Given the complexity of our time series that cover different stages of the seismic cycle including two major earthquakes (the 2005 Tarapacá and 2007 Tocopilla event) that affect velocities in our pre-Iquique-Pisagua earthquake interval, our extracted loading rates may be un-

derestimated. In this case, we should detect a time-dependent increase of upper crust weakening and the current slip deficit would be released aseismically. Another realistic explanation for coupling increase in our models involves our simplified model rheology with a homogeneous, linear Maxwell viscosity that does not account for complex rheologic features like low viscosity wedges (e.g. *Klein et al., 2016*).

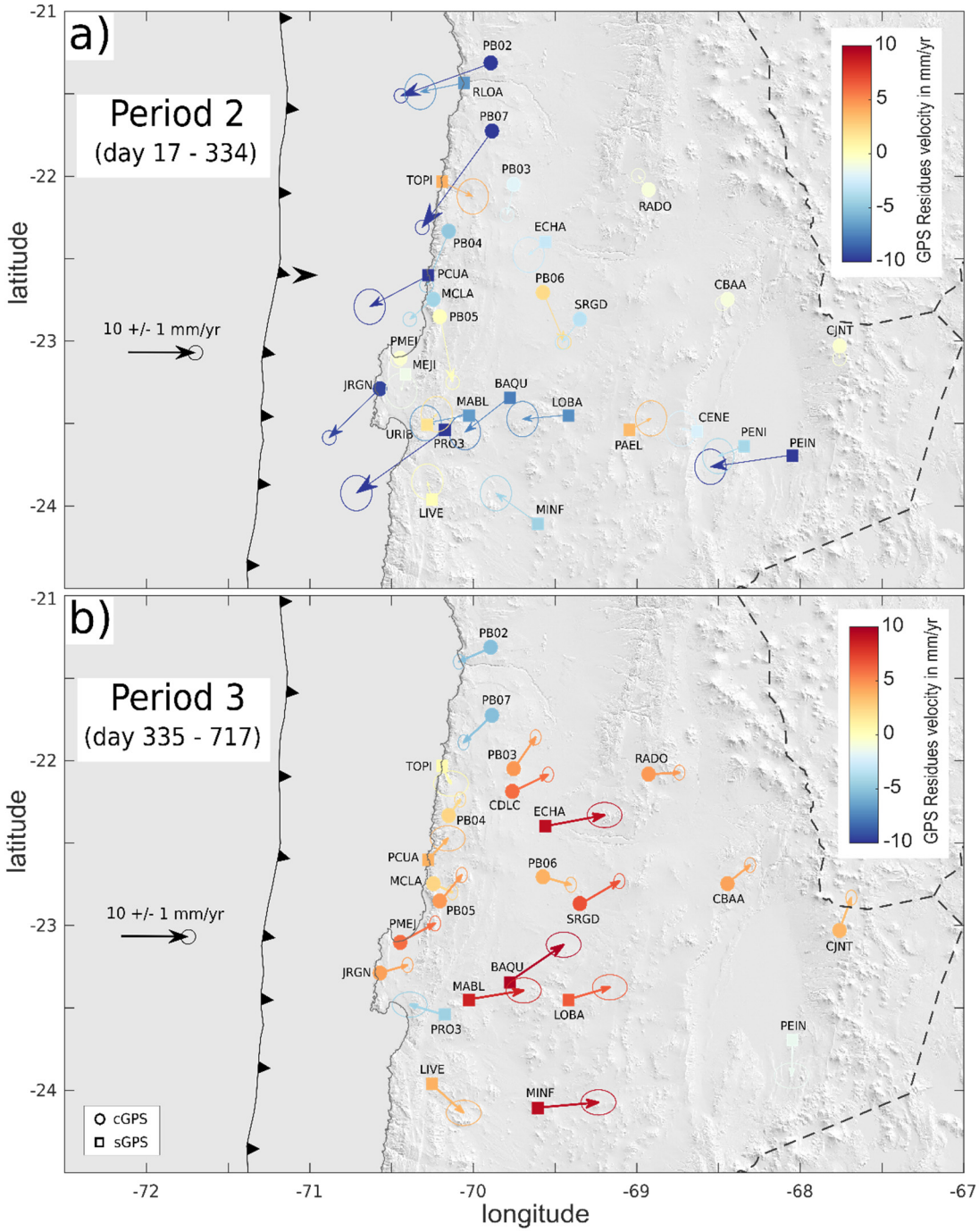

Figure 3.9: Rate changes during a) Period 2 and b) Period 3 after the Iquique-Pisagua earthquake with respect to the pre-event displacement rates. The vectors are color-coded by the amplitude of the rate change, the symbols mark continuous (circle) and campaign (square) measurements.

However, the consistency and uniformity of the change of the interseismic velocity field, observed in both, sGPS and cGPS data, suggests an increase of shortening rate at the Loa segment independent of our modelling strategy. Longer postseismic time series will provide valuable data to our findings and to further investigate the temporal variations of coupling degree.

3.6 Conclusion

Based on 152 GPS time series, we have derived an interseismic backslip model of the (former) Northern Chile-Southern Peru seismic gap and three consecutive postseismic models documenting two years of afterslip motion following the 2014 M_w 8.1 Iquique-Pisagua earthquake. Prior to the earthquake, we find a heterogeneously locked plate interface with two highly coupled patches in the central part of the gap that are separated by a narrow, low-coupling zone at 21° S (Iquique low coupling zone), probably acting as a seismotectonic barrier. Consequently, the rupture area of the 1877 M_w 8.6 Iquique earthquake should be analysed as two distinct patches.

The postseismic models exhibit peak afterslip at the location of the largest aftershock and show a relatively sharp gradient from trenchward to landward motion at ~21° S latitude. Based on this strong displacement gradient as well as mapped changes in upper plate faulting and crack orientations, we speculate that crustal strength heterogeneity may contribute to cause this seismotectonic barrier.

Cumulative afterslip reaches 89 +1.2/-0.4 cm, outlines the main rupture area down-dip and dissolves after two years. The Loa segment south of 21° S is unaffected by afterslip, but yields a significant rate increase towards interseismic gound displacement direction of up to 10 mm/yr in the second year following the earthquake. We interpret this as an increase in down-dip interface coupling due to shear stress increase as a consequence of regionally induced deformation (visco-elastic and/or elastic bending) after the 2014 earthquake. The Iquique-Pisagua earthquake may have initiated a super-interseismic phase in the southern sector with a bimodal occurrence of megathrust events (*Melnick et al., 2017*; *Loveless, 2017*). In this case, the risk of another earthquake in this unbroken part between 21-23° S has increased. An opposing interpretation suggests time-dependent crustal weakening involving aseismic slip release in the Loa segment. Longer deformation time series are needed to distinguish between these hypotheses and an increased observational attention to this segment is recommended.

4 Refining coseismic slip of the 2014 M_w 8.1 Iquique-Pisagua earthquake and the largest M_w 7.7 aftershock by jointly modelling InSAR and GPS data

4.1 Introduction

4.1.1 Iquique-Pisagua mainshock

The tectonic regime of the South American continent is mainly characterized by the subduction of the oceanic Nazca Plate underneath the continental South American Plate. Subduction zones are generally known to frequently generate large devastating megathrust events and it is assumed that approximately 80 per cent of the total seismic energy worldwide is released by events located at convergent plate boundaries (e.g. *Fowler, 1990*). The South American subduction zone is characterized by one of the most rapid convergence rates on Earth with about 6.7 cm/yr in the North of Chile (*Norabuena et al., 1998*) and, for that reason, it is not surprising that the Chilean coast has been hit by some of the largest instrumentally observed earthquakes during the past century, namely the 1960 M_w 9.5 Valdivia (*Kanamori, 1977*) and the 2010 M_w 8.8 Maule events (*Moreno et al., 2010*). A subduction plate interface is characterized by heterogeneous locking properties and can be conceptualized as consisting of asperities (or seismotectonic segments) that rupture individually (*Aki, 1979*). The rupture events at specific asperities are assumed to repeat after accumulating a characteristic slip deficit whilst being locked in the time interval referred to as earthquake recurrence time that usually lasts decades to centuries (*Shimazaki and Nakata, 1980*). Although rupture locations, extents of past events and also seismic recurrence intervals along the Chilean subduction zone are constrained either by instrumental measurements, geologic archive data or sometimes even historical reports (e.g. *Kausel et al., 1986*; *Métois et al., 2013*), we are still not able to precisely determine magnitudes and timing of future large earthquakes. Huge efforts in geodetic technology and the set-up of spatially dense networks of geophysical instrumentations, such as IPOC in Northern Chile, during the last decades has enabled extensive measurement of ground deformation changes that occur during various phases of the subduction seismic cycle. Kinematic modelling of these geodetic observations allows for the better understanding of the physical mechanisms related to the recurrence of large earthquakes and, ultimately, improves the seismic hazard prediction in the temporal as well as spatial domain. It is well known, that seismic activity along subduction

zones is very heterogeneous, in fact significant gaps in seismicity are commonplace (e.g. *Fowler 1990*). These seismic gaps are located at seismotectonic segments that are assumed to have reached the amount of characteristic slip deficit and have not ruptured within the calculated recurrence interval. Such a gap can be characterized by a region of the interface with much lower rate of smaller magnitude interseismic earthquakes than adjacent segments. Until recently, one of the most mature seismic gaps along the Chilean subduction zone was the Northern Chile- Southern Peru seismic gap between 18°-23° S latitude (**Figure 4.1**). Accordingly, the Iquique-Pisagua earthquake 2014 is thought to have ruptured the central part of the gap (*Schurr et al., 2014*; *Ruiz et al., 2014*). The last historic megathrust event in this region is documented as the 1877 Iquique-earthquake that is considered as the largest historical earthquake ever documented in Northern Chile with an estimated magnitude of M_w ~8.5-8.8 (*Comte and Pardo, 1991*; *Lomnitz, 2004; Chlieh et al., 2011*) (**Figure 4.1**).

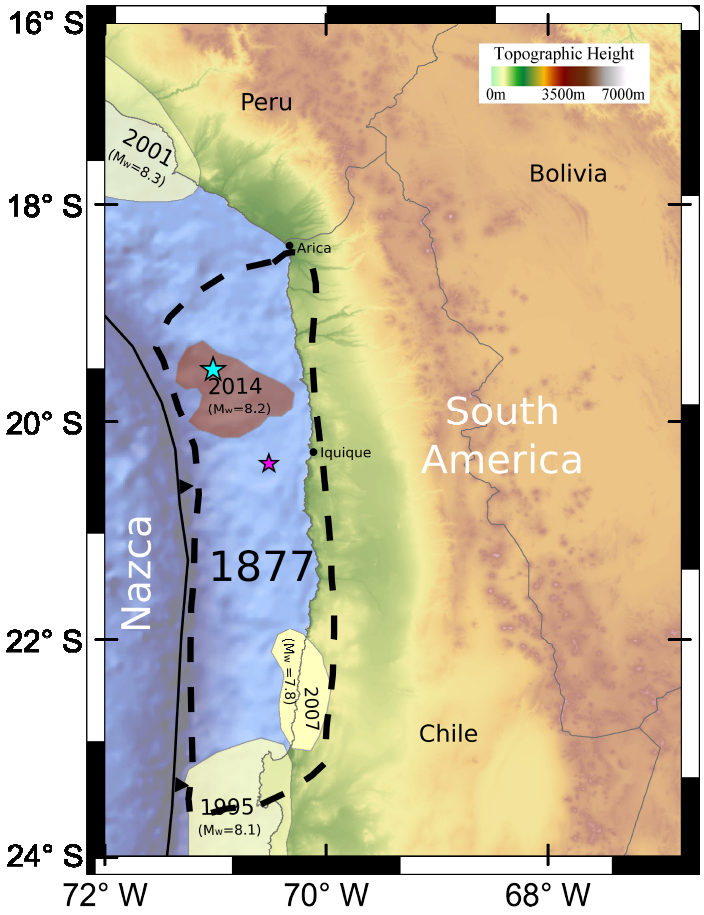

Figure 4.1: Topographic map of Northern Chile. Rupture zones of past relevant earthquakes are indicated as shaded areas (source: USGS): the 1995 Antofagasta, the 2001 Arequipa and the 2007 Tocopilla event (yellow), the 2014 Iquique-Pisagua event (red) including the epicentre locations of the mainshock (turquoise star) and its largest aftershock (magenta star). The seismic source area of the last megathrust event 1877 (Iquique event M_w ~8.6, Chlieh et al., 2011) in the Northern Chile- Southern Peru seismic gap is indicated as dashed ellipse.

However, the actual rupture length of this earthquake and whether or not it broke the entire length of the Northern Chile- Southern Peru seismic gap is still debated in scientific literature resulting in a difference of up to 0.5 units of the moment magnitude (M_w) scale (e.g. *Kausel, 1986*; *Comte and Pardo, 1991*; *Lomnitz, 2004*; *Métois et al., 2013*). The seismic moment released by the 2007 Tocopilla event at 22-23° S latitude (**Figure 4.1**) was calculated to only represent ~4% of the known moment deficit (*Chlieh et al., 2011*). Other megathrust events in Northern Chile were documented in 1615 and 1768 and the average recurrence interval was calculated to about 100 to 130 years (*Duputel et al., 2015*). Various coseismic slip models have been presented for the Iquique-Pisagua mainshock on April 1st, 2014 based on teleseismic observations (e.g. *Yagi et al., 2014*; *Ruiz et al., 2014*), GPS and tsunami records (e.g. *An et al., 2014*), seismic and GPS data (e.g. *Schurr et al., 2014*; *Hayes et al., 2014*), crack analysis (*Loveless et al., 2016*) and a combination of all of these observations (*Duputel et al., 2015*). In this study, I want to refine the existing coseismic models by combining InSAR measurements from two different satellites (Radarsat-2 and TerraSAR-X) with continuous GPS (cGPS) data to derive coseismic displacements. The unique InSAR data set allows to clearly separate coseismic slip induced by the main event from slip caused by the large aftershock on April 3rd in a joint InSAR and cGPS coseismic slip model approach.

4.1.2 Iquique-Pisagua earthquake trigger scenarios

The Iquique-Pisagua earthquake ruptured only about one third of the Northern Chile-Southern Peru seismic gap even though the calculated slip deficit of the entire seismotectonic segment was assumed to have exceeded 9 m, which would correspond to the inferred rupture size of the 1877 megathrust event in case of a total segment failure (e.g. *Schurr et al., 2014; Ruiz et al., 2014*). Thus, although a subduction megathrust event was foreseen to rupture the mature seismic gap in Northern Chile for quite a long time (e.g. *Kelleher, 1972; Comte and Pardo, 1991*), the final Iquique-Pisagua event was smaller than expected.

This fact raises the question of whether or not the 2014 earthquake was a characteristic seismic event that ruptured the same interface asperity with similar kinematics to those of the 1877-megathrust event. In order to address this question, I introduce in the following paragraphs the tectonic state and conditions that are thought to have finally led to the partial segment failure here.

The Iquique-Pisagua earthquake was preceded by a M_w 6.7 thrust event on 16th March 2014, approximately 60 km SE of the Iquique mainshock epicenter followed by a remarkable foreshore sequence that migrated towards the final rupture nucleation point

with a velocity comparable to that observed for the foreshock sequence before the great M_w 9.1 Tohoku-oki earthquake, Japan (*Yagi et al., 2014; Kato et al., 2012*). The similarity of foreshock patterns and migration velocities of both megathrust events leads to the interpretation that a slow slip event accompanied the Iquique-Pisagua precursors and accounts for up to 25% of the observed pre-shock ground displacements finally triggering the mainshock (e.g. *Kato et al., 2012; Ruiz et al., 2014*; *Yagi et al., 2014*; *Kato & Nakagawa 2014*; *Herman et al., 2016*). Additionally, repeating earthquakes in the foreshock sequence that migrate towards the hypocenter of the final mainshock are taken as indication for slow slip (e.g. *Kato & Nakagawa*, 2014; *Meng et al., 2015*), whereas other studies argue that repeaters could also be caused by fluid pressure changes rather than slow slip and question statistical robustness of the 16 days observation interval between fore- and mainshock (*Bedford et al., 2015*). Another evidence for a slow slip event may be given by the interseismically unusual trenchward motion of coastal cGPS stations for about two weeks from 16 March until April 1st, 2014 (**Figure B.11**; *Ruiz et al., 2014*). In contrast, other studies show that transient cGPS displacements before the Iquique-Pisagua mainshock can be reproduced by seismic slip caused by the foreshock sequence (e.g. *Schurr et al., 2014*; *Bedford et al., 2015*). However, the issue whether the Iquique-Pisagua mainshock was triggered by a slow slip event or not remains an ongoing discussion in scientific literature.

Alternative mainshock trigger scenarios involve the foreshock series that potentially occurred as cascading sequence of one earthquake triggering the following event finally culminating in the rupture of the mainshock. The M_w 6.7 event on 16 March 2014 is assumed to be the initiation-point of the intense precursor sequence (e.g. *Gonzáles et al., 2015*; *Herman et al., 2016*). This thrust-event ruptured at 17 km depth and is characterized by an unusually rotated strike of 277° compared to the subducting Nazca slab with a strike of 335° (*Hayes et al., 2014*). This rotation is generally attributed to the location of the rupture in the upper plate instead of on the plate interface as the strike coincides to crustal fault orientations (*Gonzales et al., 2015*). In contrast, most of the foreshocks of the Iquique-Pisagua event are located on the megathrust interface (*Hayes et al., 2014*). Triggering of the mainshock by the foreshock sequence is supported by the observation that the rupture area was characterized by a positive Coulomb failure stress (CFS), potentially loaded by preceding seismicity. Similarly, the large aftershock occurred in a region that was unaffected by precursors but most likely positively loaded by the mainshock (*Herman et al., 2016*).

4.2 Methods

4.2.1 InSAR processing

The Iquique-Pisagua earthquake on April 1, 2014 and its largest aftershock two days later induced large ground displacements that were measured by various geodetic instruments. In addition to cGPS data, I use InSAR measurements to jointly invert for ground motion and model coseismic interface slip. In my thesis, I use a total of 18 SAR images from the TerraSAR-X satellite in X-band (wavelength λ= 31.0mm) and 32 acquisitions from the Radarsat-2 satellite in C-band (56.2mm)

In general, two SAR acquisitions from the same frequency, footprint area, orbit and acquisition geometry are required for generating interferograms (*Hanssen, 2001*). In order to enlarge the spatial extent of the InSAR scenes, I concatenated three TSX and four RS2 acquisitions along-track to finally yield one single SAR image for each date (**Figure C.1**). The shortest interferometric observation interval corresponds to the satellite orbit recurrence time (11 days for TerraSAR-X and 24 days for Radarsat-2). In order to extract deformation related to an earthquake, one SAR scene before and one scene after the event is combined via different InSAR processing steps. Thus, the generation of interferograms is highly limited to the data availability in the satellite archive. In case of the Iquique-Pisagua earthquake, the data cover a time interval from 2011-2015 including deformation related to the mainshock on April 1, 2014 (**Figure 4.2**).

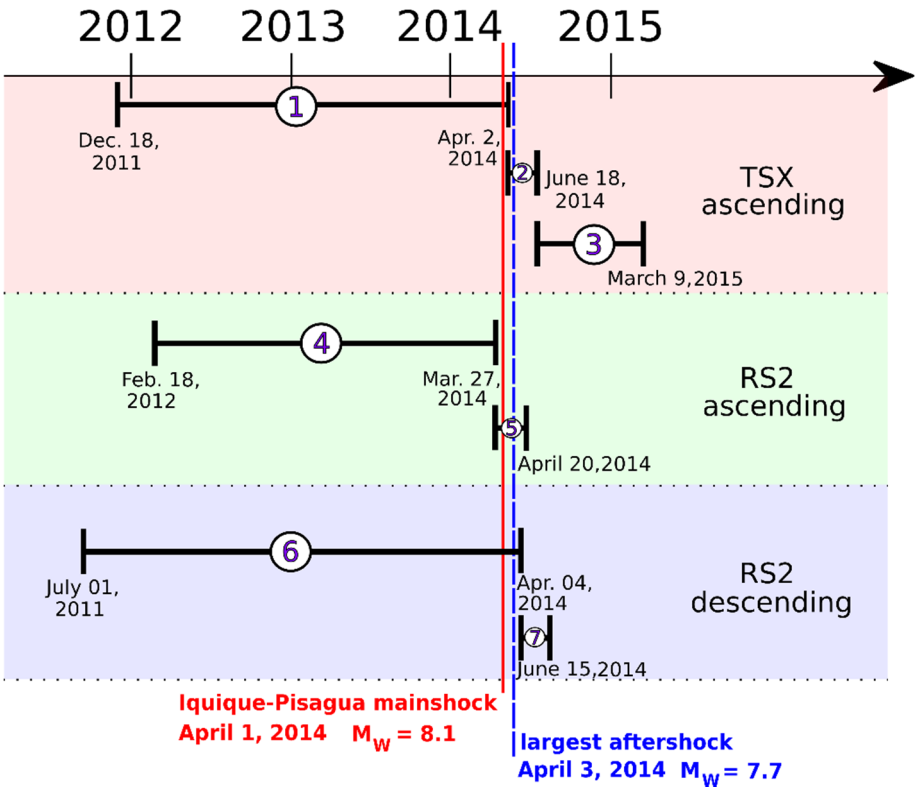

Figure 4.2: (previous page) *Overview of applied InSAR combinations with markers for the Iquique-Pisagua mainshock (red line) and the largest aftershock two days later (dashed blue line). Horizontal black lines (with numbers) indicate interferometric pairs with respective acquisition dates. The different colours reflect different acquisition modes: TSX ascending (red), RS2 ascending (green) and RS2 descending (blue).*

Processing of all SAR data is performed using the Gamma software (*Werner et al., 2000*). Here, I provide a detailed description of all applied processing operations for the interferometric approach of my data (**Text C.1**) and moreover highlight deviations and adjustments to the commonly followed processing chain presented in section 2.2.1. In general, I applied the same processing strategy for images of both sensors TerraSar-X and Radarsat-2, but used different parameter settings that are pointed out in the corresponding sections that outline the processing. First, I merged corresponding SLC tiles by estimating the offsets between two image tiles that must be overlapping along-track. I estimated range and azimuth registration offsets using cross-correlation optimization over a grid of 64 x 64 pixels with an oversampling factor of two. Based on these offsets, a four-parameter polynomial is solved with regression. I then concatenated two SLC tiles using the polynomials and the Doppler centroid information and repeated the procedure for the third SLC image for TerraSar-X respectively for the third and fourth image in case of Radarsat-2 acquisitions.

A drawback in merging several SLC tiles may be the introduction of slight image geometry changes and a shift of the Doppler frequency center location. This potentially leads to problems in the image co-registration and can result in a loss of coherence of the interferogram. When applying the common SLC-to-SLC resampling method based on correlation (see section 2.2.1), all processed interferograms experienced a significant degradation of coherence towards the edges of the merged image (**Figure 4.3**). For that reason, I applied an extended co-registration operation using look-up tables and the Shuttle Radar Topography Mission 2 (SRTM-2) DEM with a resolution of 3 arc seconds (~90 m; *Farr et al., 2007*).

The DEM-assistant co-registration provides higher accuracy than the cross-correlation algorithm and requires the generation of multi-look images (MLI) and a DEM in range-Doppler coordinates based on the geometry of the master MLI. Thus, each pixel of the reference SRTM-2 DEM is assigned to a coordinate of the corresponding pixel in the MLI. Multi-looking is a technique to reduce noise by averaging or oversampling an image which goes along with a reduction of the spatial resolution. For that reason, I chose the number of range and azimuth looks based on the best compromise between noise reduction and resolution loss based on the generation of square pixels in the SLC. For TerraSAR-X, I used 10 x 10 looks for approximately 20 m pixel spacing and for Radar-

sat-2, I used 5 x 10 looks in range and azimuth and approx. 50 m pixel spacing. The actual transformation of the SRTM-2 DEM into the radar coordinate system of the MLIs takes into account local terrain heights and image skew. First, each pixel of the DEM is transformed from map to Cartesian coordinates. Second, a correction of the Datum shift between the map projection and sensor orbit geometry reference ellipsoid is applied. Then, position and acquisition times of the pixels in map coordinates are determined and finally look vectors of those pixels are calculated to derive azimuth and slant range position.

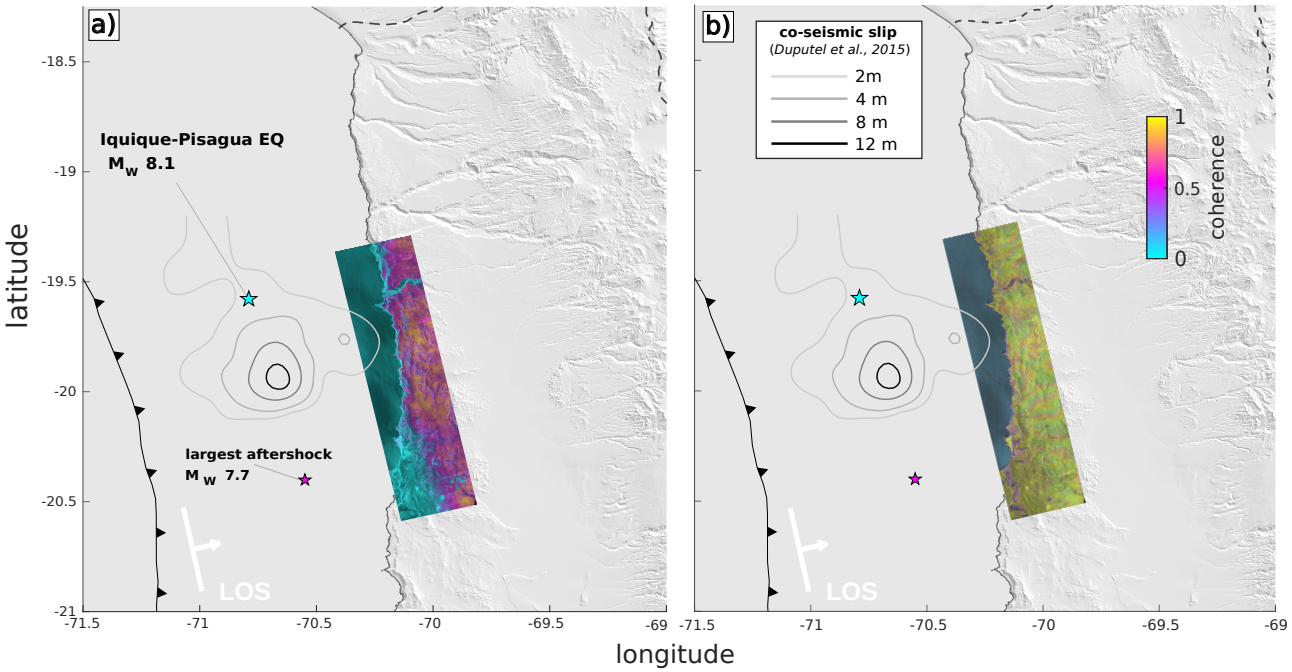

Figure 4.3: Coherence maps of interferogram 1 (Figure 4.2, asc. TSX 18122011-02042014) as a result of different processing strategies. a) The coherence is very low and decreases towards the edges of the image when applying SLC-to-SLC coregistration for merged SAR-tiles along-track. b) The coherence can be significantly improved when incorporating a DEM for coregistration procedure.

In a next processing step, I generated a co-registration look-up table by resampling the slave MLI to the master MLI geometry. The look-up table defines coordinates in the new transformation coordinate system for each image pixel in the old coordinate system. This transformation is based on image parameters and orbital data defined in the sensor parameter files. I determine initial registration offsets between the two images in different geometries using cross-correlation analysis. I performed a refinement of those offsets using bi-linear functions of range and azimuth to compensate for location errors due to imprecise orbital information. To yield refined offset model polynomials that guide the search of pixel positions, I calculate offsets in small image chips. This operation for estimating coefficients is repeated at least twice using different parameter set-

tings. In a first run, a small number of offsets is defined efficiently by choosing an oversampling factor of 1. To improve the quality and number of offsets, I chose an oversampling factor of 2 in the second run. This refinement yields the registration polynomial that is finally used to improve the quality of the initial look-up table. Using the refined look-up table, the slave SLC is then resampled to the master SLC. Due to inaccuracies in DEM terrain heights, orbit state vectors and offset estimation, a slight offset between both SLC images remains after this resampling and I applied the classical cross-correlation co-registering based on intensities to further improve the matching results. In a next step, I applied a complex multiplication of all pixels of the two co-registered SLC images yielding the complex normalized, wrapped interferogram in 10 x 10 looks (TerraSAR-X) and 5 x 10 looks (Radarsat-2) in range and azimuth. The generated interferogram now contains all phase contributions discussed in section 2.2.1 and equation 2.12 and needs to be corrected for all contributors that are not associated to ground deformation.

The baseline estimation for calculating the fraction of the orbital phase is based on the state vectors in the SLC parameter files. In case of inaccurate orbit information, large errors can arise. The provided orbits of TerraSAR-X were very precise, whereas orbits of Radarsat-2 acquisitions were inaccurate and produced large artefacts, visible as linear ramps over the entire interferogram. For that reason, more precise orbits were generated in a post-processing procedure using the enhanced definite orbit tool (EDOT) from the Canadian satellite owner, MDA. I used these definite orbits to update Radarsat-2 state vectors (**Figure C.2**). To subtract signal fractions due to topographic differences between the two SLC images (caused by the difference in orbit geometries and thus satellite look directions of each acquisition), I generated a simulated backscatter image. The height information is derived from the SRTM-2 DEM in radar coordinates and topographic information is converted into a synthetic signal in the radar domain. This operation requires a co-registration procedure between the simulated image and the wrapped interferogram, which I applied using a two-step intensity cross-correlation algorithm over image patches of first 256 x 256 pixels and second 128 x 128 pixels and an oversampling factor of 2. Subtracting the synthetic height phase from the complex interferogram yields the differential interferogram that is assumed to only contain deformation-related and error phase contributions. To prepare the wrapped differential interferogram that contains phase information modulo 2π for phase unwrapping, I apply an adaptive filtering approach. The advanced filtering step is performed to more efficiently unwrap the interferometric phase while reducing the number of residuals without losing spatial information. The adaptive filtering algorithm is based on *Goldstein & Werner (1998)* and applies filtering functions estimated from the local fringe spectrum. Thus, the inter-

ferogram power spectrum is computed locally to design a filter that is finally applied to the interferogram. The filtering is then applied using fast Fourier transformation (FFT) with a power of two. The FFT window size was set to 64, whereas the exponent for non-linear filtering was chosen to be 0.6 and hence represents the compromise between noise reduction and phase smoothing. As a result of the magnitude of the complex valued output filtered interferogram, I then derive a phase noise coherence map using an estimation window size of 9 pixels. The coherence map is an estimate for robust and non-robust unwrap areas in the interferogram. The lower the coherence, the more likely unwrapping errors will occur due to the presence of discontinuities. Unwrapping is the final and crucial step in interferometric processing, where an integer value is added to the complex phase information that is only known modulo 2π to yield the true ground range as surface deformation in the LOS of the satellite. This operation can mathematically described as path-dependent integration over all pixels. Unwrapping is realised by using the global optimization technique of minimum cost flow (MCF) with a triangular and irregular network that globally minimizes the difference in gradients of the wrapped and unwrapped phase (*Werner et al., 2002*). First, a coherence based validity mask is generated excluding areas that potentially introduce errors when unwrapping the interferometric phase. Pixels below a given coherence threshold in the interferometric correlation file are masked out for unwrapping . In my processing procedure, the coherence threshold ranges between 0.4 and 0.7. The interferometric correlation is also used for weighting pixels for the MCF processing. I then applied an adaptive sampling reduction to adaptively thin-out points. In general, patching the interferogram for unwrapping is not recommended, because it tends to introduce artefacts. But if the number of pixels exceeds the capacity of computer memory, patching becomes necessary. In the case of the Radarsat-2 data, I unwrapped the interferogram using 2x2 overlapping patches, whereas for TerraSar-X I unwrapped the entire interferogram as one single patch. For Radarsat-2, each patch is unwrapped individually and phases are merged at overlapping boundaries. The topmost left pixel of the interferogram in radar coordinates was arbitrarily set as reference point and thus phase zero for unwrapping procedure. The reason is that no areas of zero deformation could certainly be determined in the subduction zone earthquake setting with the expected long-wavelength tectonic signal. Linear ramps were accounted for in a post-processing procedure and final ground deformation values were adjusted in a joint inversion algorithm with GPS.

4.2.2 InSAR errors and subsampling

Interferometric data errors generally have individual characteristics for each single interferogram. One of the main error sources apart from unwrapping errors due to phase decorrelation is induced by the difference of the state of the atmosphere during two acquisitions (section 2.2.2). Since this error source involves turbulent atmospheric processes, InSAR processing has to be adjusted case-specifically for multi-looking, filtering and other noise reduction algorithms. The atmospheric error estimation is performed explicitly in an area that is free of surface deformation. This requires a priori knowledge about the area of interest and the expected deformation signal. For localized ground deformation sources (e.g. volcanoes) it is way easier to define areas of non-deformation close to the epicenter of deformation, whereas for earthquakes, large parts of the interferogram are affected by ground deformation. To enlarge the InSAR footprint, several SLC tiles can be merged along-track (section 4.2.1). Usually the epicenter for subduction megathrust events is located offshore and coastal InSAR footprints do not include the peak deformation location. Thus, an area that has the largest distance to the earthquake epicenter is defined as the least-deforming region. The error is assumed to be stationary, which means that error statistics are the same throughout the entire interferogram – in both deforming and non-deforming regions. For the InSAR variances, I calculate sample semi-variograms, whereas for the spatial correlation in the data, I use sample covariograms that are generated using characteristics of various point pairs throughout the defined non-deforming region in the interferogram (section 2.2.2). The point pair distance was chosen in a range between 0 and 0.5° with a bin distance of 0.02°. In this study, the level at which the semi-variogram saturates is defined as a data variance that ranges from 5 to 15 mm^2. Fitting positive-definite functions to the sample covariogram yields a continuous description of the covariance that assigns an error value to each InSAR pixel respectively each InSAR cell (**Figure 4.4**).

A single unwrapped interferogram usually consists of millions of data points (pixels), depending on the acquisition mode and coherence of the scene. In case of the Iquique-Pisagua earthquake, the expected ground motion signal has a long wavelength and a rather smooth deformation gradient. This deformation gradient can be represented with much fewer InSAR data points without any significant loss in information, and, given the number and average size of slip patches in the dislocation model, it is appropriate to downsample the InSAR data in the joint inversion with cGPS data. This InSAR resampling significantly improves the processing and inversion performance and moreover simplifies the data weighting of cGPS and InSAR data points. Thus, all interferograms are subsampled applying the Quadtree algorithm (*Jónsson et al., 2002*). For

Quadtree subsampling, the interferogram is subsequently subdivided into squares with a different size depending on a pre-defined, arbitrary variance threshold that cannot be exceeded within one square. The smooth deformation gradient for the Iquique-Pisagua earthquake results in an equal square size for all interferograms apart from the ascending TerraSAR-X interferogram (*02042014-15062014,* **Figure 4.4**), which simplifies the data weighting procedure. The number of subsampled cells varies between 130 to 196 in the interferograms and LOS deformation (location and error of each subsampled data point can be found in the auxiliary material, **Tables C.1-C.5**).

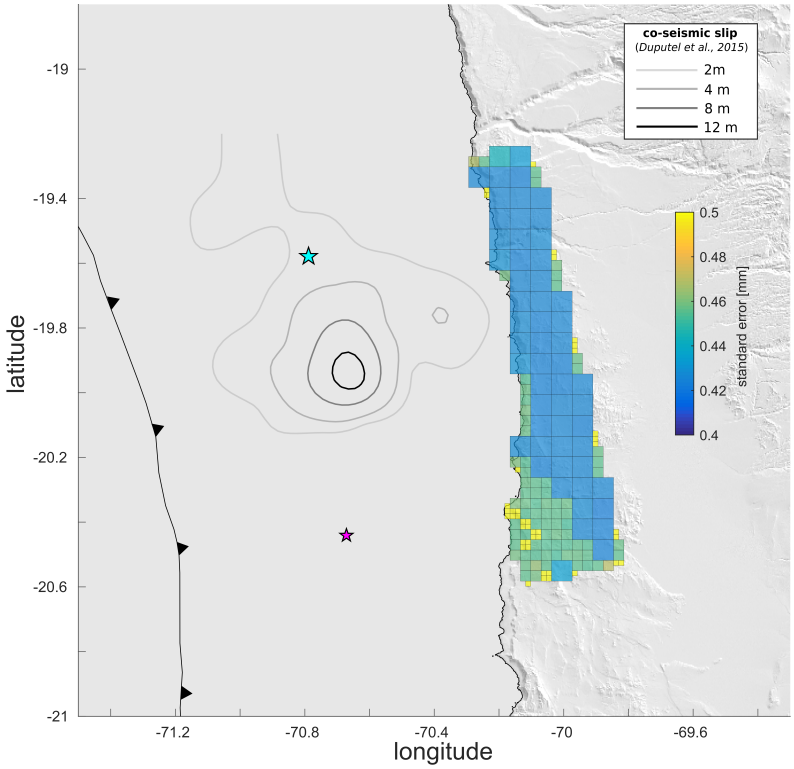

Figure 4.4: Subsampled TerraSAR-X interferogram (Figure 4.2, asc. TSX 02042014-15062014) showing irregular cell size distribution and the atmospheric error for each subsampled cell.

4.2.3 Methods GPS

The continuos GPS network used in this study includes 75 cGPS stations from the IPOC network (*Moreno et al., 2017*) and covers a latitudinal range of 18.2-23.5° S from the Chilean coast to 400 km inland. In contrast to the analysis of inter- and postseismic deformation (chapter 3), I excluded the non-stationary sGPS sites from the coseismic analysis of ground displacements, because coseismic displacements cannot be easily extracted from the timeseries due to the temporal limitation of measurement campaigns (typically re-observed every 6-18 months). The frequency of the cGPS antenna position determination is 1 Hz. In a first processing step, all position measurements within each

24 h period are averaged to a single GPS antenna position value. All cGPS data were processed in the ITRF2014 reference frame (*Altamimi et al., 2016*) using the EPOS software (*Deng et al., 2016*) that incorporates the position calibration by IGS absolute antenna phase centres (*Schmid et al., 2007*), a FES2004 tide model compensation (*Lyard et al., 2006*), an hourly random-walk parameter wet zenith delay calculation (*Gendt et al., 2013*) and a network mode coordinate estimation reducing the impact of the Earth rotation parameter (*Rebischung et al., 2015*). To compensate the non-deformational rotation of the South American Plate, I converted the resulting ITRF2014 cGPS measurements into NNR-Nuvel-1A compatible velocities (*DeMets et al., 1994*) relative to South America by applying an Euler Pole rotation (21.44° S, 125.18° W, 0.12° Myr^{-1}, *Moreno et al., 2011*).

The total cGPS time series of the IPOC network in this study covers a time interval from 2003-2016 (**Figure B.1**). The GPS signal thus contains, along with various noise signals, the tectonic ground displacement signal contributions of the inter-, co- and postseismic stage related to the Iquique-Pisagua earthquake 2014. For a tectonic analysis, the most problematic sources of noise (non-tectonic) in the time series are due to seasonal oscillations and antenna offsets (*Bevis & Brown, 2014*). For each component (East, North, and Up) at each station, I calculated model parameters for the station trajectory with a linear regression, including terms for first-order polynomial tectonic motion, seasonal oscillations, and earthquake and equipment related offsets (see also section 2.1.3). The mathematical functions for the modelled tectonic signal contributions are outlined in *Bevis & Brown (2014)*. A more detailed description of the GPS post-processing extraction of tectonic signal contributions is provided in section 3.2.2. cGPS time series (**Figure B.2**), GPS data processing (**Text B.1** and **Figure 2.2**) and reference frame realization (**Figure B.4**) are provided in the auxiliary material. Finally, I separated the coseismic displacement related to the Iquique-Pisagua mainshock on April 1, 2014 by truncating the corrected time series. The time period for coseismic cGPS measurements thus covers three days from one day before the actual mainshock until one day after (March 31 – April 2, 2014). For measurements of ground displacement in relation to the largest aftershock on April 3, 2014, I extracted cGPS data from April 2 until April 4, 2014. However, for the joint models including InSAR and cGPS data, the length of the coseismic cGPS time series corresponds to the relative time span between master and slave SAR acquisition of each interferogram individually. The cGPS measurements and error of each data point can be found in the auxiliary material (**Tables C.6-C.10**).

4.2.4 Geodetic Modelling: joint inversion of InSAR and cGPS data

The surface deformation measured by cGPS and InSAR data can be related to motion of a known fault geometry at depth by means of analytical transfer functions (Green´s functions). By inverting this system of linear equations using the least-square MATLAB routine 'lsqlin' (*Coleman and Li, 1996*), I model slip as dislocations of each sub-patch of the fault in an elastic half space (*Okada, 1985*, *Okada, 1992*). The fault plane of the Iquique-Pisagua subduction zone earthquake corresponds to the Chilean subduction plate interface geometry, which I sample from the SLAB1.0 model (*Hayes et al., 2012*). I model slip as along strike and up-dip dislocations on 1016 triangular fault patches that extend from 17.5 to 26°S latitude and from the surface down to a maximum depth of 65 km, assumed to represent the Moho depth (*Husen et al., 2000*; *Chlieh et al., 2011*). The rake is not constrained and backslip is allowed to occur. I additionally apply a Laplacian operator that minimizes slip variations of neighbouring patches based on an input smoothing weight. The strength of this regularization is determined by the trade-off between misfit and slip roughness (**Figure C.3**).

The joint inversion of cGPS and InSAR data additionally incorporates a simple model of a 3-dimensional linear ramp on InSAR cells (Quads). This linear ramp is corrected for the unwrapped interferograms (**Figure 4.5**).

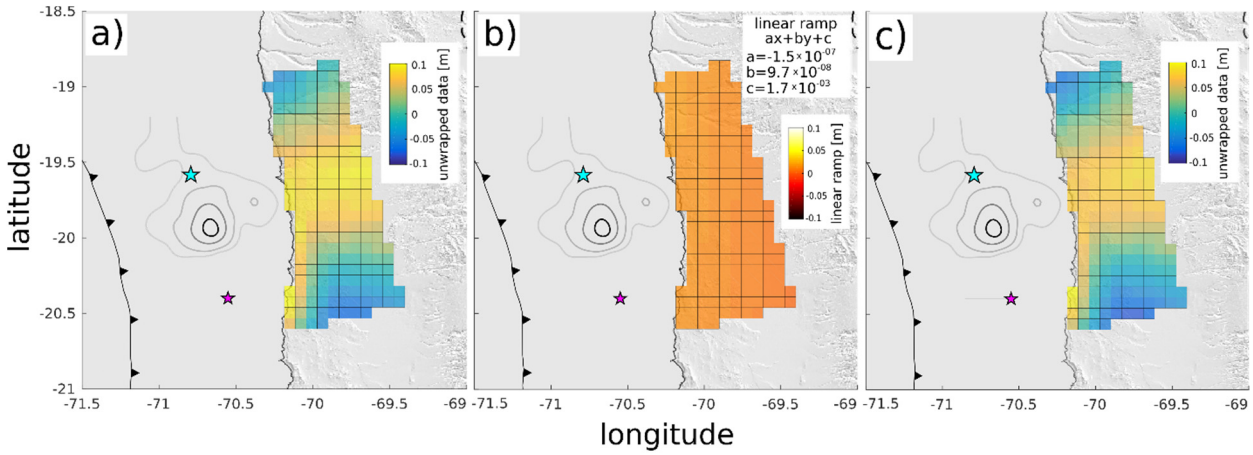

Figure 4.5:Subsampled Radarsat-2 interferogram (Figure 4.2, asc. RS2 27032014-20042014) with a) the unwrapped interferogram, b) the calculated linear ramp and c) the unwrapped interferogram corrected for the linear ramp.

To compensate shortening signal in the surface deformation rates caused by the Central Andean sliver (*Bevis et al., 2001*), I applied an Euler Pole calculated in the interseismic models (1.20° S, 77.31° W +0.30° Myr^{-1}, see section 3.3.2). The Andean sliver motion accounts for 12-14 mm/yr of measured cGPS rates, which is consistent with other stud-

ies (e.g. *Métois et al., 2013*; *Brooks et al., 2011*). This sliver contribution is removed individually from each time series.

For jointly modelling InSAR and cGPS data, the relative weights for all data points have to be adapted carefully, especially as the interferograms have a spatially extremely high resolution. As discussed earlier in this chapter, the long-wavelength tectonic signal allows for a subsampling of the InSAR data points down to a number comparable to the number of cGPS data points. Due to the higher incidence angle for SAR acquisitions, InSAR measurements are more sensitive to vertical motion, whereas GPS data better represent horizontal deformation. Despite of the higher sensitivity of GPS measurements to horizontal motions, the error for both, vertical and horizontal direction, given by the instrument is in the same order of magnitude. Thus, the vertical error may be underrepresented by the instrument. For this reason, I increased the vertical cGPS uncertainty by decreasing the weights for the vertical component by a factor of five. The weights for all InSAR data points (Quads) and cGPS stations are defined as the square of the inverse error. For each cGPS data point, the error corresponds to the total position error of a 24 h-period, whereas for the InSAR cells, the error is calculated based on a statistical approach (section 4.2.2). The distribution between both data sets spatially varies and I additionally tested different weighting ratios $w = w_{InSAR}/w_{cGPS}$ in a least rms-error analysis (*Cavalié et al., 2013*). A weighting ratio of w= 0.75 – 1.5 generates the best data fit for the individual slip models (**Figure 4.6** and **C.3**).

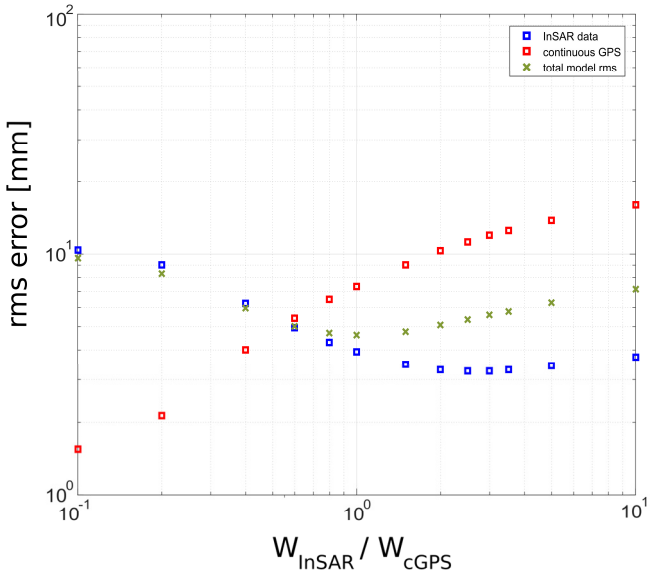

Figure 4.6: Testing different weighting ratios $w = w_{InSAR}/w_{cGPS}$ for Sub-model VI including the asc. interferogram RS2 27032014-20042014 (Figure 4.9 b,d). Single cGPS rms error (red rectangles), single InSAR error (blue rectangles) and total error (green crosses) are plotted together. The ratio with the least total rms error is considered as best fit ratio for weighting the different data sets.

The coseismic slip models generally reflect (positive) trenchward motion on fault slip patches during the mainshock and the largest aftershock of the Iquique-Pisagua earthquake 2014. But the sparse SAR data archive availability only allows the generation of long model time intervals that contain inter- co- and postseismic ground displacement signals. The superposition of different deformation mechanisms in the seismic cycle requires a higher degree of complexity in all sub-models. For this reason, (negative) landward motion of fault patches referred to as backslip (*Savage, 1983*) as an estimate for interseismic coupling is allowed in the modelling. Another reason for allowing backslip is the large spatial extent of the interface geometry that covers different seismotectonic segments that may not all be directly influenced by coseismic (trenchward) interface motion. The degree of coupling of the plate interface can be inferred from those backslip rates. Coupling is given in ratios between 0 and 1, with 1 referring to a fully locked plate interface moving with the rate of the subducting Nazca Plate which is 54 mm/yr after removal of the sliver motion (*Li et al., 2015*; *Métois et al., 2016*).

4.2.5 Model strategy: Extraction of coseismic slip

I separately analyse ground deformation caused by the Iquique-Pisagua mainshock on April 1, 2014 and its largest aftershock two days later. By jointly inverting for cGPS and InSAR data, I generate a coseismic slip model for both events. Due to the limited availability of SAR data that are suitable for interferometry in the archive, the time period of all coseismic models covers approximately four years in total, from 2011 until 2015 (**Figure 4.7**). Thus, although InSAR data allow for a highly spatially resolved investigation of coseismic deformation patterns in the coastal near-field area of the Iquique-Pisagua mainshock region, all interferometric measurements represent a superposition of deformation from different stages of the seismic cycle. To extract pure coseismic displacements, I split the ground displacement analysis into different model intervals and compensate for non-coseismic measurement contributions. Accordingly, the independent coseismic slip models of the largest aftershock (Model A) and the mainshock (Models C-D) are retrieved from a complex combination of various Sub-models (I-VI) (**Figure 4.7**)

Model A combines two Sub-models (I and II). Sub-model I contains only postseismic deformation. The descending RS2 interferogram from April 4th until June 15th 2014 is jointly inverted with cGPS data from the corresponding interval. Sub-model II incorporates the joint inversion of the ascending TSX interferogram from April 02, 2014 until June 18, 2014 with corresponding cGPS data and contains coseismic deformation caused by the largest aftershock plus postseismic deformation. Subtracting Sub-model II

from Sub-model I, while assuming that rate changes between the 15th until the 18th of June 2014 are negligible, yields the extracted ground displacement of the largest aftershock on 3rd of April.

The coseismic (mainshock) Model B is derived by first generating Sub-model III as joint inversion of ascending TSX interferogram of December 18, 2011 until April 02, 2014 with cGPS data in that interval. Sub-model III thus contains more than two years of interseismic slip and the ground displacement caused by the mainshock on 1st of April 2014. In a second step, I performed Sub-model IV that incorporates cGPS velocities calculated for the corresponding interval (December 18, 2011 until March 31, 2014) as derived from my averaged interseismic model (**Figure 3.4**, section 3.3.2) to compensate for interseismic loading**.** Finally, the subtraction of Sub-model IV from Sub-model III yields the coseismic Model B.

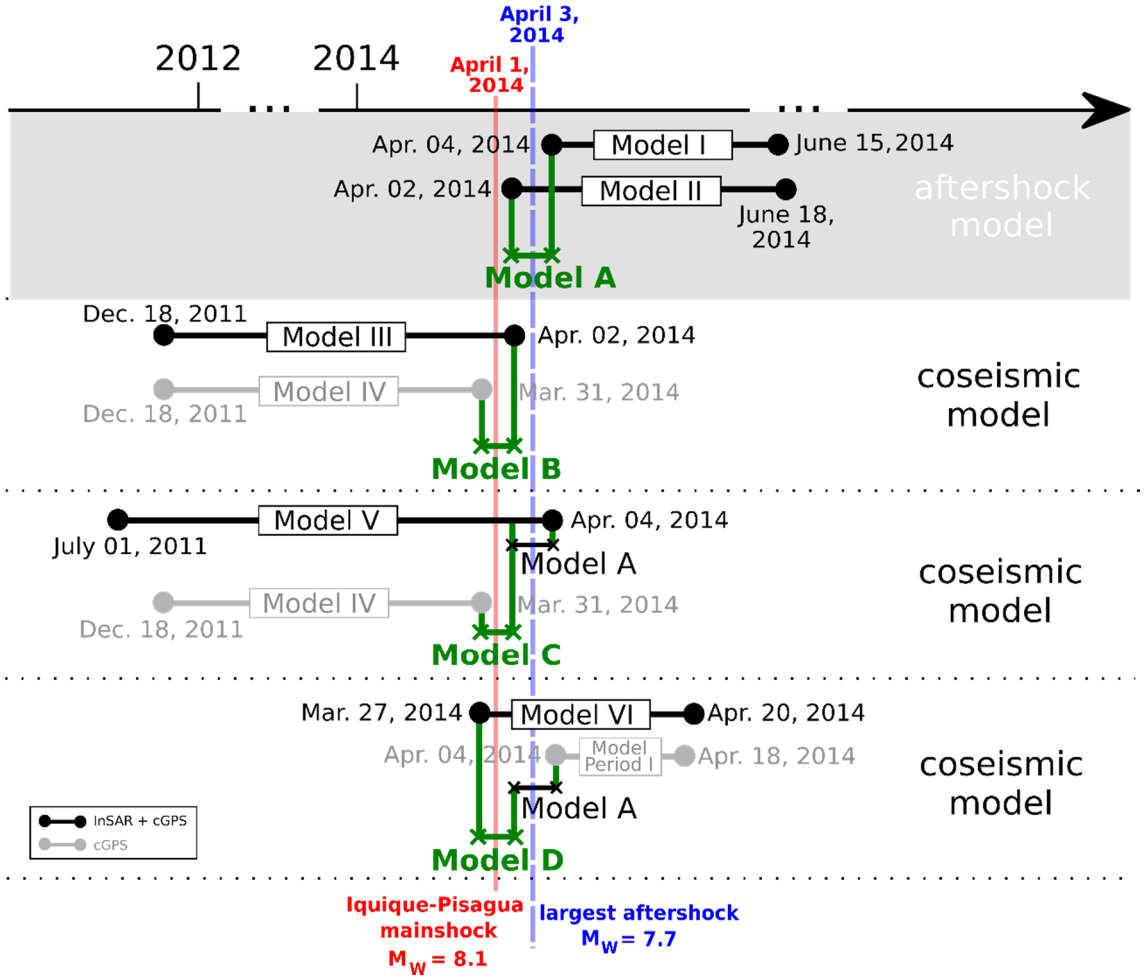

Figure 4.7: Overview of the complex model substitutions to derive an aftershock (Model A) and three coseismic (Models B-D) slip models. Models I-VI refer to Sub-models derived from the joint inversion of cGPS and InSAR data (black lines) respectively inversion of cGPS-only measurements (grey lines). The model intervals of Sub-Models I-VI correspond to the dates highlighted in the figure (grey/black dots). Subtraction of those sub-models yields the final coseismic/aftershock Models A-D (green lines).

The second coseismic (mainshock) Model C incorporates the joint inversion of the descending RS2 interferogram from July 01, 2011 until April 04, 2014 with cGPS data in the corresponding interval (Sub-model V). Since this approach incorporates more than two and a half years of interseismic loading as well as the displacement caused by the largest aftershock on 3rd of April 2014, I need to separately subtract both non-coseismically derived slip contributions from Sub-model V. Therefore, I first compensate for aftershock-related deformation by subtracting Model A from Sub-model V. In a second step, the interseismic Sub-model IV that is already applied in Model A is subtracted from the modified Sub-model V to finally derive Model C.

A third coseismic (mainshock) Model D contains the ascending Radarsat-2 interferogram from March, 27 – April 20, 2014 that is jointly inverted with cGPS data from the corresponding interval (Sub-model VI). The time period of postseismic deformation corresponds to the interval covered in model Period 1 in section 3.4.1. Subtracting Model Period 1 from Sub-model VI yields the coseismic slip of the mainshock and the main aftershock. Therefore additionally subtracting Model A from the modified Sub-model VI extracts the purely coseismic Model D.

Finally, each of the three independent mainshock slip models B, C and D is equally weighted to yield the best representation of coseismic slip on the subduction interface.

4.3 Results

4.3.1 Interferograms

In this study, I processed seven interferograms of two different satellites (TSX and RS2) in ascending and descending orbits. All interferograms cover different stages of the seismic deformation cycle in Northern Chile associated to the Iquique-Pisagua earthquake 2014. Here, I present results of wrapped and unwrapped ground displacements in the line-of-sight (LOS) direction of the satellite. Most of the processed interfergrams are combined in a joint inversion approach together with cGPS data. For two interferograms (RS2 18022012-27032014 and TSX 18062014-09032015), the complex signal contributions and spatial limitations for large-scale inter- and postseismic deformation strongly restrict a joint modelling approach. One RS2 interferogram displays the early postseismic deformation (04042014-15062014), whereas all other interferograms contain coseismic ground displacement signal contributions caused by the mainshock (TSX 18122011-02042014), the largest aftershock (TSX 02042014-18062014) or the combination of both (RS2 01072011-04042014 and RS2 27032014-20042014) (**Figure 4.2**).

In general, wrapped interferograms indicate the direction of ground motion towards or away from the LOS of the satellite. This direction can directly be inferred by the sequence of colours within one fringe that represents a full cycle (or half the wavelength) of the emitted electromagnetic wave. The number of fringes in one interferogram is equal to the integer number of full cycles of relative ground displacement throughout the footprint. The displacement measured modulo 2π (one phase cycle) is thus given by the number of fringes, whereas the spatial relation of ground deformation is given by the density and extent of those fringes. This wrapped information of ground displacement is then unwrapped by applying a path-dependet, pixelwise integration that yields the total displacements in metric length units. The reference point for the starting location of the integration (unwrapping) is defined as a zero deformation location. Its position was chosen based on the largest distance to the expected maximum deformation.

The wrapped ascending coseismic TSX interferogram (**Figure 4.8 a**) shows a dense, dominantly N-S directed fringe pattern. The fringes are interrupted in the central and southern part, and less clear and less circular shaped compared to the RS2 coseismic interferograms (**Figure 4.9 b, 4.10 a**). The unwrapped ascending coseismic TSX interferogram (**Figure 4.8 d**) reveals the maximum ground motion at the coast at the closest distance to the mainshock epicenter with 100 mm motion towards the LOS. The deformation decreases towards the south of the footprint with a minimum of about -10 mm (direction away from the satellite). The wrapped ascending coseismic TSX interferogram of the largest aftershock (**Figure 4.8 b**) has a circular-shaped and dense fringe pattern centered at the closest distance to the epicenter of the aftershock at the coast at 20.4° S latitude. These circular fringes are interrupted by N-S directed fringes at 19.8° S latitude towards the north that may reflect the influence of postseismic ground deformation of the mainshock. The unwrapped ascending TSX interferogram (**Figure 4.8 e**) reveals a maximum ground motion of 100 mm towards LOS in the center of the circularly shaped deformation pattern at closest distance to the aftershock epicentre at the Chilean coast. A minimum ground motion of -100 mm away from the LOS occurs at the same latitude further inland, at the rim of the circular deformation pattern.

Figure 4.8: (next page) *Ascending TerraSAR-X interferograms. The wrapped interferograms a)-c) are displayed in full phase cycles measured from 0 to 2π in the LOS of the satellite. Unwrapped interferograms d)-f) show deformation in metric units (mm) with look angle from the ground. The numbers at the bottom right of each image refer to interferogram numbers in Figure 4.2, where a) and d) is TSX 18122011-02042014 (1), b) and e) is TSX 02042014-18062014 (2) and c) and f) is TSX 18062014-09032015 (3). The reference point is marked with a black star in the unwrapped interferograms. Black dotted rectangles on f) show footprint size of descending and ascending RS2 interferograms. The coseismic slip contours are from Duputel et al., (2015).*

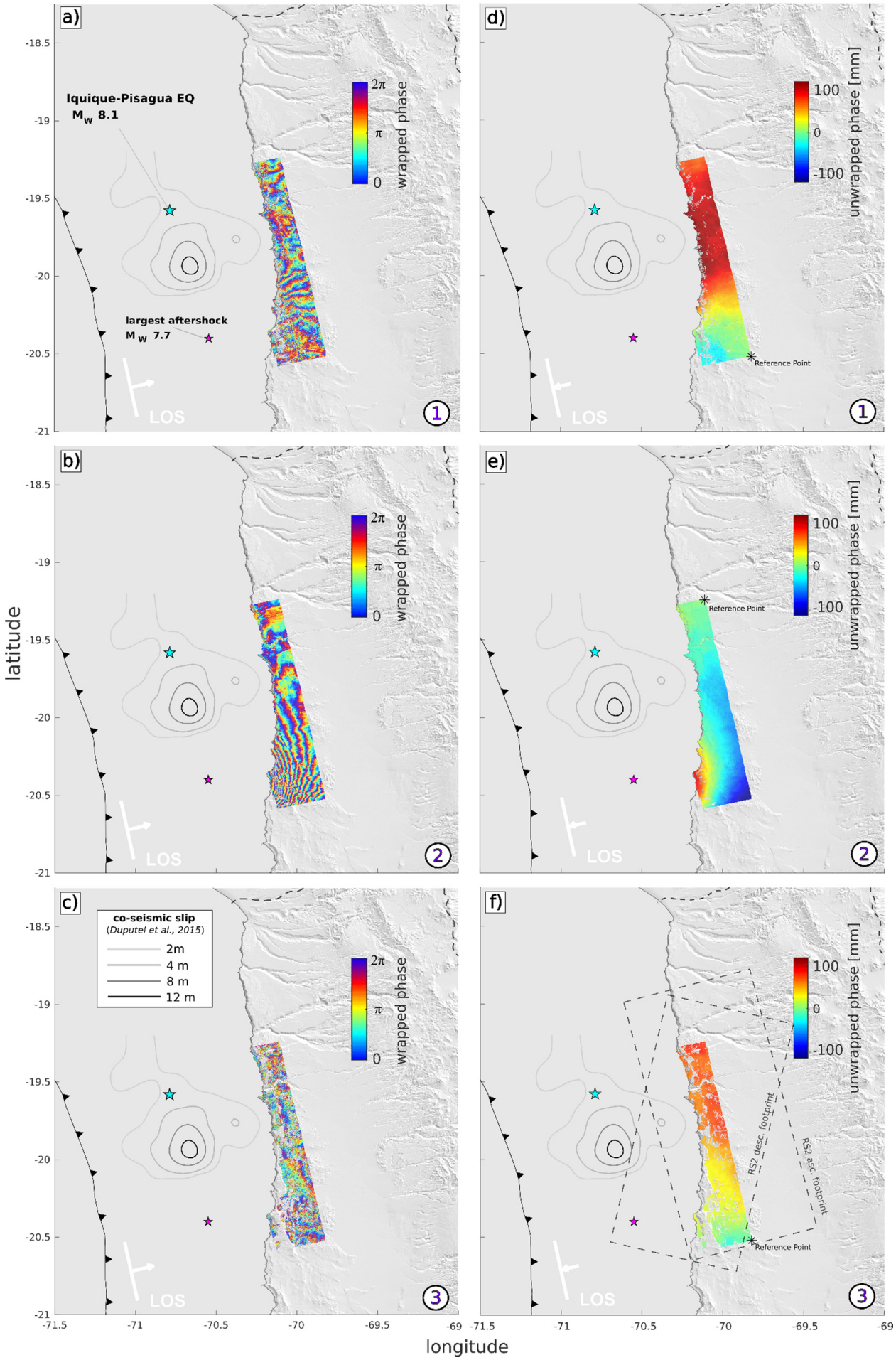
a)
Iquique-Pisagua EQ
M w 8.1
largest aftershock
M w 7.7
LOS
1
2π
π
0
wrapped phase
d)
100
0
-100
unwrapped phase [mm]
Reference Point
b)
e)
c)
co-seismic slip
(Duputel et al., 2015)
2m
4 m
8 m
12 m
f)
RS2 desc. footprint
RS2 asc. footprint
2
3
-18.5
-19
-19.5
-20
-20.5
-21
-71.5
-71
-70.5
-70
-69.5
-69
latitude
longitude

The wrapped ascending postseismic TSX interferogram (**Figure 4.8 c**) has a significantly lower coherence, which is indicated by less dense pixel (scatterer) coverage compared to all other interferograms. Thus, the fringe pattern is hardly visible and less consistent. However, the fringes are mainly N-S-oriented, perpendicular to the trench. The unwrapped ascending postseismic TSX interferogram (**Figure 4.8 f**) reveals a relative ground motion difference within an approximate range of 0 to 70 mm towards the satellite, from the south to the north of the scene.

The wrapped interseismic RS2 interferogram (**Figure 4.9 a**) shows a preferably N-S directed ground deformation. The fringes in the northern part are characterized by an elliptical shape with an extended axis in the N-S direction, whereas the geometric fringe pattern towards the south is less clear indicating less ground motion. This change of fringe geometry can be localized in the latitudinal range of the epicentre of the Iquique-Pisagua mainshock at ~20° S. A similar conclusion can be drawn based on the unwrapped interferogram (**Figure 4.9 c**) that shows maximum ground motion of 85 mm in the north and maximum subsidence of -30 mm towards the south. The location of the inferred hingeline of the change of motion roughly coincides with the latitude of the megathrust epicenter. The fringe pattern of the wrapped ascending coseismic RS2 interferogram (**Figure 4.9 b**) is very dense, indicating a high degree of deformation throughout the footprint. The highest density occurs at the coast, closest to the epicenter of the mainshock and the largest aftershock with fringes directed parallel to the trench, E-W. Those fringes are super-imposed further onshore by a second dominant fringe pattern that is directed N-S, thus perpendicular to the trench. The unwrapped interferogram (**Figure 4.9 d**) reveals the highest ground deformation at the coast of about 150 mm towards the satellite, which may be primarily due to the high horizontal, coseismically trenchward motion rate rather than to the vertical motion. The N-S directed ground deformation shows deformation away from the LOS towards the northern and southern edges of the interferogram. The complex LOS-deformation pattern may arise by the satellite acquisition geometry. In ascending mode, the satellite look direction is towards the right (East). Thus coseismic ground motion in Northern Chile is directed towards the satellite look direction and horizontal motion dominates over vertical motion in the interferogram as subsidence would be expected at this distance to the trench. Moreover, the large coseismic deformation signal exceeds the spatial coverage of the InSAR footprint. The reference point location is defined at the largest distance to the epicentre of the mainshock and the largest aftershock, and may reflect the location of least deformation (rather than zero ground motion) which would result in a possible deformation offset throughout the interferogram.

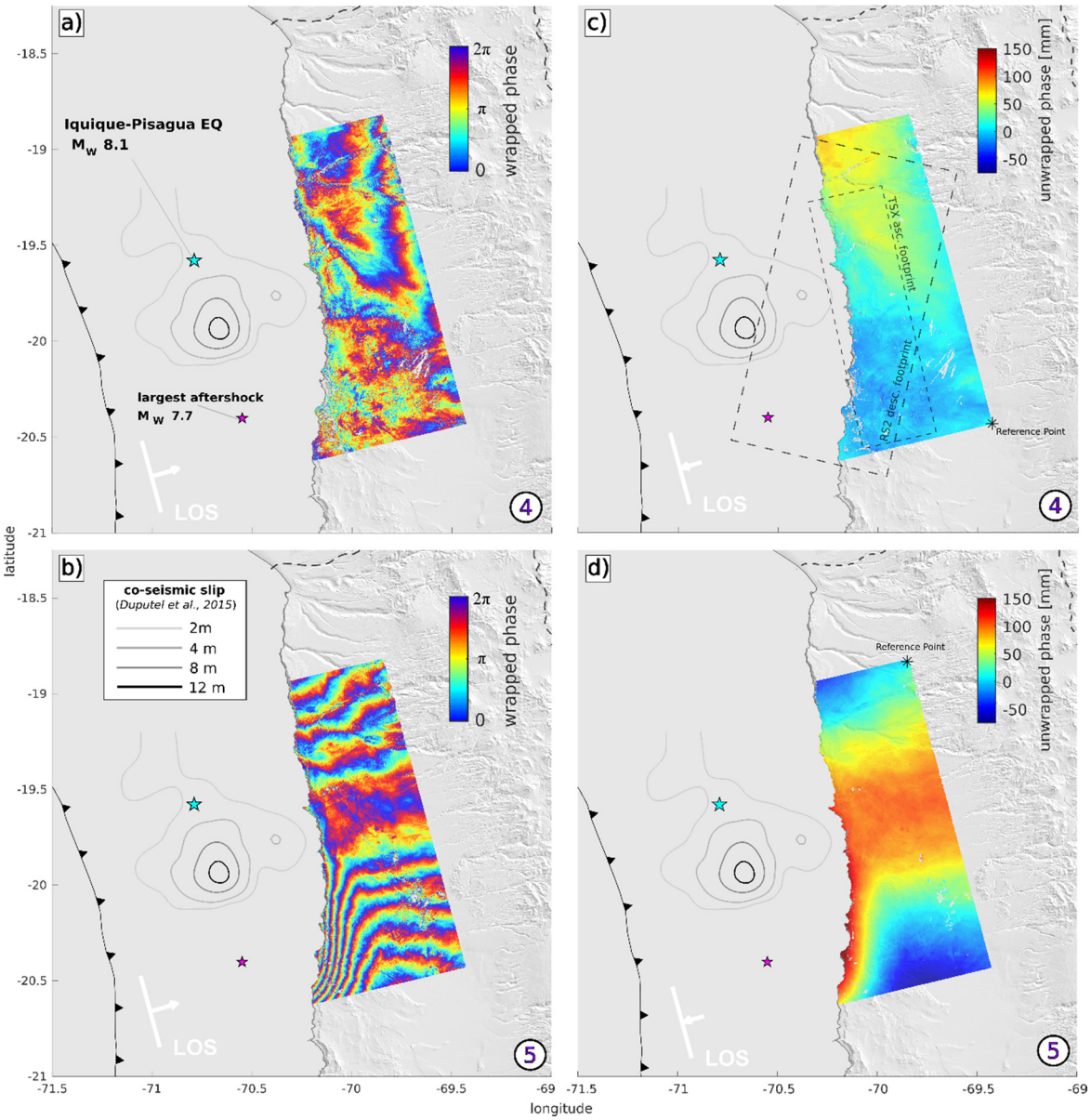

Figure 4.9: Ascending Radarsat-2 interferograms. The wrapped interferograms a)-b) are displayed in full phase cycles measured from 0 to 2π in the LOS of the satellite. Unwrapped interferograms c)-d) show deformation in metric units (mm) with look angle from the ground. The numbers at the bottom right of each image refer to interferogram numbers in Figure 4.2, where a) and c) is RS2 18022012-27032014 (4), and b) and d) is RS2 27032014-20042014 (5). The reference point is marked with a black star in the unwrapped interferograms. Black dotted rectangles on c) show footprint size of descending RS2 and ascending TSX interferograms. The coseismic slip contours are from Duputel et al., (2015).

The wrapped descending coseismic RS2 interferogram (**Figure 4.10 a**) shows a densely circular shaped fringe pattern centered at the coast at closest distance to the epicentre of the mainshock (19.8° S). The unwrapped descending coseismic RS2 interferogram (**Figure 4.10 c**) yields a maximum deformation of -600 mm away from the LOS in the center region of the circular pattern.

The fringe pattern in the wrapped descending postseismic RS2 interferogram (**Figure 4.10 b**) is less clear and less dense, but still circular shaped with the center in the latitudinal range of the mainshock epicenter. The wavelength of these fringes have changed in comparison to the coseismic pattern and is larger in the postseismic stage.

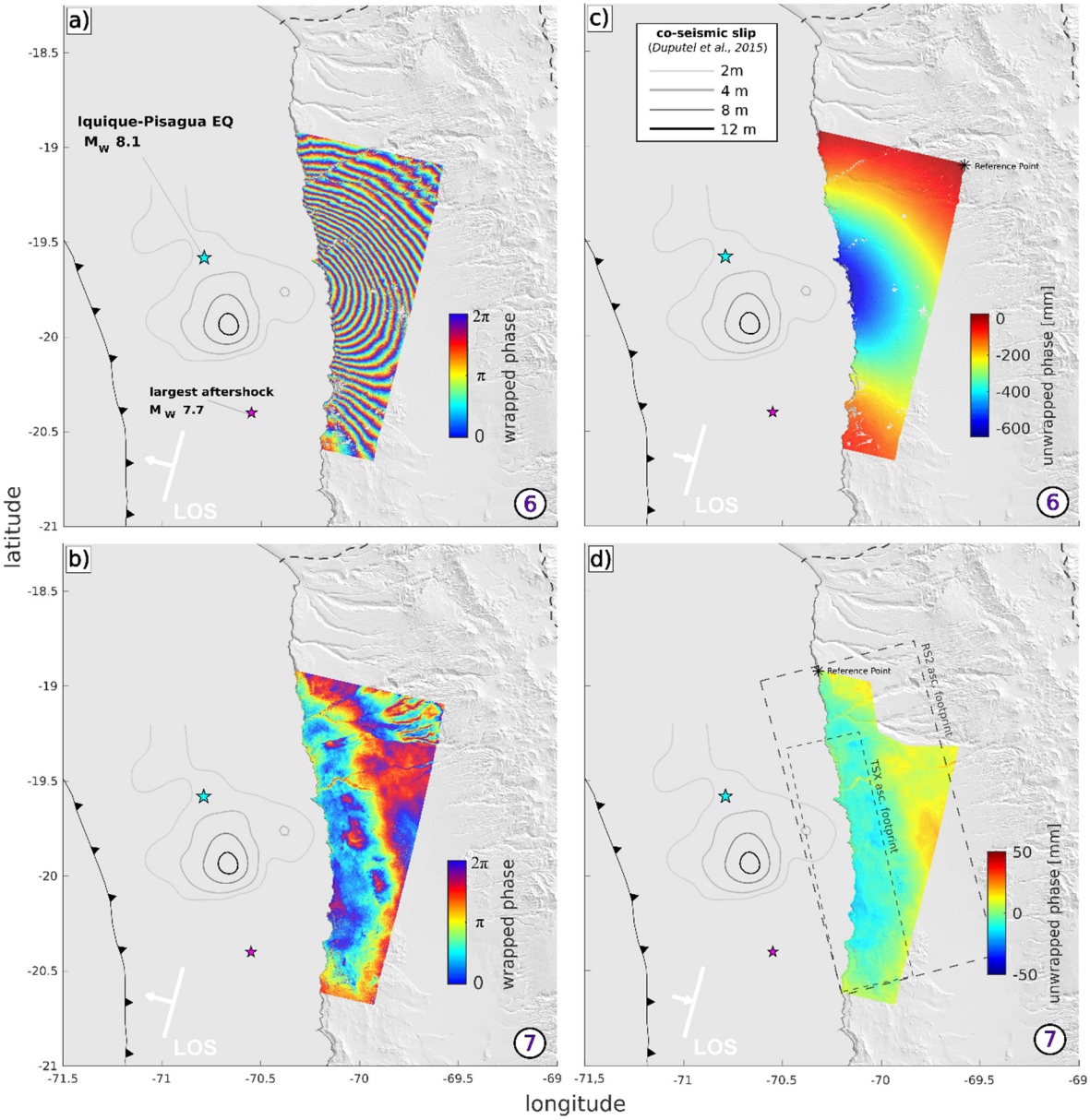

Figure 4.10: Descending RS2 interferograms. The wrapped interferograms a)-b) are displayed in full phase cycles measured from 0-2π in LOS. Unwrapped interferograms c)-d) show deformation in mm with look angle from the ground. The numbers at the bottom right refer to interferogram numbers in Figure 4.2, where a) and c) is RS2 01072011-04042014 (6), and b) and d) is RS2 04042014-15062014 (7). The reference point is marked with a black star in the unwrapped interferograms. Black dotted rectangles on d) show footprint size of ascending RS2 and TSX interferograms.

In the wrapped interferogram (**Figure 4.10 b**), a lot of small-scaled, multicolored fringe structures are apparent and can be correlated to topography gradients in the unwrapped

descending postseismic RS2 interferogram (**Figure 4.10 d**). In particular, the canyons to the north and the ridge structures in the center of the footprint are clearly visible as deformation anomalies. These anomalies can often be explained by highly varying local conditions of atmospheric water vapor availability at the image acquisition time. Those conditions lead to a correlation of topographic height with interferometric phase. These effects can be corrected by applying a linear inversion in which a linear trend is subtracted from the phase depending on terrain elevation (see also section 2.2.2). But strongly local varying conditions within the InSAR footprint as the canyons to the north (**Figure 4.10 b**) are hard to correct for without further information and are cropped in order to not contaminate the deformation signal (**Figure 4.10 d**). The corrected unwrapped interferogram (**Figure 4.10 d**) shows subsidence of -10 mm at the coast in a circular-shaped deformation pattern.

4.3.2 Models

For all models, I performed a sensitivity analysis, in which I forward model a checkerboard geometry of slip and backslip patches of +/- 1 m slip with a rectangular size of ~80x80 km on the subduction zone interface to the cGPS network and InSAR data patches. This analysis reveals a relatively better resolution of the plate interface below 15 km depth, whereas shallow slip above 10 km depth is relatively poorly resolved, which is mainly due to the lack of offshore measurements (**Figure C.4 a**).

Sub-model I covers the first two months of postseismic stage measured with InSAR and GPS. The weighting ratio $w = w_{InSAR}/w_{cGPS}$ based on the approach of *Cavalié et al. (2013*) is 0.75 (**Figure C.4 f**). The slip model reveals a quite homogeneous slip of about 0.25 m with peak slip of 0.28 m at the southern edge around the epicenter of the largest aftershock (**Figure 4.11 a**). Postseismic slip is negligible south of 21° S and north of 18.8° S. The GPS data reveal a distinct change of motion at ~21°S from trenchward to the north and (interseismically) landward motion to the south (**Figure 4.11 b**). The largest horizontal motion is 66.0 mm at cGPS station UAPE. My model fits the cGPS well with a rms-misfit of 1.0 mm in horizontal direction and 1.4 mm in vertical direction **(Figure C.4 b**). The InSAR footprint covers only the trenchward motion north of 21° S and shows very little (vertical) LOS-ground motion (less than 20 mm, **Figure 4.11 f**). The slip model represents well the LOS-motions with a rms-misfit of 3.2 mm (**Figure 4.11 g**). Original InSAR data, linear ramp reduction and InSAR model residuals can be found in the auxiliary material (**Figure C.4 c-e**).

Sub-model II (a joint inversion of GPS and InSAR data) covers the first two months of the postseismic stage and incorporates the largest aftershock on 3rd of April. The weighting ratio $w = w_{InSAR}/w_{cGPS}$ is 1.5 (**Figure C.5 a**). The slip model shows an ellipti-

cal-shaped distribution that is elongated towards N-S in the megathrust rupture area with a maximum slip of 1.5 m at the inferred hypocenter of the largest aftershock at 20.5° S latitude south of the mainshock. Slip extends slightly south of 21° S and north of 19° S latitude and is negligible beyond this latitudinal range. The slip at the southern edge of the mainshock rupture area is ~1 m and less than 0.5 m towards its northern edge (**Figure 4.11 c**). **Figure 4.11 d** shows again a distinct change of motion south of ~21.2° S from (co- and postseismically) trenchward to the north and (interseismically) landward motion towards the south. The measured GPS horizontal surface motion in the coastal vicinity of the epicenter of the largest aftershock is generally very high and reaches a maximum value of 22.46 cm (cGPS station CGTC). Overall, the model fits the horizontal cGPS data well with a rms-misfit of 2.25 mm. But some coastal and inland stations in the vicinity of the rupture area between 20-21° S show considerable divergence in horizontal ground motion direction and magnitude to the model (e.g. cGPS station CRSC). A possible reason may be local deformation effects during the coseismic rupture of the largest aftershock, which are documented as (re-)opened surface cracks in the geologic archive (*Loveless et al., 2016*). Another reason involves the data weighting in the model that favors vertical InSAR data due to the rms-error-analysis (**Figure C.5 a**). The vertical GPS data is constantly overpredicted with a rms-misfit of 9.3 mm (**Figure C.5 b**), which may be due to the high uncertainty of vertical GPS data. The InSAR data shows a circular deformation pattern with the maximum of 9.8 cm at the coast at 20.8° S at closest distance to the epicenter of the largest aftershock with (**Figure 4.11 h**). The model slightly underpredicts the InSAR data with an average rms-error of 7.2 mm (**Figure 4.11 i)**. Original InSAR data, linear ramp reduction and InSAR model residuals can be found in the auxiliary material (**Figure C.5 c-e**).

The aftershock slip Model A (**Figure 4.11 e**) is the result of the subtraction of Sub-model II from I. The interface slip pattern is elliptically shaped with a maximum of ~1.1m, centered at the epicenter of the largest aftershock. Main slip generally occurs south of the inferred rupture area of the mainshock in a slightly lower depth range of 30-35 km. North of the inferred rupture area of the mainshock, the aftershock slip decreases to less than 0.2 m and only ocurrs at depth below 30 km. Slip north of 19°S and south of 21° S as well as below 50 km becomes negligible.

Figure 4.11: (next page) *The left panel shows the coseismic slip models of a) Sub-model I, c) Sub-model II and e) Model A on triangular fault patches on the subduction interface. The middle panel displays the modelled (red) and observed (blue) horizontal cGPS displacements with 1-sigma uncertainties in a stable South America reference frame for b) Sub-model I and d) Sub-model II. Additionally, the subsampled InSAR cells (Quads) are plotted as grid in b) and d). The right panel shows the subsampled unwrapped and ramp-corrected InSAR data for Sub-model I (f)) and Sub-model II (h)) and the modelled*

unwrapped InSAR data from the slip models for Sub-model I (g)) and Sub-model II (i). Other features represent the coastline (solid black line), the fault trench (solid black line with triangles), political boundaries (dashed lines) and the inferred coseismic slip model and mainshock and aftershock location from Duputel et al., 2015.

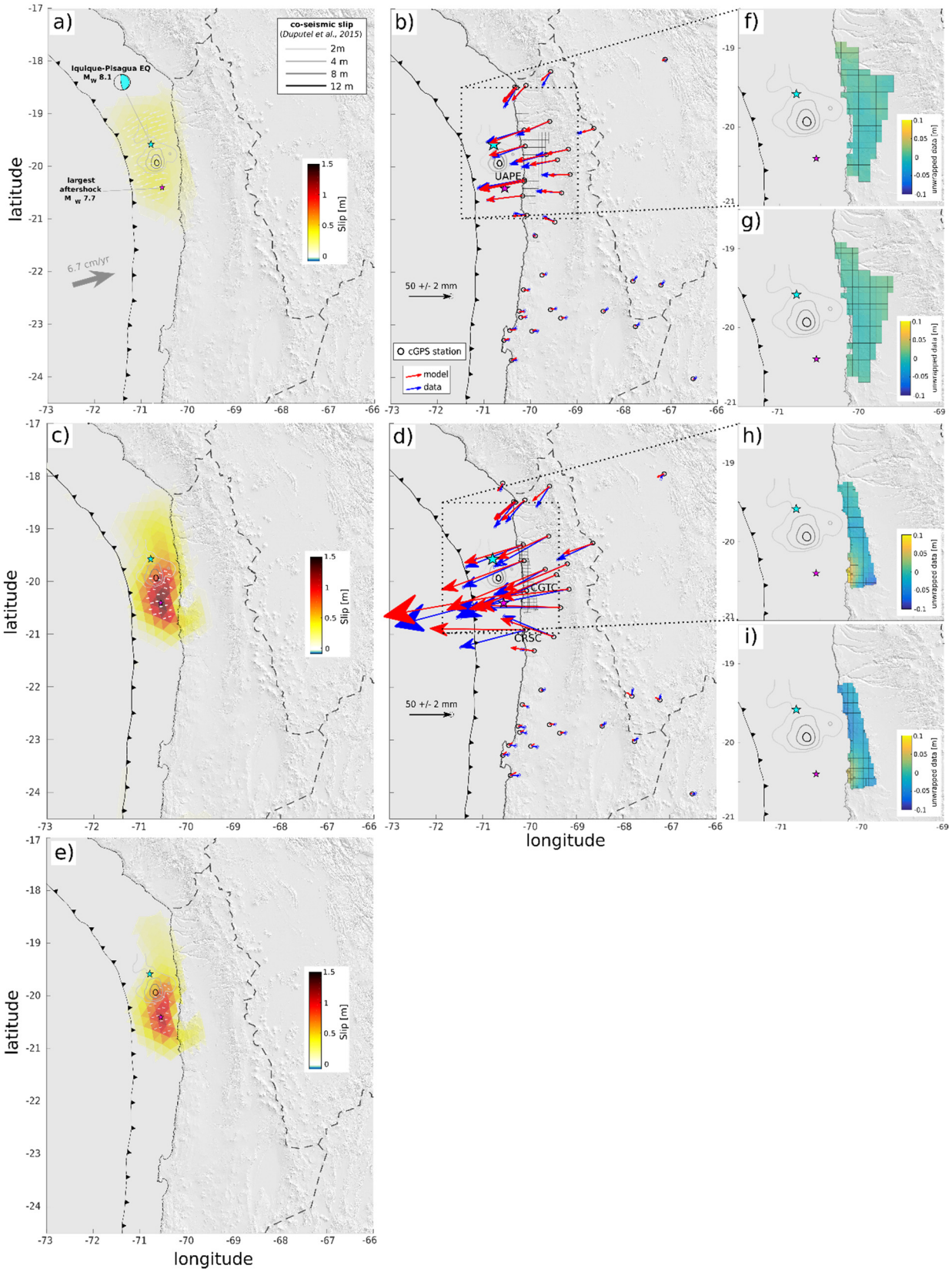

Sub-model III covers more than two years of interseismic ground displacement and the purely coseismic motion of the mainshock without the largest aftershock. The weighting ratio between InSAR and cGPS measurements is $w = w_{InSAR}/w_{cGPS}$ is 1 (**Figure C.6 a**). The slip model shows backslip interface motion south of the inferred mainshock area with maximum rates of 0.2 m at 21° S latitude reflecting more than two years of interseismic motion. The main slip area has an elliptical shape, elongated north-southwards from 19.2-20.5° S latitude. Peak slip of 4.4 m ocurrs S-E of the mainshock epicenter at depth of 35 km (**Figure 4.12 a**). The GPS data shows trenchward motion of up to 56.9 cm (ATJN) north of 21° S latitude, whereas towards the south the sense of motion for all stations corresponds to interseismically landward motion (**Figure 4.12 b**). In general, my model fits the cGPS well with a rms-misfit of 6.5 mm in horizontal and 9.7 mm in vertical direction (**Figure C.6 b**), except for the magnitude of coastal stations with an extremely high motion vector close to the mainshock epicenter. A possible explanation for the cGPS misfit may be the presence of local coseismic effects as surface crack openings (*Loveless et al., 2016*) or lithology-driven velocity effects. The InSAR footprint only covers the trenchward motion north of 21° S and shows ground motion towards the LOS of ~10 cm (**Figure 4.12 f**). The slip model represents well the LOS-motions with a rms-misfit of 12.9 mm (**Figure 4.12 g**). Original InSAR data, linear ramp reduction and InSAR model residuals can be found in the auxiliary material (**Figure C.6 c-e**).

The (back)slip Sub-model IV (**Figure 4.12 c**) represents the cumulative interseismic backslip rates for the time covered by the ascending TSX interfeogram (Sub-model III) until right before the mainshock on April 1, 2014. Those rates and their influence to interface coupling are extensively discussed in section 3.3.2. The interseismic stage is best represented by a heterogeneously coupled interface (**Figure 4.12 c**) with GPS vectors collinear to the subduction convergence vector of the Nazca Plate (**Figure 4.12 d**). The horizontal model fit is exceptionally well with a rms-misfit of 1.8 mm and the higher vertical rms-misfit of 2.7 mm represents well the less sensitive vertical domain for GPS measurements (**Figure C.7**)**.**

The coseismic slip Model B (**Figure 4.12 e**) is the result of the subtraction of Sub-model IV from III. The slip pattern is centered SE of the mainshock epicenter with a maximum of ~4.6 m at 30-35 km depth. Peak slip does not extend southwards to the aftershock epicenter and becomes negligible south of 20.5° S latitude and below a depth of 45 km.

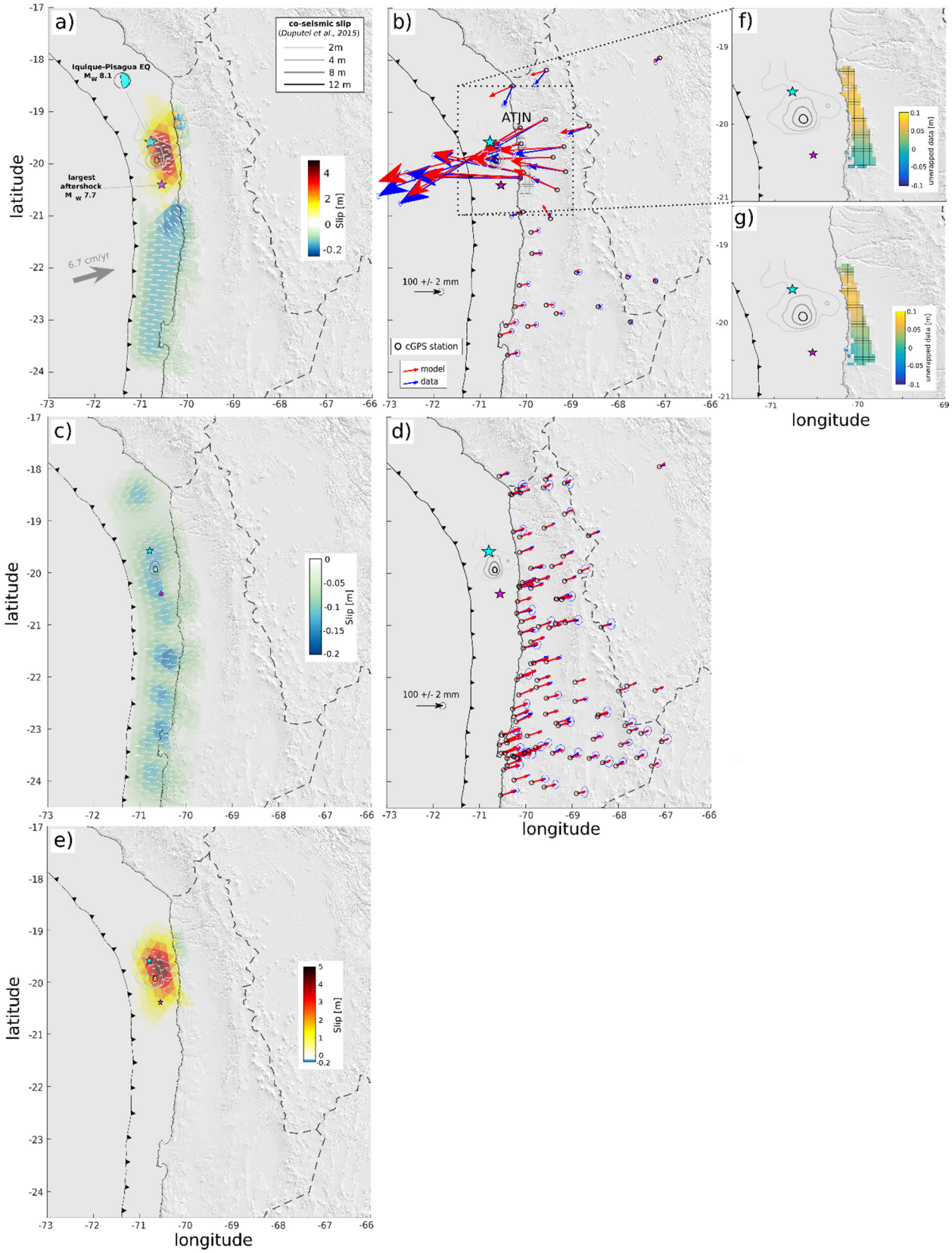

Figure 4.12: The left panel shows the coseismic slip models of a) Sub-model III, c) Sub-model IV and e) Model B on triangular fault patches on the subduction interface. The middle panel displays the modelled (red) and observed (blue) horizontal cGPS displacements with 1-sigma uncertainties in a stable South America reference frame for b) Sub-model III and d) Sub-model IV. Additionally, the subsampled InSAR cells are plot-

ted as grid in b). The right panel shows the subsampled unwrapped and ramp-corrected InSAR data for Sub-model III (f)) and the modelled unwrapped InSAR data from the slip models for Sub-model III (g)).

Sub-model V incorporates InSAR and cGPS data of more than two and a half years of interseismic ground displacement and additionally includes the purely coseismic motion and the largest aftershock. The weighting ratio $w = w_{InSAR}/w_{cGPS}$ is 1 (**Figure C.8 a**). The slip model reveals interseismic backslip motion with a maximum of 0.2 m, south of 21° S and north of 19° S latitude. The spatial extent of the maximum coseismic slip zone coincides well with the inferred rupture area modelled by *Duputel et al.* (*2015*). Maximum slip is ~4.3 m located SW of the mainshock epicenter at ~25 km depth (**Figure 4.13 a**). The coseismic slip decreases to ~1.5 m at the epicenter of the largest aftershock. The transition from coseismic slip to interseismic backslip is characterized by a very sharp gradient at 21° S latitude. GPS stations between 19-20.5° S show high rates of trenchward ground motion of up to 58.7 cm (ATJN). Stations south of 21° S are dominated by interseismic ground displacement collinear to the motion vector of the Nazca Plate (**Figure 4.13 b**). The horizontal cGPS model fit is very good with a rms-misfit of 6.9 mm. The vertical cGPS model fit is slightly underrepresented at the coseismically affected latitudinal range of 19-20.5° S, but generally fits well with a rms-misfit of 12.8 mm (**Figure C.8 b**). The descending RS2 InSAR data reveal very high ground motion rates in a cyclindrically shaped deformation pattern with a maximum of up to 60 cm away from the LOS of the satellite, centered at the coast at 20.5° S latitude (**Figure 4.13 f**). The slip model represents very well the magnitude of the ground motion and has an overall rms-misfit of 23 mm (**Figure 4.13 g**). The center of deformation in the model is slightly shifted northwards. This may be related to the inhomogeneous distribution of InSAR and GPS stations and the lack of data south of 20.5° S. Original InSAR data, linear ramp reductions and InSAR model residuals can be found in the auxiliary material (**Figure C.8 c-e**).

Slip Models A (**Figure 4.13 c**) and IV (**Figure 4.13 d**) were shown and discussed before and are subtracted from Sub-model V to compensate interface motion related to the largest aftershock (Model A) respectively interseismic deformation (Sub-model IV). The resulting model represents the coseismic Model C (**Figure 4.13 e**). The coseismic slip is centered SW of the mainshock epicenter with a maximum of ~4.3 m at 25 km depth. Interface slip extends from 19-20.5° S at a depth range from 0-50 km. The maximum slip zone is slighly shallower than modelled by *Duputel et al.* (*2015*) but coincides well in overall extent and shape.

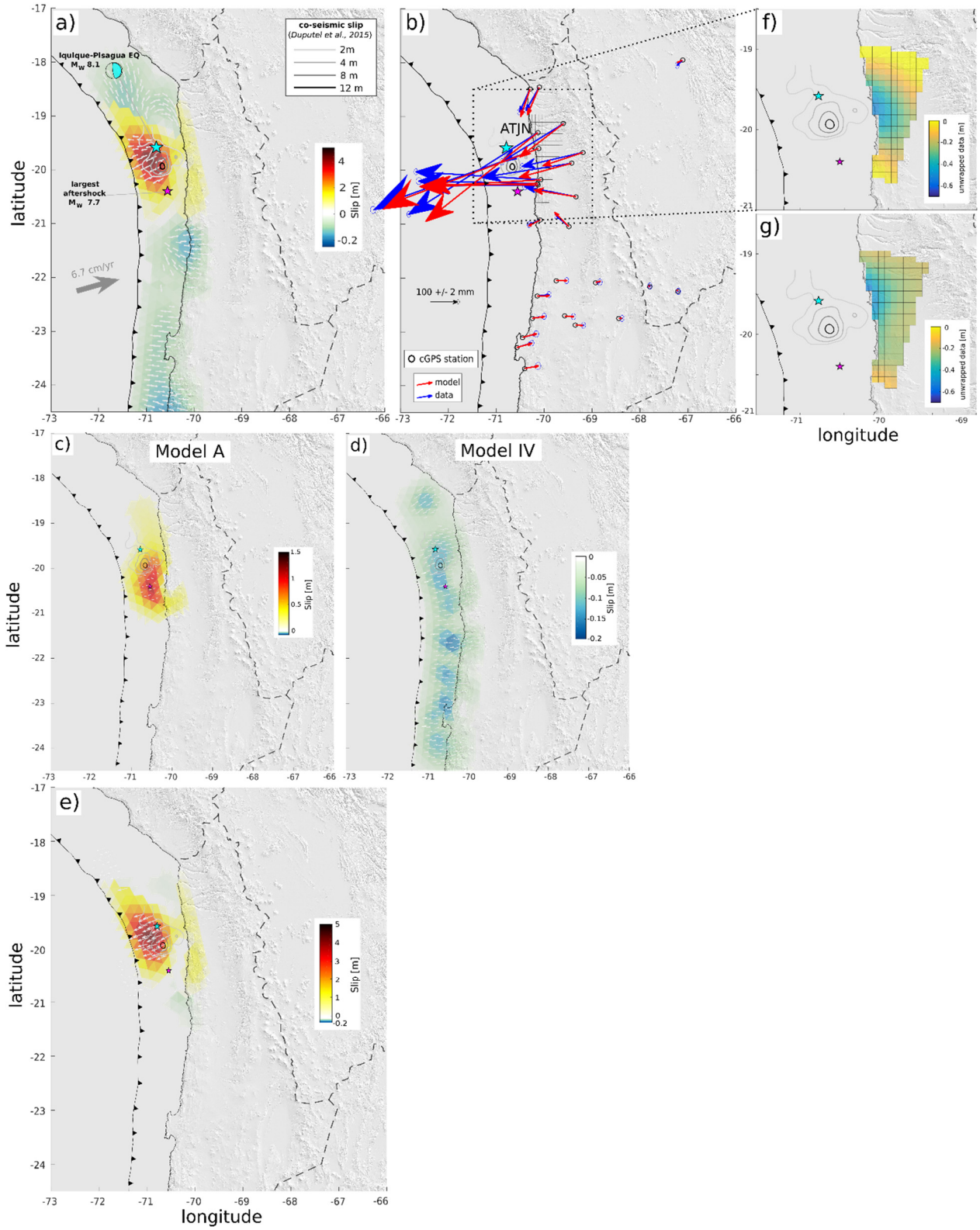

Figure 4.13: The left panel shows the coseismic slip models of a) Sub-model V, c) Model A, d) Sub-model IV and e) Model C on triangular subduction interface fault patches. The middle panel displays the modelled (red) and observed (blue) hor. cGPS displacements with 1-sigma uncertainties in SOAM reference frame for b) Sub-model V. Additionally, the subsampled InSAR cells are plotted as grid in b). The right panel shows the subsampled unwrapped and ramp-corrected InSAR data for Sub-model V (f)) and the modelled unwrapped InSAR data from slip models for Sub-model V (g)).

Sub-model VI covers the interface slip motion related to the Iquique-Pisagua mainshock and the largest aftershock two days later and about two weeks of postseismic deformation measured by InSAR and cGPS data. The weighting ratio $w = w_{InSAR}/w_{cGPS}$ is 1.5 (**Figure 4.6***)*. The model reveals a circular-shaped interface slip pattern centered at the epicenter of the mainshock at 19.6° S latitude with a peak slip of ~5.0 m (**Figure 4.14 a**). The spatial extent of maximum coseismic slip is in very good coincidence with the inferred rupture area modelled by *Duputel et al.* (*2015*). GPS stations in the coastal near-field of deformation between 19-20.5° S show very high displacements of trenchward ground motion of up to 91.1 cm (PSGA). Ground motion for stations south of the inferred transition zone at 21° S are negligible (**Figure 4.14 b**). The cGPS model fit has a rms-misfit of 4.3 mm for horizontal and 8.5 mm for vertical motion (**Figure C.9 a**). The ascending RS2 InSAR data show a complex deformation pattern with a maximum motion of 0.1 m towards LOS at the coast and motion of 0.1 m in opposite direction to the north and south of the footprint. This diverse deformation pattern is mainly due to the complex relation between acquisition geometry of the SAR satellite and the sense of deformation in satellite range direction (**Figure 4.14 f**). However, the slip model generally reproduces the InSAR data with an overall rms-misfit of 15 mm, but slightly underrepresents the motion away from the LOS (**Figure 4.14 g**). Original InSAR data and linear ramp reduction (**Figure 4.5**). InSAR model residuals can be found in the auxiliary material (**Figure C.9 b**). Slip Model A (**Figure 4.14 c**) and Model Period I (**Figure 4.14 d**, see also section 3.4.1) are subtracted from Sub-model VI to compensate interface motion related to the largest aftershock (Model A) respectively postseismic deformation of the first two weeks after the main shock (Model Period I). The resulting model represents the third independent coseismic Model D (**Figure 4.14 e**).

In Model D, the coseismic slip is centered at the location of the mainshock epicenter with a maximum of ~4.9 m at 30 km depth. Interface slip extends from 19.2-20.4° S at a depth range from 5-45 km and the transition zones to zero interface slip are relatively sharp. The spatial extent of the coseismic slip zone coincides remarkably well with the inferred rupture zone modelled by *Duputel et al.* (*2015*).

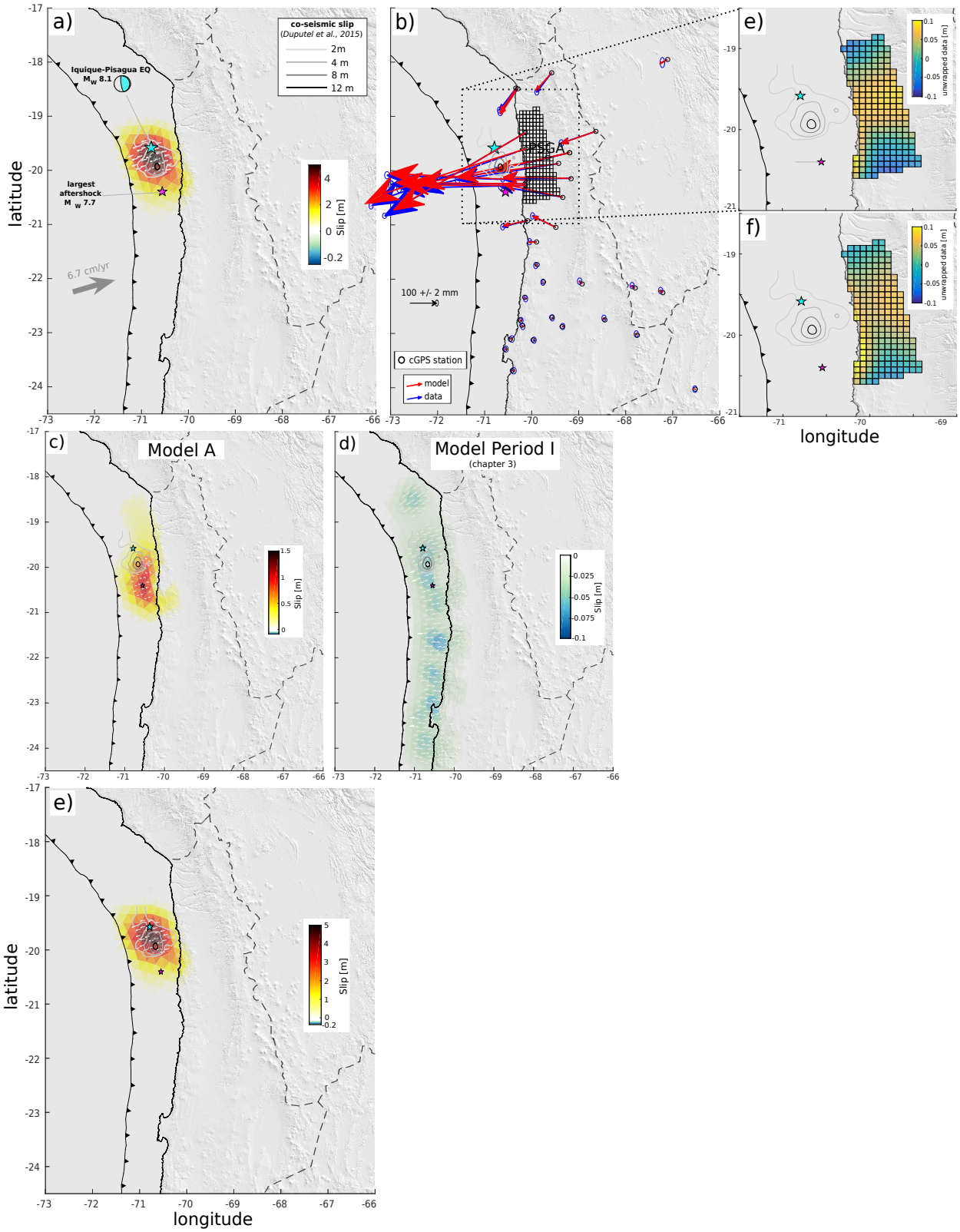

Figure 4.14: The left panel shows the coseismic slip models of a) Sub-model VI, c) Model A, d) Model Period I (see section 3.4.1) and e) Model D on triangular fault patches on the subduction interface. The middle panel displays the modelled (red) and observed (blue) hor. cGPS displacements with 1-sigma uncertainties in SOAM reference frame for b) Sub-model VI. Additionally, the subsampled InSAR cells are plotted as grid in b). The right panel shows the subsampled unwrapped and ramp-corrected InSAR data for Sub-model VI (f)) and the modelled unwrapped InSAR data from the slip models for Sub-model VI (g)).

4.4 Discussion

4.4.1 Refined mainshock and aftershock coseismic slip model

The InSAR footprints may be spatially too small to cover the full range of ground motion for the long wavelength tectonic signal induced by megathrust earthquakes. For that reason, InSAR measurements at subduction zones should not be applied as unique geodetic input for slip inversions. Moreover, InSAR data are massively influenced by local weather conditions as e.g. temporally variable water availability. Those local effects often correlate with topography and cannot be corrected for without implementing additional and spatially dense weather information at the time of the two SAR-acquisitions. However, the InSAR footprints provide a spatially dense and continuous deformation map in the near-field of the tectonic deformation at the Chilean coast and highly complement the few cGPS point measurements. The resolution of the interface slip models is improved in the rupture area taking into account InSAR data in addition to cGPS measurements (compare **Figure B.14** and **Figure C.4 a**). In general, InSAR data also improve the vertical data fit in the slip inversions due to the SAR-acquisition geometry.
All three Models B, C and D represent purely coseismic interface slip of the Iquique-Pisagua mainshock on 1st of April 2014. The three models are generally very similar regarding interface slip magnitude ranging between ~4.3 and ~4.9 m and north-south extent of the rupture zone (~19.5-20.5° S) but also incorporate distinct features as especially peak slip depth range. Largest differences in peak slip depth occur between Model C (~25 km) and Model B (~35 km). Model D has the smallest N-S extent, thus the most compact (circular) spatial rupture zone compared to all three coseismic models. Model C has the northernmost extent of the inferred rupture zone. These differences may be explained by the complex model set-up including various sub-model substitutions. Different data sources and corresponding model parameterization of Models B-D result in different spatial resolutions. However, these models have similar slip characteristics and show mainshock coseismic slips that overlap the epicentre location of the largest aftershock towards the south. The final coseismic mainshock model (**Figure 4.15**) thus represents the joint average interface slip of equally weighted Models B-D.

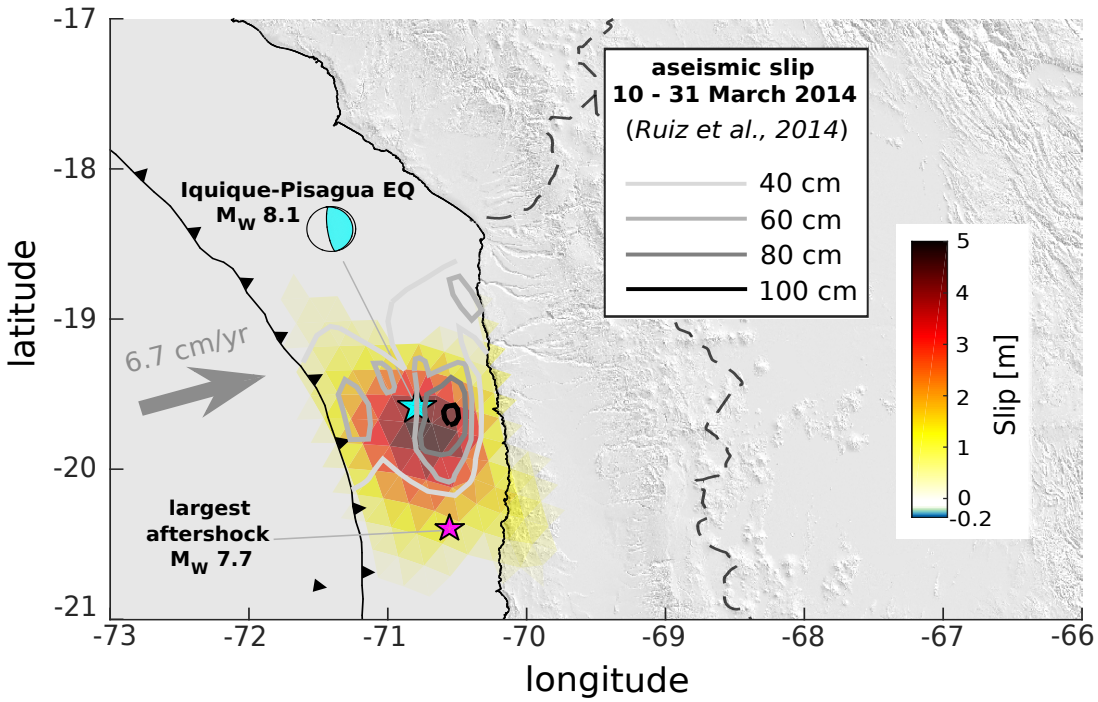

Figure 4.15: Joint coseismic slip model (as average of Model B, C and D). The isolines show cumulative aseismic slip in the period from 10th to 31st of March 2014 (Ruiz et al., 2014).

The final coseismic mainshock model peak slip is 4.4 m (**Figure 4.15**). The fact that the mainshock rupture zone spatially overlaps the largest aftershock hypocenter may indicate seismic triggering effects. This means that the seismic energy release pattern of the Iquique-Pisagua mainshock may have directly led to the rupturing of the plate interface further south, two days later.

Model A represents the effects of the largest aftershock separated from the Iquique-Pisagua mainshock deformation. The ascending TSX aftershock InSAR model (Submodel II) displays the near-field deformation related to the large aftershock in unprecedented detail as the master image was acquired right before the largest aftershock ruptured the plate interface. Although three InSAR scenes were merged to enlarge the spatial coverage, the long-wavelength deformation signal could not be fully covered by the InSAR footprint, especially towards the inferred seismotectonic barrier at 21° S latitude (*Hoffmann et al., 2018*). Nevertheless, due to the combination of InSAR data with the dense network of cGPS stations, my aftershock slip model (Model A, **Figure 4.11 e**) gives a reliable evidence to interface slip with a maximum slip of 1.1 m. The measured ground motion, especially for coastal stations in closest distance to the epicenter of the largest aftershock is very high in relation to the surface motion measured for the mainshock. Thus, the surface motion is higher than expected from the magnitudinal range of the aftershock rupture, which is also shown by the slip potency. The slip poten-

cy of the subduction interface fault model is the integral of the cumulative slip over the patch area, calculated with 1.1543^{10} m^3 for the coseismic aftershock model. With a typical shear modulus of 50 GPa, the moment magnitude M_0 is 5.7715^{20} Nm. The common seismic magnitude M_w can be calculated with:

$$M_W = (2/3)*(\log (M_0/10^{-7}) - 16.1) \text{ (Kanamori, 1977)}. \quad (4.1)$$

The calculated magnitude is M_w 7.9, thus significantly higher than the actual measured one (M_w 7.7). This potentially reflects a coseismically induced reactivation of inherent crustal faults and opening of surface cracks (*Loveless et al., 2016*). The fault reactivation may have released accumulated crustal stress and measured surface motion is larger than expected from a M_w 7.7 event. High surface deformation could thus have a significant impact on permanent deformation in Northern Chile triggered by large seismic events. An alternative explanation for the higher slip is the potential contamination of coseismic geodetic data with postseismic deformation.

All in all, the quality of my final slip sub-models is very good based on the analysis on absolute model residuals that range between 1.0 – 6.9 mm for horizonatl GPS, 1.4 – 12.8 mm for vertical GPS and 3.2 – 23.0 mm for InSAR measurements (see chapter 4.3.2 and **Figures C.4 – C.8**). However, InSAR model residuals of Sub-models that exhibit large co-seismic deformation signal, especially Sub-model II (**Figure C.5 e**) and Sub-model V (**Figure C.8 e**), have significantly high values and moreover show similar geometry patterns as the original data. This means, that the model approach only partly relates the surface motion measured by InSAR to motion on the plate interface. A possible explanation for the relatively high model residuals may be the inhomogenoeus distribution of surface data in the deformation near-field. GPS data is well distributed at the coastal and inland region between 18 – 23° S latitude, whereas the spatially highly resolved InSAR data is concentrated only at the coast between 19 – 20.5° S. The size of the interface fault patches in the model may be to large to translate these high-gradient surface motion changes. Moreover, single orbit InSAR data is given in LOS direction of the satellite and cannot be separated into purely horizontal and vertical surface motion. The surface LOS information may be more difficult to translate into dip slip and strike slip motion of single fault patches of the interface. Furthermore, my error approach may be unprecise for interferograms that are entirely affected by surface deformation. The defined non-deformation area in my error approach is contaminated by the deformation signal, which influences the error assessment as variance of subsampled InSAR cells. This may lead to inaccuracies in the data weighting and potentially has an influence on the model.

4.4.2 Analysis of coseismic slip distribution

A range of diverse coseismic slip models of the Iquique-Pisagua mainshock have been published in scientific literature (**Figure 4.16**). All models are derived from distinct data sets and differ in extent, size and location from each other. In general, most of those slip models are characterized by a compact slip zone with the highest slip southeast of the mainshock. Thus, the range of slip models can be categorized into lower and higher peak slip models. The coseismic slip pattern suggested by my final coseismic slip model (**Figure 4.15**) corresponds in size to the slip models at the lower range of magnitude (e.g. *Schurr et al., 2014*, **Figure 4.16 b**; *Yagi et al., 2014*, **Figure 4.16 c**). In those models, peak slip does not exceed 5 m and the general slip geometry is characterized by a bullseye shape. *Yagi et al.* (*2014*) documented highest slip of 4.6 m as bullseye pattern at around 20.2° S latitude, centered between the mainshock and the largest aftershock hypocenters. A similar extent and size can be found by *Schurr et al.* (*2014*), in which a peak slip of 4.4 m at 19.8° S latitude, southeast of the mainshock is suggested. *Kato et al.* (*2014*, **Figure 4.16 i**) present a comparable slip of ~5m, but a different location, centered at the Chilean coast. A similar location can only be found in the study of *Lay et al.* (*2014*, **Figure 4.16 d**), that propose a peak slip of 6.7 m and can be categorized in the second group of higher peak slip models. This second category models also mostly correspond in location and extent to my coseismic slip model. Those slip models suggest highest slip to occur southeast or east of the mainshock characterized by a circular and compact shape with varying peak slip: ~6 m (*Ruiz et al., 2014*, **Figure 4.16 e**), 6.5 m (*Liu et al., 2015*, **Figure 4.16 f**), ~7 m (*Gusman et al., 2015*, **Figure 4.16 g**), ~7 m (*Loveless et al., 2016*, **Figure 4.16 h**), 8 m (*Hayes et al., 2014*, **Figure 4.16 j**). The highest slip of more than 10 m, centered at 20° S latitude is documented in the model of *Duputel et al.* (*2015*, **Figure 4.16 a**), that use a pervasive data set. Coseismic slip stopped at an area of relatively low coupling (**Figure 3.4** and *Métois et al., 2013*; *Li et al, 2015*), that was already identified as seismotectonic barrier in chapter 3. The main difference between my model and the slip models with higher peak slip (e.g. *Hayes et al., 2014*; *Duputel et al., 2015*) is the compactness of slip geometry. The spatial extent of the coseismic slip region is larger in my model compared to the second category models.

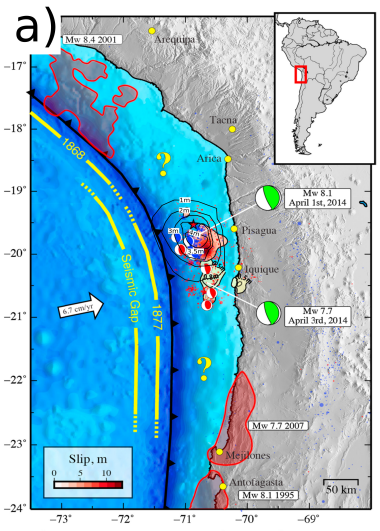

Figure 1 (Duputel et al., 2015)

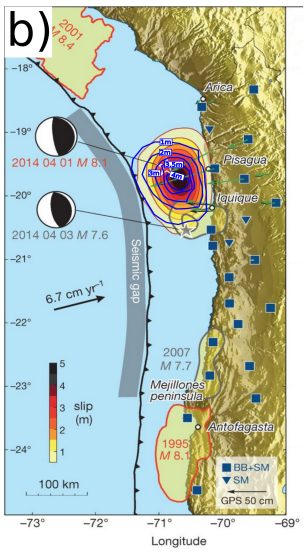

Figure 1 (Schurr et al., 2014)

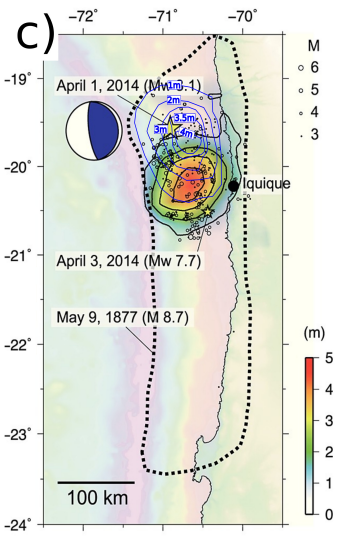

Figure 1a (Yagi et al., 2014)

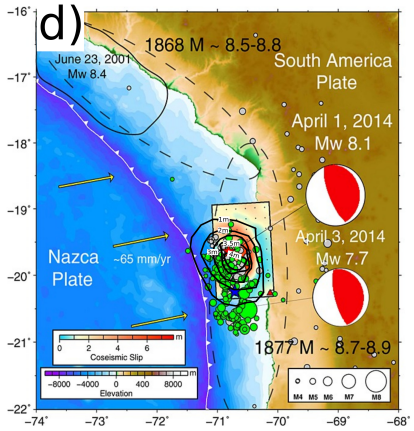

Figure 1 (Lay et al., 2014)

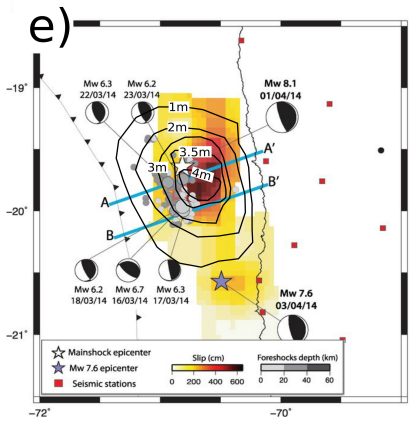

Figure 2a (Ruiz et al., 2014)

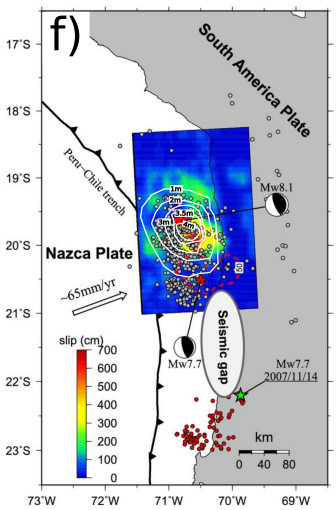

Figure 3a (Liu et al., 2015)

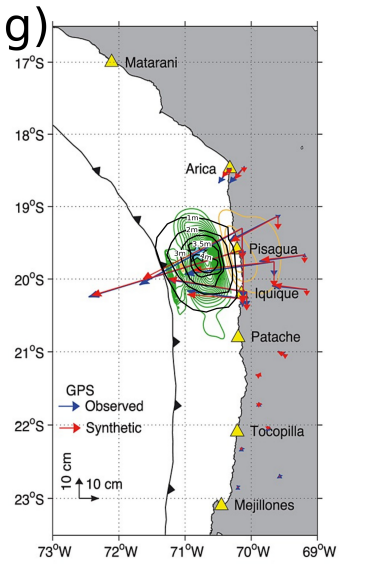

Figure 2a (Gusman et al., 2015)

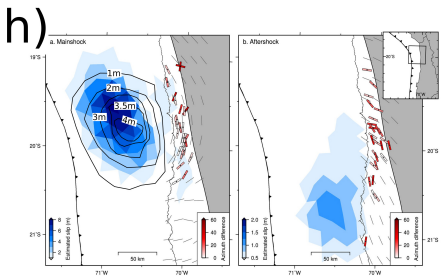

Figure 1a,b (Loveless et al., 2016)

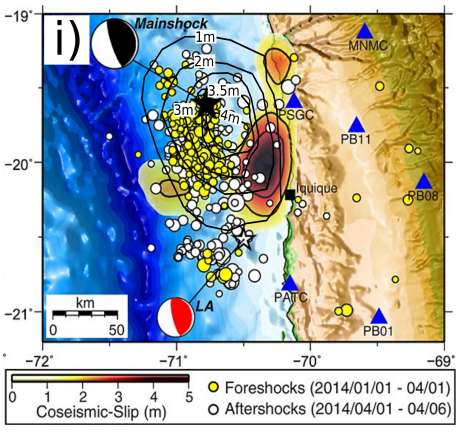

Figure 1b (Kato et al., 2014)

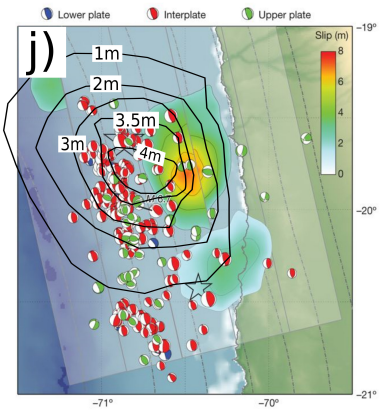

Figure 2 (Hayes et al., 2014)

*Figure 4.16 (*previous page*): Coseismic Iquique-Pisagua slip models from literature: a) Duputel et al., 2015; b) Schurr et al., 2014; c) Yagi et al., 2014; d) Lay et al., 2014; e) Ruiz et al., 2014; f) Liu et al., 2015; g) Gusman et al., 2015; h) Loveless et al., 2016; i) Kato et al., 2014 ; and j) Hayes et al., 2014. All published slip-models a) - j) were copied and modified from original manuscripts. The mainshock coseismic isolines (1 m, 2 m, 3 m, 3.5 m and 4 m) calculated in this study are plotted on top of each image.*

My models indicate that the stress drop may not have been complete and the interseismic strain accumulated since the last megathrust event in 1877 may not be released totally in the rupture area of the Iquique-Pisagua earthquake 2014 in contrast to higher slip models. In my final coseismic model, slip is concentrated at shallower plate interface depths further away from the coast. This may be due to incorporating spatially highly resolved near-field InSAR data that seem not to favour down-dip slip, similar to the model of *Hayes et al.* (*2014*) that also use InSAR data. Another reason, why my final model exhibits less slip than others may be given by considering the data base. I only use geodetic data (GPS and InSAR), that are measured at minimum distance of ~100 km away from the trench, which leads to a lack of resolution at shallower interface parts in my models (**Figure C.4 a**). Most of the second category models have another data basis as tsunami records (e.g. *Duputel et al., 2015*; *An et al., 2014*) or teleseismic data (e.g. *Ruiz et al., 2014*; *Yagi et al., 2014*), that allow spatially broader investigations on subduction interface slip with higher resolution close to the trench. Thus, limitations of resolution may cause underrepresentation of coseismic slip. On the other hand, continuous GPS observations on a daily basis allow a high temporal resolution and the combination with InSAR data improves spatial resolution at a certain interface depth range of ~30-40 km, where most of coseismic slip is assumed to occur (e.g. *Schurr et al.,2014; Duputel et al., 2015*). An important modelling parameter, that highly influences maximum slip and geometry of the model is the smoothing factor. In general, the higher the smoothing, the more weight is given to a rounded shape of the slip area at the cost of maximum peak slip in the modelling. For that reason, a comparison between different slip models is very difficult, especially when using different input data. However, my coseismic slip model uniquely implements TerraSAR-X InSAR data, that are temporally very well resolved (with an acquisition between the mainshock and largest aftershock). My coseismic slip model represents an important contribution to already existing slip models due to the extraordinarily good spatial resolution in a depth range of the inferred hypocenter (~30-40 km) by means of joint GPS and InSAR inversion.

The model of the largest aftershock on 3rd April 2014 presented in this study is in good agreement to already existing slip models regarding extent and magnitude (e.g. *Hayes et*

al., 2014; Schurr et al., 2014; Duputel et al., 2015). Most of these slip models are characterized by an elliptical shape, elongated in E-W direction and extending down-dip underneath the Chilean coast up to ~50 km interface depth. The range of peak slip magnitudes involves 0.8 m (*Duputel et al., 2015*), 1.2 m (*Schurr et al., 2014*), ~2 m (*Ruiz et al., 2014*) up to a maximum of more than 2.5 m (*Hayes et al., 2014*). In my model, highest slip reaches 1.1 m. Similar to all other models, the location of highest slip in my model is about 40-50 km south of peak coseismic slip, close to the hypocentre of the largest aftershock. Given the joint incorporation of InSAR and GPS data separately for the mainshock and the largest aftershock, my presented model extends the spatio-temporal resolution of other models. As previously discussed, the aftershock rupture zone extends into the Iquique low coupling zone at 21° S. A possible explanation for this location is, that this area was seismically loaded by the mainshock and also by the first 27 h of aftershocks (e.g. *Hayes et al., 2014*). The low number of foreshocks in the area of the largest aftershock as well as the stress change to positive Coulomb Failure Stress values right after the Iquique-Pisagua rupture (**Figure 3.8 b**) are a clear indication that the M_w 7.7 aftershock occurred as response to mainshock static stress changes.

My model results demonstrate, that the Iquique-Pisagua event and its largest aftershock did not rupture the shallow parts of the interface up to the trench (**Figure 4.15**), similar to the 1995 Antofagasta and the 2007 Tocopilla earthquakes in Northern Chile (*Pritchard et al., 2006; Motagh et al., 2010*). The interseismic coupling degree at shallow depth <30 km varies much between all existing backslip/coupling models (**Figure 3.4** and e.g. *Chlieh et al., 2011; Metois et al., 2013; Li et al., 2015*) mainly due to the lack of resolution close to the trench when using only onshore geodetic data. For that reason, it remains unclear whether or not the shallow part of the interface is seismogenic. However, a failure of the entire interface including also shallow parts in one single event, as is assumed to have occurred for the 1877-megathrust event (e.g. *Kausel 1986*) is theoretically possible for the Northern Chile- Southern Peru seismic gap. Mechanisms causing such shallow slip could involve fault weakening properties as observed during the 2011 Tohoku-oki earthquake (e.g. *Noda & Lapusta, 2013*). The absence of shallow slip for the Iquique-Pisagua event and its largest aftershock shows that dynamic weakening processes may play a minor role up-dip of the rupture.

4.4.3 Tectonic pre-conditions control coseismic slip distribution of the Iquique-Pisagua earthquake

The rupture propagation process of the Iquique-Pisagua event is described as occurring in two distinct stages: (1) the rupture initially propagated down-dip through a cascading

failure of minor asperities, while larger asperities remained unbroken due to the surprisingly low level of stress release (*Schurr et al., 2014*) and (2) subsequently during the propagation process, dynamic stress was transferred to shallower depths triggering unbroken asperities and moreover leading to re-rupturing of asperities along a circular rim (*Meng et al., 2015*). This re-rupturing is assumed to be controlled by initial stress heterogeneities and is thus comparable with mechanisms observed for the 2011 Tohoku-oki event (e.g. *Lee et al., 2011; Kato et al., 2012*).

An open question is, what kind of conditions could have caused the abnormally low level of stress release and high fracture energy in the initial rupture phase of the Iquique-Pisagua mainshock? The fact that only the central part of the inferred 1877-Iquique rupture area broke during the recent Iquique-Pisagua event in 2014 may be a direct consequence of the low level of stress release. Different scenarios describe possible reasons for the spatially rather narrow coseismic slip distribution. One theory is, that the deficiency of moment rate and the low level of stress in the hypocenter region can be explained by the recurrence of slow slip events, preceding the mainshock (e.g. *Meng et al., 2015; Kato et al. 2016; Ruiz et al., 2014*). The comparison between the area of slow slip inferred by scientific literature (e.g. *Kato et al., 2016*, *Ruiz et al., 2014*) and the coseismic rupture area yield by the slip inversion of this study reveals a high degree of spatial coincidence (**Figure 4.15**). The slow slip event may have occurred in the nucleation zone of the Iquique-Pisagua megathrust which indicates a potential rupture triggering through aseismic creeping. A slow slip event would have released portions of the accumulated slip deficit aseismically, thus reducing the overall stress level in the hypocentre region. The indication of slow slip would explain the similarity of rupture mechanisms between the Iquique-Pisagua and the Tohoku-oki event that is assumed to also have been preceded by a slow slip event (e.g. *Kato et al., 2012*). Another hypothesis of the low stress release during the Iquique-Pisagua mainshock emphasizes the role of the M_w 6.7 foreshock on 16 March 2014. The foreshock is assumed to represent an upper plate reverse fault reactivation that could have triggered the precursor sequence finally leading to the Iquique-Pisagua mainshock (*Gonzáles et al., 2015*). In this scenario, the low level of coseismic stress release during the Iquique-Pisagua would be a direct consequence of the upper plate earthquake triggering of static unclamping of the megathrust and thus partial unlocking of the plate interface (*Gonzáles et al., 2015*). To further investigate the role of the M_w 6.7 foreshock on 16 March 2014, I performed a slip model based on horizontal static displacements of 39 continuos GPS stations from the two weeks between fore- and mainshock (17^{th} – 31^{th} March). The model approach is completely based on the elastic modelling described in detail in chapter 3.2.3. The rake is not constrained and the inversion is regularized by a Laplacian operator that is deter-

mined by the trade-off between misfit and slip roughness. The GPS vectors south of 21° S are predominantly collinear to the plate convergence vector, whereas coastal stations close to the later Iquique-Pisagua mainshock epicenter show trenchward motion (**Figure 4.17**). The overall model misfit is 0.1 mm.

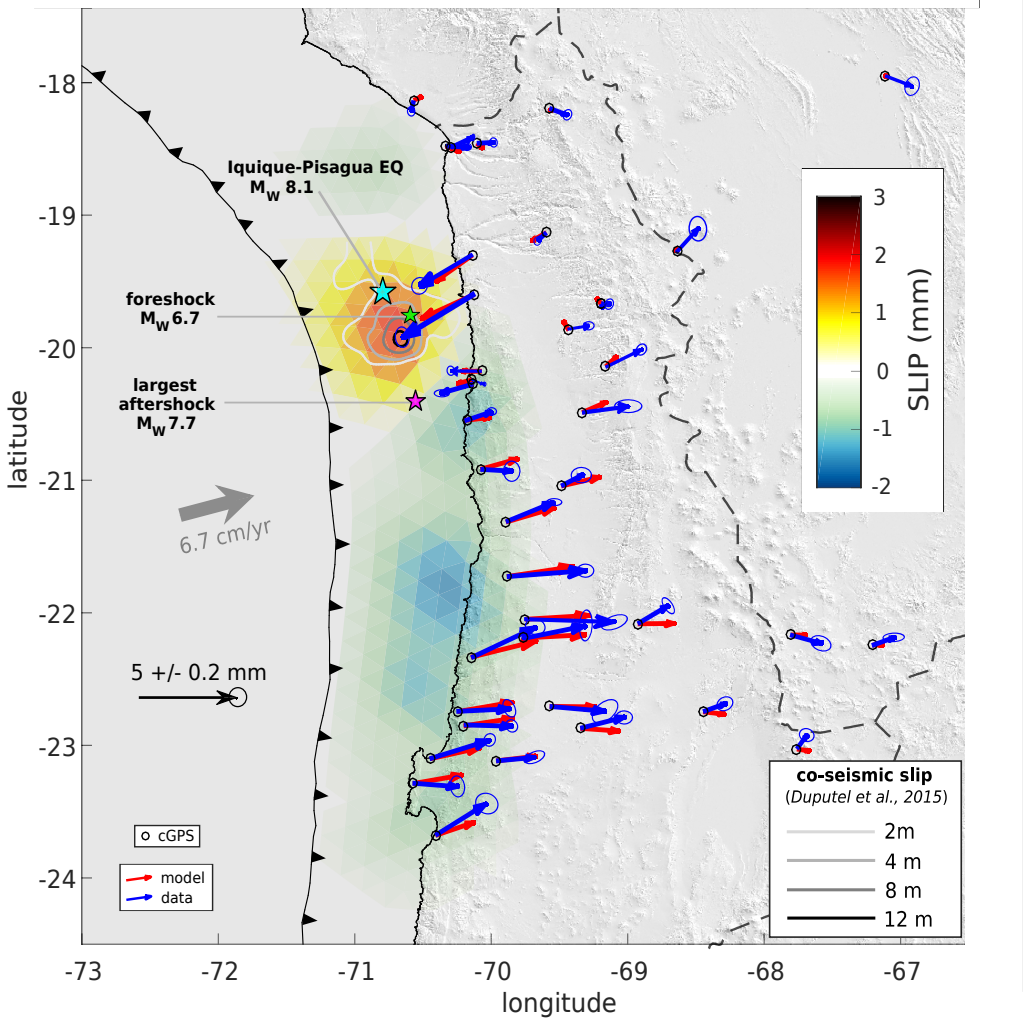

Figure 4.17: Slip model of the 15 days (17th – 31th March 2014) between the M_w 6.7 foreshock and the Iquique-Pisagua mainshock. The colored stars highlight the epicentres of seismic events: foreshock (green), mainshock (turquoise) and magenta (largest aftershock). The observed horizontal continuous GPS measurements with respective errors (blue) are plotted together with modelled data (red).

The striking conclusion from the slip model between fore- and mainshock (**Figure 4.17**) is the clear deviation from the interseismic slip model (**Figure 3.4**) that displays the inversion of averaged interseismic rates. Directly after the intraplate foreshock, the hypocenter region of the Iquique-Pisagua earthquake that ruptured two weeks later shows slip between 19-21° S. The slip of ~2 mm in the later mainshock slip region may be a direct consequence of the intraplate foreshock. The limitation of this model approach is that it remains unclear, whether the surface deformation is induced by the plate interface

or by elastic crustal motions as consequence of the intraplate foreshock. If the plate interface was the main driver for the measured GPS surface deformation in the two weeks between fore- and mainshock, the 16th March foreshock can be interpreted as potentially triggering the Iquique-Pisagua megathrust event. Whether or not the displayed slip on the plate interface in my scenario (**Figure 4.17**) can be attributed to aseismic creeping is beyond the content of this inversion approach. But an indication that the displayed scenario (**Figure 4.17**) may reflect a realistic tectonic setting is given by the shape of the transient displacements in the GPS time-series (**Figure B.11**). The onset of these transients is not abrupt (mathematically modelled via Heavyside functions, see chapter 3.2.2, equation 3.2) as would be expected from coseismically induced displacements (compare to **Figure 3.2a**). Based on this tectonic scenario, I evaluate that the 16th March foreshock directly influenced the plate interface, which corresponds to the conclusion of Ruiz et al. (2014) and Meng et al. (2015). A third hypothesis, why the initial stress release of the Iquique-Pisagua earthquake was surprisingly low, involves the presence of fluids. The M_w 6.7 earthquake is assumed to represent an intraplate event not rupturing the subduction plate interface (e.g. *Schurr et al., 2014*; *Gonzáles et al., 2015*). Such failure in the upper crust in a subduction zone setting potentially favours fluid release and migration onto the plate interface, which would directly affect the coseismic slip distribution of the Iquique-Pisagua mainshock two weeks later. A fluid pressure increase at the mainshock hypocenter area could explain the low level of effective normal stress as the locking degree is thought to be locally reduced by the presence of fluids (*Audet and Schwartz, 2013*; *Moreno et al., 2014*).

Apart from the influence of seismic or aseismic precursors, also local interface rheology and topography could have an impact on controlling slip distribution and the low mainshock stress level. The up-dip limit of the mainshock rupture spatially coincides with the borders of the eroded continental wedge, which can be explained by the presence of fluids in the wedge. In contrast to other megathrust events such as the 2010 M_w 8.8 Maule event (e.g. *Moscoso et al. 2011; Cubas et al. 2013*) or the 2005 M_w 8.7 Nias event (e.g. *Hughes et al. 2010*), a large number of aftershocks occurred up-dip of the mainshock and thus closer to the trench at shallower depth (**Figure 3.7 b**). This can be explained by a lack of a large accretionary prism due to the erosive character of this segment of the Chilean margin (e.g. *Contreras Reyes et al., 2012*). Instead of the accretionary prism, the bathymetry with an extensive horst and graben structure is thought to may control aftershock characteristics (*Léon-Ríos et al., 2016*). If this is true, the bathymetry may also has a strong influence on coseismic slip distribution. *Geersen et al.* (*2015*) assume that the rupture propagation of the Iquique-Pisgagua earthquake 2014 may have been controlled by a difference in seafloor roughness between the lowly cou-

pled area at ~20.5-21° S and the moderately coupled central part of the Northern Chile-Southern Peru seismic gap. Thus, the presence of seamounts at ~21° S could potentially create favourable aseismic conditions impeding the rupture to propagate southwards (*Wang and Bilek, 2011*). Moreover, also the lack of coseismic up-dip slip is assumed to be controlled by topographic differences that cause extensive fracturing in the shallow part of the subducting Nazca plate (*Geersen et al., 2015*).

The Iquique-Pisagua mainshock was very likely triggered by a combination of a slow slip event and cascading seismic energy release of precursors triggered by a crustal event two weeks before the megathrust rupture (*Ruiz et al., 2014*; *Gonzáles et al., 2015*). However, the Northern Chile- Southern Peru seismic gap was mature and the calculated slip deficit would theoretically have been sufficient to generate a comparable megathrust event to the 1877-rupture (e.g. *Schurr et al., 2014*). Thus, triggering mechanisms did not lead to a premature rupturing of the seismic gap before the calculated recurrence time. The rupture area of the 2014 Iquique-Pisagua megathrust event is smaller than the inferred rupture zone of the 1877 Iquique event, which indicates a non-characteristic megathrust generation at the Northern Chilean subduction zone.

4.4.4 Temporal and longterm changes in the deformational regime of Northern Chile as a consequence of the Iquique-Pisagua earthquake

An analysis of the focal mechanisms of fore- and aftershocks of the Iquique-Pisagua earthquake 2014 reveals that thrust faulting is the dominant mechanism in both periods, whereas normal faulting is only present after the mainshock (*Cesca et al., 2016*). The normal fault mechanisms are a consequence of the increased extensional stress. Similar observations were also made for the Tohoku-oki megathrust event 2011 (e.g. *Asano et al., 2011; Hasegawa et al., 2012*) and seem to indicate a minor temporal perturbation of the stress field caused by a potential rotation of the principal strain axis (σ_1) of 6°. In Northern Chile, the deformational regime was not changed permanently and pre-megathrust stress conditions were restored after only a few weeks (*Cesca et al., 2016*). Nevertheless, geologic evidence for permanent deformation caused by coseismic stress transfer and the short-term change of the compressional axis can be observed after the Iquique-Pisagua rupture. Subsidence of 20-30 mm related to the mainshock in the near-field coastal deformation area is measured by cGPS data (**Figure C.5 b**, **C.6 b**; **Tables C.7**, **C.8**). This coseismic vertical motion is in contrast to interseismically measured uplift (**Figure C.7**). Vertical motion is hard to interpret for the unwrapped interferograms, because InSAR images give evidence about deformation in the line-of-sight of the satellite. In general, InSAR is more sensitive to vertical motion, but in case of ex-

tremely large coseismic horizontal deformation for subduction zone megathrust events, the LOS motion may be dominated by horizontal movements. However, in ascending mode, the unwrapped interferograms show LOS deformation towards the satellite at coastal regions south of 20° S (**Figure 4.14 e** and **Figure 4.11 h**), which may indicate uplift. These coseismically induced land-level changes are in agreement with other measurements as GPS and intertidal biota analysis for the Northern Chilean margin, where a ~100 km coastal stretch north of 20° S experienced subsidence and the coastal area ~50 km along the southern part of the mainshock was uplifted (*Jarmillo et al., 2017*). The uplift south of the mainshock may be associated with the large aftershock on 3rd April, an event that ruptured deeper and is generally assumed to contribute to the rise of the Central Andean coastline (*Melnick, 2016*). These contrary coseismic vertical motion directions in the near-field deformation area were also observed for other megathrust events such as the 2010 M_w 8.8 Maule event (e.g. *Lin et al., 2013* (*Fig. 2d therein*); *Métois et al., 2013*) and the 2005 M_w 8.7 Nias event (e.g. *Hughes et al., 2010*, *Fig. 4c therein*) and may be related to the distance to the epicentre. Thus, regions closer to the trench are generally uplifted at coseismic stage, whereas areas further away experience subsidence. In the case of the 2014 Iquique-Pisagua earthquake, the southern part of the mainshock deformation area is closer to the trench, which may explain the uplift.
Geologic evidences of co-seismically transferred stresses through the upper continental crust are also inferred from surface crack analysis (*Loveless et al., 2016*; *Scott et al., 2016*). The direction perpendicular to the strike of coseismically opened cracks indicate the axis of maximum static tension. These cracks reflect permanent deformation generated during the megathrust event and thus clearly demonstrate the influence of local crustal tectonic processes on geodetic ground deformation measurements (*Loveless et al., 2016*). That means, a portion of the measured ground deformation may be generated by surface crack opening or other crustal deformational features and cannot be attributed to plate interface motion. Taking into account this hypothesis, the slip in my coseismic models derived by inverted geodetic ground motion observations may be overrepresented.

4.5 Conclusion

The final coseismic mainshock slip model is characterized by an eliptically shaped rupture zone with peak slip of 4.4 m at ~30 km depth located at 19.8° S. The coseismic slip model of the largest aftershock has a peak slip of 1.1 m centered at the aftershock hypocentre at ~32-35 km depth. The geometry and spatial extent of my coseismic slip mod-

els coincides well with already published rupture models, but is generally less compact and also ranges at the lower magnitudinal level (e.g. Duputel et al., 2015; *Hayes et al., 2014*). Mainshock cosesimic slip stopped at the Iquique low coupling zone identified as seismotectonic barrier at ~21° S (*Hoffmann et al., 2018*), potentially induced by bathymetry roughness differences. Slip of the largest aftershock extends further south, which is interpreted as consequence of seismic loading effects. The Iquique-Pisagua mainshock is characterized by a lack of shallow slip, mainly due to a minor influence of dynamic weakening processes up-dip of the rupture.

The generally low magnitude and related low stress level in the mainshock hypocentre region may be a consequence of two processes preceding the Iquique-Pisagua rupture:

(1) a slow slip event that released accumulated slip deficit aseismically (*Kato et al., 2016*; *Ruiz et al., 2014*) and spatially coincides well with my coseismic slip model (**Figure 4.15***)*
(2) seismic triggering and related partial unlocking (respectively pre-seismic slip, **Figure 4.17**) and fluid pressure increase at the subduction plate interface induced by a crustal earthquake two weeks before the mainshock

The Iquique-Pisagua coseismic rupture may have a large influence on permanent crustal deformation changes that are indicated by significant vertical land level change between 20-30 mm coastal subsidence north of the epicentre latitude based on cGPS data. Moreover, calculated slip potency based on the geodetic slip inversion is higher than the actual seismically derived magnitude of the largest aftershock. This may indicate high surface deformation that is potentially induced by local tectonic effects as surface crack openings or crustal fault reactivation reflected by localized cGPS misfits. The Northern Chilean seismotectonic segment may not generate characteristic megathrust events taking into account the larger extent and magnitude of the last megathrust rupture in 1877 (M_w 8.6) compared to the Iquique-Pisagua event 2014.

5 Synthesis

5.1 Conclusion

In the following chapter, I further discuss and summarise the relevant results of my thesis and relate the main findings to the research questions that were posed in the introduction to formulate the scientific goals and objectives of this study:

1. **Do interseismic ground deformation rates give direct insights to coseismic motions, thus location and extent of future megathrust events?**

Interseismic ground deformation rates at the Northern Chilean subduction zone location give direct insight into the coupling of the subduction zone interface. Fully or strongly coupled interface patches are prone to accumulating large slip deficits and finally may rupture as megathrust earthquakes. In the case of the Iquique-Pisagua earthquake 2014, the location of the mainshock coincides with a local peak in coupling at 19.8° S, whereas the rupture extent towards the south was limited by a local low coupling zone at 21° S that is identified as seismotectonic barrier in this study. For that reason, interseismic backlip rates potentially indicate future location and extent of megathrust events as in case of the Iquique-Pisagua earthquake 2014, but are not a direct and reliable marker for future earthquake characteristics.

2. **What does the comparison of the inter- and postseismic ground deformation in neighbouring segments of a subduction zone earthquake tell us about the risk of a future megathrust event?**

Comparing deformation rates before and after a megathrust event in neighbouring seismotectonic segments of a subduction interface rupture have not been studied extensively in scientific literature due to a lack of long time series of geodetic measurements. For the Northern Chilean subduction zone seismic cycle that culminated in the Iquique-Pisagua earthquake 2014, there exists an unprecendened set of various geodetic data in the near- and far-field of tectonic deformation. In this study, I clearly demonstrate that in the second year of postseismic deformation following the Iquique-Pisagua earthquake in the Camarones segment, the interseismic ground motion rates in the southern (neighbouring) Loa segment have been increased by up to 10 mm/yr compared to pre-shock

rates. I interpret this behaviour as an indication for an increased risk of another megathrust event in this southern segment due to an increase in down-dip interface coupling as response to a raise of shear stress. The calculated slip deficit (e.g. *Schurr et al., 2014*) accumulated in the Northern Chile- Southern Peru seismic gap has not been released completely by the Iquique-Pisagua earthquake 2014. For that reason, the risk of a seismic stress release of the remaining slip deficit in the Loa segment remains high.

3. Is there any evidence that megathrust events behave characteristically over multiple seismic cycles?

The theory that the extent and magnitude of a future megathrust event can be directly inferred from historic archive seems to be obselete. During the past decade, many seismic events at subduction zone settings ocurred that were characterized by rupture extents completely different to previously predicted results. The most famous example is the Tohoki-oki earthquake in 2011 at an epicentre area, where only events with magnitudes less than 8 occurred periodically (e.g. *Geller, 2011*). An opposing example is the M_w 7.8 Ecuador earthquake 2016 that occurred at an area that was not assumed to have accumulated sufficient slip deficit for such a megathrust event (*Noquet et al., 2017*). Both examples demonstrate that tectonic, rheologic and/or kinematic conditions that led to historic megathrust events may change more quickly than previously thought. Thus, the general assumption that seismotectonic segments produce characteristic seismic events may be obselete.

The Iquique-Pisagua earthquake 2014 is another example showing that seismic gaps do not behave constantly over time. A megathrust event has been expected for more than 30 years in the Northern Chile- Southern Peru seismic gap (e.g. *Kelleher, 1972*). Seismic predictions for this expected rupture were based on the last megathrust, the M_w ~8.6 Iquique earthquake 1877 in this gap (*Lomnitz 1970; Kausel 1986*). The slip deficit at the Camarones segment, where this last megathrust occurred, was assumed to have reached a critical status, thus soon to generate another megathrust event with similar extent. The Iquique-Pisagua event 2014 does not correspond to the expected characteristic megathrust (e.g. *Nishenko et al., 1985*) and is characterized by a suprisingly low level of stress release and magnitude. In previously published models, coseismic slip has a circular geometry and peak slip ranges between 4.4 m (*Schurr et al., 2014*) to ~10 m (*Duputel et al., 2015*). In my model, peak coseismic slip has reached 4.4 m centered at 19.8° S latitude characterized by a bullseye shape geometry. Main differences to other models can be explained by the incorporation of different sets of data into modelling

and different smoothing operations. The unexpected low magnitude of the Iquique-Pisagua rupture raises the question of why the earthquake occurred differently than the previous large event and what we can learn from this event. It is assumed that the 1877-earthquake broke through the interseismic low coupling area at 21° S interpreted as seismotectonic barrier in this study (e.g. *Kausel et al., 1986*; *Comte & Pardo et al., 1991*). If this was the case, a possible interpretation of the seismotectonic barrier is that coupling conditions may vary during one completed seismic cycle. The 1877 megathrust potentially changed stress conditions on the subduction plate interface and led to the activation of different locking asperities compared to interseismic stage. Thus, locking conditions varied in the following post- and interseismic stage of the 1877 quake until 2014. These interface conditions could have separated a formerly joint large seismotectonic segment between 18°-23° into at least two segments: the Camarones and Loa segment that now behave differently. This has significant consequences for the future rupture scenarios as also indicated by postseismic deformation analysis.

These factors are very specific for the location and seem hard to predict. However, the megathrust recurrence times and also forecasted rupture scenarios are based on only few available historical data, often extracted from witness reports (e.g. *Kausel et al., 1986*). But none of the tectonic or seismic gap concepts were available in the time when those earthquakes were documented. This means, that these data incorporate a large diversity that is not taken into account in the traditional interpretation of subduction zone seismicity. In this traditional interpretation, the main hypothesis for the seismic gap model includes the existence of characteristic earthquakes for seismotectonic segments in Northern Chile (e.g. *Kelleher, 1978*; *Nishenko et al., 1985*). As shown by *Ruiz & Madariaga* (*2018*), very few seismic events break the entire plate interface from the trench to the down-dip end of the seismogenic zone like the 2010 Maule event (e.g. *Moreno et al., 2010*). But most events at a magnitude range around M_w ~8.0 affect the intermediate depth regions of the plate interface like the case study shown in my coseismic model of the Iquique-Pisagua rupture. To yield a more accurate estimation of future rupture scenarios at the Chilean subduction zone, both types of megathrust events, (1) earthquakes above M_w ~8.5 and (2) earthquakes M_w ~8.0 may need to be clearly seperated in the seismic recurrence analysis. Averaging of both types in a joint analyis may distort statistics as category (1) events are assumed to repeat after ~300 years and category (2) events have a recurrence time of 80-100 years only (*Ruiz & Madriga, 2018*). Taking into account this categorization, the Iquique-Pisagua 2014 event may not be the expected characteristic category (1) megathrust event, that is assumed to ocurr every ~ 300 years (*Ruiz & Madariaga, 2018*), but however could be characteristic for category (2). In the last century, seven smaller events (1905, 1906, 1911, 1933, 1945, 1956, 1967)

with $M_s > 7$ (surface magnitude) are reported for the central part of the Northern Chile-Southern Peru seismic gap (*Comte & Pardo 1991*). The location of the largest event occurring in 1933 roughly corresponds to the main slip patch of the Iquique-Pisagua earthquake and could thus indicate rupturing of the same asperity.
A future seismic scenario of Northern Chile could be that another M_w ~8 will rupture the southern Loa segment as also indicated by increased locking rates during the next years to decades, followed by a $M_w > 8.5$ event that potentially break the entire interface in the 1877-seismic gap region in more than a century. As this hypothesis is very speculative, we need longer time series and also a spatially denser network of geodetic measurements including offshore observations to test different scenarios.

The following two questions are highly related to each other and are answered together:

4. **Why did the entire Northern Chile- Southern Peru seismic gap not rupture during the Iquique-Pisagua event 2014?**

and

5. **What factors may control the coseismic slip distribution of subduction zone earthquakes?**

The Iquique-Pisagua earthquake 2014 was much smaller in magnitude and extent than expected for the mature Northern Chile- Southern Peru seismic gap based on the calculated slip deficit of ~9 m (e.g. *Schurr et al., 2014*). A complete single-event stress release of the pre-seismic slip deficit would have ruptured the entire seismic gap resulting in a comparable rupture extent to the inferred 1877 M_w 8.6 Iquique event (e.g. *Kausel et al., 1986*). My analysis on inter- and coseismic backslip/slip distribution shows that tectonic preconditions may have the potential to stop the rupture. My interseismic backslip model (**Figure 3.4**) as direct indication for plate coupling reveals two highly coupled patches separated by a narrow low coupling zone at 21° S latitude that is also identified by other studies (Iquique low coupling zone, *Métois et al., 2016; Li et al., 2015*). The final coseismic slip model (**Figure 4.15**) and all afterslip models (**Figure 3.5**) show that slip stopped at this low coupling zone at 21° S interpreted as seismotectonic barrier. The provenance of the barrier may arise in (1) the heterogeneity of seafloor roughness (e.g. seamounts as the Iquique Ridge at 21° S; *Geersen et al., 2015*) that induce plate coupling variations and/or (2) a heterogeneity in the continental (forearc) crustal strength and/or (3) in differences in the subducting plate geometry as a slab dip (slab bending) at 21° S (*e.g. León-Ríos et al., 2016*). However, the small extent and magnitude of the Iquique-Pisagua earthquake 2014 was also a consequence of the unusually

low level of initial stress release. An explanation for this seismic pre-condition may be the occurrence of preceding slow slip events that result in an aseismic stress release in the three months before the mainshock on 1st April (e.g. *Meng et al., 2015; Kato et al. 2016; Ruiz et al., 2014*). Another explanation involves the crustal M_w 6.7 foreshock on 16 March 2014 that may have triggered a seismic precursor sequence. This seismic triggering may led to a temporary unlocking of the plate interface and the release of fluids lowering the effective normal stress in the hypercenter area which finally led to the Iquique-Pisagua mainshock (*Gonzáles et al., 2015*). The interpretation of different scenarios of whether slow slip event was a dominating mechanism before the Iquique-Pisagua mainshock or not has significant implications towards the evaluation of future rupture events in the former Northern Chile- Southern Peru gap region. If seismic slip caused by precursors was the driving force for detected ground displacement transients (*Schurr et al., 2014*; *Bedford et al., 2015*), the rupture area of the Iquique-Pisagua mainshock would not act as barrier for a future large megathrust event affecting the entire gap region. In contrast, if slow slip preceding the mainshock accommodated most of the surface displacements (e.g. *Ruiz et al., 2014*; *Yagi et al., 2014*), calculated slip deficit would be smaller implying that future events will rather rupture smaller patches to the south and north of the Iquique-Pisagua rupture area.

Subduction zone megathrust rupture extent and magnitude seem not only be linked with a potential slip deficit, but also size and limitations of seismotectonic segments and characteristics of interseismic (crustal) tectonic conditions. Due to the complexity of those tectonic conditions and strongly time-dependent interface coupling patterns, subduction zone earthquakes do not necessarily show same rupture characteristics over time. The Iquique-Pisagua case-study with the comparison of the M_w 8.6 event in 1877 and the M_w 8.1 event in 2014 support this hypothesis.

6. How long does afterslip of the recent Iquique-Pisagua earthquake dominate over relocking in the postseismic stage?

The postseismic stage of the Iquique-Pisagua earthquake 2014 lasts for about two years. After this time, the interseismic linear trend (relocking) dominates over the postseismically logarithmic decay in the GPS time series of stations in the Camarones segment in Northern Chile. Cumulative afterslip after two years reached 89 +1.2/-0.4 cm and is located down-dip the main rupture. The southern neighbouring Loa segment south of 21° S is mostly unaffected by afterslip. The transition from afterslip dominated deformation to interseismic ground motion south of 21° S is relatively sharp and interpreted

as seismotectonic barrier. Afterslip extends further south of the seismotectonic barrier (Iquique low coupling zone), which mainly can be attributed to postseismic interface motion due to the largest aftershock on April 3rd that occurred in response to seismic loading by the mainshock (e.g. *Herman et al., 2015*). However, the slip inversion analysis shows that viscoelastic mantle relaxation plays a minor role in postseismic near-field deformation and crustal mechanisms seem to be the driving tectonic force for inter- and postseismic ground deformation rates for megathrust events with a comparable magnitude to the Iquique- Pisagua earthquake 2014.

7. Can we improve methodological aspects for the applied geodetic measurements to yield more reliable slip inversion results?

The intensive post-processing efforts for geodetic data in this study show that exploiting objective measurements is not a trivial problem. The GPS measurements contain various signal contributions of non-tectonic and tectonic ground motion sources that need to be separated for the slip inversion. The oscillatory signal contribution is clearly dependent from local conditions and can be subtracted based on a statistical approach that requires a dense network of continuous GPS stations for mathematical robustness. My approach clearly demonstrates that sGPS measurements will need to be corrected for the oscillatory signal contribution, if not measured at the exact time each year. Another improvement of slip inversion results can be realized by combining different independent (geodetic) data sources. An implementation of dense continuous GPS networks is very expensive concerning material and manpower, whereas InSAR data are often even freely available (e.g. Sentinel-1 data), but strongly limited to data in the archive. The correction of a linear ramp in the InSAR measurements also shows that this data source may not be used as standalone approach for slip inversion. Best results may be received by the joint inversion of both geodetic technologies that highly improves slip model resolution, especially in the deformation near-field as shown in this study.

5.2 Outlook

My thesis gives evidence that improving geodetic data quality by carefully post-processing ground motion measurements and moreover jointly inverting different geodetic data types has a significant impact in subduction zone theory by providing high-resolution reliable interface slip models at all stages of the seismic subduction zone cycle. Data quality in general is often not the main focus of deformation studies and complicated modelling algorithms and model parameterizations become more and more important in evaluating the scientific impact. Of course, modelling is a major step in analysing slip at different stages of the seismic cycle and huge efforts can be achieved by a more reliable modelling approach (e.g. Bayesian modelling). But even the best model is just as reliable as its input data set.

In my thesis, I mainly used two different kinds of geodetic input data: GPS and InSAR measurements (and additionally seismologic data in chapter 3). The resolution of my slip models is best between a depth range of 15-65 km due to the dense GPS network in Northern Chile and the high spatial resolution of near-field InSAR data. But a problem at subduction zones is usually the large gap of data between the trench and the onshore areas that influences interface model resolution in a shallow depth range, which can easily visualized by checkerboard test. To be able to better resolve shallow slip and special tectonic motion features such as aseismic creeping, offshore ground motion measurements and sea-floor geodesy are required. However, these technologies require huge efforts in infrastructure, are very expensive and less accurate than onshore GPS (e.g. *Brodsky & Lay, 2014*).

The availability of high-resolution InSAR data may improve geometric resolution of slip models, especially through larger satellite footprints such as the "Terrain Observation by Progressive Scans" (TOPS) -mode for the recent ESA Sentinel-1 mission (C-band) that potentially fully cover ground motion of long wavelength tectonic signals at seismically hazardous regions like subduction zones. The potential of SAR and InSAR measurements for slip inversions has not yet been fully exploited and SAR-background missions (images without explicit commissioning) needs to be expanded.

Despite huge efforts in the development and application of geodetic technologies within the past four decades, we still lack long deformation time series for each stage of the seismic cycle to really draw reliable conclusions from our ground motion statistics. All information about recurrence intervals or historic earthquake characteristics are taken from the geologic archive or witness reports, thus are burdened with an inherent error. The establishment of permanent long-term geophysical and geodetic measurements in a dense station network will improve statistical robustness of slip models in the future.

Supplementary Material

A: Illapel Earthquake

The Chilean subduction zone is a highly active convergent margin, segmented into frequently rupturing seismotectonic units. The main focus of my thesis is the ground deformation related to the subduction zone seismic cycle in Northern Chile. The presented methods and algorithms for the joint slip inversion of InSAR and GPS data in all stages of the seimic cycle can easily be applied to other segments at the Chilean subduction zone and maybe even at other subduction zones on Earth.

I contributed to a study of Tilman et al. (2016), that applies similar InSAR data processing algorithms and jointly inverts geodetic data to yield a slip model for the M_w 8.2 Illapel erathquake in Central Chile:

Tilmann, F., Y. Zhang, M. Moreno, J. Saul, ***F. Eckelmann****, M. Palo, Z. Deng, A.Y. Babeyko, K. Chen, J.C. Baez, B. Schurr, R. Wang, and T. Dahm (2016), The 2015 Illapel earthquake, central Chile: a type case for a characteristic earthquake?, Geophysical Research Letters, 43, 2, pp. 574—583, doi:10.1002/2015GL066963.*

This chapters contains parts of the published manuscript Tilmann et al. (2016). In the following, I present restructured and partly rephrased chapters of the manuscript in order to highlight my contributions to this study and to explain how my methods and processed geodetic data are used to improve the slip model of the Central Chilean subduction zone setting.

A.1. Introduction and Tectonic Setting

(*compare: 1. Introduction and 2. Tectonic Setting in Tilmann et al., 2016*)

The Central Chilean margin was hit by a M_w 8.2 Illapel megathrust earthquake on 16 September 2015. By combining an inversion of cGPS and InSAR displacement measurements with other geophysical data (sesimic waveforms, high frequency teleseismic backprojection), we derive a detailed subduction interface coseismic slip model. The earthquake caused a tsunami of considerable height of up to 4.5m at Coqimbo and ~2m in Valparaiso.

The area has last been hit by a great earthquake in 1943, estimated to be slightly smaller at M_w = 7.8–7.9 by *Beck et al.* (1998) (**Figure A.1**). The area immediately to the north ruptured in 1922 in a much larger earthquake, whereas to the south earthquakes in 1971 and 1985 broke the coupled interface and partially overlap with the 2010 Maule earthquake. A patch of relatively low interseismic coupling was inferred between the rupture areas of the 1922 and 1943 events at ~30°S by *Métois et al.* (2012) and is also seen in our coupling model (**Figure A.1**). The area between this boundary and the northern edge of the 2010 Maule earthquake is termed the Metropolitan segment (e.g., *Métois et al.*, 2012). In 1997 the region 29.6°–31°S experienced swarm-like activity (Coquimbo swarm), which included several $M_w > 6$ events and involved both the plate interface and intraplate events within the downgoing plate (*Lemoine et al.*, 2001) (**Figure A.1**).The major bathymetric feature in the area is the Juan-Fernandez Ridge (JFR), a hot spot chain, which intersects the trench near 32.5°S. The ridge blocks northward flow of sediments, yielding a sharp contrast between a trench filled with ample sediment in the south to a sediment starved trench with less than 1 km of sediments within the Metropolitan segment (*Contreras-Reyes et al.*, 2015). As a direct result of the contrasting sediment thickness, the subduction style changes from accretionary in the south to erosive in the north (*von Huene et al.*, 1997). The JFR further marks the transition to flat slab subduction in the north (*Pardo et al.*, 2002), but the slab interface at seismogenic depths ($\lesssim$ 50 km depth) has a dip of 20–22° both to the north and south (*Lange et al.* (2012), *Hayes et al.* (2012), and this study). In the north the Challenger Fracture Zone (CFZ), which intersects the margin at 30°S, is associated with an age offset of 3.5 Myr but does not exhibit significant relief (**Figure A.1**).

***Figure A.1**:* **(**next page) *(compare Figure 1 in Tilmann et al., 2016) Map of the study area with incoming seafloor relief (Smith and Sandwell, 1997) shown seaward of the deformation front and the locking model landward of it. Black contours show 2 Ma increments of oceanic plate age (Müller et al., 2008). Two-meter coseismic slip contours are shown in dark green (this study). White lines indicates aftershock area of 1971 and 1985 according to Comte et al. (1986), and white bars mark the approximate along-strike extent of historical ruptures (after compilation in Beck et al. (1998) and Kelleher (1972)). Earthquakes with magnitude greater or equal 5.0 between 1963 and just before the Illapel event are shown as gray dots (Engdahl catalog up to 2008 (Engdahl et al., 1998) and ISC bulletin from 2009 onward) with events between July 1997 and January 1998 plotted in magenta in order to highlight the events of the Coquimbo swarm. The main shock epicenter and focal mechanism are also marked (both GEOFON catalog). Plate convergence is shown for MORVEL plate model (DeMets et al., 2010). JFR is the Juan-Fernandez Ridge, and CFZ is the Challenger Fracture Zone.*

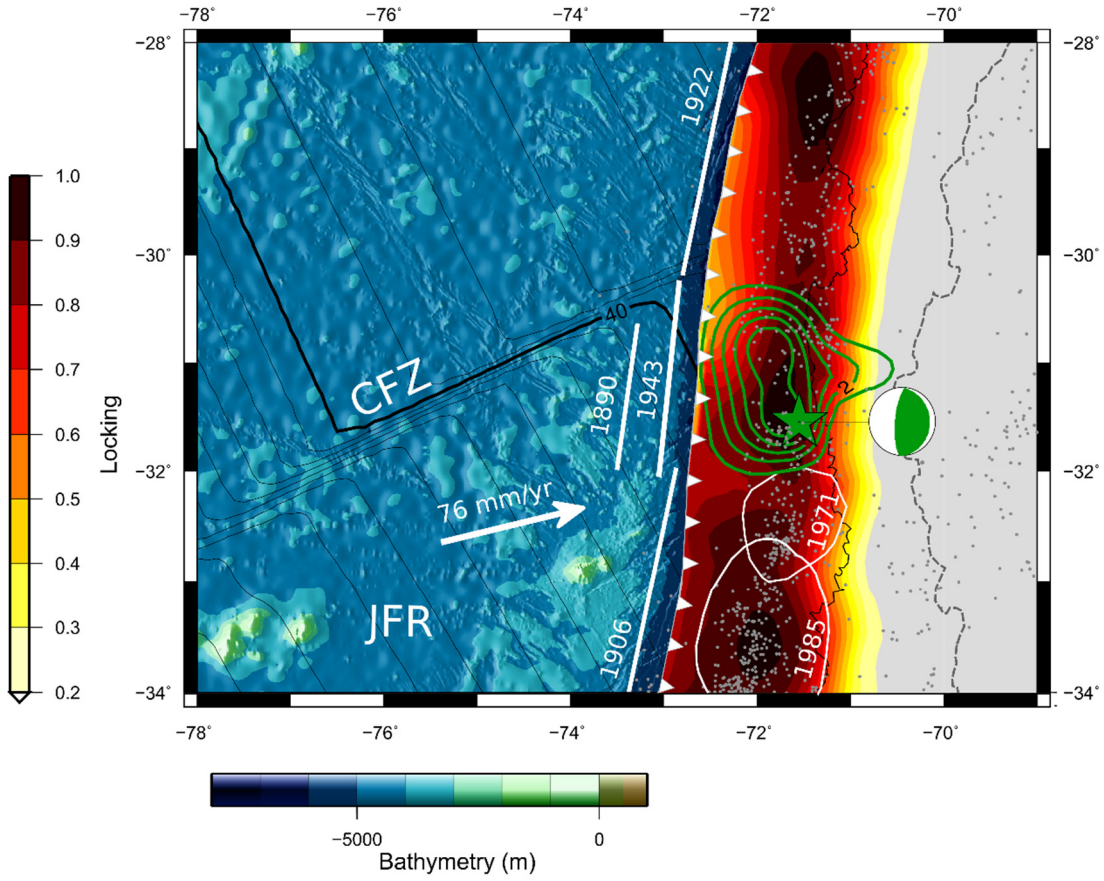

A.2. Methods

(*compare: S1 InSAR data processing, S2 GNSS processing and S3 Geodetic inversion in Tilman et al., 2016*)

A.2.1. InSAR data processing

For estimating the coseismic surface deformation, we use freely available Sentinel-1 data in descending orbit. The Sentinel-1 satellite operates in C-Band (wavelength= 5.62 cm). We processed level-1 data in the Interferometric Wide Swath Mode with a spatial resolution of 5 x 20m (single look). In this mode, each acquisition contains three subswaths using Terrain Observation with Progressive Scans SAR (TOPSAR). Altogether, four Sentinel acquisitions each with dates 14-08-2015 and 17-09-2015 were merged in order to cover an area of approximately 600 x 250 km2, encompassing the central Chilean margin around the city of Illapel. The interferogram was processed by using Gamma software (*Werner et al., 2000*). First, four burst mode TOPS single look complex (SLC) data sets were concatenated, in which each SLC starting time differs by about one second. The coregistration - as a key step in the InSAR processing - was done by resampling the concatenated slave image to the geometry of the master image using a

lookup table that is derived from a DEM in radar coordinates and the given orbit state vectors. We used the 90m-resolution SRTM-v4 DEM as input. A differential interferogram with 20 looks in range and 4 looks in azimuth was calculated using the coregistered SLC data and a simulated interferogram derived from the DEM and baseline model. Afterwards, we adaptively filtered the interferogram based on the local fringe spectrum with an alpha exponent of 0.6 and a filtering FFT window size of 64 (*Goldstein and Werner, 1998*) (see **Figure A.2** for the processed interferogram).

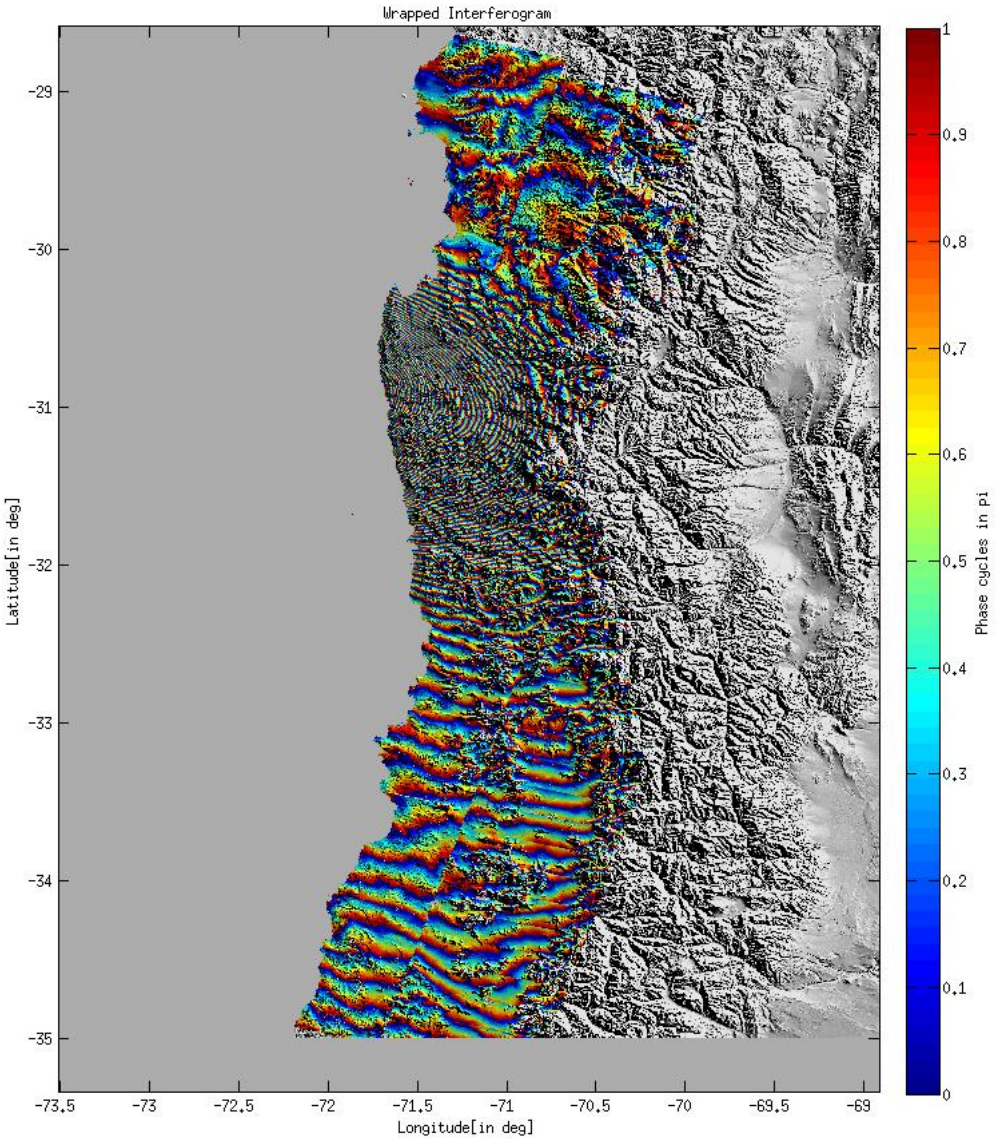

***Figure A.2**: Interferogram constructed from four Sentinel-1 (C-band) images taken between 14 August and 17 September 2015. Each fringe corresponds to a displacement of 2.81 cm along the LOS direction during the earthquake and in the early coseismic phase.*

Unwrapping was done using the Minimum Cost Flow approach, which is based on triangulation. Finally, downsampling of the interferogram is required in order to make the

model computations more feasible, creating 379 data cells in the process (**Figure A.3**), which were then used in the coseismic slip models. The subsampling was realized using the Quadtree partitioning method (*Jonsson et al., 2002*). Because of high spatial correlation, the dataset can be reduced without any loss of significant information in the deformation signal. Quadtree squares were chosen to be equally spaced throughout the entire image. Thus we created 379 data cells.

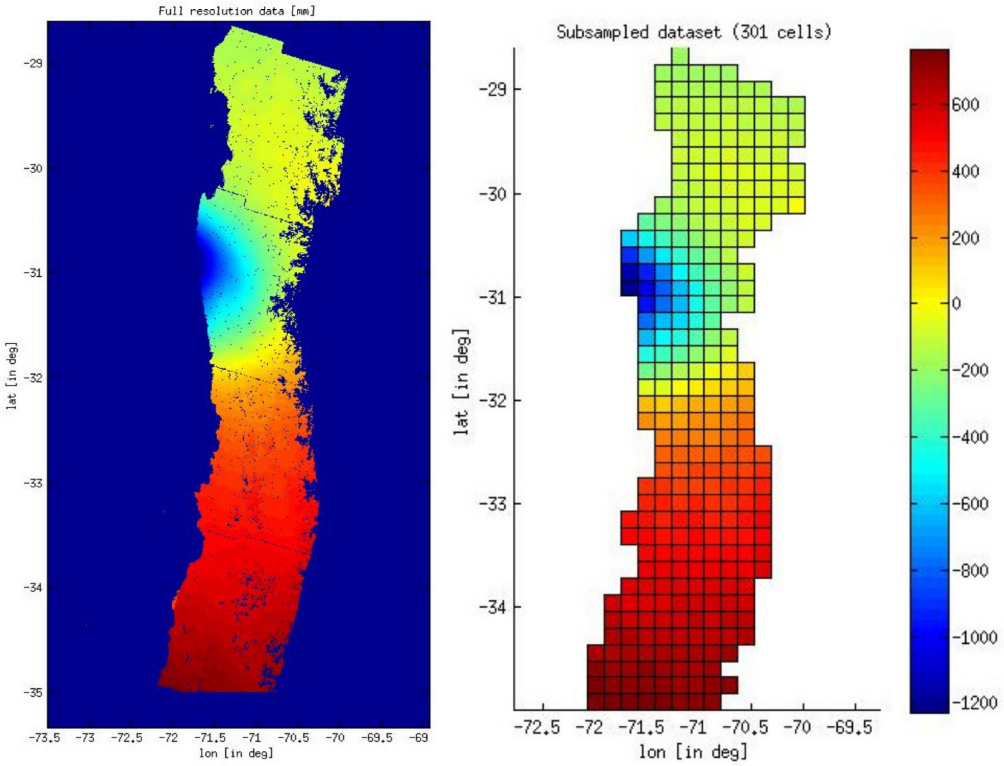

Figure A.3*: Unwrapped LOS displacement. The LOS direction is pointing upwards and in ENE direction with an angle of inclination varying from 45° in the northwest corner to 60° in the southeast, i.e. the area of negative LOS motion north of the epicenter corresponds to depression and/or motion to the west. The right hand side shows the unwrapped LOS displacement on a coarser grid, which was used as constraint for the coseismic slip inversions. The colour scale shows the displacement in mm relative to an arbitrary baseline.*

A.2.2. GNSS processing and geodetic inversion (*applied by Z. Deng and M. Moreno*)

In this paper, GPS data from 122 stations on 16 September 2015 are processed, which are located in South America operated by 20 different organizations and universities. In addition to the GPS observations, 54 stations have recorded also GLONASS satellite observations. To study the dynamic motion during the earthquake 18 stations with 1 Hz high-rate observations have also been processed.

The 122 GPS stations are processed using the last version of GFZ GNSS software, Earth Parameter and Orbit System (EPOS) (*Deng et al., 2015*). To retrieve the dis-

placement caused by the Illapel earthquake two processing strategies are used, static Precise Point Positioning (PPP) model using daily 30 second GPS+GLONASS observations and kinematic PPP model using two hour 1 Hz high-rate GPS observations.

In the daily static PPP model the displacements of the GPS stations are calculated from the differences between 22 hour coordinate solution (00:00-22:00 UTC) on 16 September 2015 and 24 hour coordinate solution (00:00-23:59 UTC) on 17 September 2015. […] In the kinematic PPP solution the station coordinates are estimated every second for the time period 22:00-23:59 UTC on 16 September 2015.

GPS data processing is applied in a similar way as extensively described in the Iquique-Pisagua study. Inter- and coseismic slip distributions of both dip-slip and strike-slip components were estimated using a damped linear least squares inversion based on Green's functions generated with a Finite Element model. This model is an update of the model of Moreno et al. (2012) including a refined mesh. Our model incorporates the geometrical complexities of the Chile subduction zone taking into account the precise geometry of the subduction interface according to the SLAB1.0 model (*Hayes et al., 2012*), topography and bathymetry data and the continental Moho (*Tassara and Echaurren, 2012*). The structure of our 3-D model consists of four blocks: continental plate, viscoelastic continental mantle, oceanic plate, and viscoelastic oceanic mantle. The megathrust fault used in the inversion was discretized into 1321 triangular patches with an average patch size of 60 km2 and extends from the trench to a depth of 70 km. We specifed a Young's modulus of 100, 120 and 160 GPa, for the continental crust, oceanic crust, and mantle, respectively. Poisson's ratio was set to 0.265 and 0.30 for continental and oceanic crust, respectively, and 0.25 for the mantle. All numerical simulations in this study were solved with the finite element modelling software PyLith (*Aagaard et al., 2013*) and the mesh was created using the Cubit software. The Green's functions were created for the center of each fault triangular element to allow a better representation of the fault curvature. The MATLAB routine ‘lsqlin’, a subspace trust-region method based on the interior-reflective Newton method described by Coleman and *Li* (*1996*), was used to solve the inversion.

Daily solutions of vertical and horizontal displacements from 18 cGPS were inverted together with InSAR data to produce a slip distribution that represents the main deformation. Unwrapped InSAR data have a subtle ramp. We therefore introduce an additional three auxiliary parameters into the inversion to represent a planar ramp and offset in the InSAR data (but not the GPS data). The ramp parameters are inverted for jointly with the slip distribution. The combined solution fits the GNSS and InSAR observations very well in terms of both direction and amplitude (**Figure A.4**). It clearly shows the

influence of the deformation of aftershocks, which may have cancelled part of the deformation produced by the main event in the downdip part of the rupture.

For more details on data processing or model set-up, please refer to the auxiliary material of *Tilmann et al.* (*2016*).

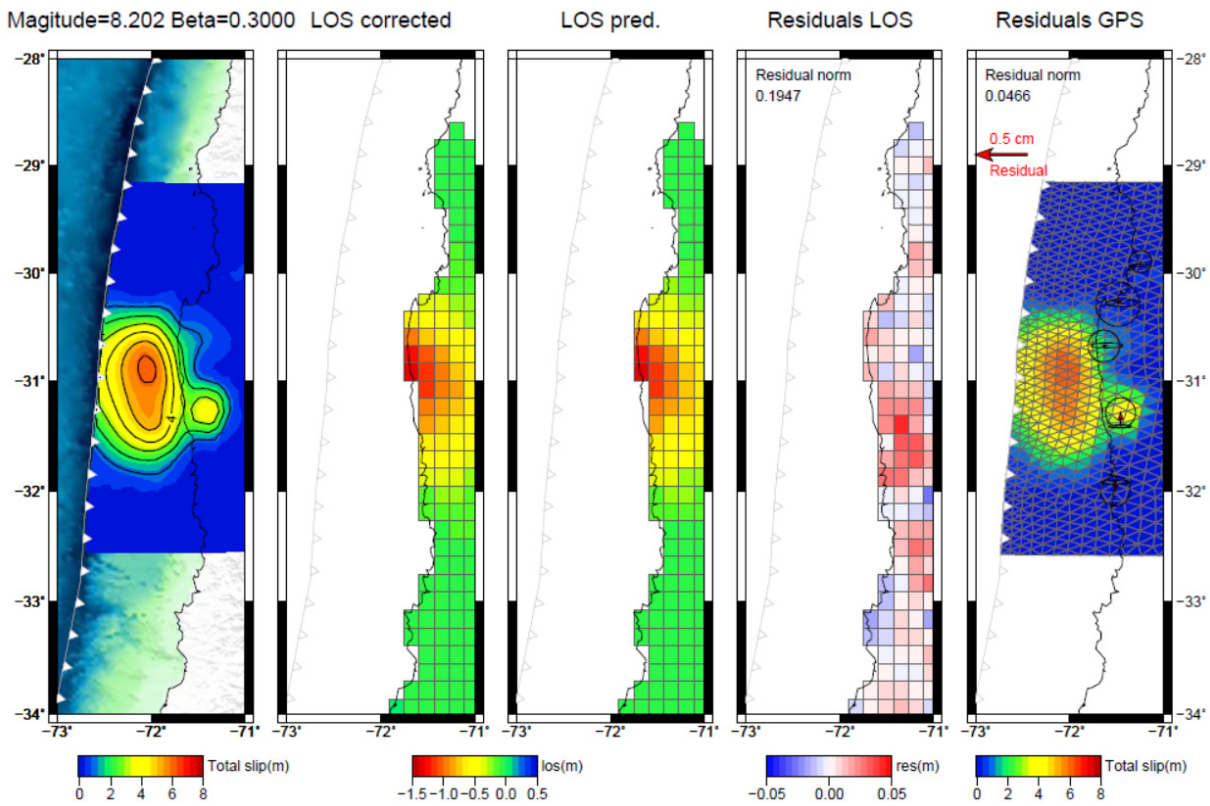

Figure A.4*: Optimal coseismic slip obtained by using a joint inversion of GPS and InSAR. Line of sights (LOS) were corrected for a ramp during the inversion. The modelled slip includes the e_ect of an* M_W *= 7:0 aftershock.*

A.3. Coseismic Rupture

(*compare: 3. Coseismic Rupture in Tilmann et al., 2016*)

Displacements measured at continuous GNSS stations indicate uplift of the coastline and westward motion approximately radially toward a point offshore near 31.2°S. Near-field interferometric synthetic aperture radar (InSAR) fringes also align along a circular pattern (**Figure A.1**) focused on this area. These observations point to a simple rupture with peak slip located offshore at this latitude. We applied different approaches for inferring coseismic slip and rupture evolution. First, we model the coseismic displacement field as recorded by continuous GNSS stations using a realistic geometry for the plate interface (SLAB1.0) (*Hayes et al.*, 2012) and laterally heterogeneous elastic structure

(*Tassara and Echaurren*, 2012), following the methodology of *Moreno et al.* (2012). In **Figure A.3** we show the model for the purely coseismic displacement [..] on the daily GNSS solution and InSAR data, which also includes the effects of the first day of post-seismic slip including an *Mw* = 7.0 aftershock […]. Slip is additionally inverted in a second approach by using geophysical data (strong motion, teleseismic data, backprojection of seismic arrivals). The coseismic slip estimated by the two methods results in a broadly similar rupture pattern (**Figure A.5**), albeit with a somewhat different peak slip of ~6 m and 4.8 m in the geodetic finite element model and joint inversion models, respectively. The geodetic solution also has a more elongated region of maximum slip.

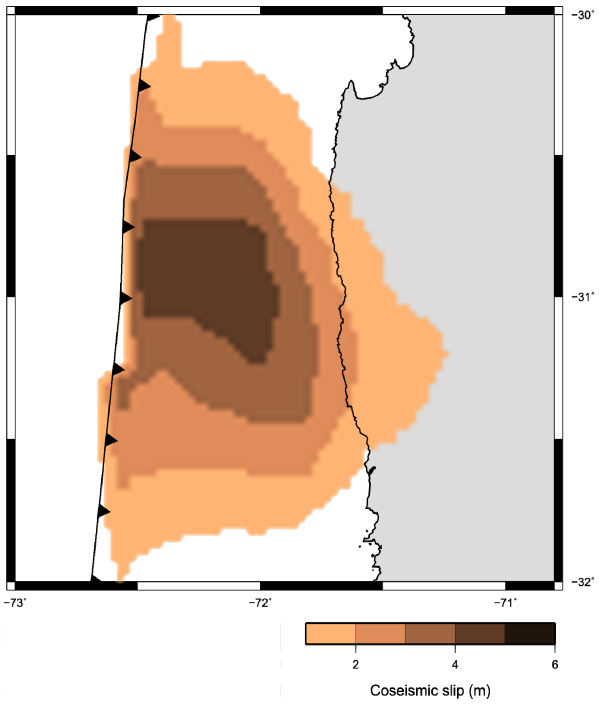

***Figure A.5*:** Coseismic slip model. The colour image shows the dip component of coseismic slip in the joint inversion model, with slip less than 1 m omitted, as this is not well constrained.

A.4. Discussion and Conclusion

(*compare: 5. Discussion and Conclusion in Tilmann et al., 2016*)

The slip model reveals details on rupture evolution and shows, that the earthquake nucleated close to the coast and propagated northwards and up-dip with a maximum slip of 5-6m.

The along-strike extent of the Illapel rupture coincides approximately with a local high in interseismic locking in our updated locking map (**Figure A.1**). A similar pattern is

found in the locking map of *Métois et al.* (*2012*). The up-dip extent of locking is very hard to constrain such that the shift in dip direction between peak slip and maximum locking is not significant. The aftershocks extend into the areas of intermediate locking to the south and north. *Métois et al.* (*2012*) had already pointed out the possible role of incoming seafloor features, i.e., the JFR and CFZ, in controlling the segment boundaries as their projection below the forearc approximately coincides with the region of low locking. However, the actual coseismic rupture is clearly much smaller than the gap between these features (**Figure A.1**), such that it is hard to make the argument that the main shock rupture was arrested by either of them. […]

The presence of a local high in locking and the fact that prior earthquakes in 1943 and 1880 seem to have broken a similar part of the margin justify the identification of the area between 30° and 32°S as a distinct segment (*Métois et al.*, 2012, 2014), even though in the earlier earthquake history its southern boundary seems to have been breached by earthquakes in 1730 and maybe in 1647 (*Beck et al.*, *1998*). The accumulated margin-normal slip deficit since 1943 is 5.31m for full locking (based on convergence of 78 mm/year at 19° obliqueness) (*DeMets et al.*, 2010), similar to the actual peak slip of the Illapel earthquake. Leaving the case of the eighteenth century multisegment rupture aside, the Coquimbo-Illapel margin thus seems to be an ideal host for characteristic earthquakes, i.e., earthquakes with very similar properties in subsequent seismic cycles. […]

In contrast to this superficial similarity stands the much smaller seismic moment determined for the 1943 event by *Beck et al.*, *1998* (6 × 1020 Nm, only about a fourth of the moment of the recent event). […] Even if we discount the early weak phase of the 2015 shock it is clear that the recent event ruptured at least twice as long. […]

In conclusion even this simple segment does not seem to produce characteristic earthquakes in the strict sense, and slip predictability can be rejected. This finding is consistent with statistical approaches, which find that the frequency-magnitude distributions determined for the major subduction zones are consistent with the standard Gutenberg-Richter power law distribution, contrary to the prediction of the characteristic earthquake hypothesis (*Naylor et al.*, 2009). Considering the events in 1971, 1985, and 2010, the area to the south has arguably completed its seismic cycle for this generation, and no $M > 8$ earthquake is expected there in the near future. This throws the spotlight on the Atacama segment to the north, which has ruptured in a great earthquake in 1922 and has not experienced an event with $M > 7.5$ since but is likely to be further loaded by the postseismic response to the Illapel earthquake in the months to come. This segment thus remains at significant risk for another great earthquake and accompanying tsunami.

B: Supporting Information for *Characterizing afterslip and ground displacement rate increase following the 2014 Iquique-Pisagua M_w 8.1 earthquake, Northern Chile*

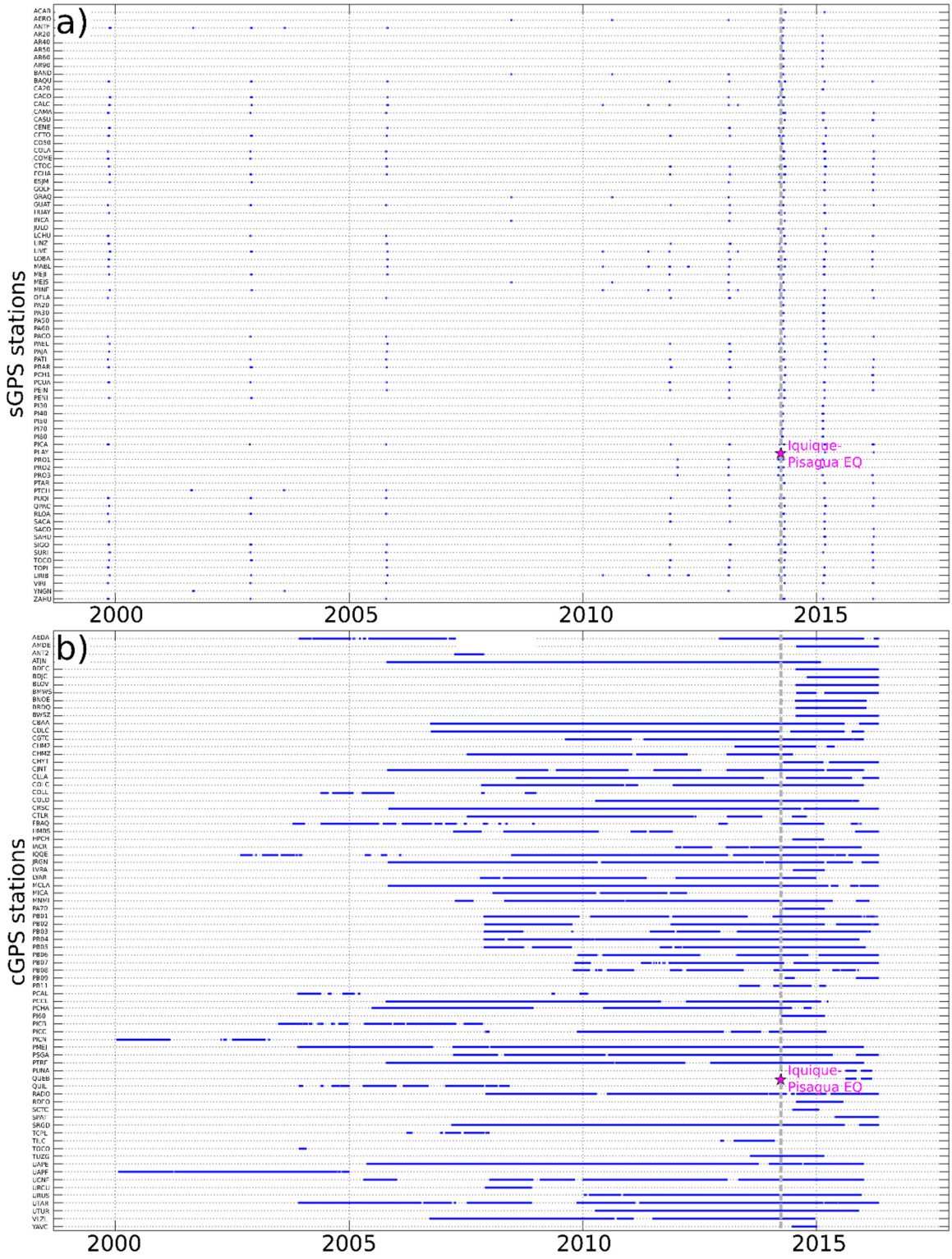

***Figure B.1**: Availability of a) survey GPS (sGPS) and b) continuous GPS (cGPS) data sorted by station name. The pink star marks the time of the Iquique-Pisagua earthquake.*

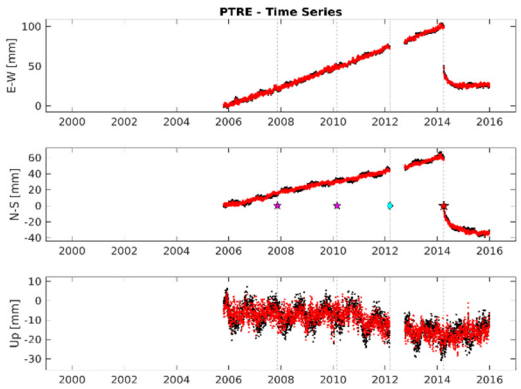
PTRE - Time Series
E-W [mm]
N-S [mm]
Up [mm]

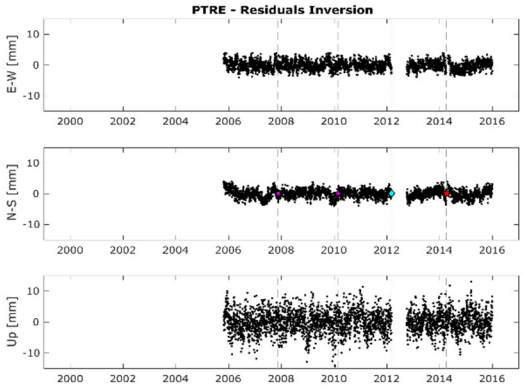
PTRE - Residuals Inversion
E-W [mm]
N-S [mm]
Up [mm]

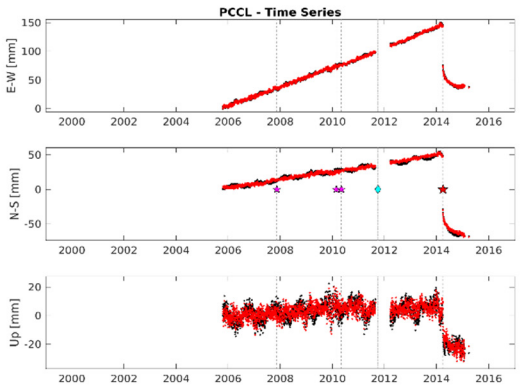
PCCL - Time Series
E-W [mm]
N-S [mm]
Up [mm]

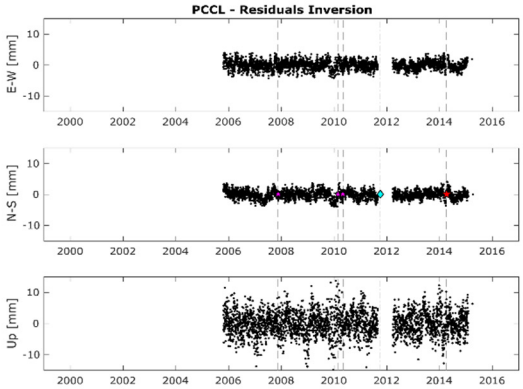
PCCL - Residuals Inversion
E-W [mm]
N-S [mm]
Up [mm]

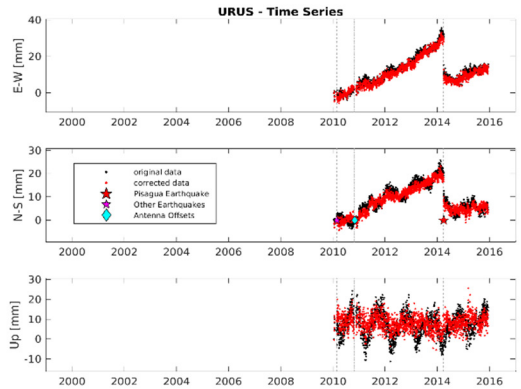
URUS - Time Series
E-W [mm]
N-S [mm]
Up [mm]
original data
corrected data
Pisagua Earthquake
Other Earthquakes
Antenna Offsets

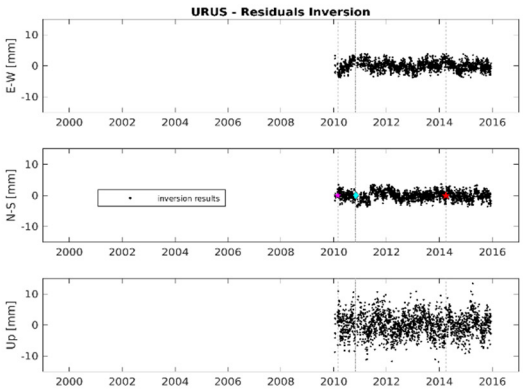
URUS - Residuals Inversion
E-W [mm]
N-S [mm]
Up [mm]
inversion results

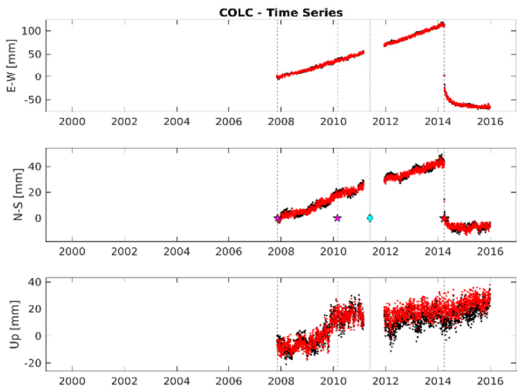
COLC - Time Series
E-W [mm]
N-S [mm]
Up [mm]

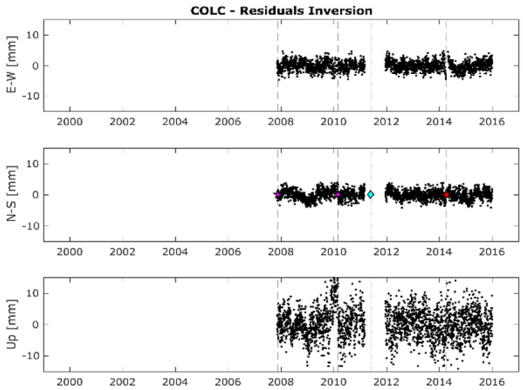
COLC - Residuals Inversion
E-W [mm]
N-S [mm]
Up [mm]

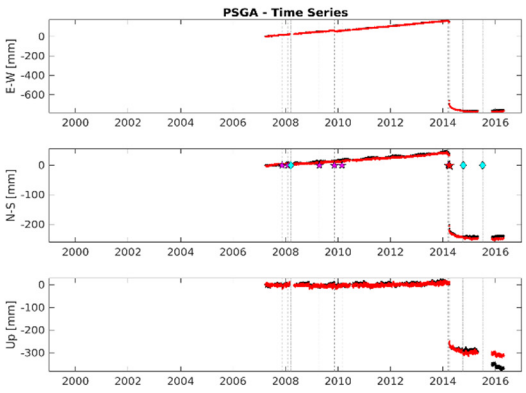
PSGA - Time Series
E-W [mm]
N-S [mm]
Up [mm]

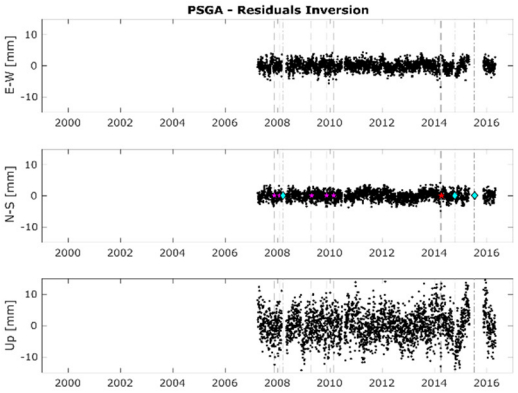
PSGA - Residuals Inversion
E-W [mm]
N-S [mm]
Up [mm]

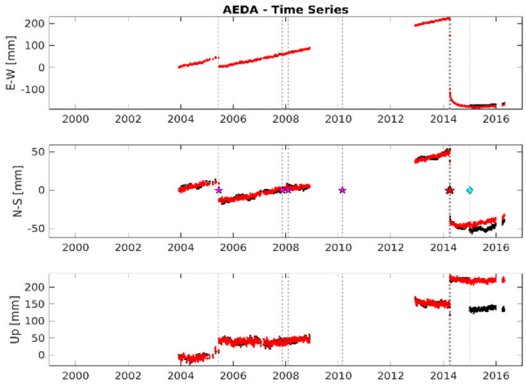
AEDA - Time Series
E-W [mm]
N-S [mm]
Up [mm]

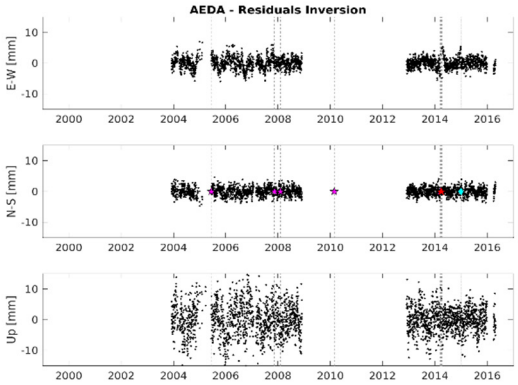
AEDA - Residuals Inversion
E-W [mm]
N-S [mm]
Up [mm]

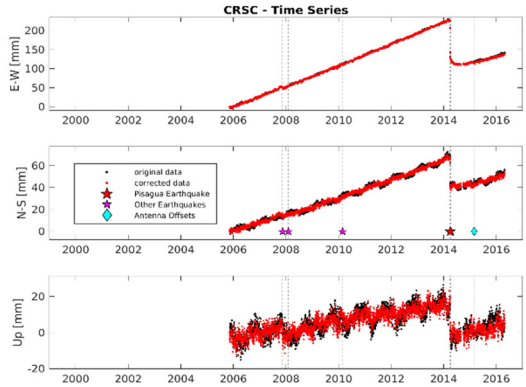
CRSC - Time Series
E-W [mm]
N-S [mm]
Up [mm]
original data
corrected data
Pisagua Earthquake
Other Earthquakes
Antenna Offsets

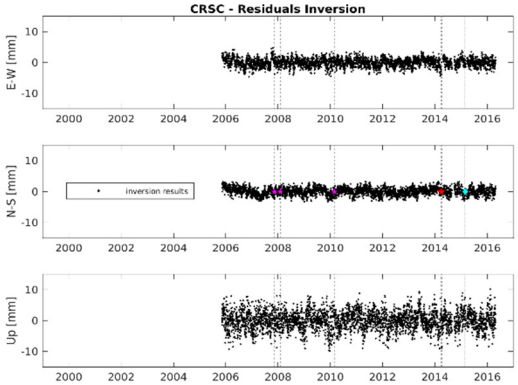
CRSC - Residuals Inversion
E-W [mm]
N-S [mm]
Up [mm]
inversion results

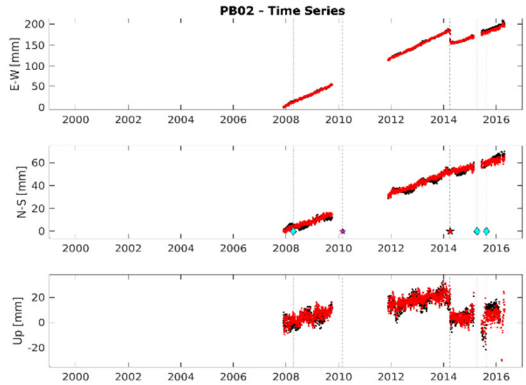
PB02 - Time Series
E-W [mm]
N-S [mm]
Up [mm]

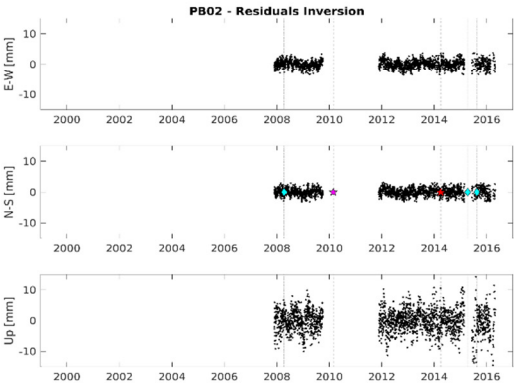
PB02 - Residuals Inversion
E-W [mm]
N-S [mm]
Up [mm]

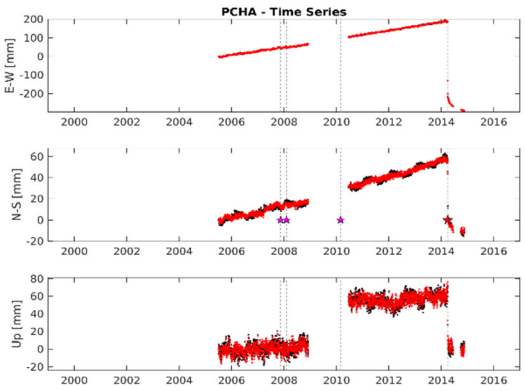
PCHA - Time Series
E-W [mm]
N-S [mm]
Up [mm]

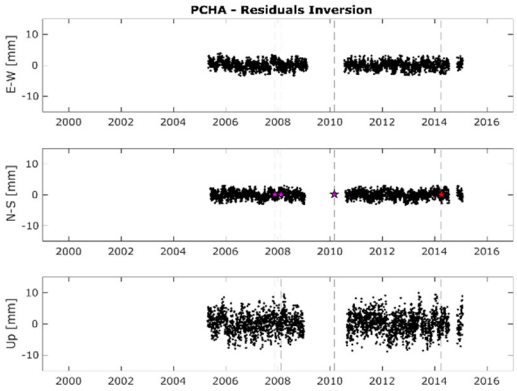
PCHA - Residuals Inversion
E-W [mm]
N-S [mm]
Up [mm]

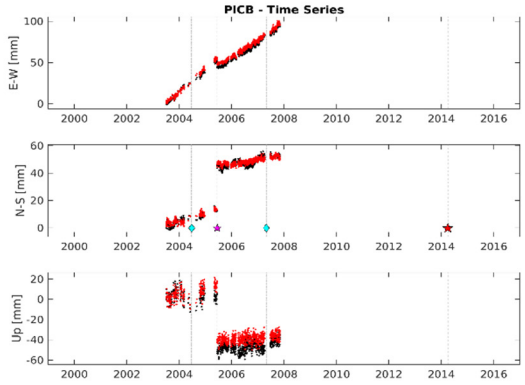
PICB - Time Series
E-W [mm]
N-S [mm]
Up [mm]

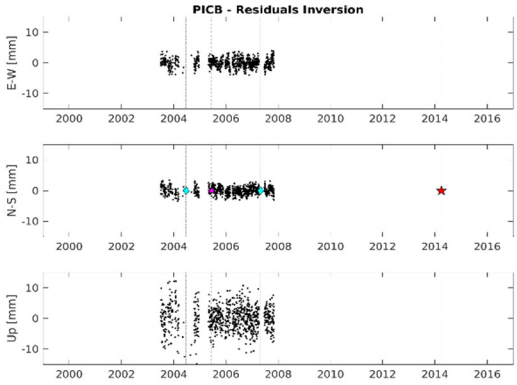
PICB - Residuals Inversion
E-W [mm]
N-S [mm]
Up [mm]

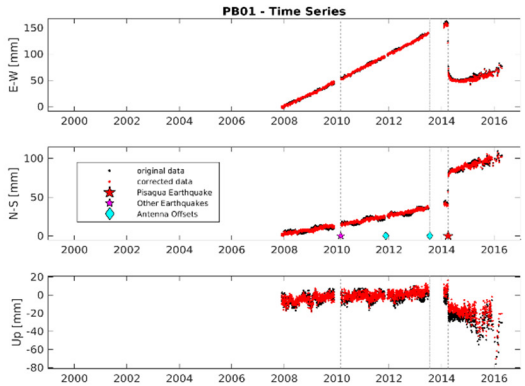
PB01 - Time Series
E-W [mm]
N-S [mm]
Up [mm]
original data
corrected data
Pisagua Earthquake
Other Earthquakes
Antenna Offsets

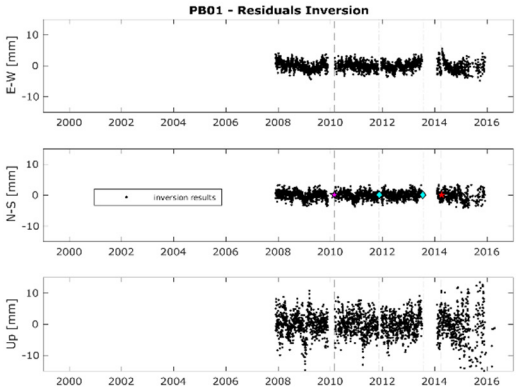
PB01 - Residuals Inversion
E-W [mm]
N-S [mm]
Up [mm]
inversion results

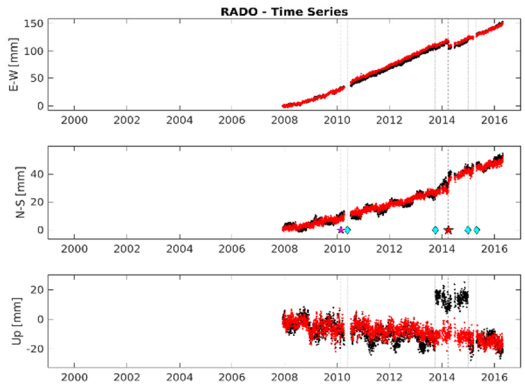
RADO - Time Series
E-W [mm]
N-S [mm]
Up [mm]

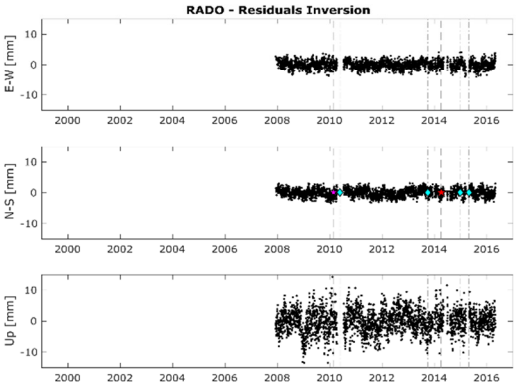
RADO - Residuals Inversion
E-W [mm]
N-S [mm]
Up [mm]

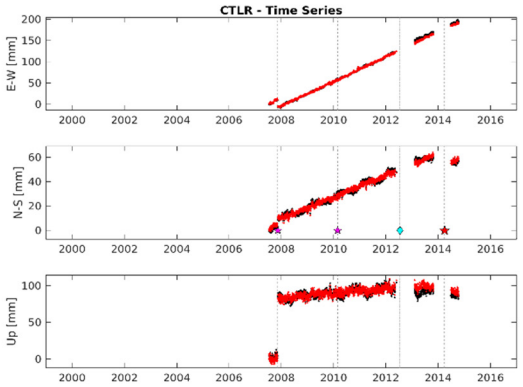
CTLR - Time Series
E-W [mm]
N-S [mm]
Up [mm]

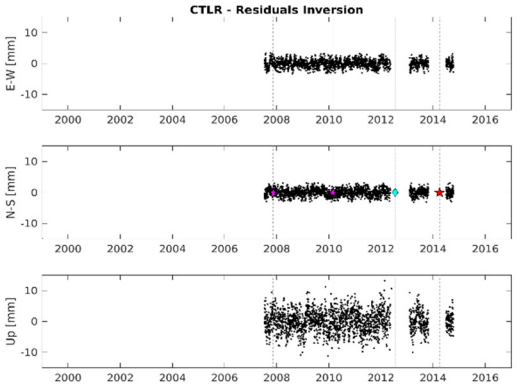
CTLR - Residuals Inversion
E-W [mm]
N-S [mm]
Up [mm]

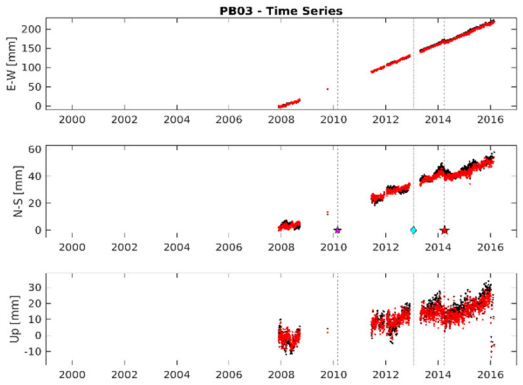
PB03 - Time Series
E-W [mm]
N-S [mm]
Up [mm]

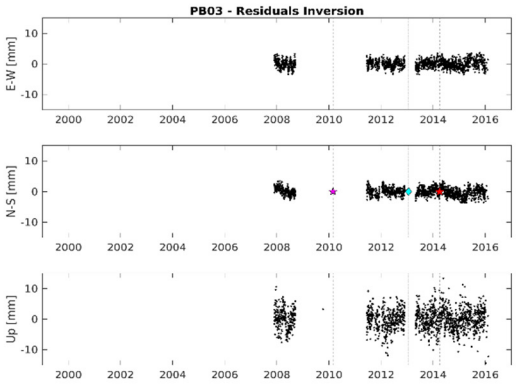
PB03 - Residuals Inversion
E-W [mm]
N-S [mm]
Up [mm]

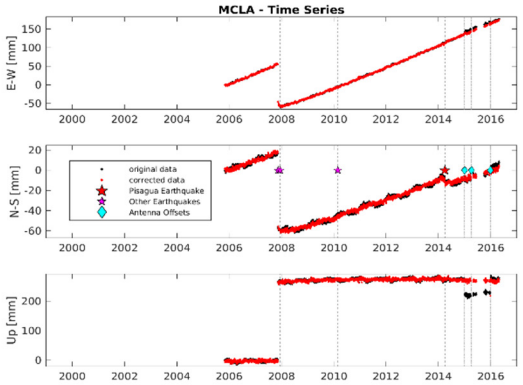
MCLA - Time Series
E-W [mm]
N-S [mm]
Up [mm]
original data
corrected data
Pisagua Earthquake
Other Earthquakes
Antenna Offsets

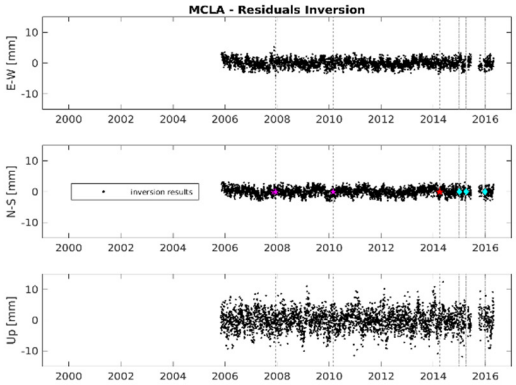
MCLA - Residuals Inversion
E-W [mm]
N-S [mm]
Up [mm]
inversion results

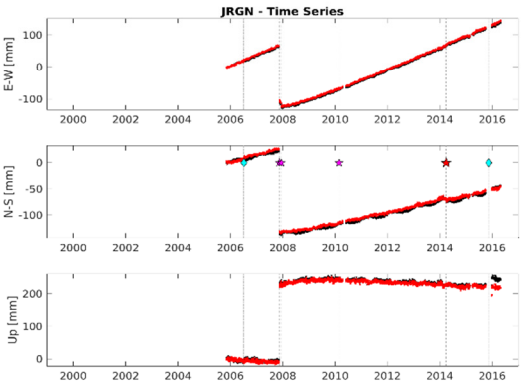
JRGN - Time Series
E-W [mm]
N-S [mm]
Up [mm]

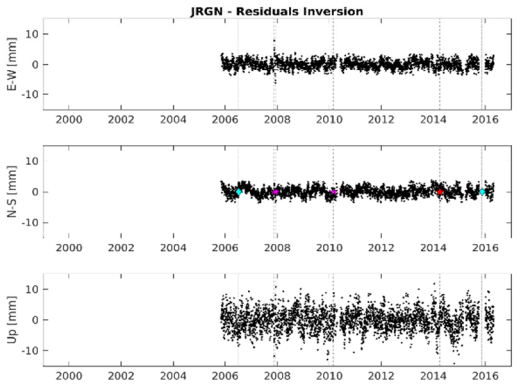
JRGN - Residuals Inversion
E-W [mm]
N-S [mm]
Up [mm]

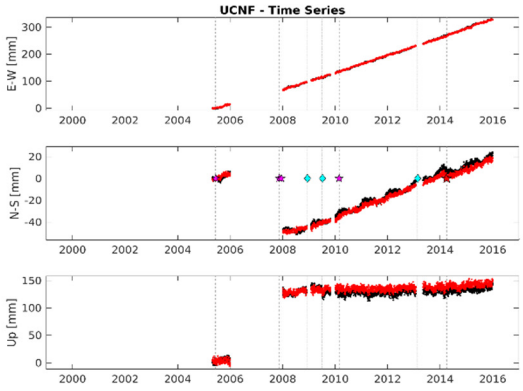
UCNF - Time Series
E-W [mm]
N-S [mm]
Up [mm]

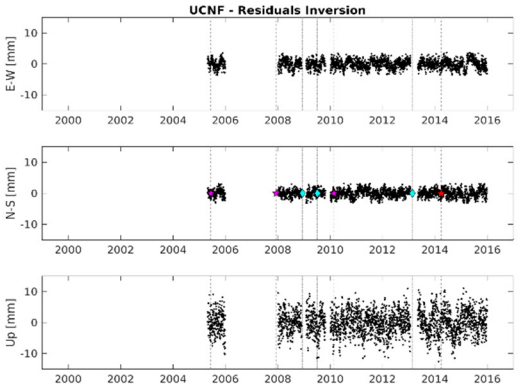
UCNF - Residuals Inversion
E-W [mm]
N-S [mm]
Up [mm]

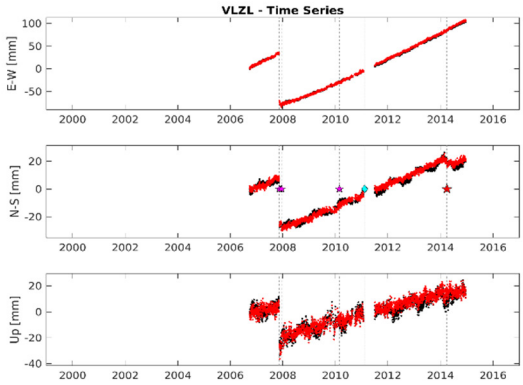
VLZL - Time Series
E-W [mm]
N-S [mm]
Up [mm]

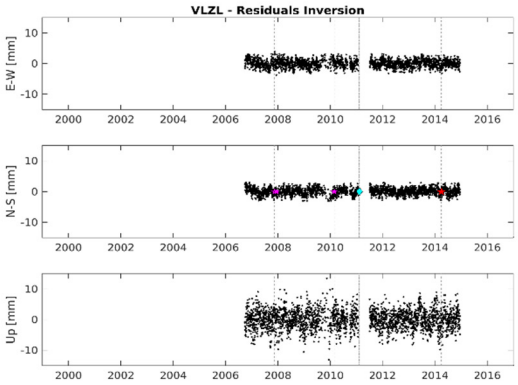
VLZL - Residuals Inversion
E-W [mm]
N-S [mm]
Up [mm]

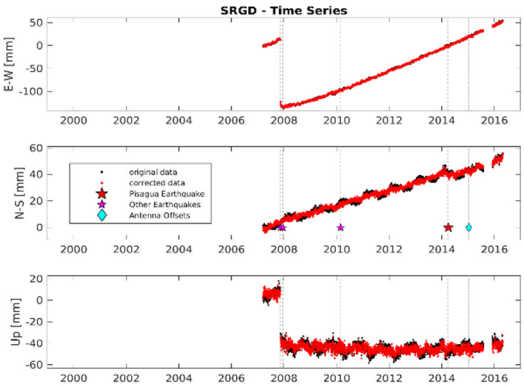
SRGD - Time Series
E-W [mm]
N-S [mm]
Up [mm]
original data
corrected data
Pisagua Earthquake
Other Earthquakes
Antenna Offsets

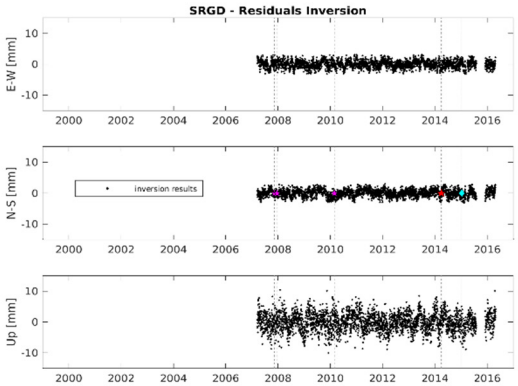
SRGD - Residuals Inversion
E-W [mm]
N-S [mm]
Up [mm]
inversion results

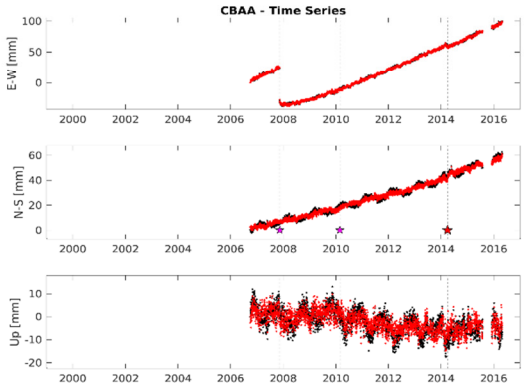
CBAA - Time Series
E-W [mm]
N-S [mm]
Up [mm]

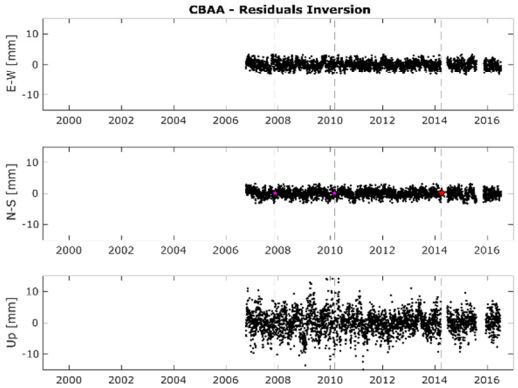
CBAA - Residuals Inversion
E-W [mm]
N-S [mm]
Up [mm]

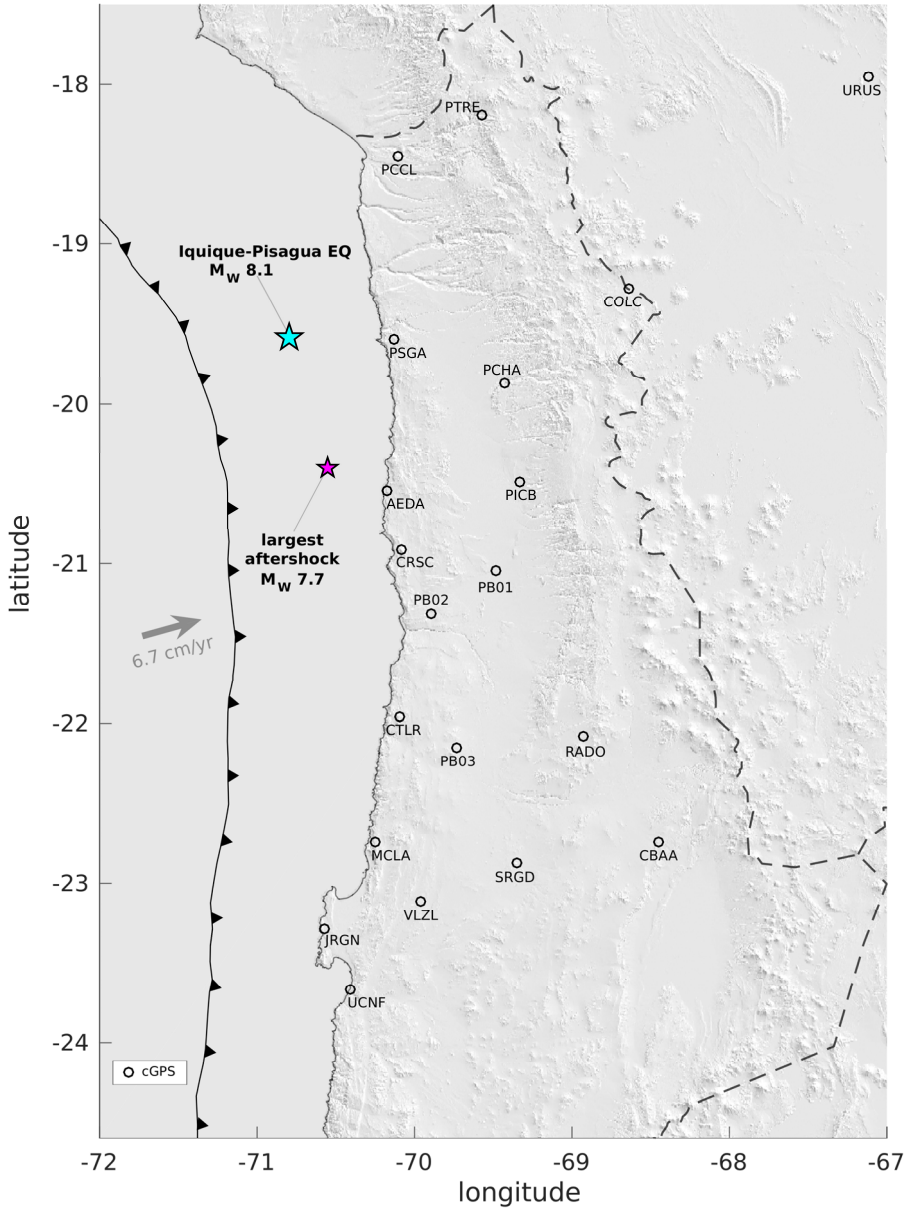

***Figure B.2**: Time series of the three components East, North and Up for a selection of cGPS stations, chosen on best spatial representation of the network that we use for our model approach (left panel) and corresponding time series inversion for all three components and signal contributions explained in the main text (right panel). The map shows the station locations.*

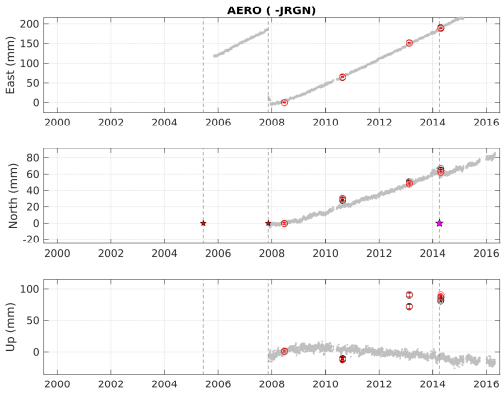
AERO (-JRGN)
East (mm)
North (mm)
Up (mm)

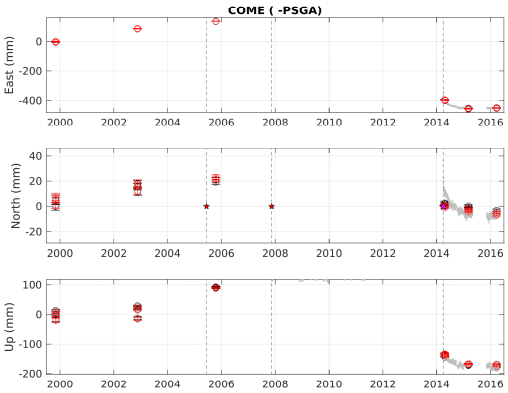
COME (-PSGA)
East (mm)
North (mm)
Up (mm)

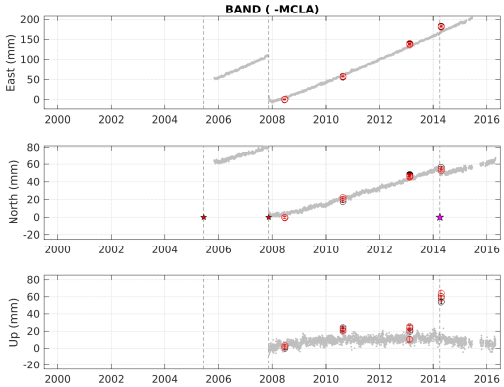
BAND (-MCLA)
East (mm)
North (mm)
Up (mm)

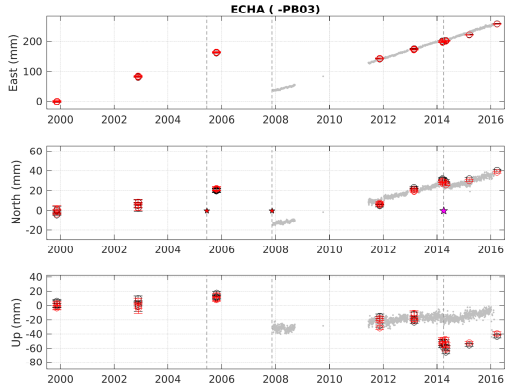
ECHA (-PB03)
East (mm)
North (mm)
Up (mm)

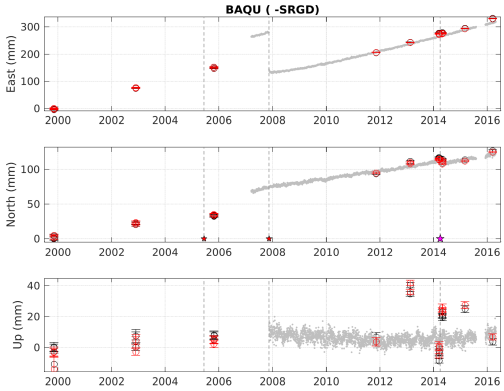
BAQU (-SRGD)
East (mm)
North (mm)
Up (mm)

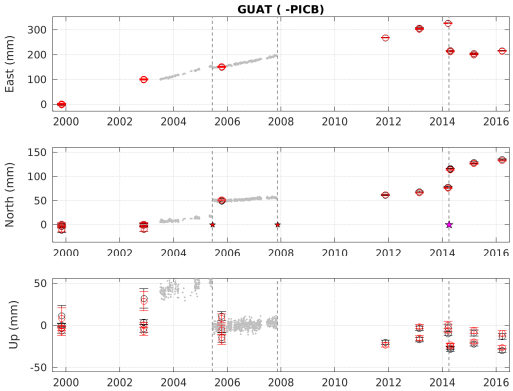
GUAT (-PICB)
East (mm)
North (mm)
Up (mm)

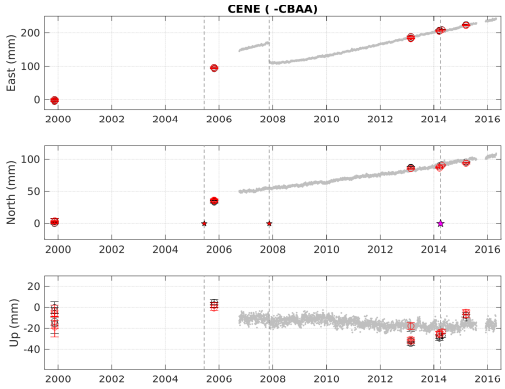
CENE (-CBAA)
East (mm)
North (mm)
Up (mm)

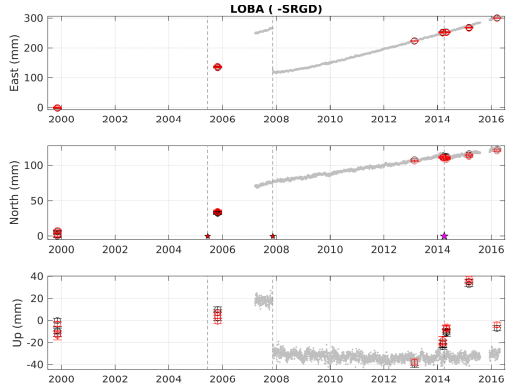
LOBA (-SRGD)
East (mm)
North (mm)
Up (mm)

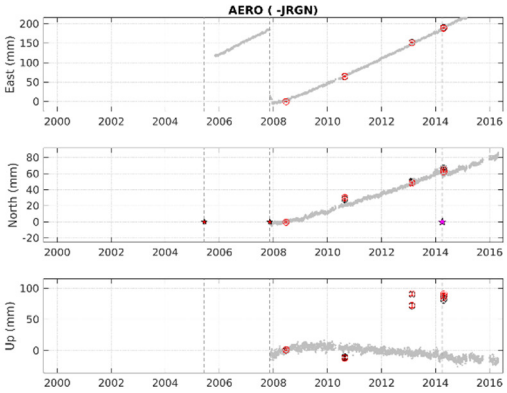
AERO (-JRGN)
East (mm)
North (mm)
Up (mm)

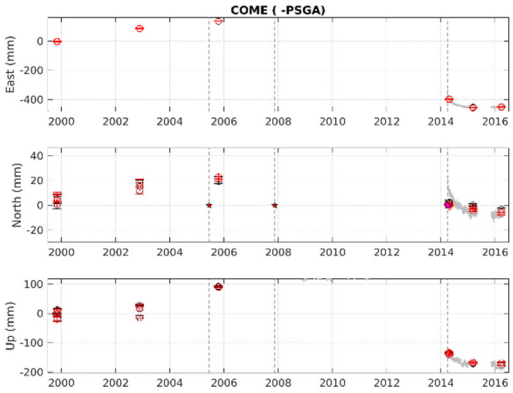
COME (-PSGA)
East (mm)
North (mm)
Up (mm)

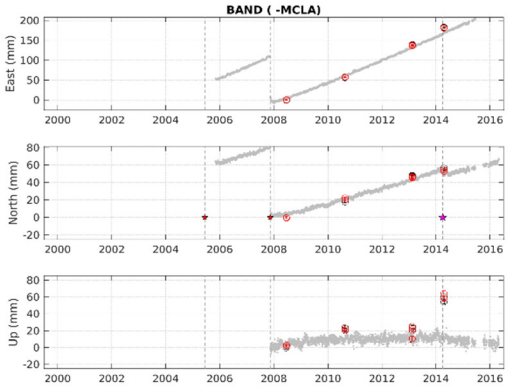
BAND (-MCLA)
East (mm)
North (mm)
Up (mm)

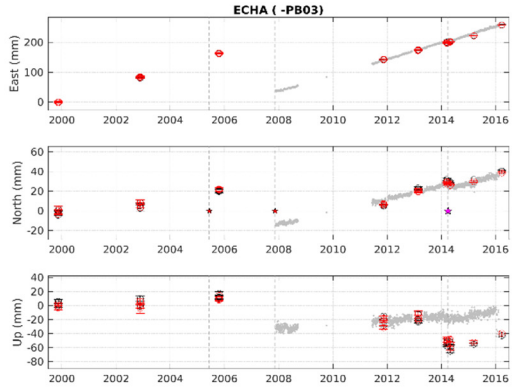
ECHA (-PB03)
East (mm)
North (mm)
Up (mm)

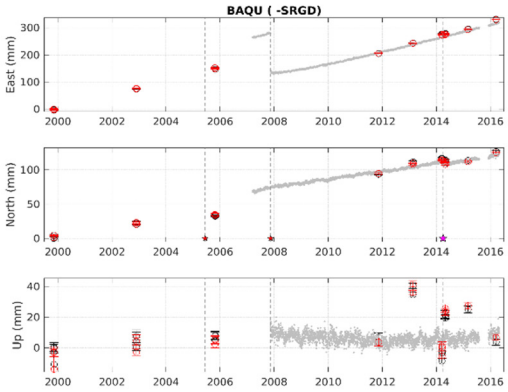
BAQU (-SRGD)
East (mm)
North (mm)
Up (mm)

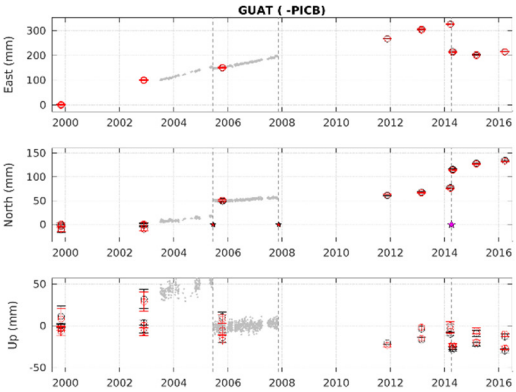
GUAT (-PICB)
East (mm)
North (mm)
Up (mm)

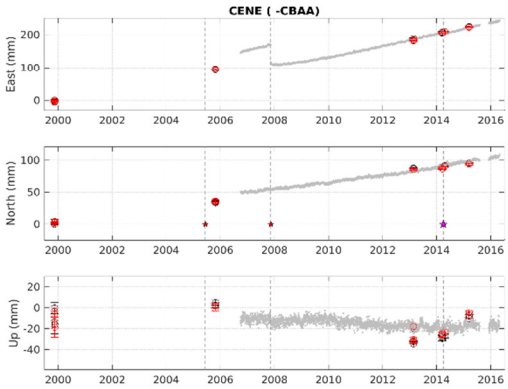
CENE (-CBAA)
East (mm)
North (mm)
Up (mm)

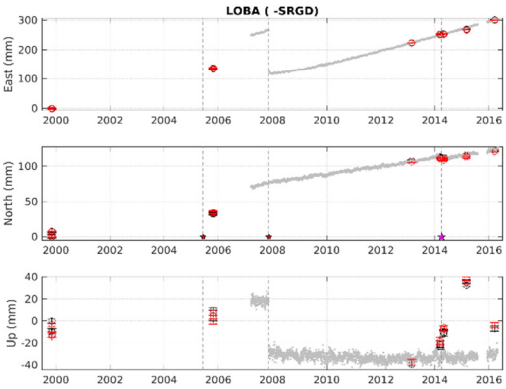
LOBA (-SRGD)
East (mm)
North (mm)
Up (mm)

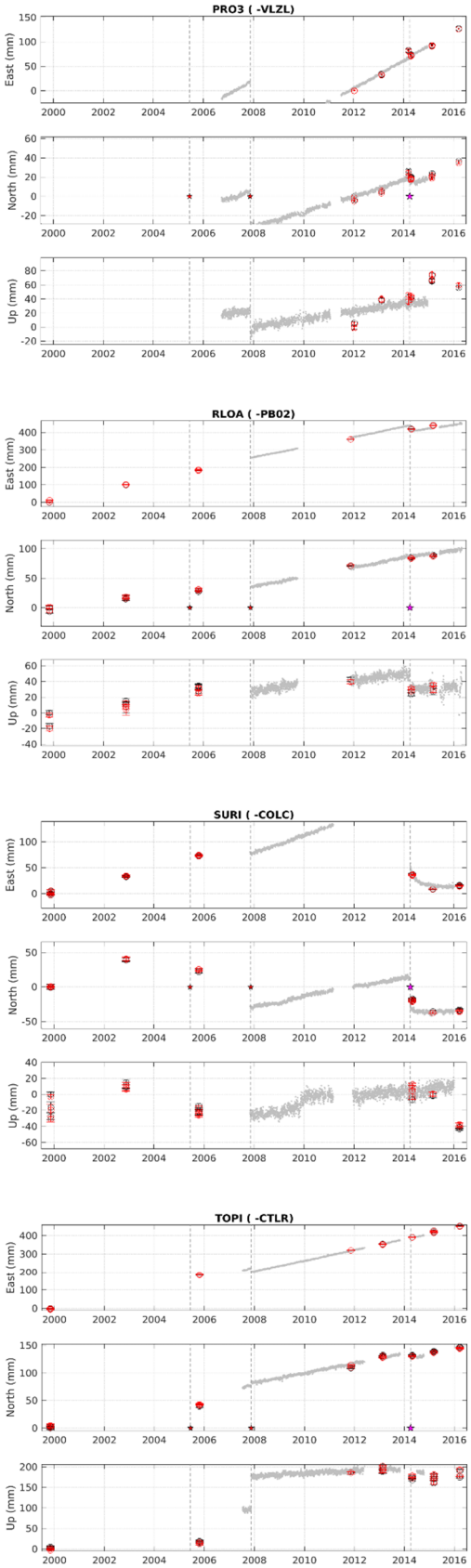

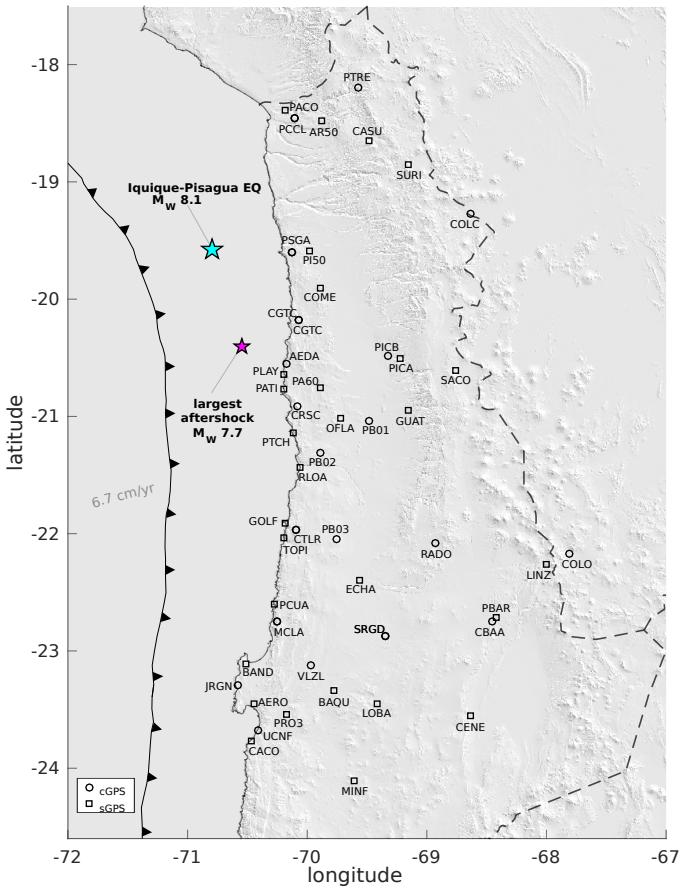

Figure B.3: *Time series of the three components East, North and Up for a selection of sGPS stations, chosen as best spatial representation of the network. Black circles are the original and red circles the corrected sGPS data. Campaign GPS data are jointly plotted with the closest cGPS ("twin"-) station to demonstrate their similarity. The map shows the station locations, including all "twin"-stations.*

Text B.1: GPS processing details

The data is processed in three steps (**Figure 2.2**) using the EPOS software (*Gendt et al., 2013*). First, a precise point positioning (PPP) is applied to all GPS stations using updated GPS satellite clock and orbit products (*Deng et al., 2016*). After outlier removal, the single station PPP coordinate results have an accuracy of ~1-2 cm (GFZ_PPP solution). The second step applies a network algorithm to these apriori solutions. The total number of South American GPS stations exceeds 800 stations, so we processed about 250 stations at once in several sub-network approaches. For each sub-network, we include 56 densely distributed IGS stations (**Figure B.4**). All stations are weighted equally and no station position is fixed (free network solution). The datum of the coordinate solution is defined by the International Terrestrial Reference Frame 2008 (ITRF2008) to yield the GFZ_NET solution. Finally, the network solutions are aligned to the International GNSS service (IGS) reprocessing combined daily coordinate product in ITRF2014 (*Rebischung et al., 2015*; *Altamimi et al., 2016*) to reduce the impact of a datum effect. The final coordinates have an accuracy of a few millimeters (GFZ_NT2 solution).

A detailed list of applied models and algorithms is given below:

Observation data:

- Ionosphere-free linear combination, indifference carrier phase and pseudo-range observables
- Sampling rate: 5 minutes
- Elevation cut-off angle: 7°
- Elevation depended weighting: ½*sin(e) for elevation e < 30°

External models used in the processing:

- Updated satellite and ground antenna phase center offsets and phase center variations in IGS08_XXXX.ATX file
- Ocean tide loading: FES2004 (*Lyard et al., 2006*)
- Atmosphere pressure tide loading effects: International Earth Rotation and Reference Systems (IERS) Conventions 2010 (*Petit & Luzum, 2010*)
- Troposphere: a priori zenith delay from *Saastamoinen* (*1973*), Global Pressure and Temperature model (GPT2) and Vienna Mapping Function (VMF) (*Boehm et al., 2009*; *Lagler et al., 2013*)
- Ionosphere: include second order ionosphere correction

Reference frames:

- Terrestrial: IGS realization of ITRF2008/ITRF2014 (*Altamimi et al., 2016*)
- IAU 2000A Precision-Nutation model (*Capitaine et al., 2005*)
- Earth Orientation Parameters (EOP) are constrained as a priori values (Bulletin A)

Estimated parameters (Least Square):

- Station coordinates of stations
- Receiver clocks per epoch
- Troposphere: Zenith delay estimation (ZTD) per hour, gradients per 24 h
- Ambiguities: fixed
- Earth rotation parameters (ERP): pole coordinates and rates, length of day (LOD)

Figure B.4: *Location of 56 reference stations used to tie the GPS network solution to the ITRF2014 daily coordinate solution.*

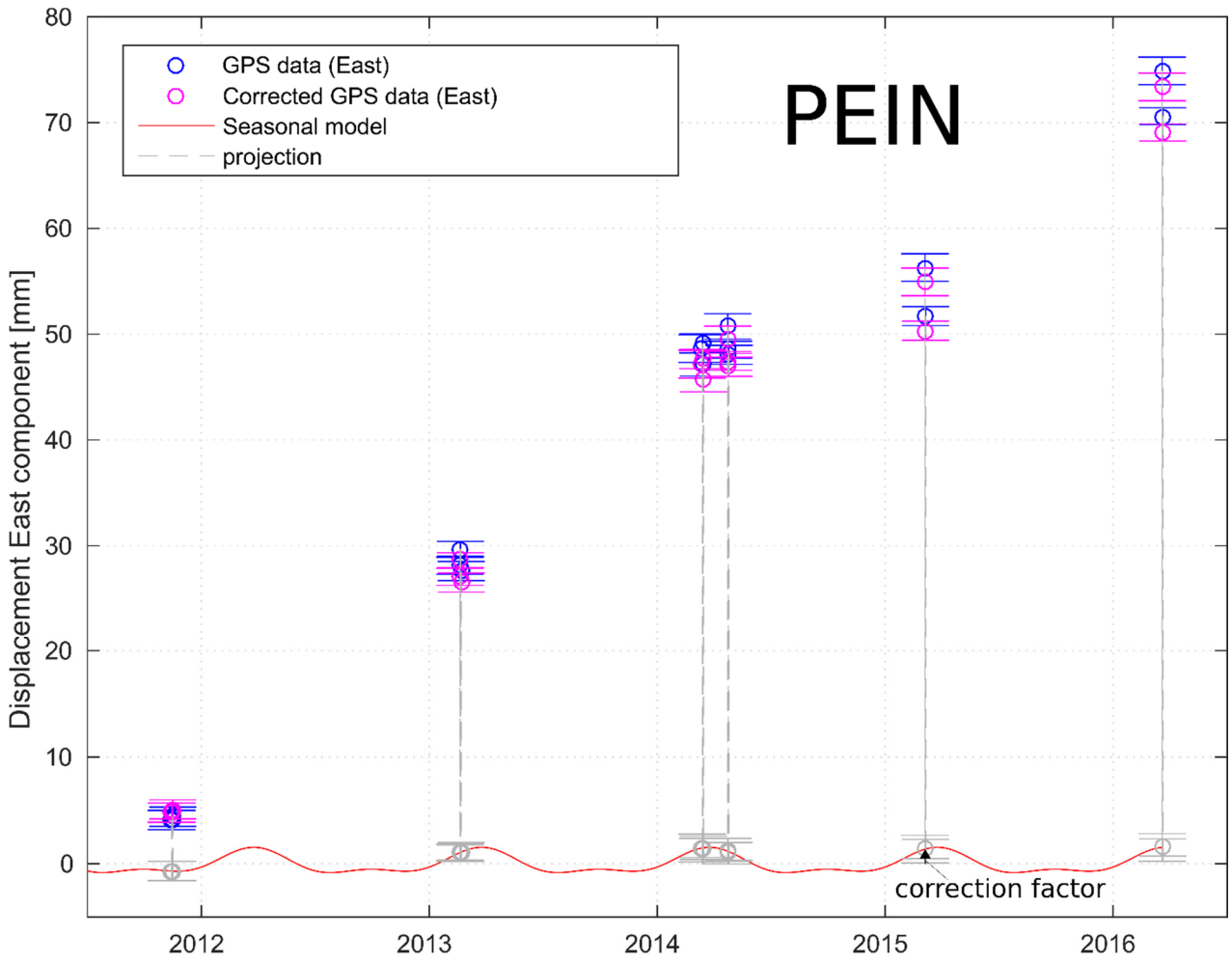

Figure B.5: *Original (blue) and corrected (magenta) East component of sGPS station PEIN after applying the seasonal model (red). Grey circles represent the projection of the measurements onto the seasonal model. The correction factor for the 2015 campaign data (black arrow) illustrated that the seasonal signal affects each campaign subset differently by about 1 to 5 mm, if not measured at the same period each year.*

Text B.2: Details on the visco-elastic model

Three dimensional visco-elastic simulations were performed using the PyLith software (*Aagaard et al., 2013*). We model the surface deformation component caused by post-seismic visco-elastic mantle relaxation using a finite element model (FEM), consisting of four blocks with different material properties: (1) an elastic continental plate with a mean thickness of 45 km, (2) an elastic oceanic plate with a mean thickness 30 km, (3) a viscoelastic continental mantle, and (4) a viscoelastic oceanic mantle (**Figure A.10**). Our model is about 2500 km in the E-W direction, 1100 km in the N-S direction, and 500 km in the vertical direction to make sure that the boundaries are sufficiently far away from our study area (**Figure A.10**). The model mesh consists of over 10^6 elements. For cumulative displacements at short time periods, we used a Maxwell (linear) rheology to model the spatial pattern of postseismic displacements and estimate an effective viscosity. Recent studies, however, have used a more complex, transient rheology, e.g. bi-viscous Burgers rheology (e.g. *Trubienko et al., 2013*; *Klein et al., 2016*) to model the temporal decay in postseismic GPS time series. As we are only interested in fitting the cumulative postseismic displacement during specific time periods, we use a linear Maxwell rheology in the viscoelastic bodies, see also *Li et al. (2017)* and *Bedford et al. (2016)*. The component of the visco-elastic mantle response was combined with the elastic inversion of afterslip to account for viscous processes contributing to post-seismic deformation (more details can be found in section 3.4.1).

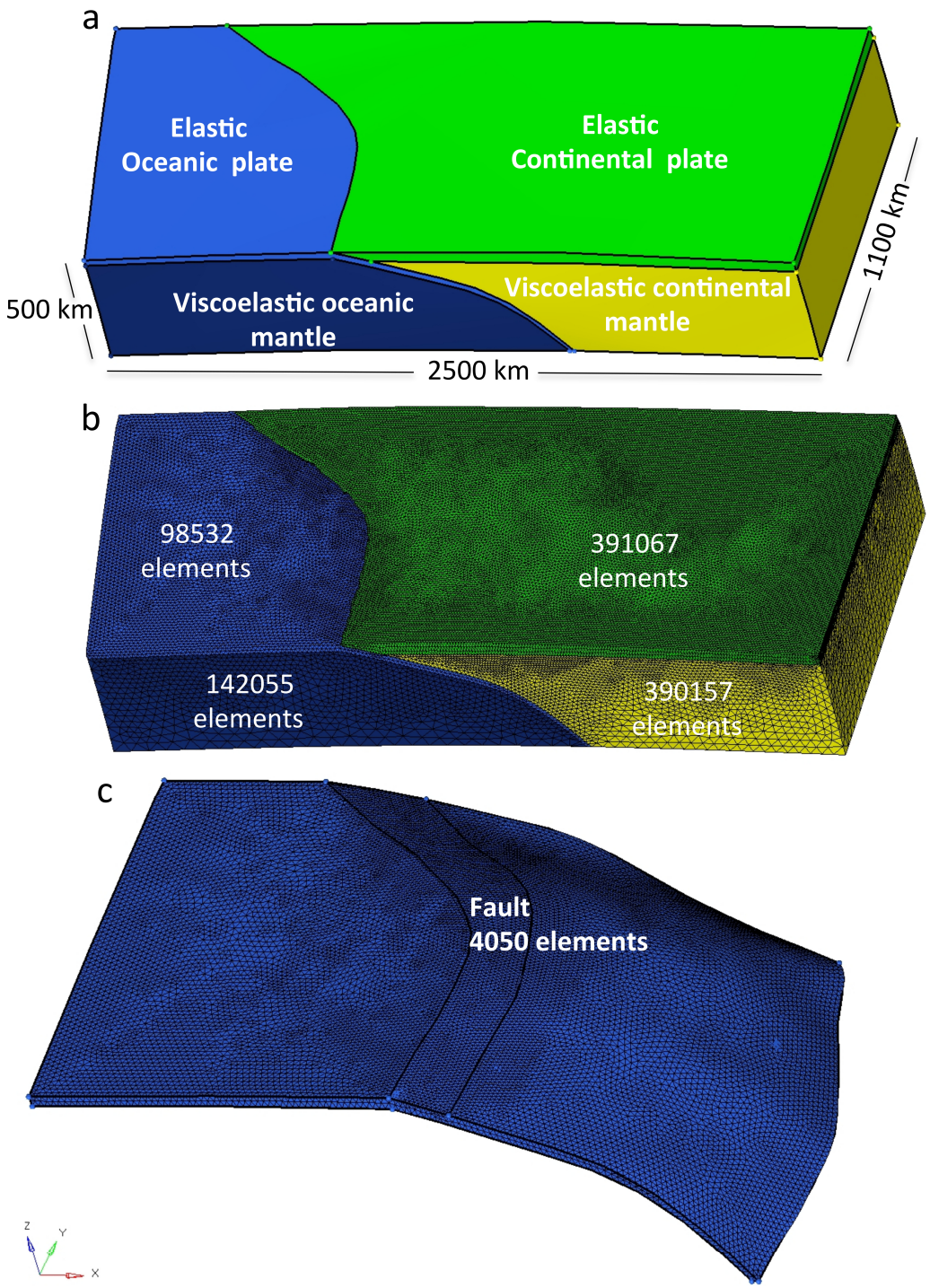

Figure B.6: *Model set up in the Pylith software for determining the contribution of visco-elastic mantle relaxation to the overall postseismic ground displacement. a) Geometry and b) finite-element mesh of the four block subduction geometry and c) geometry and mesh of the subduction plate interface. The geometry is based on the SLAB 1.0 plate interface model (Hayes et al., 2012) and the Moho of Tassara & Echaurren (2012).*

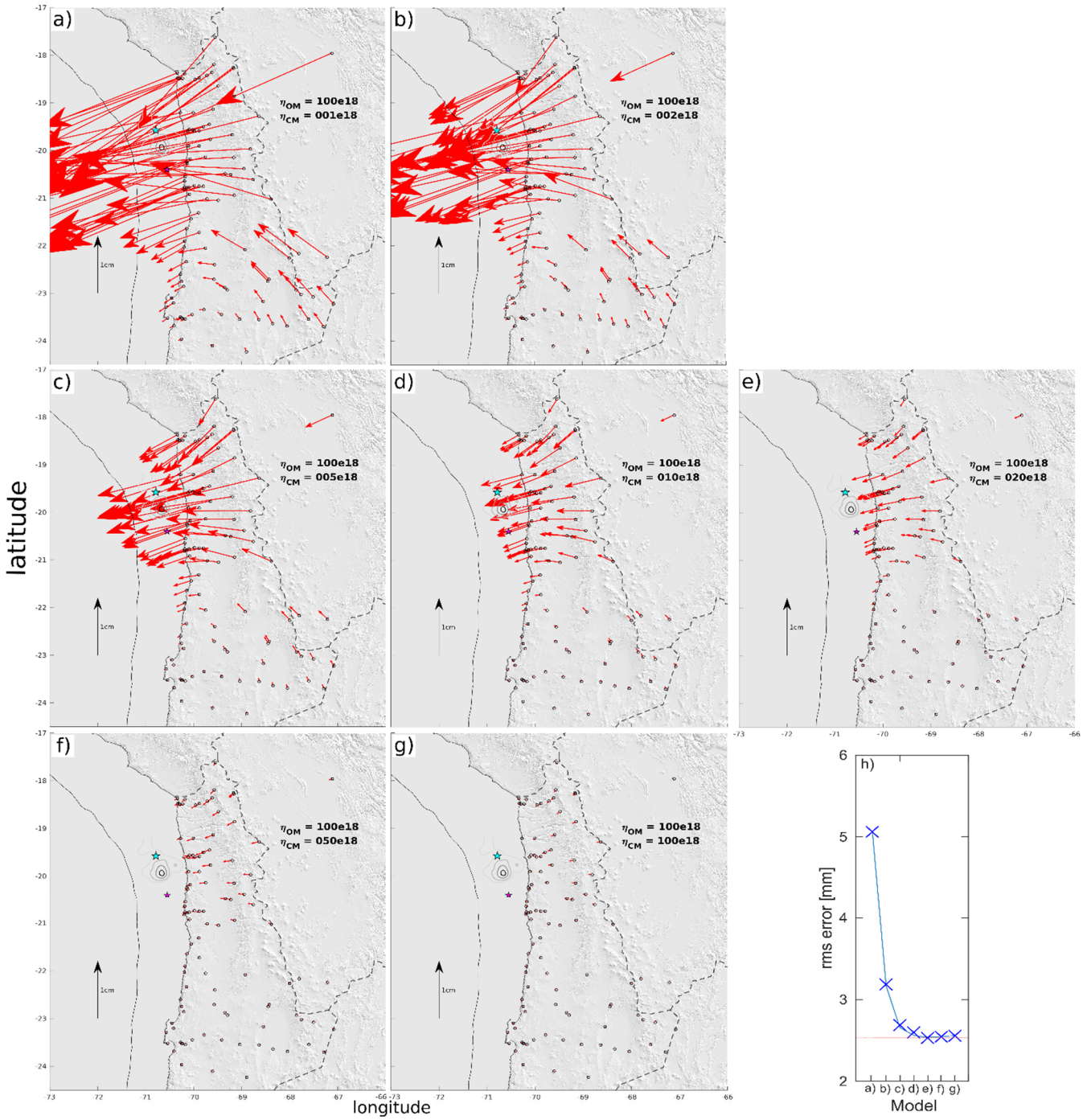

Figure B.7: *a)-g) Predicted horizontal visco-elastic mantle relaxation of Period 2 for different continental mantle viscosities η_{CM} ranging from 1 x 10^{18} to 100 x 10^{18} Pa s, while oceanic mantle viscosity η_{OM} was fixed to 100 x 10^{18} Pa s. h) Trade-off curve between best fit (rms error) and viscosity of the continental mantle. The best fit is observed at η_{CM} = 2 x 10^{19} Pa s (subfigure e).*

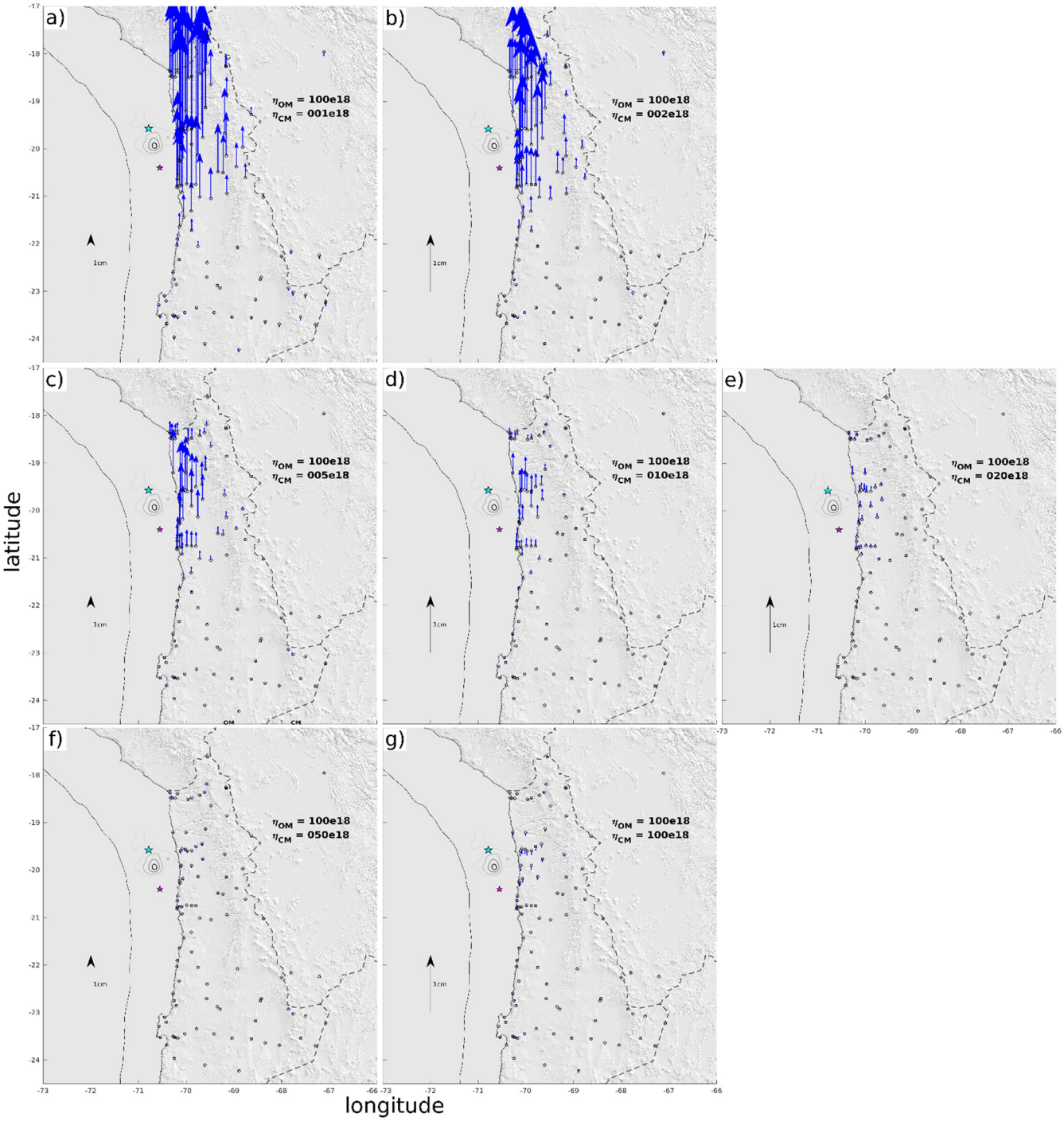

Figure B.8: a)-g) Predicted vertical visco-elastic mantle relaxation of Period 2 for different continental mantle viscosities η_{CM} ranging from 1 x 10^{18} to 100 x 10^{18} Pa s, while oceanic mantle viscosity η_{OM} was fixed to 100 x 10^{18} Pa s.

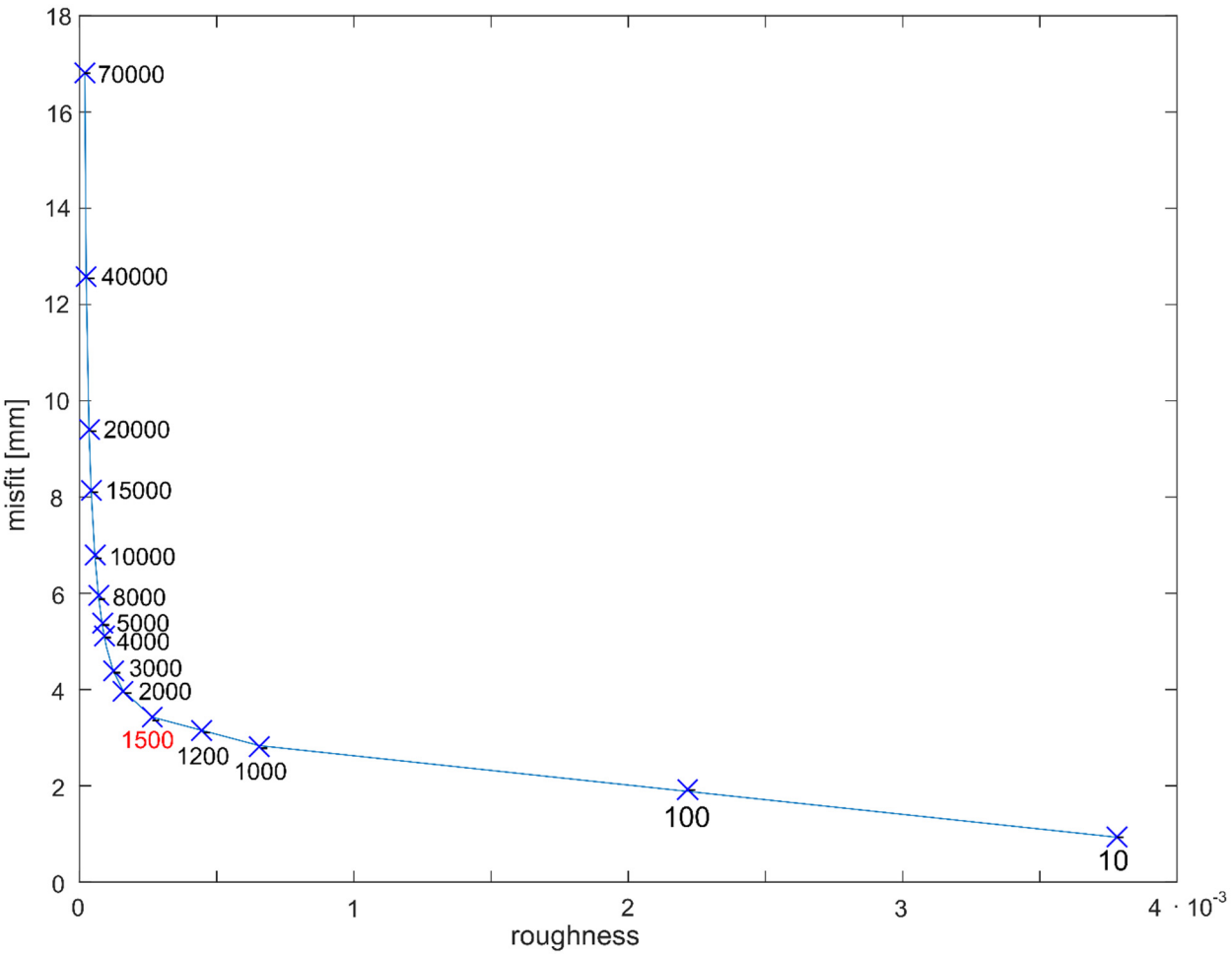

Figure B.9: *Trade-off curve between roughness and misfit (in mm) of the interseismic model, using different smoothing values, the preferred one indicated in red. For the postseismic models we used a smoothing of 800 (Period 1), 1200 (Period 2) and 1000 (Period 3), respectively. Misfit and roughness were calculated based on Menke (2012):*

$$misfit = (G \cdot \mathrm{X}) - data$$

, where G are the Greens functions and X is the modelled slip and

$$roughness = [DX]^T \cdot [DX]$$

, where D is the roughness matrix defined in Menke (2012).

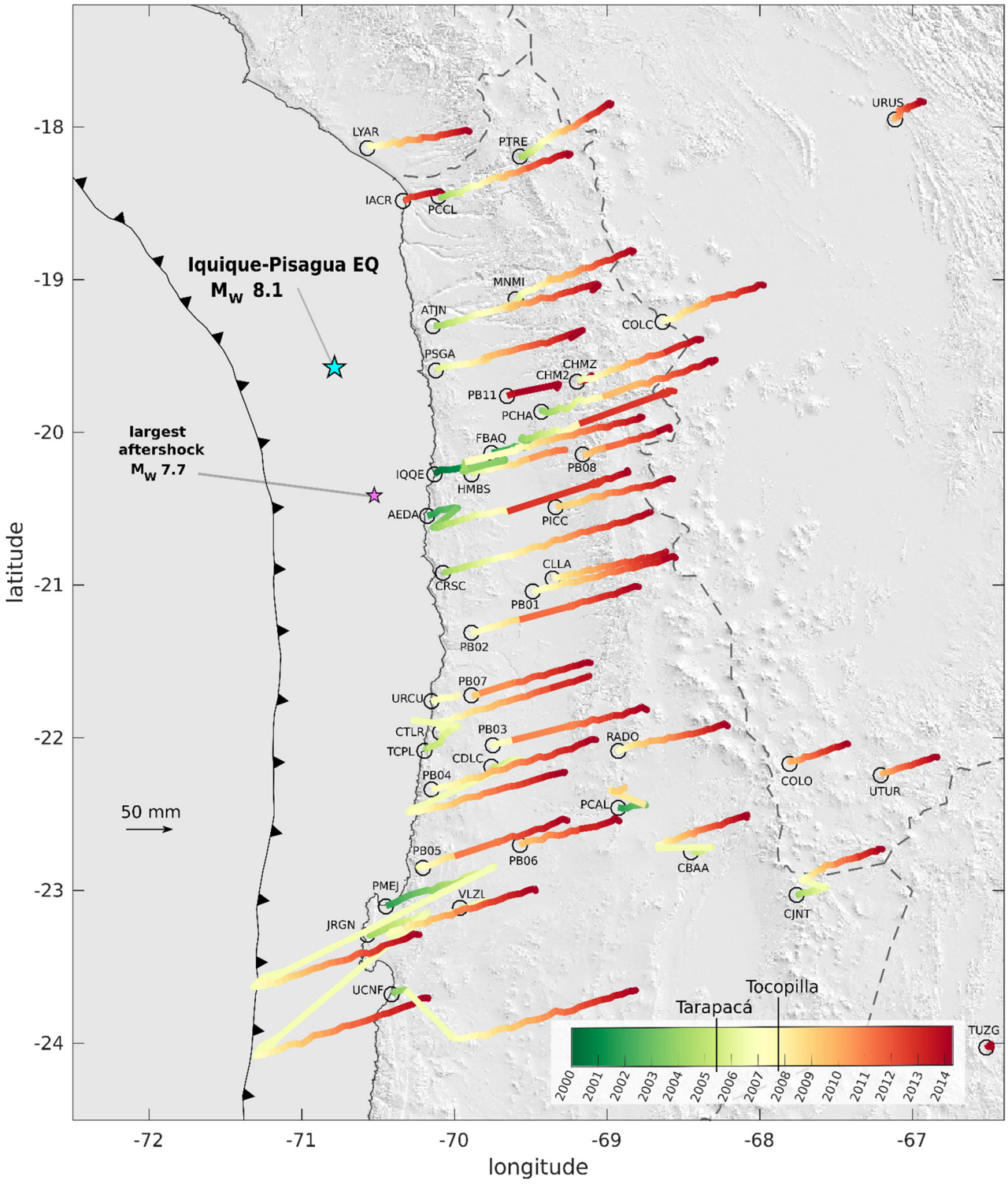

Figure B.10: *Temporal evolution (color-coded by time in years) of the interseismic ground displacement (sampled by 90 days) of cGPS stations in our network. Note that the 2005 Tarrapaca and the 2007 Tocopilla earthquake clearly influenced ground displacements of several GPS stations. For other features see Figure 3.4 in the main text.*

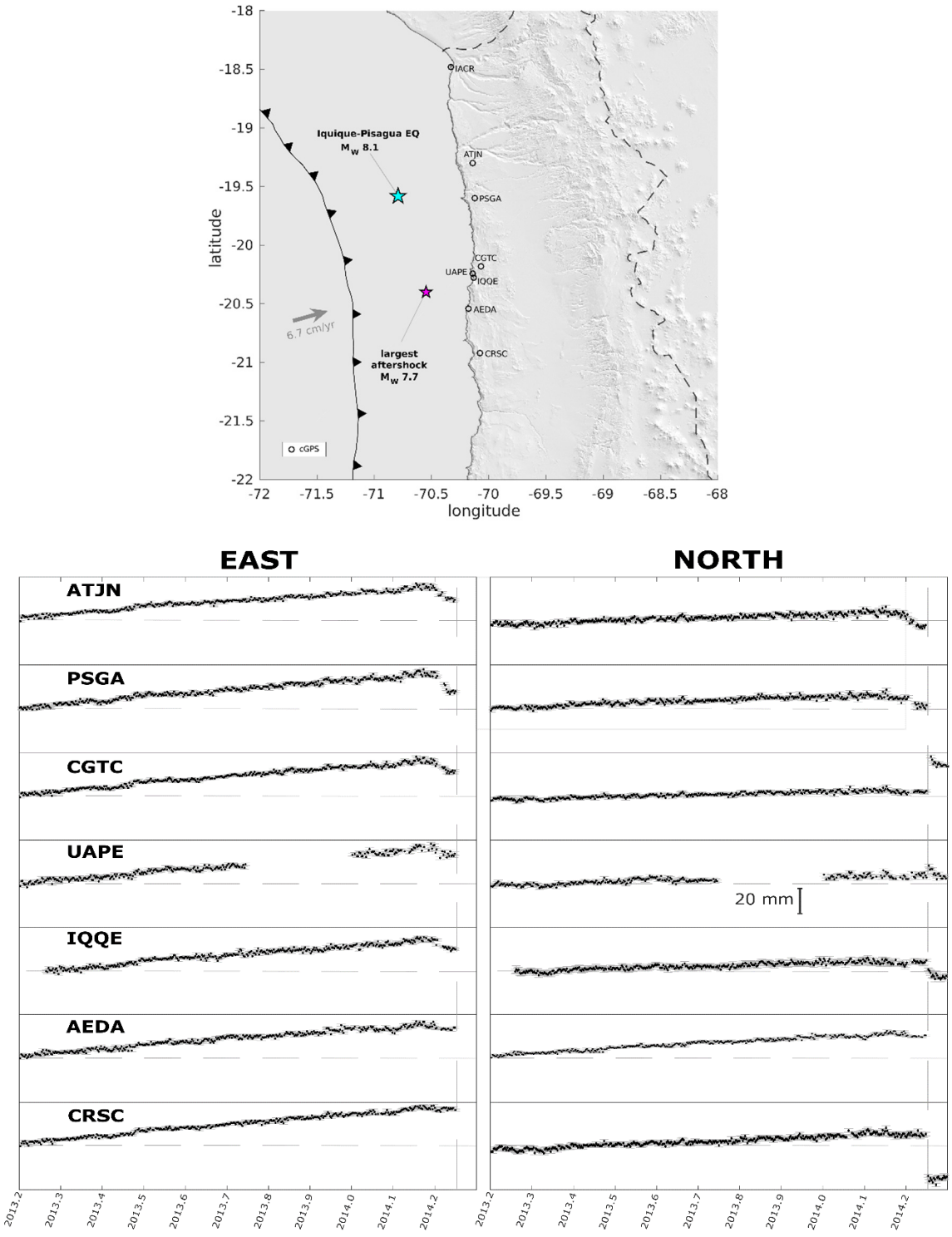

Figure B.11: *Ground deformation transients for coastal cGPS stations for East (left) and North (right) components after the large M_w 6.7 foreshock on 16 March 2014. The station and earthquake locations are indicated in the map.*

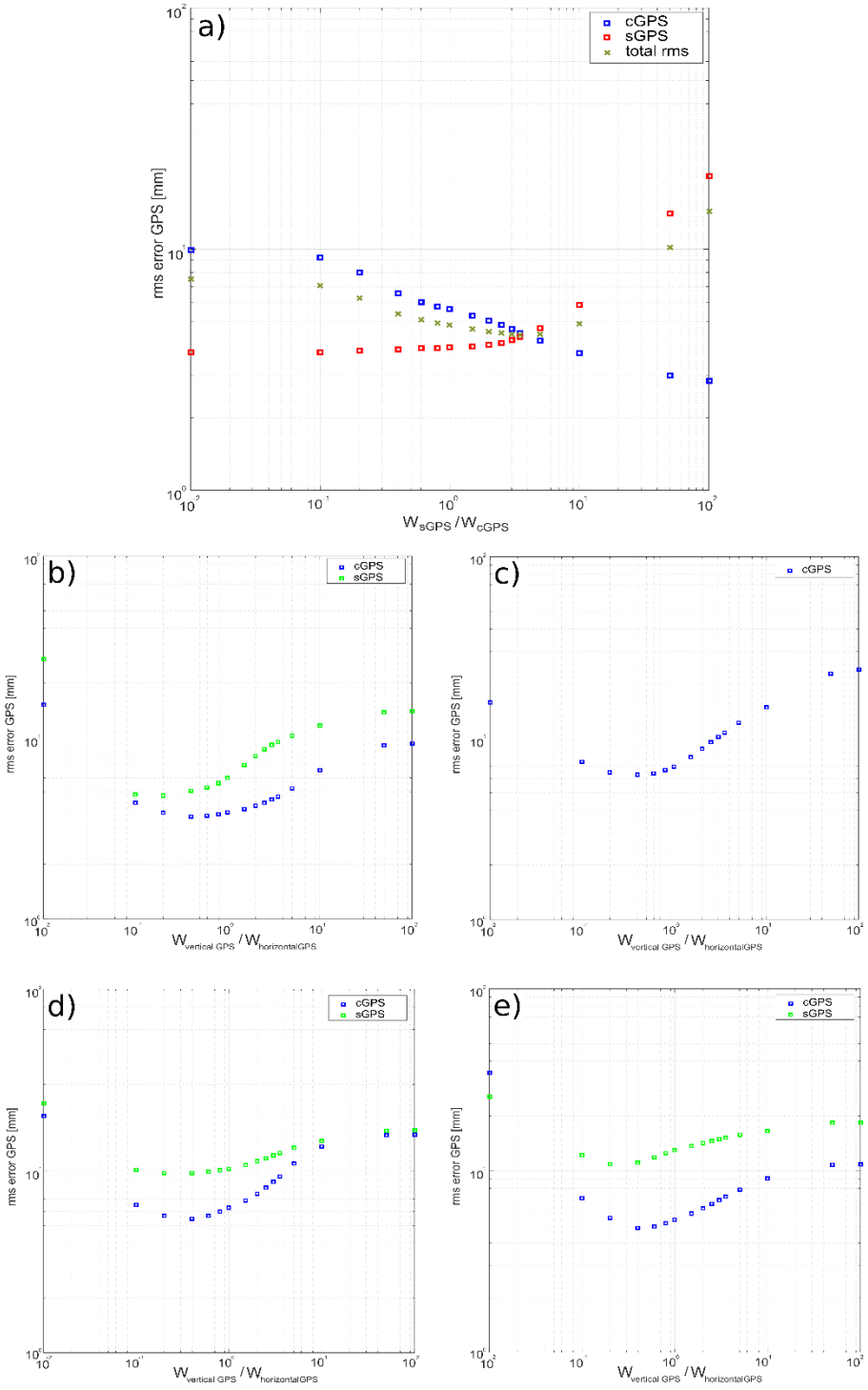

Figure B.12: *a) Following the weighting approach of Cavalié et al. (2013) for different input data types, we tested various weighting factors w in a range of 10^{-2} to 10^{2}, where $w = w_{sGPS}/w_{cGPS}$ is the ratio of sGPS to cGPS weight. The best-fit (based on the rms-error) for the interseismic period is obtained with a weighting factor of 2.5. The optimal weighting factor differs from one model period to another, since the spatial distribution of the input data varies. Best-fit ratios of w_{sGPS}/w_{cGPS} are 2.5 (interseismic model), 2.0 (Period 2 model) and 1.5 (Period 3 model).*
b)-d) Weighting factors between the vertical and horizontal GPS data for interseismic period (b), Period 1 (c), Period 2 (d) and Period 3 (e). Overall, the best-fit is obtained, when weighting the vertical cGPS components five times less and the sGPS vertical components ten times less than the corresponding horizontal data.

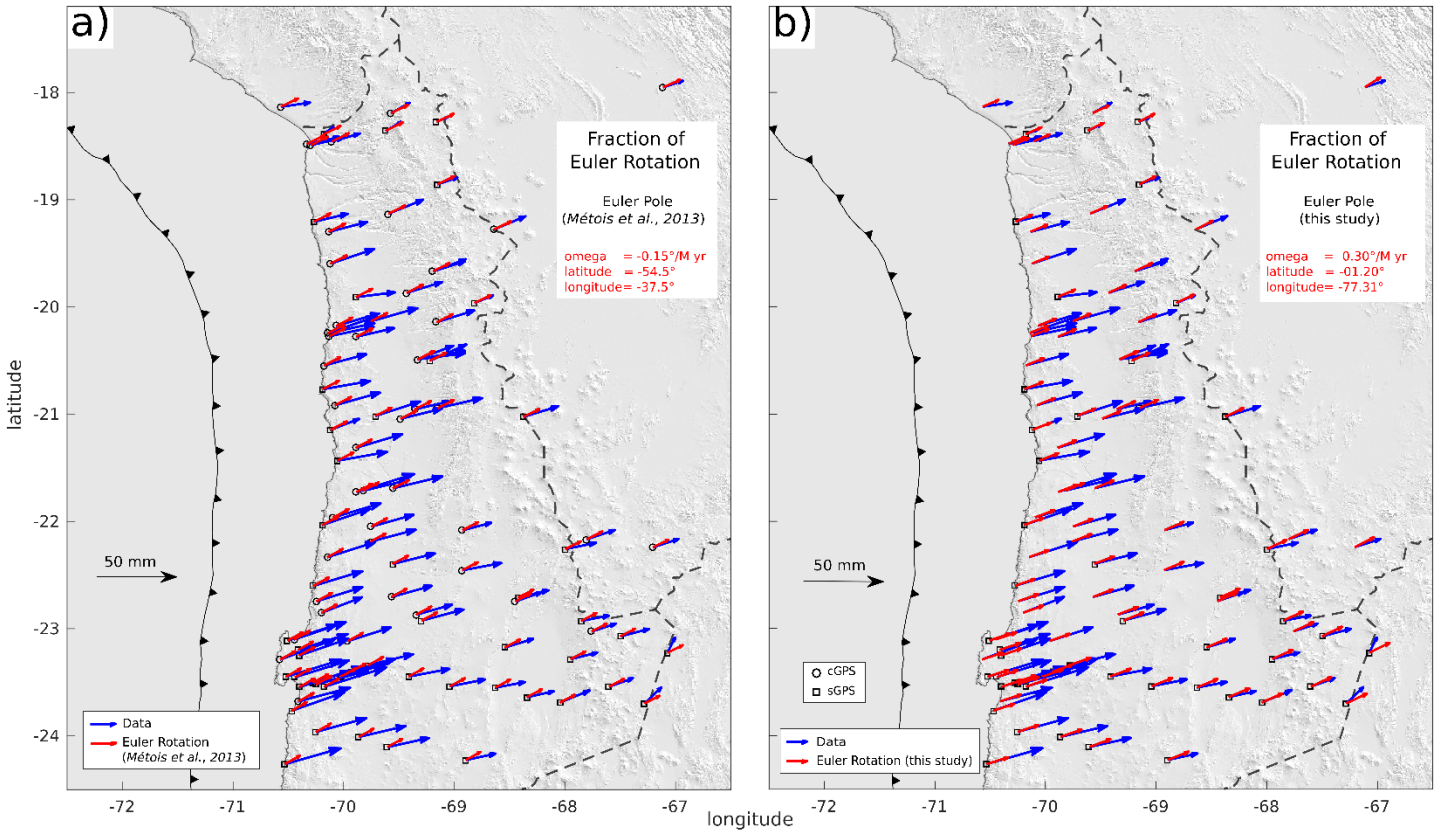

Figure B.13: *GPS rates (blue) and their corresponding component of Andean sliver motion (red) using a) the Euler Pole from Métois et al. (2013) and b) the one from our own inversion, showing insignificant differences. Details on the poles are indicated in the legend. For other features see Figure 3.4 in the main text.*

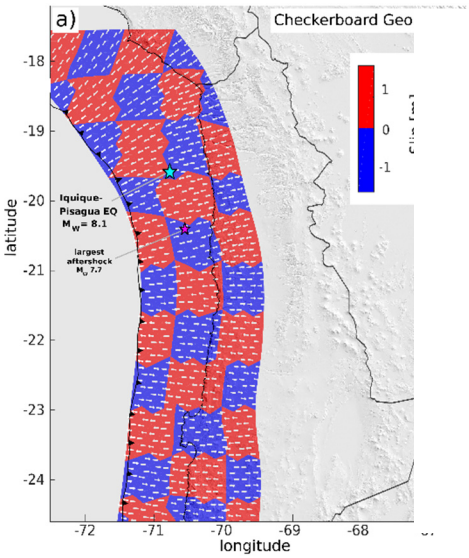

Figure B.14:
Checkerboard resolution tests for the different model periods.
a) Original input data with slip and backslip of +/-1 m, and inversion results of
b) the interseismic period,
c) of model Period 1,
d) of model Period 2 and
e) of model Period 3.
For other features see Figure 3.4 in the main text.

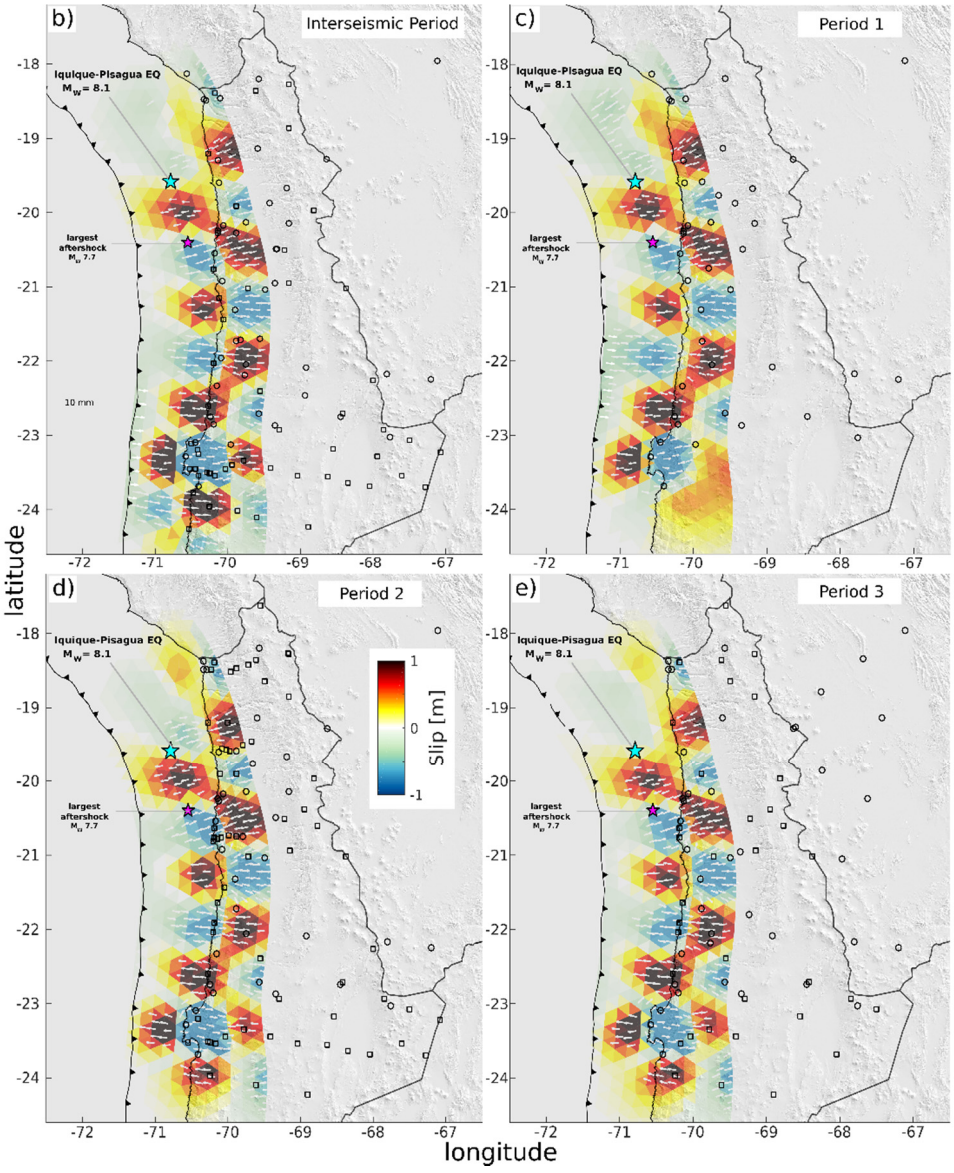

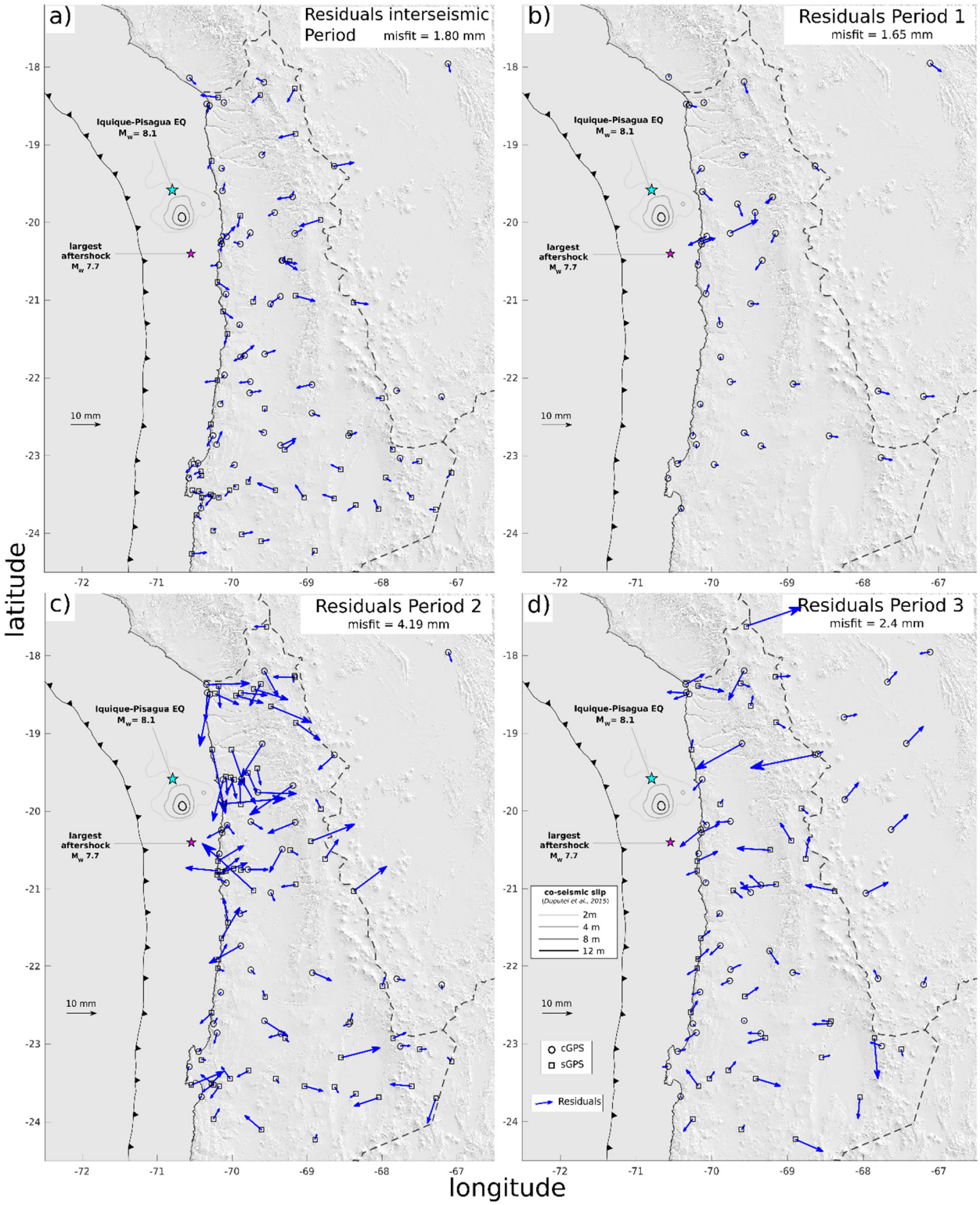

Figure B.15: *Horizontal residuals between the observed data and the predicitions of a) the interseismic model, b) Period 1, c) Period 2 and d) Period 3 model. The misfit indicated in the legend is the averaged rms-misfit of all stations in the respective model. For other features see Figure 3.4 in the main text.*

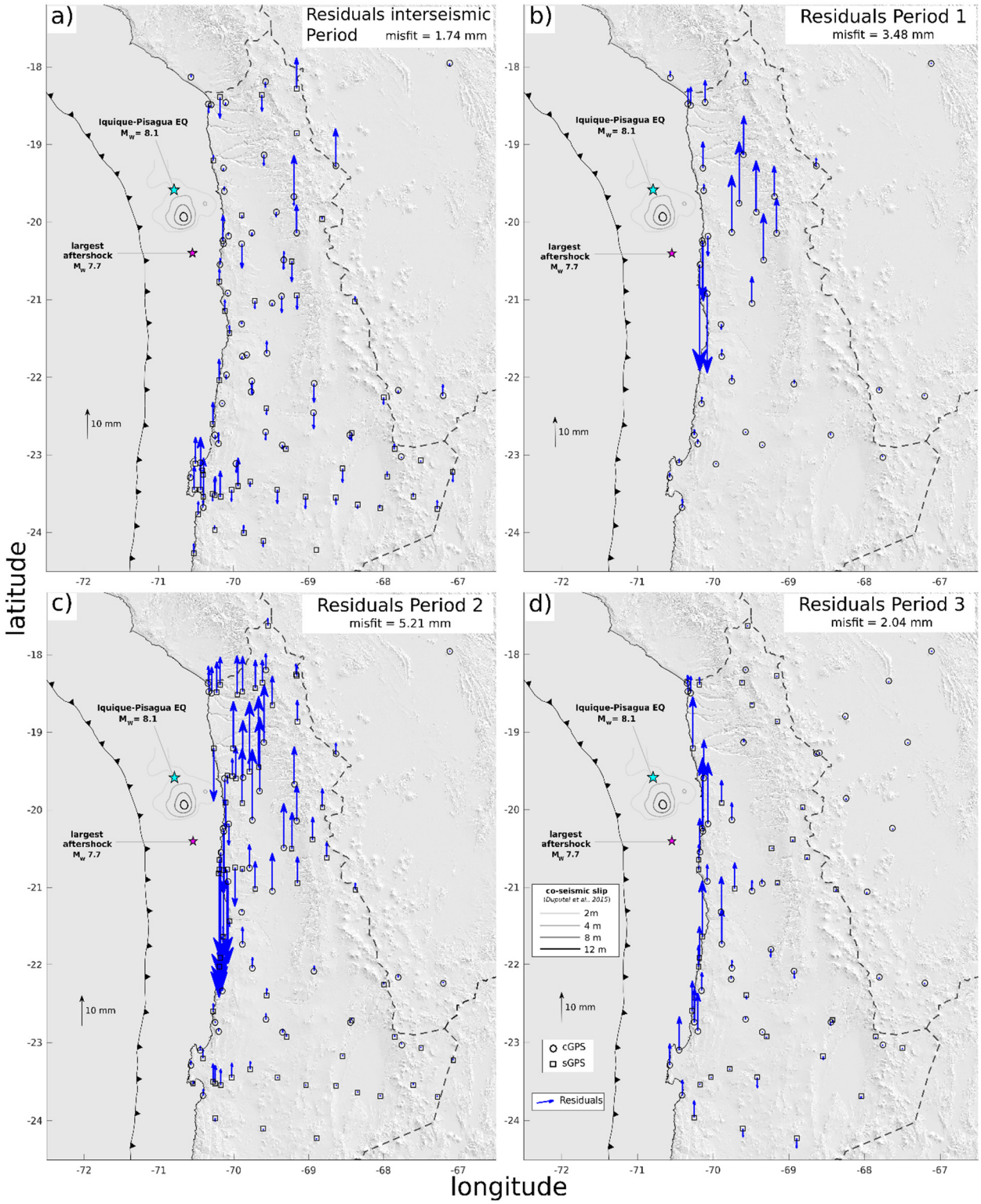

Figure B.16: *The vertical residuals between the observed data and the predictions of a) the interseismic model, b) Period 1, c) Period 2 and d) Period 3 model. The misfit indicated in the legend is the averaged rms-misfit of all stations in the respective model. For other features see Figure 3.4 in the main text.*

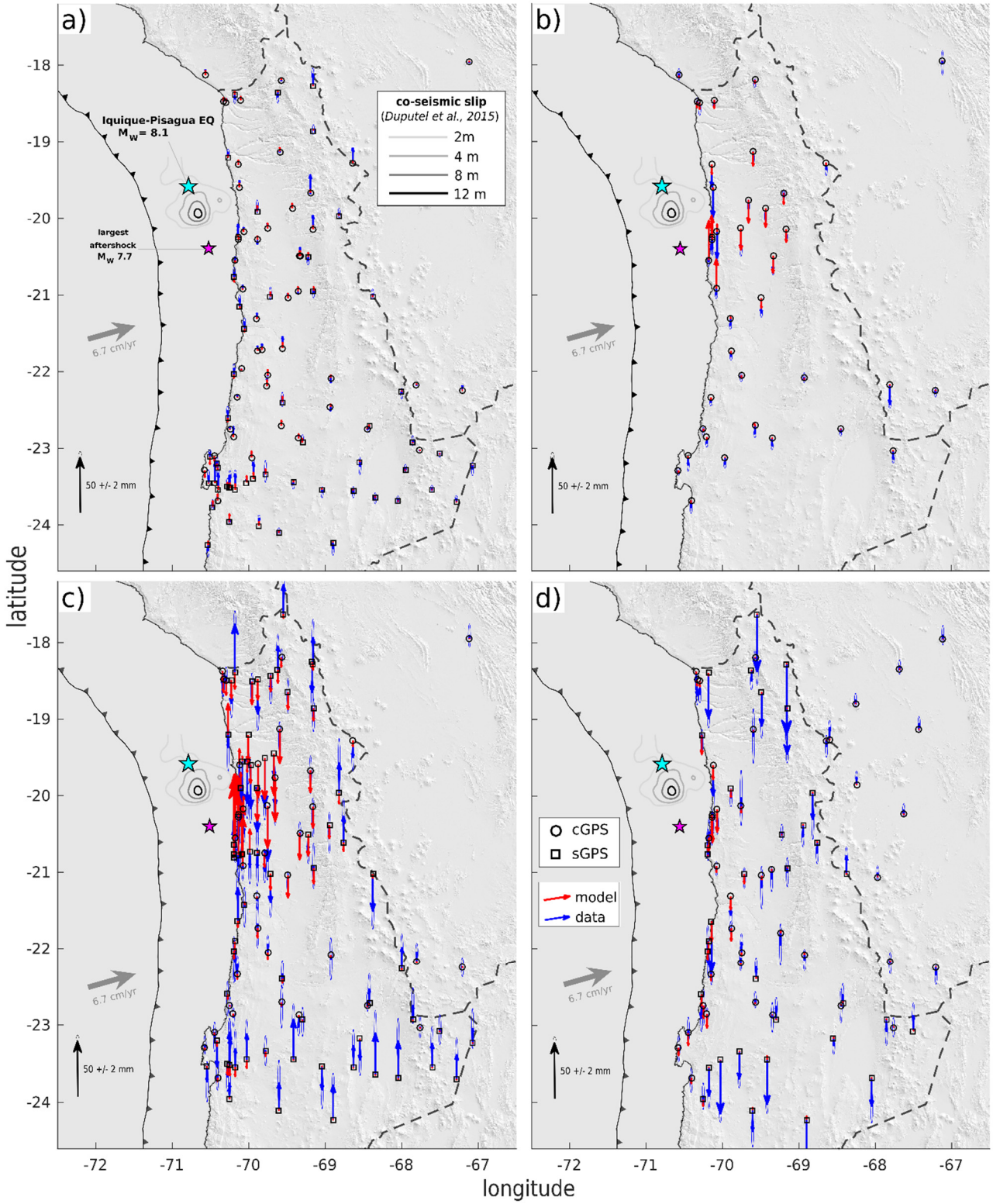

Figure B.17: *Vertical GPS components of a) the interseismic model, b) Period 1, c) Period 2 and d) Period 3, with observations in blue and respective model predictions in red. For other features see Figure 3.4 in the main text.*

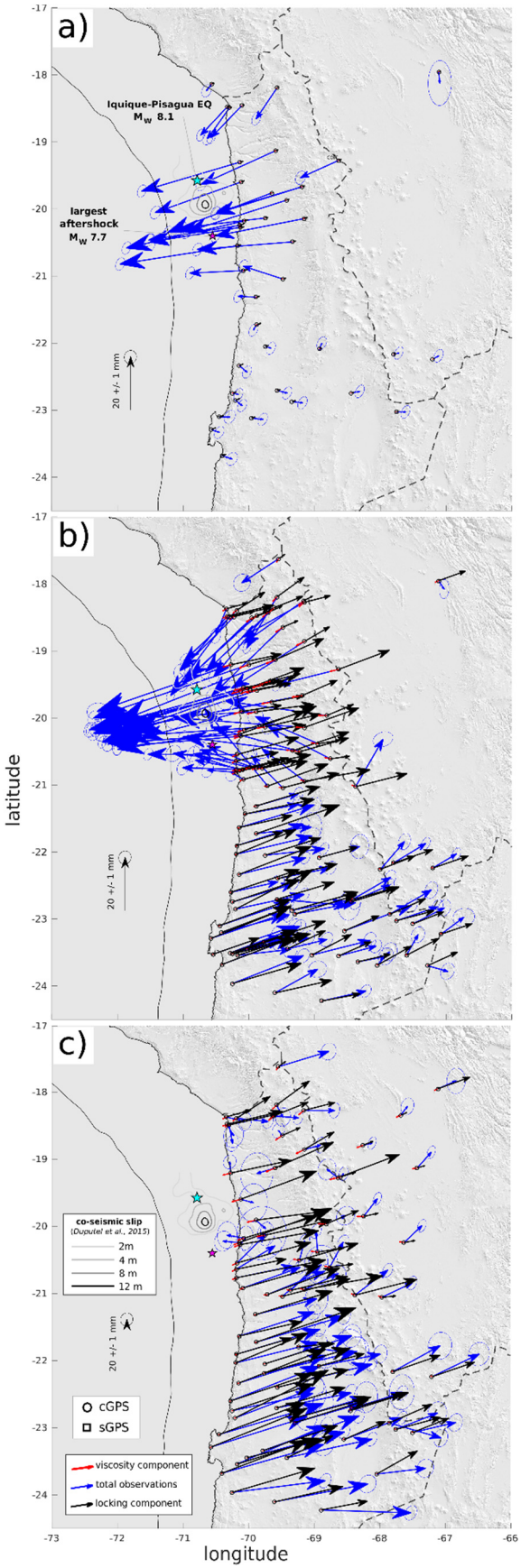

Figure B.18: *Modelled partition of the observed GPS displacement signal (blue) into interseismic locking (black) and the viscoelastic relaxation (red) for a) Period 1, b) Period 2 and c) Period 3. For other features, we refer to Figure 3.4 in the main text.*

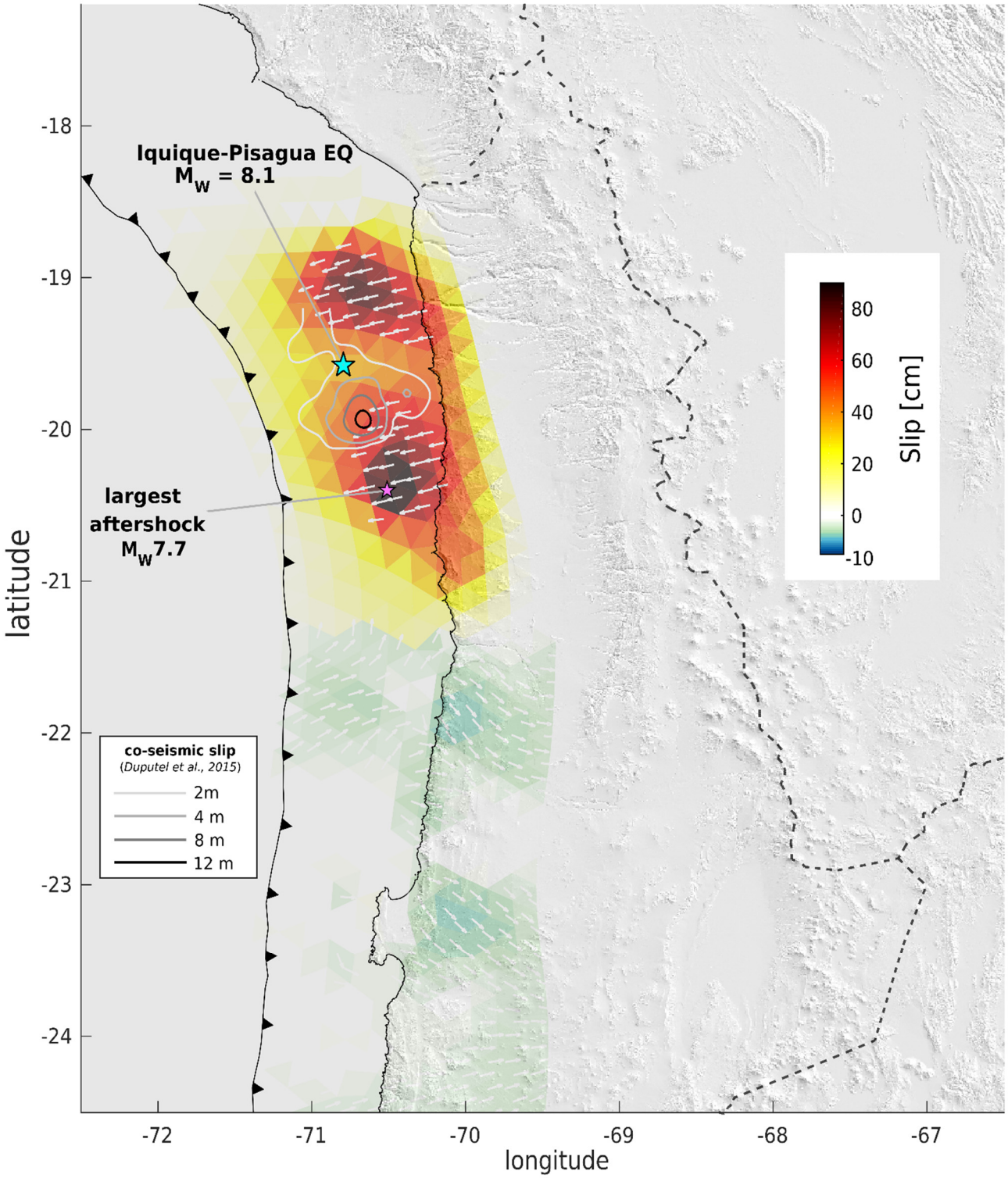

Figure B.19: *Afterslip cumulated over two years (white arrows indicate the normalized rake). For other features see Figure 3.4 in the main text.*

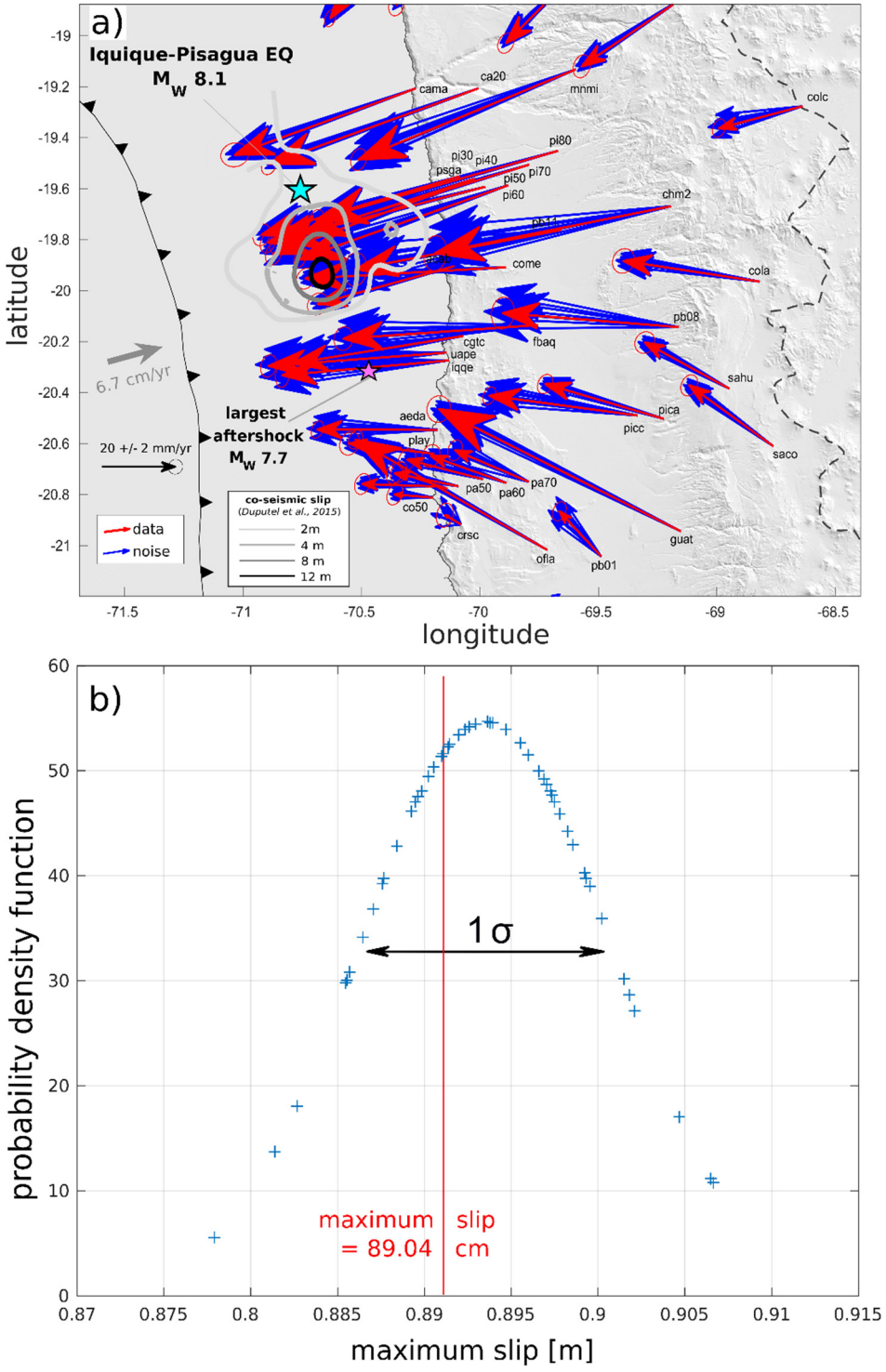

Figure B.20: *a) Original (red) and modified (blue) model input data, where random noise is scaled with the GPS data error and added to the original data for 50 model runs to estimate the b) uncertainty of the maximum cumulative slip parameter. By fitting a probability density function, we find that the maximum slip of 89.04 cm (red line, estimated using the original input data) varies asymmetrically with -0.4/+1.2 cm.*

GPS station	Residual East [mm]	Residual North [mm]	Residual Up [mm]
AEDA	1.4	1.1	2.2
AMDE	1.0	0.9	2.0
ANT2	1.0	0.8	2.1
ATJN	1.2	1.0	1.9
BDEC	1.6	1.4	2.3
BDJC	1.0	1.0	1.7
BLOV	1.3	1.0	1.8
BMWS	1.1	1.4	2.2
BNOE	1.3	1.4	2.0
BRDQ	1.0	0.9	1.5
BWSZ	1.2	1.0	2.2
CBAA	1.0	0.9	1.7
CDLC	1.0	1.0	2.1
CGTC	1.1	0.9	1.7
CHM2	1.7	0.9	2.2
CHMZ	1.1	0.9	1.9
CHYT	1.6	1.3	2.7
CJNT	1.0	0.9	1.9
CLLA	1.6	1.0	2.0
COLC	1.3	1.2	1.9
COLO	1.4	1.1	2.1
CRSC	1.0	1.0	2.0
CTLR	1.0	0.9	1.7
FBAQ	1.4	1.3	2.5
HMBS	1.3	1.1	2.1
HPCH	1.1	1.0	1.7
IACR	1.4	1.1	2.1
IQQE	1.2	1.0	1.7
JRGN	1.1	1.1	1.9
LVRA	0.9	1.0	1.7
LYAR	1.0	0.9	1.9
MCLA	1.0	0.9	1.5
MICA	1.0	0.9	1.7
MNMI	1.4	1.1	2.4
PA70	0.9	0.9	1.9
PB01	1.2	1.0	2.3
PB02	1.0	1.0	1.7
PB03	1.0	1.0	2.3
PB04	1.0	1.0	1.7
PB05	1.0	0.9	1.6
PB06	1.1	1.1	2.1
PB07	1.0	1.0	1.7
PB08	1.5	1.0	2.1
PB09	1.0	1.1	1.9
PB11	1.4	0.9	1.8
PCAL	2.0	1.2	2.4
PCCL	1.2	1.0	1.9
PCHA	1.4	1.3	2.0
PI60	1.0	0.9	1.6
PICB	1.2	1.0	1.9
PICC	1.3	0.9	2.0
PICN	1.6	2.3	2.7
PMEJ	1.2	1.1	1.9
PSGA	1.2	1.0	2.1
PTRE	1.1	1.1	1.8
PUNA	1.1	1.0	1.7
QUEB	0.9	0.9	1.9
QUIL	1.3	1.1	2.2
RADO	1.3	1.0	2.0
RDEO	0.9	1.0	1.8
SCTC	1.1	1.0	2.0
SPAT	0.9	0.9	1.9
SRGD	1.0	0.9	1.7
TCPL	1.7	1.3	2.6
TILC	1.3	0.9	1.9
TUZG	1.5	0.9	2.1
UAPE	1.3	1.0	2.0
UAPF	1.6	1.5	2.5
UCNF	1.1	1.0	1.9
URCU	1.1	0.8	1.8
URUS	1.2	1.1	1.7
UTAR	1.5	1.2	2.7
UTUR	1.0	1.0	2.0
VLZL	1.0	0.9	1.9
YAVC	0.8	0.9	1.9

Table B.1: *Residuals of the GPS time series after removing of the seasonal model (equation 3.2 in the main text) for cGPS components. The average rms-misfit is 1.2 mm in East, 1.0 mm in North and 2.0 mm in vertical component.*

GPS station	Parameters East component (in mm)				Parameters North component (in mm)				Parameters Up component (in mm)			
	F_1	F_2	F_3	F_4	F_1	F_2	F_3	F_4	F_1	F_2	F_3	F_4
AEDA	0.412	0.341	-0.544	-0.378	1.967	0.821	-0.257	0.159	-2.915	1.397	0.379	0.759
AMDE	0.750	-0.198	0.052	-0.213	2.085	1.214	-0.751	0.252	-2.377	0.985	-0.963	0.817
ATJN	1.228	0.271	-0.048	-0.465	2.218	0.715	-0.087	0.189	-3.105	1.335	-0.034	0.783
BDEC	1.176	1.094	1.156	-0.477	1.463	-2.507	-1.413	0.309	-3.754	1.512	-0.100	0.640
BLOV	0.667	0.504	0.214	-0.525	2.197	0.158	-0.889	0.326	-4.556	-0.816	-1.607	2.833
BMWS	1.381	-0.857	0.015	-0.316	1.566	-0.529	-1.435	-0.327	-3.105	1.335	-0.034	0.783
BWSZ	1.107	0.216	0.299	-0.214	1.852	0.267	-0.624	0.086	-2.832	0.895	-1.185	0.979
CBAA	0.672	-0.031	0.114	-0.593	2.146	0.790	-0.012	0.190	-1.766	0.572	-1.036	1.319
CDLC	0.795	0.082	0.146	-0.550	2.099	0.767	0.007	0.176	-3.105	1.335	-0.034	0.783
CGTC	1.430	-0.071	0.202	-0.391	2.134	0.650	-0.169	0.304	-3.105	1.335	-0.034	0.783
CHMZ	0.766	-0.253	0.180	-0.587	2.122	0.293	-0.036	0.261	-3.521	1.263	-0.712	1.176
CHYT	2.708	-0.494	-0.034	-0.302	3.632	-0.070	-0.477	-0.152	-3.175	1.540	0.181	0.596
CJNT	0.866	-0.032	0.079	-0.479	1.958	0.690	-0.068	0.143	-2.808	1.404	0.028	0.695
CLLA	1.014	0.089	0.258	-0.604	2.170	0.487	-0.005	0.064	-3.775	1.388	-0.309	1.225
COLC	1.119	-0.011	0.202	-0.740	1.853	0.789	-0.055	0.205	-3.105	1.335	-0.034	0.783
COLO	1.333	0.279	0.051	-0.782	2.164	0.959	-0.264	0.395	-4.272	1.495	-0.234	0.129
CRSC	0.849	0.129	0.019	-0.487	2.018	0.703	-0.111	0.128	-0.945	2.556	-0.211	-0.137
CTLR	0.695	0.274	0.195	-0.626	2.121	0.301	0.167	0.175	-3.148	1.301	-0.319	0.476
FBAQ	1.500	0.849	-0.597	-0.172	2.760	0.948	-0.397	0.100	-2.783	1.233	0.469	0.512
HMBS	0.789	-0.304	0.212	-1.020	2.316	0.240	-0.044	0.107	-3.460	1.350	-0.062	0.923
IACR	1.043	0.245	-0.434	-0.255	1.941	1.302	-0.806	0.197	-3.086	3.193	-0.056	1.028
IQQE	1.068	0.039	0.138	-0.304	2.059	0.742	-0.071	0.131	-3.348	1.757	0.086	0.526
JRGN	0.592	0.445	0.020	-0.420	2.223	0.910	0.047	0.119	-2.940	1.363	0.336	0.368
LYAR	1.098	0.003	0.189	-0.564	2.287	0.891	0.075	0.160	-2.920	2.587	0.019	0.663
MCLA	0.701	0.306	0.095	-0.431	2.027	0.751	-0.010	0.165	-5.000	0.998	-0.194	0.362
MICA	0.699	0.567	0.277	-0.692	2.343	0.337	-0.015	0.034	-3.105	1.335	-0.034	0.783
MNMI	1.442	0.336	0.496	-0.749	2.487	0.787	0.104	0.142	-3.674	2.898	-0.582	1.495
PB01	1.151	0.126	-0.024	-0.688	2.291	0.691	-0.038	0.423	-2.654	1.479	0.561	0.983
PB02	1.040	0.206	0.162	-0.549	1.824	0.956	-0.260	0.106	-2.061	0.599	0.086	0.577
PB03	0.967	0.101	0.298	-0.291	2.021	0.953	-0.267	0.018	-3.105	1.335	-0.034	0.783
PB04	0.855	0.327	0.185	-0.549	2.181	0.665	-0.057	0.148	-3.680	1.971	0.763	0.732
PB05	0.799	0.127	0.114	-0.294	1.996	0.706	-0.340	0.053	-2.952	1.300	0.063	0.512
PB06	1.305	0.325	0.244	-0.331	1.685	0.834	-0.262	0.059	-3.519	1.322	0.454	0.269
PB07	0.896	-0.026	0.010	-0.634	2.081	0.786	-0.301	0.245	-2.908	1.270	0.986	1.080
PB08	1.685	1.121	-0.065	-1.187	2.438	0.894	0.003	0.172	-3.105	1.335	-0.034	0.783
PCCL	1.200	0.036	0.100	-0.547	2.495	0.828	-0.131	0.059	-2.561	1.952	0.218	0.382
PCHA	0.581	0.235	0.278	-0.368	2.104	0.929	0.288	0.180	-2.610	0.834	-0.169	0.537
PICB	1.442	0.611	-0.377	-0.452	2.031	1.111	0.007	-0.055	-2.425	1.280	-0.184	0.322
PICC	1.173	0.535	0.671	-0.277	2.239	1.399	0.159	0.195	-2.584	1.195	0.110	0.704
PMEJ	0.982	0.219	0.227	-0.348	1.919	1.116	-0.188	0.067	-1.816	1.091	0.012	0.586
PSGA	0.827	0.360	0.320	-0.644	2.099	0.896	-0.025	0.061	-3.002	1.272	-0.169	1.196
PTRE	1.409	-0.163	-0.054	-0.525	2.454	0.523	-0.250	0.159	-2.555	1.055	-0.671	1.128
QUIL	0.320	0.404	-0.949	-0.256	1.414	0.637	-0.153	0.167	-4.024	0.365	-0.633	1.003
RADO	0.645	0.253	0.368	-0.523	2.123	0.779	0.059	0.201	-3.105	1.335	-0.034	0.783
SRGD	0.822	0.126	0.167	-0.499	2.148	0.646	-0.063	0.183	-3.105	1.335	-0.034	0.783
UAPE	0.863	0.145	-0.149	-0.580	2.017	1.011	-0.058	0.263	-3.105	1.335	-0.034	0.783
UAPF	1.193	-0.550	-0.329	-0.704	0.939	-0.249	-0.248	0.886	-3.740	1.487	0.251	0.571
UCNF	0.640	0.594	0.416	-0.381	1.984	1.166	-0.211	0.190	-4.119	0.480	0.359	0.709
URUS	1.136	0.058	0.148	-0.286	2.222	0.525	-0.322	0.447	-3.105	1.335	-0.034	0.783
UTAR	1.243	0.224	0.177	-0.477	2.643	1.389	-0.024	-0.048	-2.851	1.909	0.329	0.601
UTUR	1.042	-0.116	0.222	-0.598	2.200	0.557	-0.068	0.396	-2.894	1.707	0.941	1.245
VLZL	0.776	0.220	0.187	-0.452	1.982	0.797	-0.010	0.243	-3.105	1.335	-0.034	0.783

Table B.2: *Best-fit model parameters F_1 to F_4 representing the seasonal oscillation in the cGPS time series (see equation 3.2 in the main text).Parameters of stations with significant data gaps were estimated using the mean oscillation signal (see Table B.3).*

East component parameters (in mm)				North component parameters (in mm)				Up component parameters (in mm)			
F_1	F_2	F_3	F_4	F_1	F_2	F_3	F_4	F_1	F_2	F_3	F_4
1.017	0.179	0.102	-0.496	2.110	0.653	-0.199	0.170	-3.105	0.134	-0.034	0.783

Table B.3: *Mean seasonal parameters extracted from all cGPS stations (see Table B.2) for correcting the seasonal signal of the campaign sites.*

GPS station	interseismic velocity (before Tarapacá)	interseismic velocity (between Tarapacá and Tocopilla)	interseismic velocity (after Tocopilla)
AEDA	30.04	27.43	25.43
AERO	-	-	34.12
ANTF	32.12	-	-
ATJN	-	22.87	25.40
BAND	-	-	31.21
BAQU	26.18	-	29.82
CACO	33.93	-	-
CALC	33.96	-	35.28
CAMA	23.24	-	-
CBAA	-	22.13	21.76
CDLC	-	32.10	32.80
CENE	-	-	17.33
CETO	18.54	-	17.05
CGTC	-	-	27.73
CHM2	-	-	16.68
CHMZ	-	-	22.47
CJNT	-	16.99	16.99
CLLA	-	-	21.14
COLC	-	-	23.67
COLO	-	-	18.14
COME	26.32	-	-
CRSC	-	28.72	-
CTLR	-	-	31.18
CTOC	-	-	16.78
ECHA	27.84	-	26.07
ESJM	17.18	-	-
FBAQ	28.49	26.21	-
GRAQ	-	-	31.42
GUAT	32.65	-	28.58
IACR	-	-	20.65
INCA	-	-	28.58
IQQE	28.95	-	26.85
JRGN	-	37.40	-
LINZ	-	-	19.11
LIVE	31.38	-	31.08
LYAR	-	-	20.36
MABL	-	-	30.15
MCLA	-	30.65	-
MEJI	29.35	-	32.62
MEJS	-	-	35.26
MICA	-	-	28.28
MINF	24.40	-	26.31
MNMI	-	-	22.95
OFLA	-	-	29.52
PACO	11.44	-	-
PAEL	-	-	23.69
PATI	32.50	-	33.57
PB01	-	-	25.42
PB02	-	-	29.06
PB03	-	-	25.32
PB04	-	-	33.63
PB05	-	-	37.70
PB06	-	-	25.88
PB07	-	-	38.18
PB08	-	-	25.12
PB08	-	-	25.12
PBAR	19.09	-	19.18
PCAL	24.04	-	-
PCCL	-	17.18	19.36
PCHA	-	21.69	-
PCUA	32.35	-	30.36
PEIN	-	-	20.48
PENI	16.37	-	-
PICA	23.86	-	20.77
PICB	-	28.78	-
PICC	-	-	25.71
PICN	28.60	-	-
PMEJ	33.96	32.08	-
PRO1	-	-	28.91
PRO2	-	-	27.70
PRO3	-	-	30.52
PSGA	-	-	-
PTCH	32.28	-	-
PTRE	-	13.34	15.85
PUQI	22.92	-	24.13
QUIL	-	32.18	-
RADO	-	-	16.98
RLOA	31.83	-	-
SACA	-	-	17.17
SIGO	25.96	-	31.52
SRGD	-	-	29.90
SURI	16.12	-	-
TCPL	-	27.98	-
TILC	-	-	15.20
TOCO	14.79	-	16.46
TOPI	-	-	29.33
UAPE	32.15	33.55	30.58
UAPF	28.62	-	-
UCNF	-	30.64	32.29
URIB	30.54	-	31.51
URUS	-	-	12.37
UTAR	19.29	17.76	21.40
UTUR	-	-	16.31
VIRI	7.15	-	-
VLZL	-	30.27	-

Table B.4: *Absolute (i.e. full) interseismic, horizontal ground rates (in mm/yr) split into a pre-Tarapacá, a between-Tarapacá-and-Tocopilla and a post-Tocopilla rate as described in section 3.3.1 (East and North velocity is summarized into a 1-d horizontal velocity).*

GPS station	East displacement [mm/yr]	North displacement [mm/yr]	Up displacement [mm/yr]	East error [mm/yr]	North error [mm/yr]	Up error [mm/yr]
AEDA	26.75	7.28	2.74	1.1	1.5	2.2
AERO	32.50	10.41	17.82	3.3	3.5	11.5
ANTF	30.59	9.79	14.37	4.0	2.6	15.1
ATJN	24.53	7.43	3.57	0.8	1.2	1.4
BAND	29.59	9.95	3.50	3.4	3.1	9.2
BAQU	27.02	8.88	2.75	3.1	3.3	31.4
CACO	33.91	8.39	1.98	3.3	3.3	15.6
CALC	32.77	9.47	-4.70	2.6	1.6	18.1
CAMA	21.91	4.51	4.20	3.1	3.5	11.0
CBAA	21.01	6.33	-0.49	0.8	1.1	1.4
CDLC	31.21	8.86	6.77	0.8	1.1	1.6
CENE	14.19	6.06	-1.40	3.0	2.9	15.9
CETO	14.96	6.45	-3.60	2.7	3.0	24.8
CGTC	26.58	7.92	3.78	0.7	1.0	1.4
CHM2	15.32	6.60	15.67	0.7	0.9	1.5
CHMZ	20.61	8.97	-0.40	0.8	1.1	1.4
CJNT	16.44	4.29	0.04	0.9	1.3	1.5
CLLA	20.57	4.88	-1.31	0.7	1.0	1.3
COLA	11.69	4.76	2.39	3.9	3.6	13.8
COLC	22.29	8.23	12.71	0.8	1.1	1.9
COLO	17.17	5.84	-0.53	0.7	1.0	1.4
COME	25.10	3.14	4.27	2.9	1.7	18.5
CRSC	27.64	7.78	3.06	0.8	1.2	1.4
CTLR	29.72	9.03	-0.38	0.8	1.1	1.6
CTOC	15.45	6.55	1.90	3.3	3.7	14.5
ECHA	25.82	6.29	2.23	3.1	2.8	20.8
ESJM	16.90	3.11	-5.14	2.8	4.3	20.7
FBAQ	24.23	5.51	4.28	1.2	1.9	1.7
GRAQ	29.67	10.36	2.97	2.5	1.2	6.7
GUAT	28.50	4.87	-1.48	3.6	3.7	15.2
HMBS	24.20	8.13	-3.45	0.9	1.2	2.0
HUAY	13.02	5.85	2.77	3.0	3.2	9.4
IACR	20.13	4.62	0.92	0.6	0.9	1.4
INCA	27.35	8.29	14.41	3.6	3.3	8.4
IQQE	28.53	4.93	2.38	0.9	1.3	1.8
JRGN	34.81	13.67	-5.32	0.9	1.2	1.4
LCHU	11.29	2.80	10.51	3.4	5.0	17.5
LINZ	14.90	5.68	-1.82	3.0	3.1	15.3
LIVE	30.01	8.59	1.41	2.6	0.7	7.5
LOBA	16.63	7.82	-1.66	4.0	3.3	13.1
LYAR	19.56	5.65	4.75	0.7	1.0	1.4
MABL	27.51	6.47	2.25	3.2	1.1	6.2
MCLA	29.17	9.40	0.99	0.9	1.2	1.4
MEJI	29.06	10.73	2.00	1.8	2.7	12.8
MEJS	33.63	10.61	5.91	2.6	1.6	17.5
MICA	27.44	6.83	4.88	0.8	1.1	1.6
MINF	24.76	5.44	1.42	2.8	3.5	10.7
MNMI	21.08	9.08	0.08	0.8	1.1	2.1
OFLA	26.28	9.44	2.78	3.4	3.6	18.7
PACO	12.08	7.70	-3.30	3.9	4.1	12.2
PAEL	17.19	8.81	-2.26	3.2	4.1	16.2
PAJA	13.36	4.42	-2.98	3.6	3.8	19.2
PATI	32.40	6.30	3.93	3.0	4.0	14.9
PB01	24.64	6.24	3.80	0.8	1.1	1.5
PB02	27.84	8.34	5.11	0.7	1.0	1.4
PB03	24.19	7.47	-0.16	0.8	1.0	1.4
PB04	31.42	11.98	1.59	0.8	1.0	1.4
PB05	33.70	16.90	8.98	0.8	1.0	1.4
PB06	24.83	7.29	2.15	0.7	1.0	1.4
PB07	36.18	12.21	3.87	0.7	0.9	1.4
PB08	23.71	8.30	11.98	0.7	1.0	1.5
PBAR	18.21	4.98	-1.83	3.2	4.1	11.3
PCAL	23.61	4.53	-3.19	1.4	2.1	2.3
PCCL	18.00	6.83	2.49	0.8	1.2	1.4
PCHA	20.79	6.20	2.51	0.9	1.3	2.2
PCUA	29.81	9.73	6.17	2.6	3.7	12.5
PEIN	14.78	8.16	1.34	2.9	2.7	11.2
PENI	14.22	3.21	-0.74	3.5	4.5	15.4
PICA	21.15	5.88	-3.03	3.5	3.7	12.5
PICB	28.20	5.74	6.87	1.2	1.9	2.3
PICC	24.44	7.99	1.38	0.8	1.0	2.1
PICN	28.35	3.82	1.41	0.9	1.4	2.1
PMEJ	31.04	11.27	-3.05	1.1	1.4	2.2
PRO1	27.07	9.16	10.43	2.8	1.6	3.0
PRO2	27.39	6.13	11.23	3.3	3.9	13.3
PRO3	29.69	9.07	13.84	3.9	4.5	11.6
PSGA	27.49	9.97	5.89	0.8	1.1	2.1
PTCH	30.61	6.53	6.12	4.1	1.9	12.3
PTRE	11.87	8.48	-0.39	0.8	1.2	1.5
PUQI	22.46	5.60	2.41	3.5	4.2	14.8
QPAC	13.24	5.11	-0.14	3.3	3.4	9.3
QUIL	31.06	8.41	9.68	1.2	1.8	1.8
RADO	16.39	4.44	-3.78	0.8	1.1	2.0
RLOA	30.20	6.33	5.34	3.3	3.6	12.7
SACA	14.11	7.14	1.27	3.8	3.3	9.5
SIGO	26.73	8.14	3.55	2.9	3.9	11.7
SRGD	28.87	7.80	2.25	0.8	1.1	1.4
SURI	10.79	6.19	1.18	2.4	2.5	13.6
TILC	14.56	4.37	19.55	0.7	1.0	1.6
TOCO	17.99	4.22	1.83	3.1	2.4	10.4
TOPI	26.02	10.53	5.05	3.3	4.3	14.0
UAPE	33.45	12.03	10.83	1.0	1.3	2.4
UAPF	27.96	6.09	3.73	1.1	1.8	2.5
UCNF	31.07	11.57	2.81	1.0	1.2	2.1
URIB	28.88	9.61	2.81	3.7	2.6	15.4
URUS	11.66	4.14	-0.74	0.7	1.0	1.4
UTAR	18.06	3.99	3.13	0.9	1.4	2.2
UTUR	15.47	5.19	3.71	0.7	1.0	1.5
VLZL	29.10	8.32	3.64	0.9	1.1	1.4
YNGY	28.30	6.83	6.35	3.5	2.7	10.2
ZAHU	12.48	4.87	-3.73	3.5	3.9	18.3

Table B.5: *Interseismic rates and errors of all GPS stations as described in section 3.3.1., used for the joint interseismic model in SOAM reference frame. Values represent mean annual deformation rates.*

GPS station	East [mm/yr]	North [mm/yr]	Up [mm/yr]
AEDA	24.62	17.78	2.74
AERO	30.82	20.87	17.82
ANTF	28.93	20.26	14.37
ATJN	22.20	17.94	3.57
BAND	27.87	20.40	3.50
BAQU	25.29	19.43	2.75
CACO	32.29	18.85	1.98
CALC	31.23	19.92	-4.70
CAMA	19.59	15.00	4.20
CBAA	19.08	17.05	-0.49
CDLC	29.30	19.41	6.77
CENE	12.40	16.75	-1.40
CETO	13.11	17.15	-3.60
CGTC	24.38	18.43	3.78
CHM2	12.99	17.22	15.67
CHMZ	18.28	19.59	-0.40
CJNT	14.51	15.09	0.04
CLLA	18.44	15.48	-1.31
COLA	9.39	15.43	2.39
COLC	19.87	18.92	12.71
COLO	15.12	16.63	-0.53
COME	22.85	13.68	4.27
CRSC	25.56	18.29	3.06
CTLR	27.80	19.53	-0.38
CTOC	13.51	17.34	1.90
ECHA	23.92	16.86	2.23
ESJM	15.23	13.77	-5.14
FBAQ	22.01	16.06	4.28
GRAQ	27.96	20.82	2.97
GUAT	26.36	15.50	-1.48
HMBS	22.01	18.67	-3.45
HUAY	11.15	16.71	2.77
IACR	17.69	15.10	0.92
INCA	25.63	18.82	14.41
IQQE	26.35	15.43	2.38
JRGN	33.12	24.12	-5.32
LCHU	8.76	13.42	10.51
LINZ	12.87	16.45	-1.82
LIVE	28.40	19.08	1.41
LOBA	14.88	18.41	-1.66
LYAR	17.08	16.09	4.75
MABL	25.81	16.99	2.25
MCLA	27.38	19.89	0.99
MEJI	27.35	21.19	2.00
MEJS	31.96	21.06	5.91
MICA	25.46	17.37	4.88
MINF	23.12	16.01	1.42
MNMI	18.70	19.65	0.08
OFLA	24.19	19.99	2.78
PACO	9.62	18.19	-3.30
PAEL	15.43	19.45	-2.26
PAJA	11.41	15.30	-2.98
PATI	30.30	16.80	3.93
PB01	22.53	16.83	3.80
PB02	25.80	18.87	5.11
PB03	22.26	18.02	-0.16
PB04	29.56	22.48	1.59
PB05	31.91	27.40	8.98
PB06	22.98	17.86	2.15
PB07	34.20	22.75	3.87
PB08	21.46	18.93	11.98
PBAR	16.28	15.69	-1.83
PCAL	21.67	15.18	-3.19
PCCL	15.54	17.33	2.49
PCHA	18.51	16.79	2.51
PCUA	27.99	20.22	6.17
PEIN	12.97	18.92	1.34
PENI	12.42	13.94	-0.74
PICA	18.95	16.50	-3.03
PICB	26.00	16.35	6.87
PICC	22.24	18.59	1.38
PICN	26.15	14.42	1.41
PMEJ	29.31	21.73	-3.05
PRO1	25.39	19.64	10.43
PRO2	25.71	16.62	11.23
PRO3	28.01	19.56	13.84
PSGA	25.21	20.47	5.89
PTCH	28.56	17.04	6.12
PTRE	9.35	19.05	-0.39
PUQI	20.28	16.32	2.41
QPAC	11.30	15.94	-0.14
QUIL	29.06	18.99	9.68
RADO	14.40	15.09	-3.78
RLOA	28.19	16.84	5.34
SACA	12.24	17.96	1.27
SIGO	24.89	18.75	3.55
SRGD	27.03	18.41	2.25
SURI	8.34	16.82	1.18
TILC	12.52	15.45	19.55
TOCO	16.10	14.99	1.83
TOPI	24.11	21.02	5.05
UAPE	31.27	22.53	10.83
UAPF	25.78	16.59	3.73
UCNF	29.43	22.04	2.81
URIB	27.21	20.10	2.81
URUS	8.96	15.01	-0.74
UTAR	15.63	14.47	3.13
UTUR	13.38	16.05	3.71
VLZL	27.34	18.85	3.64
YNGY	26.67	17.37	6.35
ZAHU	9.99	15.44	-3.73

Table B.6: *Same as Table B.5, but in ITRF2014 reference frame.*

GPS station	Data observation (total)			Visco-elastic fraction			East error [mm]	North error [mm]	Up error [mm]
	East [mm]	North [mm]	Up [mm]	East [mm]	North [mm]	Up [mm]			
AEDA	-44.52	-6.85	-0.95	-0.082	-0.034	0.027	0.7	1.0	1.7
ATJN	-37.34	-10.79	-18.95	-0.159	-0.049	0.057	0.7	0.9	1.5
CBAA	3.30	0.65	-2.95	-0.007	0.012	0.001	0.7	1.0	1.4
CGTC	-44.86	-10.12	-22.60	-0.120	-0.038	0.038	0.7	0.9	1.4
CHM2	-32.54	-9.97	-1.00	-0.171	-0.024	-0.002	0.7	1.0	1.5
CHMZ	-32.91	-9.65	-0.85	-0.171	-0.024	-0.002	0.7	1.0	1.4
CJNT	3.57	0.04	-7.55	-0.006	0.012	0.000	0.7	1.0	1.4
COLC	-14.39	-6.38	-5.30	-0.142	-0.034	-0.006	0.8	1.0	2.3
COLO	2.04	0.49	-17.30	-0.018	0.019	0.000	0.7	1.0	1.5
CRSC	-20.41	-0.96	-5.00	-0.060	-0.022	0.019	0.7	0.9	1.4
FBAQ	-32.07	-3.72	-17.95	-0.138	-0.023	0.030	0.9	1.0	2.4
IACR	-9.97	-10.41	0.00	-0.072	-0.036	0.021	0.7	0.9	1.4
IQQE	-34.25	-5.51	-8.65	-0.106	-0.038	0.034	0.8	1.3	2.1
JRGN	3.04	-1.06	-1.00	-0.005	-0.002	0.001	0.8	0.9	1.4
LYAR	-1.93	-2.55	1.00	-0.037	-0.021	0.010	0.8	1.0	2.1
MCLA	2.15	-0.50	-2.25	-0.006	-0.002	0.001	0.7	0.9	1.4
MNMI	-28.24	-12.51	-5.45	-0.165	-0.068	0.009	0.8	1.0	2.3
PB01	-14.99	4.79	-12.65	-0.057	0.010	0.004	0.7	1.0	1.5
PB02	-6.70	0.38	-5.15	-0.038	-0.007	0.011	0.7	0.9	1.4
PB03	2.19	-0.66	-2.15	-0.012	0.003	0.001	0.7	0.9	1.5
PB04	2.98	-2.39	-4.30	-0.009	-0.003	0.001	0.7	0.9	1.4
PB05	2.49	-1.96	-5.05	-0.005	-0.001	0.001	0.7	0.9	1.4
PB06	3.84	-0.96	-6.80	-0.005	0.004	0.001	0.7	0.9	1.4
PB07	-1.14	-1.95	-4.75	-0.021	-0.003	0.004	0.7	0.9	1.4
PB08	-33.65	-6.45	-5.90	-0.140	0.004	0.001	0.7	1.0	1.5
PB11	-39.44	-14.67	-5.50	-0.172	-0.033	0.024	0.7	0.9	1.4
PCCL	-11.71	-11.86	-3.80	-0.077	-0.056	0.017	0.7	0.9	1.4
PCHA	-38.17	-11.86	-6.75	-0.166	-0.019	0.009	0.8	1.0	2.4
PICC	-36.24	-2.84	-12.50	-0.108	0.010	0.004	0.8	1.0	1.8
PMEJ	3.89	0.02	-7.95	-0.005	-0.002	0.001	0.9	1.0	2.3
PSGA	-32.47	-11.35	-25.40	-0.161	-0.047	0.058	0.8	1.0	2.3
PTRE	-7.88	-11.52	-3.15	-0.069	-0.073	0.002	0.7	1.0	1.5
RADO	0.84	2.03	-0.05	-0.015	0.017	0.001	0.8	1.0	1.8
SRGD	4.05	-0.51	-6.30	-0.004	0.005	0.001	0.7	1.0	1.4
UAPE	-34.58	-5.51	-9.35	-0.107	-0.039	0.035	0.8	1.0	1.8
UCNF	3.75	-1.19	-5.75	-0.003	-0.001	0.001	0.9	1.0	2.3
URUS	0.42	-4.20	-1.38	-0.052	-0.024	-0.003	1.8	3.4	4.4
UTAR	-8.29	-11.43	-5.35	-0.075	-0.040	0.022	0.8	1.0	2.3
UTUR	2.25	1.33	-2.05	-0.017	0.017	-0.001	0.7	1.0	1.5
VLZL	4.38	-0.50	-5.90	-0.003	0.000	0.001	0.8	1.0	1.4

Table B.7: *Static displacements in three components ENU in SOAM reference frame, viscous components and errors as described in section 4.1 used for the joint model of Period 1 (days 2-16 after the main event). The observations are corrected for the seasonal trend and antenna offsets. The relocking rate (Table B.13) is not yet subtracted.*

GPS station	East [mm]	North [mm]	Up [mm]
AEDA	-46.66	3.65	-0.95
ATJN	-39.66	-0.29	-18.95
CBAA	1.37	11.37	-2.95
CGTC	-47.05	0.39	-22.60
CHM2	-34.86	0.65	-1.00
CHMZ	-35.23	0.97	-0.85
CJNT	1.64	10.84	-7.55
COLC	-16.81	4.31	-5.30
COLO	-0.01	11.29	-17.30
CRSC	-22.49	9.55	-5.00
FBAQ	-34.29	6.83	-17.95
IACR	-12.41	0.06	0.00
IQQE	-36.43	4.99	-8.65
JRGN	1.35	9.38	-1.00
LYAR	-4.41	7.89	1.00
MCLA	0.35	9.99	-2.25
MNMI	-30.62	-1.94	-5.45
PB01	-17.09	15.37	-12.65
PB02	-8.74	10.91	-5.15
PB03	0.26	9.90	-2.15
PB04	1.11	8.11	-4.30
PB05	0.71	8.53	-5.05
PB06	1.99	9.62	-6.80
PB07	-3.11	8.59	-4.75
PB08	-35.90	4.18	-5.90
PB11	-41.72	-4.11	-5.50
PCCL	-14.16	-1.35	-3.80
PCHA	-40.45	-1.26	-6.75
PICC	-38.44	7.76	-12.50
PMEJ	2.16	10.48	-7.95
PSGA	-34.75	-0.85	-25.40
PTRE	-10.40	-0.94	-3.15
RADO	-1.15	12.69	-0.05
SRGD	2.21	10.10	-6.30
UAPE	-36.76	4.99	-9.35
UCNF	2.11	9.28	-5.75
URUS	-2.28	6.67	-1.38
UTAR	-10.73	-0.95	-5.35
UTUR	0.17	12.19	-2.05
VLZL	2.62	10.02	-5.90

***Table B.8*:** *Same as Table B.7, but in ITRF2014 reference frame.*

GPS station	Data observation (total)			Visco-elastic fraction			East error	North error	Up error
	East [mm]	North [mm]	Up [mm]	East [mm]	North [mm]	Up [mm]	[mm]	[mm]	[mm]
ACAB	-38.45	-9.93	-25.40	-3.0	-0.9	1.0	1.2	1.2	3.3
AEDA	-33.93	0.09	-9.48	-1.7	-0.7	0.6	0.7	0.9	1.7
AR20	-20.77	-20.27	-16.79	-1.7	-1.0	0.4	0.9	1.1	2.3
AR40	-26.27	-24.53	-3.60	-1.9	-1.4	0.3	0.9	1.2	2.6
AR50	-25.33	-22.64	-27.90	-1.9	-1.5	0.2	0.9	1.1	2.6
AR60	-20.48	-23.85	-10.20	-1.9	-1.6	0.1	0.8	1.1	2.4
AR90	-22.48	-15.68	-25.60	-1.8	-1.6	-0.1	0.9	1.1	2.5
BAQU	17.20	1.40	3.10	-0.1	0.0	0.0	0.9	1.1	2.4
CA20	-58.87	-19.84	-21.10	-3.5	-1.2	0.9	0.9	1.1	3.0
CAMA	-50.94	-17.37	-5.90	-3.1	-0.8	1.2	1.6	1.3	4.1
CASU	-26.87	-25.40	-1.60	-2.6	-1.7	0.0	0.9	1.1	2.7
CBAA	14.71	6.28	2.68	-0.1	0.3	0.0	0.7	1.0	1.5
CENE	14.12	3.58	17.40	0.0	0.1	0.0	0.9	1.0	2.6
CETO	25.49	9.41	-21.40	-0.1	0.2	0.0	0.9	1.0	2.5
CGTC	-48.15	-7.23	-16.82	-2.5	-0.8	0.8	0.7	0.9	1.5
CHM2	-66.33	-12.28	9.86	-3.7	-0.5	-0.1	1.3	1.9	3.0
CHYT	-4.14	-10.06	-8.55	-1.3	-0.8	0.4	0.8	1.1	1.8
CJNT	15.78	5.17	0.08	-0.1	0.2	0.0	0.8	1.1	1.7
CO50	-10.81	0.83	25.10	-1.4	-0.6	0.4	0.9	1.1	2.4
COLA	-38.36	5.42	27.90	-3.1	0.0	-0.1	1.3	1.3	4.0
COLC	-23.47	-5.75	-3.98	-3.1	-0.7	-0.1	0.8	1.0	2.2
COLO	12.38	7.34	7.35	-0.4	0.4	0.0	0.7	0.9	1.4
COME	-56.45	-2.95	-32.70	-3.4	-0.8	0.9	1.1	1.1	3.1
CRSC	-4.57	2.47	1.58	-1.3	-0.5	0.4	1.0	1.3	2.0
CTOC	15.76	9.01	13.70	-0.1	0.3	0.0	1.0	1.3	2.8
ECHA	20.01	3.97	5.90	-0.2	0.1	0.0	0.9	1.0	2.2
ESJM	16.89	3.75	25.30	0.0	0.1	0.0	0.9	1.0	1.9
FBAQ	-54.70	-3.59	-43.60	-3.0	-0.5	0.6	1.1	1.3	3.1
GOLF	25.12	8.00	-18.50	-0.4	-0.2	0.1	1.0	1.1	3.2
GUAT	-16.14	11.99	0.40	-1.5	0.4	0.0	1.4	1.4	3.6
HUAY	7.61	-2.07	23.20	-0.1	0.2	0.0	1.1	1.2	2.7
IACR	-16.19	-19.18	-3.92	-1.6	-0.8	0.5	0.8	1.2	1.8
IQQE	-46.84	-3.89	-10.92	-2.2	-0.8	0.7	0.8	1.3	2.0
JRGN	28.07	9.26	-2.55	-0.1	0.0	0.0	0.8	0.9	1.5
JULO	31.07	10.59	-15.70	-0.1	0.0	0.0	1.0	1.1	3.2
LCHU	-23.52	-12.93	31.60	-1.9	-1.6	-0.1	1.0	1.2	2.9
LINZ	9.13	10.35	16.40	-0.3	0.4	0.0	1.0	1.3	2.2
LIVE	26.98	10.37	15.10	0.0	0.0	0.0	1.0	1.1	2.4
LOBA	14.99	3.55	33.20	0.0	0.1	0.0	1.0	1.1	2.5
MABL	17.82	5.70	24.10	-0.1	0.0	0.0	0.9	1.1	2.3
MCLA	23.37	6.79	0.73	-0.1	-0.1	0.0	0.7	0.9	1.4
MEJI	25.73	6.55	-20.70	-0.1	0.0	0.0	0.9	1.1	1.9
MINF	16.23	8.86	24.90	0.0	0.0	0.0	1.4	1.3	3.6
MNMI	-61.09	-23.62	-8.18	-3.6	-1.5	0.2	0.9	1.2	2.7
OFLA	-23.98	28.87	-22.30	-1.2	-0.1	0.2	0.8	1.0	2.4
PA20	-13.75	4.32	-6.60	-1.4	-0.6	0.5	1.0	1.1	2.6
PA30	-17.98	3.40	0.90	-1.5	-0.6	0.5	0.9	1.1	2.3
PA50	-21.36	5.14	-8.90	-1.6	-0.5	0.5	1.0	1.2	2.7
PA60	-21.25	7.06	-7.50	-1.6	-0.4	0.5	1.1	1.2	3.0
PA70	-20.76	8.25	-10.53	-1.6	-0.2	0.4	0.9	1.1	1.9
PACO	-19.80	-18.70	39.50	-1.5	-1.1	0.3	0.8	1.0	2.2
PAEL	22.07	5.44	-21.70	0.0	0.1	0.0	1.0	1.2	3.0
PAJA	8.56	6.23	9.40	-0.1	0.2	0.0	1.7	1.4	3.1
PATI	-20.44	0.62	12.80	-1.4	-0.6	0.5	0.9	1.1	2.2
PB01	-11.79	11.86	-3.63	-1.2	0.2	0.1	0.8	1.0	1.9
PB02	16.08	4.55	1.23	-0.8	-0.2	0.2	0.8	1.0	1.6
PB03	22.40	2.41	6.78	-0.3	0.0	0.0	0.7	0.9	1.5
PB04	25.22	6.15	9.48	-0.2	-0.1	0.0	0.7	0.9	1.4

PB05	26.08	5.48	4.89	-0.1	0.0	0.0	0.8	1.0	1.5
PB06	27.38	-2.42	-1.83	-0.1	0.1	0.0	1.7	2.2	3.4
PB07	20.77	2.47	6.58	-0.5	-0.1	0.1	1.7	2.2	3.8
PB08	-49.50	3.67	1.14	-3.0	0.1	0.0	1.3	1.7	3.1
PB11	-58.01	-10.33	-19.40	-3.7	-0.7	0.5	1.3	1.8	3.1
PBAR	14.46	8.26	10.10	-0.2	0.3	0.0	0.9	1.1	2.5
PCUA	17.86	3.88	1.90	-0.2	-0.1	0.0	1.1	1.0	2.7
PEIN	4.68	5.00	33.30	0.0	0.1	0.0	1.2	1.4	3.6
PENI	10.76	2.01	35.00	0.0	0.1	0.0	1.2	1.3	3.6
PI30	-55.80	-15.32	-30.90	-3.5	-1.0	1.2	1.0	1.2	2.8
PI40	-55.64	-16.87	-29.90	-3.6	-1.0	1.1	0.9	1.1	2.5
PI50	-61.20	-14.58	-32.40	-3.7	-1.0	1.0	0.9	1.1	2.4
PI60	-58.75	-19.33	-19.75	-3.8	-1.0	0.9	0.7	0.9	1.5
PI70	-64.20	-18.09	-35.90	-3.9	-1.1	0.7	0.9	1.1	2.3
PI80	-68.09	-18.09	-14.90	-3.9	-1.1	0.4	0.9	1.1	2.4
PICA	-33.45	9.12	-16.00	-2.3	0.3	0.0	0.9	1.0	2.2
PICC	-41.70	5.18	1.67	-2.3	0.2	0.1	0.8	0.9	1.7
PLAY	-23.95	2.77	5.80	-1.6	-0.7	0.5	1.2	1.3	3.1
PMEJ	26.35	8.71	-6.10	-0.1	-0.1	0.0	0.8	1.0	2.4
PRO1	17.66	4.13	37.20	-0.1	0.0	0.0	1.0	1.3	2.3
PRO2	17.17	6.90	33.00	-0.1	0.0	0.0	1.1	1.4	2.8
PRO3	20.22	2.21	27.60	-0.1	0.0	0.0	1.1	1.3	3.0
PSGA	-50.00	-17.30	-23.90	-3.4	-1.0	1.2	0.9	1.1	2.6
PTAR	28.33	8.37	29.90	-0.6	-0.3	0.1	1.2	1.2	3.1
PTRE	-11.41	-18.90	-0.50	-1.5	-1.6	0.0	0.6	0.9	1.4
PUQI	10.45	17.68	-29.80	-1.3	0.6	0.0	1.6	1.2	2.9
QPAC	11.88	5.93	0.80	-0.1	0.2	0.0	1.0	1.3	2.4
RADO	15.23	4.11	-6.82	-0.3	0.3	0.0	1.4	1.8	3.4
RLOA	20.30	3.58	3.30	-0.7	-0.3	0.2	1.0	1.3	3.2
SACA	4.39	7.63	21.30	-0.1	0.2	0.0	1.1	1.2	2.7
SACO	-23.67	11.97	23.90	-2.0	0.5	0.0	1.0	1.1	2.8
SAHU	-23.78	10.08	-4.80	-2.5	0.3	0.0	1.2	1.2	3.2
SIGO	22.96	4.24	1.00	-0.1	0.1	0.0	0.9	1.0	2.3
SRGD	19.38	3.58	-8.23	-0.1	0.1	0.0	0.7	0.9	1.4
SURI	-27.75	-17.48	-5.40	-3.0	-1.5	-0.2	1.0	1.2	2.6
TOPI	28.84	6.74	-3.00	-0.3	-0.1	0.0	1.4	1.3	3.7
UAPE	-50.05	-3.48	-11.18	-2.3	-0.8	0.7	0.9	1.2	2.2
UCNF	25.95	9.54	3.73	-0.1	0.0	0.0	0.8	1.0	2.2
URIB	26.26	9.83	-8.50	-0.1	0.0	0.0	1.0	1.0	2.3
URUS	2.15	-3.11	2.15	-1.1	-0.5	-0.1	0.8	1.5	1.8
UTAR	-22.36	-29.36	6.40	-1.6	-0.8	0.5	0.7	0.9	1.5
UTUR	9.04	5.27	3.00	-0.4	0.4	0.0	0.7	0.9	1.5
VIRI	-13.98	-8.95	25.90	-0.7	-1.2	0.1	1.3	1.3	4.2
ZAHU	-25.94	-23.84	17.30	-1.8	-1.7	0.0	0.8	1.1	1.9

Table B.9: *Static displacements in three components ENU in SOAM reference frame, viscous components and errors as described in section 3.4.1 used for the joint model of Period 2 (days 17-334 after the main event). The observations are corrected for the seasonal trend and antenna offsets. The relocking rate (Table B.13) is not yet subtracted.*

GPS station	East [mm]	North [mm]	Up [mm]	GPS station	East [mm]	North [mm]	Up [mm]
ACAB	-40.68	0.57	-25.40	PAEL	20.31	16.08	-21.70
AEDA	-36.06	10.59	-9.48	PAJA	6.60	17.11	9.40
AR20	-23.21	-9.78	-16.79	PATI	-22.54	11.12	12.80
AR40	-28.72	-14.00	-3.60	PB01	-13.89	22.44	-3.63
AR50	-27.79	-12.10	-27.90	PB02	14.05	15.08	1.23
AR60	-22.96	-13.30	-10.20	PB03	20.47	12.96	6.78
AR90	-25.02	-5.05	-25.60	PB04	23.35	16.65	9.48
BAQU	15.46	11.95	3.10	PB05	24.30	15.97	4.89
CA20	-61.21	-9.32	-21.10	PB06	25.53	8.16	-1.83
CAMA	-53.27	-6.89	-5.90	PB07	18.79	13.00	6.58
CASU	-29.33	-14.81	-1.60	PB08	-51.76	14.30	1.14
CBAA	12.79	17.00	2.68	PB11	-60.29	0.23	-19.40
CENE	12.33	14.27	17.40	PBAR	12.53	18.98	10.10
CETO	23.63	20.11	-21.40	PCUA	16.04	14.37	1.90
CGTC	-50.34	3.28	-16.82	PEIN	2.87	15.76	33.30
CHM2	-68.65	-1.66	9.86	PENI	8.96	12.74	35.00
CHYT	-6.59	0.42	-8.55	PI30	-58.09	-4.81	-30.90
CJNT	13.85	15.96	0.08	PI40	-57.93	-6.35	-29.90
CO50	-12.90	11.33	25.10	PI50	-63.49	-4.06	-32.40
COLA	-40.67	16.09	27.90	PI60	-61.04	-8.79	-19.75
COLC	-25.88	4.94	-3.98	PI70	-66.51	-7.55	-35.90
COLO	10.33	18.13	7.35	PI80	-70.42	-7.52	-14.90
COME	-58.70	7.59	-32.70	PICA	-35.65	19.74	-16.00
CRSC	-6.66	12.98	1.58	PICC	-43.89	15.79	1.67
CTOC	13.82	19.80	13.70	PLAY	-26.07	13.27	5.80
ECHA	18.11	14.55	5.90	PMEJ	24.63	19.18	-6.10
ESJM	15.22	14.40	25.30	PRO1	15.98	14.62	37.20
FBAQ	-56.93	6.96	-43.60	PRO2	15.49	17.39	33.00
GOLF	23.19	18.50	-18.50	PRO3	18.54	12.71	27.60
GUAT	-18.28	22.62	0.40	PSGA	-52.28	-6.79	-23.90
HUAY	5.74	8.78	23.20	PTAR	26.36	18.87	29.90
IACR	-18.63	-8.70	-3.92	PTRE	-13.93	-8.32	-0.50
IQQE	-49.01	6.62	-10.92	PUQI	8.27	28.40	-29.80
JRGN	26.38	19.71	-2.55	QPAC	9.94	16.76	0.80
JULO	29.41	21.04	-15.70	RADO	13.24	14.76	-6.82
LCHU	-26.05	-2.31	31.60	RLOA	18.30	14.09	3.30
LINZ	7.11	21.12	16.40	SACA	2.52	18.44	21.30
LIVE	25.37	20.86	15.10	SACO	-25.88	22.64	23.90
LOBA	13.25	14.14	33.20	SAHU	-26.01	20.73	-4.80
MABL	16.11	16.22	24.10	SIGO	21.12	14.85	1.00
MCLA	21.58	17.28	0.73	SRGD	17.54	14.19	-8.23
MEJI	24.02	17.02	-20.70	SURI	-30.20	-6.86	-5.40
MINF	14.60	19.43	24.90	TOPI	26.93	17.24	-3.00
MNMI	-63.47	-13.04	-8.18	UAPE	-52.23	7.02	-11.18
OFLA	-26.08	39.43	-22.30	UCNF	24.31	20.01	3.73
PA20	-15.85	14.82	-6.60	URIB	24.59	20.32	-8.50
PA30	-20.09	13.91	0.90	URUS	-0.55	7.76	2.15
PA50	-23.48	15.66	-8.90	UTAR	-24.80	-18.88	6.40
PA60	-23.37	17.60	-7.50	UTUR	6.95	16.14	3.00
PA70	-22.89	18.80	-10.53	VIRI	-16.58	1.63	25.90
PACO	-22.26	-8.20	39.50	ZAHU	-28.44	-13.27	17.30

Table B.10: *Same as Table B.9, but in ITRF2014 reference frame.*

GPS station	Data observation (total)			Visco-elastic fraction					
	East [mm]	North [mm]	Up [mm]	East [mm]	North [mm]	Up [mm]	East error [mm]	North error [mm]	Up error [mm]
AEDA	11.05	10.69	8.22	-1.6	-0.7	0.5	1.4	1.8	3.3
AMDE	6.77	6.24	3.82	-1.6	0.3	0.0	0.7	1.0	1.6
BAQU	36.63	12.96	-20.60	-0.1	0.0	0.0	0.9	1.1	2.2
BDEC	1.16	1.24	10.99	-2.9	-0.7	-0.1	0.7	1.1	1.8
BDJC	5.32	5.84	5.13	-1.7	-0.3	-0.1	0.7	1.0	1.7
BLOV	5.21	6.59	6.92	-2.4	0.0	0.0	0.7	1.0	1.5
BMWS	11.56	5.36	3.70	-1.1	0.5	0.0	0.8	1.0	1.7
BRDQ	2.60	3.29	2.03	-1.5	-0.7	-0.1	1.0	1.3	1.7
BWSZ	3.54	0.82	3.47	-2.3	-0.9	-0.1	0.7	1.0	1.6
CAMA	-0.40	4.13	-0.60	-2.9	-0.8	1.2	1.0	1.1	3.1
CASU	-1.42	1.82	-27.20	-2.5	-1.6	0.0	1.0	1.1	2.9
CBAA	19.64	6.93	-0.67	-0.1	0.2	0.0	2.0	2.7	4.0
CDLC	35.27	8.16	11.49	-0.2	0.0	0.0	1.9	2.2	3.1
CETO	22.17	8.13	-9.30	-0.1	0.2	0.0	0.8	1.0	2.2
CGTC	-6.46	1.13	-7.25	-2.4	-0.8	0.7	1.5	2.0	2.7
CHYT	7.19	-1.77	-5.67	-1.3	-0.7	0.4	1.0	1.4	2.2
CJNT	15.96	6.10	0.17	-0.1	0.2	0.0	1.5	1.7	2.3
CLLA	10.48	10.30	-9.97	-1.4	0.2	0.0	1.5	2.0	3.0
COLA	7.48	3.05	-20.20	-2.9	0.0	0.0	1.4	1.4	4.8
COLC	-4.15	3.14	8.27	-3.0	-0.7	-0.1	1.4	1.6	2.7
COLO	18.11	9.68	-1.92	-0.4	0.4	0.0	1.8	2.1	2.6
COME	3.75	-3.15	-2.30	-3.2	-0.8	0.8	0.8	1.0	2.1
CRSC	21.59	7.68	1.43	-1.2	-0.5	0.4	0.8	1.1	1.7
CTOC	19.72	-5.60	-7.80	-0.1	0.2	0.0	1.1	1.4	3.4
ECHA	35.99	8.54	12.80	-0.2	0.1	0.0	0.8	1.0	2.2
ESJM	34.33	-1.05	-47.10	0.0	0.0	0.0	1.0	1.1	2.8
FBAQ	-1.09	0.84	12.41	-2.8	-0.5	0.6	3.8	4.1	6.6
GOLF	31.74	9.31	-21.40	-0.4	-0.2	0.1	1.0	1.1	3.1
GUAT	13.00	6.02	-5.00	-1.4	0.4	0.0	1.2	1.3	3.5
IACR	2.58	-4.15	-12.24	-1.5	-0.7	0.5	1.5	1.8	2.3
IQQE	2.15	2.47	-4.02	-2.1	-0.8	0.7	1.2	1.8	3.3
JRGN	36.57	11.29	-6.63	-0.1	-0.1	0.0	1.6	2.0	3.1
LCHU	11.80	-0.02	-50.70	-1.8	-1.5	-0.1	0.8	1.2	2.2
LIVE	35.50	4.36	4.50	0.0	0.0	0.0	1.0	1.1	3.2
LOBA	32.38	6.93	-40.10	0.0	0.0	0.0	0.9	1.1	2.3
MABL	37.24	9.62	-44.10	-0.1	0.0	0.0	0.9	1.1	2.0
MCLA	30.59	6.34	-0.35	-0.1	-0.1	0.0	2.1	2.7	4.2
MINF	35.57	6.67	-16.30	0.0	0.0	0.0	1.3	1.4	3.8
MNMI	-7.00	-2.10	-5.50	-3.4	-1.4	0.2	2.5	3.2	6.5
OFLA	21.83	8.71	-0.40	-1.1	-0.1	0.2	0.9	1.0	2.5
PACO	11.97	-1.20	-42.80	-1.4	-1.0	0.3	0.8	1.1	2.2
PATI	21.81	4.39	7.80	-1.3	-0.6	0.4	0.9	1.1	2.3
PB01	14.86	11.75	-6.11	-1.2	0.1	0.1	2.6	3.0	5.1
PB02	23.22	5.86	-10.44	-0.8	-0.2	0.2	1.8	2.3	3.8
PB03	33.10	10.40	8.59	-0.3	0.0	0.0	1.5	1.7	2.2
PB04	33.24	10.28	5.78	-0.2	-0.1	0.0	1.7	1.9	2.3
PB05	30.37	11.28	7.25	-0.1	0.0	0.0	1.4	1.7	2.1
PB06	28.36	5.60	4.78	-0.1	0.1	0.0	1.0	1.3	2.0
PB07	33.68	9.79	3.25	-0.4	-0.1	0.1	1.0	1.3	1.9
PB09	19.44	-2.01	-5.80	-0.5	0.3	0.0	2.6	3.5	5.0
PBAR	19.16	5.74	5.10	-0.2	0.2	0.0	0.9	1.1	2.7
PCUA	34.05	13.02	-13.80	-0.2	-0.1	0.0	1.0	1.2	3.2
PEIN	18.58	2.16	-22.20	0.0	0.1	0.0	1.3	1.4	4.1
PICA	1.88	7.11	-1.50	-2.2	0.2	0.0	0.8	1.0	2.0
PLAY	14.83	8.72	3.20	-1.5	-0.7	0.5	1.1	1.3	3.1
PMEJ	39.63	11.43	-0.95	-0.1	-0.1	0.0	1.7	1.8	3.2

PRO3	34.26	14.57	-10.30	-0.1	0.0	0.0	1.0	1.2	3.0
PSGA	4.84	-1.26	-19.27	-3.2	-0.9	1.1	2.2	2.9	6.1
PTAR	28.53	8.94	-43.30	-0.5	-0.3	0.1	1.0	1.2	3.1
PTRE	2.51	-4.50	-0.96	-1.5	-1.5	0.0	1.2	1.4	1.9
PUQI	12.50	9.30	18.50	-1.3	0.5	0.0	0.8	1.1	2.2
QPAC	16.46	3.76	12.90	-0.1	0.2	0.0	1.1	1.4	3.0
RADO	23.37	4.44	-8.12	-0.3	0.3	0.0	1.1	1.4	2.6
SACO	5.10	9.38	-7.30	-1.9	0.4	0.0	0.9	1.1	2.6
SAHU	-0.63	7.70	-7.60	-2.4	0.3	0.0	0.9	1.1	2.5
SIGO	25.02	7.10	14.90	-0.1	0.1	0.0	0.9	1.1	2.2
SRGD	28.42	8.13	0.65	-0.1	0.1	0.0	1.8	2.3	3.5
SURI	6.36	1.69	-38.60	-2.9	-1.5	-0.2	0.9	1.2	2.1
TOPI	31.21	7.66	13.50	-0.3	-0.2	0.0	1.5	1.3	4.0
UAPE	-6.16	0.53	-6.91	-2.1	-0.8	0.7	1.4	1.5	2.2
UCNF	38.86	10.76	0.61	-0.1	0.0	0.0	1.6	1.7	2.9
URUS	6.99	2.98	2.83	-1.1	-0.5	-0.1	1.4	1.9	2.3
UTAR	1.28	-6.79	-8.10	-1.6	-0.8	0.5	0.9	1.3	2.1
UTUR	18.00	8.45	-3.05	-0.4	0.3	0.0	1.6	1.8	2.2
VIRI	19.20	5.70	-49.10	-0.7	-1.1	0.1	1.2	1.3	3.3
ZAHU	9.44	-0.71	-13.20	-1.7	-1.6	0.1	0.8	1.0	2.1

Table B.11: *Static displacements in three components ENU in SOAM reference frame, viscous components and errors as described in section 3.4.1 used for the joint model of Period 3 (days 335-717 after the main event). The observations are corrected for the seasonal trend and antenna offsets. The relocking rate (Table B.13) is not yet subtracted.*

GPS station	East [mm]	North [mm]	Up [mm]	GPS station	East [mm]	North [mm]	Up [mm]
AEDA	8.91	21.19	8.22	PB01	12.75	22.33	-6.11
AMDE	4.43	17.06	3.82	PB02	21.19	16.39	-10.44
BAQU	34.89	23.51	-20.60	PB03	31.17	20.95	8.59
BDEC	-1.27	11.93	10.99	PB04	31.37	20.78	5.78
BDJC	2.81	16.68	5.13	PB05	28.58	21.78	7.25
BLOV	2.85	17.33	6.92	PB06	26.51	16.17	4.78
BMWS	9.36	16.14	3.70	PB07	31.71	20.33	3.25
BRDQ	-0.01	14.10	2.03	PB09	17.44	8.61	-5.80
BWSZ	1.03	11.55	3.47	PBAR	17.23	16.45	5.10
CAMA	-2.73	14.61	-0.60	PCUA	32.23	23.50	-13.80
CASU	-3.88	12.41	-27.20	PEIN	16.77	12.92	-22.20
CBAA	17.71	17.64	-0.67	PICA	-0.32	17.72	-1.50
CDLC	33.36	18.71	11.49	PLAY	12.72	19.21	3.20
CETO	20.32	18.84	-9.30	PMEJ	37.90	21.89	-0.95
CGTC	-8.66	11.64	-7.25	PRO3	32.58	25.06	-10.30
CHYT	4.74	8.71	-5.67	PSGA	2.56	9.24	-19.27
CJNT	14.02	16.89	0.17	PTAR	26.56	19.45	-43.30
CLLA	8.36	20.90	-9.97	PTRE	-0.01	6.07	-0.96
COLA	5.17	13.72	-20.20	PUQI	10.32	20.02	18.50
COLC	-6.57	13.83	8.27	QPAC	14.51	14.58	12.90
COLO	16.06	20.48	-1.92	RADO	21.38	15.10	-8.12
COME	1.50	7.38	-2.30	SACO	2.89	20.05	-7.30
CRSC	19.50	18.19	1.43	SAHU	-2.86	18.36	-7.60
CTOC	17.78	5.18	-7.80	SIGO	23.19	17.71	14.90
ECHA	34.09	19.12	12.80	SRGD	26.58	18.74	0.65
ESJM	32.66	9.61	-47.10	SURI	3.92	12.32	-38.60
FBAQ	-3.31	11.39	12.41	TOPI	29.30	18.15	13.50
GOLF	29.81	19.80	-21.40	UAPE	-8.34	11.03	-6.91
GUAT	10.86	16.65	-5.00	UCNF	37.22	21.22	0.61
IACR	0.14	6.32	-12.24	URUS	4.29	13.86	2.83
IQQE	-0.03	12.97	-4.02	UTAR	-1.16	3.69	-8.10
JRGN	34.88	21.73	-6.63	UTUR	15.91	19.32	-3.05
LCHU	9.27	10.61	-50.70	VIRI	16.60	16.27	-49.10
LIVE	33.89	14.84	4.50	ZAHU	6.95	9.86	-13.20
LOBA	30.63	17.53	-40.10				
MABL	35.54	20.14	-44.10				
MCLA	28.80	16.83	-0.35				
MINF	33.93	17.24	-16.30				
MNMI	-9.38	8.47	-5.50				
OFLA	19.73	19.26	-0.40				
PACO	9.51	9.30	-42.80				
PATI	19.71	14.89	7.80				

Table B.12: *Same as Table B.11, but in ITRF2014 reference frame.*

GPS station	relocking signal component: Period 1			GPS station	relocking signal component: Period 2			GPS station	relocking signal component: Period 3		
	East [mm/y]	North [mm/yr]	Up [mm/yr]		East [mm/y]	North [mm/y]	Up [mm/yr]		East [mm/y]	North [mm/y]	Up [mm/yr]
AEDA	1.22	0.33	0.13	ACAB	15.0	2.3	3.4	AEDA	28.1	7.6	2.9
ATJN	1.11	0.34	0.16	AEDA	23.3	6.3	2.4	AMDE	4.1	0.7	0.1
CBAA	0.95	0.29	-0.02	AR20	7.6	1.9	3.0	BAQU	28.4	9.3	2.9
CGTC	1.21	0.36	0.17	AR40	6.6	2.4	2.5	BDEC	5.7	1.8	0.7
CHM2	0.70	0.30	0.71	AR50	6.2	2.5	2.2	BDJC	2.9	0.9	0.1
CHMZ	0.94	0.41	-0.02	AR60	5.4	2.4	1.7	BLOV	5.5	1.2	0.5
CJNT	0.75	0.20	0.00	AR90	3.5	1.8	0.7	BMWS	5.3	0.6	0.4
COLC	1.01	0.37	0.58	BAQU	23.5	7.7	2.4	BRDQ	2.4	1.0	0.1
COLO	0.78	0.27	-0.02	CA20	10.8	3.0	4.3	BWSZ	3.8	1.4	0.3
CRSC	1.26	0.35	0.14	CAMA	19.1	3.9	3.7	CAMA	23.0	4.7	4.4
FBAQ	1.10	0.25	0.19	CASU	5.7	2.4	1.5	CASU	6.8	3.0	1.9
IACR	0.91	0.21	0.04	CBAA	18.3	5.5	-0.4	CBAA	22.1	6.6	-0.5
IQQE	1.30	0.22	0.11	CENE	12.3	5.3	-1.2	CDLC	32.8	9.3	7.1
JRGN	1.58	0.62	-0.24	CETO	13.0	5.6	-3.1	CETO	15.7	6.8	-3.8
LYAR	0.89	0.26	0.22	CGTC	23.1	6.9	3.3	CGTC	27.9	8.3	4.0
MCLA	1.33	0.43	0.05	CHM2	13.3	5.7	13.6	CHYT	9.4	2.5	4.0
MNMI	0.96	0.41	0.00	CHYT	7.8	2.1	3.3	CJNT	17.3	4.5	0.0
PB01	1.12	0.28	0.17	CJNT	14.3	3.7	0.0	CLLA	21.6	5.1	-1.4
PB02	1.26	0.38	0.23	CO50	15.2	4.0	-0.1	COLA	12.3	5.0	2.5
PB03	1.10	0.34	-0.01	COLA	10.2	4.1	2.1	COLC	23.4	8.6	13.3
PB04	1.43	0.54	0.07	COLC	19.4	7.2	11.1	COLO	18.0	6.1	-0.6
PB05	1.53	0.77	0.41	COLO	14.9	5.1	-0.5	COME	26.3	3.3	4.5
PB06	1.13	0.33	0.10	COME	21.8	2.7	3.7	CRSC	29.0	8.2	3.2
PB07	1.64	0.55	0.18	CRSC	24.1	6.8	2.7	CTOC	16.2	6.9	2.0
PB08	1.08	0.38	0.54	CTOC	13.4	5.7	1.7	ECHA	27.1	6.6	2.3
PB11	0.49	0.09	0.08	ECHA	22.5	5.5	1.9	ESJM	17.7	3.3	-5.4
PCCL	0.82	0.31	0.11	ESJM	14.7	2.7	-4.5	FBAQ	25.4	5.8	4.5
PCHA	0.94	0.28	0.11	FBAQ	21.1	4.8	3.7	GOLF	20.9	6.0	-1.1
PICC	1.11	0.36	0.06	GOLF	17.3	5.0	-0.9	GUAT	29.9	5.1	-1.6
PMEJ	1.41	0.51	-0.14	GUAT	24.8	4.2	-1.3	IACR	21.1	4.9	1.0
PSGA	1.25	0.45	0.27	HUAY	11.3	5.1	2.4	IQQE	29.9	5.2	2.5
PTRE	0.54	0.39	-0.02	IACR	17.5	4.0	0.8	JRGN	36.5	14.4	-5.6
RADO	0.74	0.20	-0.17	IQQE	24.8	4.3	2.1	LCHU	11.9	2.9	11.0
SRGD	1.31	0.35	0.10	JRGN	30.3	11.9	-4.6	LIVE	31.5	9.0	1.5
UAPE	1.52	0.55	0.49	JULO	17.4	5.9	-1.9	LOBA	17.5	8.2	-1.7
UCNF	1.41	0.53	0.13	LCHU	9.8	2.4	9.2	MABL	28.9	6.8	2.4
URUS	0.53	0.19	-0.03	LINZ	13.0	4.9	-1.6	MCLA	30.6	9.9	1.0
UTAR	0.82	0.18	0.14	LIVE	26.1	7.5	1.2	MINF	26.0	5.7	1.5
UTUR	0.70	0.24	0.17	LOBA	14.5	6.8	-1.4	MNMI	22.1	9.5	0.1
VLZL	1.32	0.38	0.17	MABL	23.9	5.6	2.0	OFLA	27.6	9.9	2.9
				MCLA	25.4	8.2	0.9	PACO	12.7	8.1	-3.5
				MEJI	25.3	9.3	1.7	PATI	34.0	6.6	4.1
				MINF	21.6	4.7	1.2	PB01	25.9	6.6	4.0
				MNMI	18.3	7.9	0.1	PB02	29.2	8.8	5.4
				OFLA	22.9	8.2	2.4	PB03	25.4	7.8	-0.2
				PA20	15.1	3.8	1.2	PB04	33.0	12.6	1.7
				PA30	15.0	3.8	2.0	PB05	35.4	17.7	9.4
				PA50	14.6	3.5	3.4	PB06	26.1	7.6	2.3
				PA60	14.0	3.2	4.3	PB07	38.0	12.8	4.1
				PA70	13.4	2.8	4.7	PB09	13.7	1.2	4.3
				PACO	10.5	6.7	-2.9	PBAR	19.1	5.2	-1.9
				PAEL	15.0	7.7	-2.0	PCUA	31.3	10.2	6.5
				PAJA	11.6	3.9	-2.6	PEIN	15.5	8.6	1.4
				PATI	28.2	5.5	3.4	PICA	22.2	6.2	-3.2
				PB01	21.4	5.4	3.3	PLAY	19.1	3.8	0.1
				PB02	24.2	7.3	4.4	PMEJ	32.6	11.8	-3.2
				PB03	21.1	6.5	-0.1	PRO3	31.2	9.5	14.5
				PB04	27.4	10.4	1.4	PSGA	28.9	10.5	6.2
				PB05	29.3	14.7	7.8	PTAR	24.0	5.4	1.4

PB06	21.6	6.3	1.9
PB07	31.5	10.6	3.4
PB08	20.6	7.2	10.4
PB11	11.9	2.2	4.5
PBAR	15.9	4.3	-1.6
PCUA	25.9	8.5	5.4
PEIN	12.9	7.1	1.2
PENI	12.4	2.8	-0.6
PI30	13.8	2.7	4.4
PI40	13.6	2.7	4.8
PI50	13.5	2.5	5.0
PI60	12.9	2.5	5.1
PI70	12.1	2.7	4.9
PI80	11.1	2.7	4.2
PICA	18.4	5.1	-2.6
PICC	21.3	7.0	1.2
PLAY	15.8	3.2	0.1
PMEJ	27.0	9.8	-2.7
PRO1	23.6	8.0	9.1
PRO2	23.8	5.3	9.8
PRO3	25.8	7.9	12.0
PSGA	23.9	8.7	5.1
PTAR	19.9	4.5	1.2
PTRE	10.3	7.4	-0.3
PUQI	19.5	4.9	2.1
QPAC	11.5	4.4	-0.1
RADO	14.3	3.9	-3.3
RLOA	26.3	5.5	4.7
SACA	12.3	6.2	1.1
SACO	7.2	1.0	1.3
SAHU	8.2	1.3	1.8
SIGO	23.3	7.1	3.1
SRGD	25.1	6.8	2.0
SURI	9.4	5.4	1.0
TOPI	22.6	9.2	4.4
UAPE	29.1	10.5	9.4
UCNF	27.0	10.1	2.4
URIB	25.1	8.4	2.4
URUS	10.1	3.6	-0.6
UTAR	15.7	3.5	2.7
UTUR	13.5	4.5	3.2
VIRI	2.3	1.6	0.6
ZAHU	10.9	4.2	-3.2

PTRE	12.5	8.9	-0.4
PUQI	23.6	5.9	2.5
QPAC	13.9	5.4	-0.1
RADO	17.2	4.7	-4.0
SACO	8.7	1.2	1.6
SAHU	9.9	1.5	2.2
SIGO	28.1	8.6	3.7
SRGD	30.3	8.2	2.4
SURI	11.3	6.5	1.2
TOPI	27.3	11.1	5.3
UAPE	35.1	12.6	11.4
UCNF	32.6	12.1	3.0
URUS	12.2	4.3	-0.8
UTAR	19.0	4.2	3.3
UTUR	16.2	5.4	3.9
VIRI	2.7	1.9	0.7
ZAHU	13.1	5.1	-3.9

Table B.13: *Relocking rates derived from interseismic rates (Table B.5), multiplied by the duration of each period or, respectively, for time series starting only after 2014, predicted from the forward model of the interseismic backlsip (interseismic period). The rates are subtracted from the observations of respective model Periods 1–3 (Tables B.7 to B.12).*

C: Supporting Information for *Refining coseismic slip of the 2014 M_w 8.1 Iquique-Pisagua earthquake and the largest M_w 7.7 aftershock by jointly modelling InSAR and GPS data*

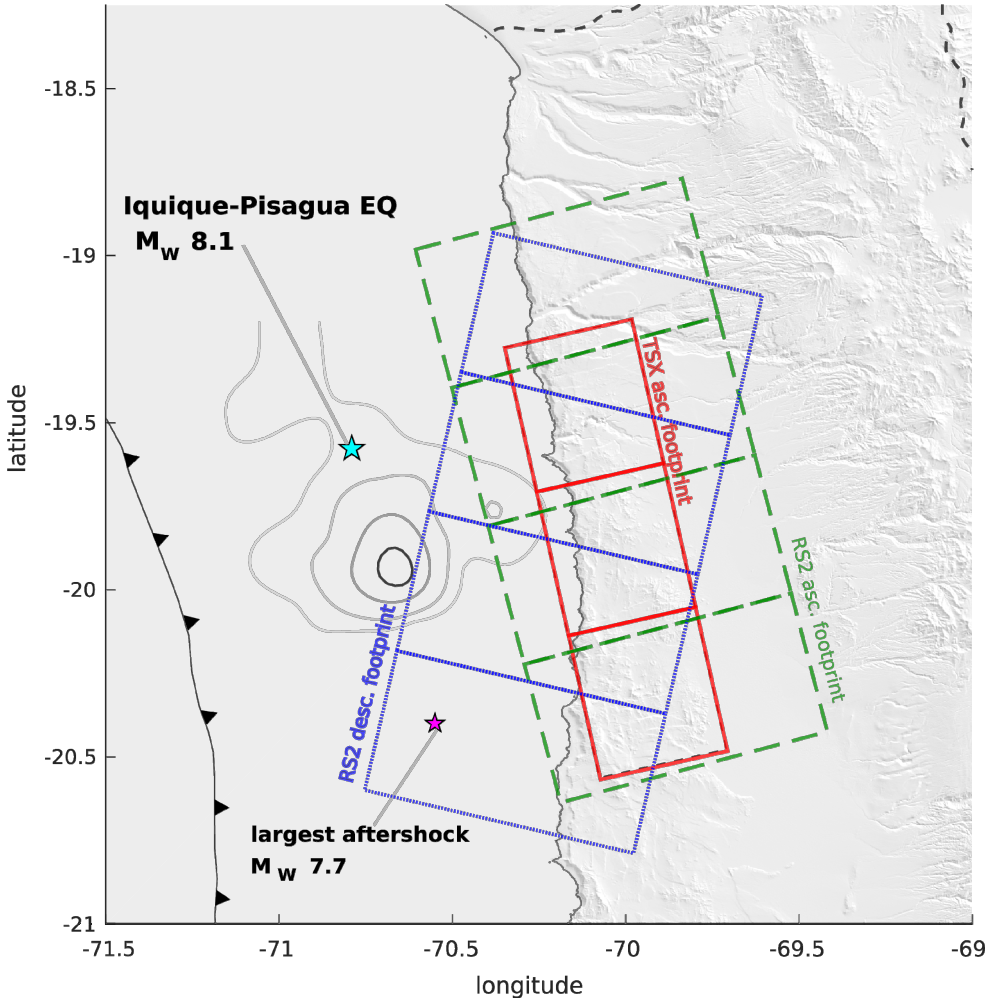

Figure C.1: *Concatenating multiple SAR SLC images for the interferometric approach. A total of four scenes are concatenated along-track for RS2, whereas for TSX three scenes are merged.*

Text C.1: Processing Script

This simplified pseudo-processing script gives an overview about the applied Gamma operations for the example of the Radarsat-2 processing chain. Those steps require knowledge about the command structure of the software and include small explanations (red) and comments (green):

1. update (precise) orbits

RSAT2_vec *.slc.par *_def.orb *% Orbits: 32804, 33147, 33490, 32911*

2. import SLC products

par_RSAT2_SLC *product.xml *lutSigma.xml *imagery_HH.tif HH *.slc.par *.slc

3. Concatenation procedure

a) **create_offset *_1.slc.par *_2.slc.par *1_2.off**

b) **init_offset_orbit *_1.slc.par _2.slc.par *_1_2.off**

c) **offset_pwr *_1.slc *_2.slc *_1.slc.par *_2.slc.par *_1_2.off *_1_2.offs *_1_2.snr - - *_1_2.offset**

d) **offset_fit *_1_2.offs *_1_2.snr *_1_2.off *_1_2.coffs *_1_2.coffset**

e) **SLC_cat _1.slc *_2.slc *_1.slc.par *_2.slc.par *_1_2.off *_1_2.slc *_1_2.slc.par**

f) **multi_look *_1_2.slc *_1_2.slc.par *_1_2.mli *_1_2.mli.par 5 10**

h) % Repeat steps 2. a) - g) with SLCs *_3.slc and *_4.slc to yield *_3_4.slc

i) % Repeat steps 2. a) - g) with SLCs *_1_2.slc and *_3_4.slc to yield *_1_2_3_4.slc

4. co-registration procedure

a) **gc_map *.mli.par - *.dem.par *.dem DEM_segment_gc.dem.par DEM_segment_gc.dem lookup_table 2 2** % Converts DEM from Geocoordinates to radar coordinates

b) **geocode lookup_table DEM_segment_gc.dem width-from-DEM_segment_gc.dem.par DEM_segment_rdc.dem width-and-lines-from-master-mli**

c) **SLC_resamp_lt_all SLC_tab *_1_2_3_4.slc *slave_1_2_3_4.slc.par master.mli.par DEM_segment_rdc.dem /MLI_directory /RSLC_directory /RSLC_tab 0 -m** % performs coregistration

5. interferogram generation

SLC_intf master_1_2_3_4.rslc slave_1_2_3_4.rslc master.rslc.par slave_1_2_3_4.rslc.par master_slave_2.off master_slave.int 5 10

6. generation of baseline file

base_orbit master_1_2_3_4.rslc.par slave_1_2_3_4.rslc.par master_slave.base

7. geocoding look-up table for DEM (geocoordinates to radar coordinates)

gc_map master_1_2_3_4.rslc.par master_slave_2.off pisagua_descending.dem.par pisagua_descending.dem DEM_segment_2.gc.par DEM_segment_2.gc map_to_rdc_2 2 2 pwr_sim_map_2

8. geocode DEM from geocoordinates to radar coordinates

geocode map_to_rdc_2 pwr_sim_map_2 widt-from-dem pwr_sim widt_and_nlines-from-mli 0 0

9. create parameter file for differential interferogram

create_diff_par master_slave_2.off - diff.par 0 1 % window size: 128 128

10. calculate range and azimuth registration offsets between master and slave using cross correlation

a) **offset_pwrm pwr_sim master.mli diff.par master_slave_new.offs master_slave_new.snr 256 256 master_slave_new.offsets 1**

b) **offset_fitm master_slave_new.offs master_slave_new.snr diff.par master_slave_new.coffs master_slave_new.coffsets**

c) **offset_pwrm pwr_sim master.mli diff.par master_slave_new2.offs master_slave_new2.snr 128 128 master_slave_new2.offsets 2**

d) **offset_fitm master_slave_new2.offs master_slave_new2.snr diff.par master_slave_new2.coffs master_slave_new2.coffsets**

11. geocoding lookup table correction using registration offsets of step 10

gc_map_fine map_to_rdc_2 width-dem diff.par MAP_to_RDC_refined_2 1

12. improved geocoding for DEM to radar coordinates

geocode MAP_to_RDC_refined_2 DEM_segment_2.gc width-new-dem-in-gc radarkoordinaten.sint width-mli

13. simulation of unwrapped topographic phase (SINT)

phase_sim master.rslc.par master_slave_2.off master_slave.base radarkoordinaten.sint TOPO_UNW_2.sint

14. Subtraction of SINT from original interferogram returning the wrapped differential interferogram (DINT)

sub_phase master_slave.int TOPO_UNW_2.sint diff.par master_slave.dint 1

15. Geocoding back from radar coordinates to geo-coordinates

geocode_back master_slave.dint width-mli MAP_to_RDC_refined_2 master_slave.dint.gc width-dem-in-gc 0 0 1

16. adaptive filtering

adf master_slave.dint master_slave.dint.sm master_slave.sm.cc width-mli 0.6 64 9

17. Applying coherence masks

rascc_mask master_slave.sm.cc master.mli width-mli 1 1 0 1 1 0.7 0. 0. 0.9 1. .35 1 master_slave.sm.cc_mask.ras

18. minimum cost flow method for unwrapping

mcf master_slave.dint.sm master_slave.sm.cc master_slave.sm.cc_mask.ras master_slave.unw width-mli 0 0 0 - - 1 2 - - - 1

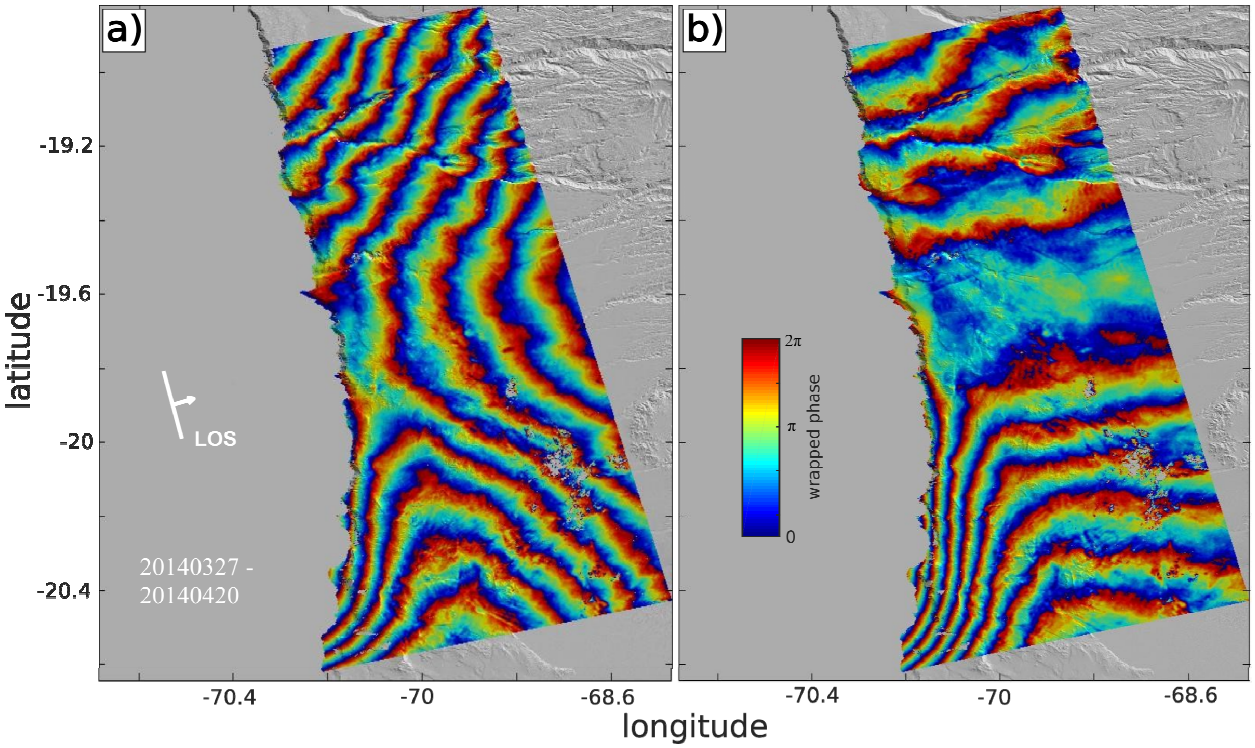

Figure C.2: *a) First processing results of the RS2 27032014-20042014 Wide Multi-look Fine beam mode wrapped interferogram revealed large orbital ramps, b) By applying the new enhanced definitive orbit tool (EDOT) provided by MDA, orbital ramps could be corrected and the quality of RS2 interferograms was significantly improved.*

InSAR cell center coordinates		LOS Deformation [cm]	Error [mm]	InSAR cell center coordinates		LOS Deformation [cm]	Error [mm]	InSAR cell center coordinates		LOS Deformation [cm]	Error [mm]
Lon [°]	Lat [°]			Lon [°]	Lat [°]			Lon [°]	Lat [°]		
-70.29	-18.95	2.37	1.44	-69.93	-19.59	-0.98	1.43	-70.07	-20.02	-10.57	1.43
-70.22	-18.95	8.83	1.45	-70.00	-19.59	-7.19	1.43	-70.22	-19.59	-5.84	1.44
-70.22	-19.02	6.35	1.43	-70.00	-19.66	-9.94	1.43	-70.07	-20.09	-10.56	1.43
-70.29	-19.02	-3.05	1.43	-69.93	-19.66	-3.05	1.43	-70.07	-20.16	-14.42	1.43
-70.29	-19.09	-4.46	1.43	-69.93	-19.73	-3.57	1.43	-70.00	-20.09	-9.10	1.43
-70.22	-19.09	-2.72	1.43	-70.00	-19.73	-11.28	1.43	-69.93	-20.09	-6.93	1.44
-70.22	-19.17	-6.03	1.43	-70.14	-19.66	-9.43	1.43	-69.93	-20.16	-5.53	1.43
-70.22	-19.24	-9.46	1.43	-70.07	-19.66	-9.92	1.43	-70.00	-20.16	-10.06	1.43
-70.22	-19.31	-4.99	1.43	-70.07	-19.73	-8.13	1.43	-70.00	-20.23	-12.52	1.43
-70.22	-19.38	-2.67	1.43	-70.14	-19.73	-9.10	1.43	-69.93	-20.23	-6.71	1.43
-70.22	-19.45	-5.13	1.43	-69.86	-19.52	6.97	1.43	-69.93	-20.30	-3.37	1.43
-70.07	-19.02	11.91	1.43	-69.79	-19.52	8.08	1.43	-70.00	-20.30	-9.09	1.43
-70.14	-19.02	7.94	1.43	-69.79	-19.59	8.72	1.43	-70.14	-20.23	-13.79	1.43
-70.14	-19.09	4.07	1.43	-69.86	-19.59	7.81	1.43	-70.07	-20.23	-12.82	1.43
-70.07	-19.09	7.61	1.43	-69.72	-19.52	8.58	1.43	-70.07	-20.30	-11.07	1.43
-70.07	-19.17	0.59	1.43	-69.65	-19.52	8.71	1.43	-69.86	-20.09	-4.79	1.43
-70.14	-19.17	-1.18	1.43	-69.72	-19.59	9.34	1.43	-69.79	-20.09	5.21	1.43
-69.72	-19.38	8.14	1.43	-69.72	-19.66	12.03	1.43	-69.79	-20.16	6.97	1.43
-69.65	-19.38	9.36	1.43	-69.72	-19.73	16.46	1.43	-69.86	-20.16	-1.18	1.43
-69.65	-19.45	10.15	1.43	-69.86	-19.66	7.70	1.43	-69.86	-20.23	2.48	1.43
-69.72	-19.45	7.36	1.43	-69.79	-19.66	12.05	1.43	-69.86	-20.30	2.11	1.43
-69.86	-19.38	8.87	1.43	-69.79	-19.73	14.42	1.43	-69.86	-20.37	6.86	1.43
-69.79	-19.38	8.44	1.43	-69.86	-19.73	5.16	1.43	-70.14	-20.37	-9.85	1.43
-69.79	-19.45	6.80	1.43	-69.86	-19.81	4.89	1.43	-70.07	-20.37	-12.78	1.43
-69.86	-19.45	9.69	1.43	-69.79	-19.81	14.35	1.43	-70.07	-20.45	-6.45	1.43
-70.14	-19.24	-7.03	1.44	-69.79	-19.88	12.05	1.43	-70.14	-20.45	-2.82	1.43
-70.07	-19.24	-1.55	1.43	-69.86	-19.88	0.45	1.43	-70.00	-20.37	-6.80	1.43
-70.07	-19.31	-7.37	1.43	-69.72	-19.81	15.94	1.43	-69.93	-20.37	-1.18	1.43
-70.14	-19.31	-9.25	1.43	-69.72	-19.88	15.19	1.43	-69.93	-20.45	0.21	1.43
-69.93	-19.31	4.47	1.44	-69.86	-19.95	-2.64	1.43	-70.00	-20.45	-4.07	1.43
-70.00	-19.31	-0.29	1.43	-69.79	-19.95	7.39	1.43	-70.00	-20.52	-3.19	1.43
-70.00	-19.38	3.06	1.43	-69.79	-20.02	4.67	1.43	-69.93	-20.52	3.25	1.43
-69.93	-19.38	8.37	1.43	-69.86	-20.02	-3.86	1.42	-69.93	-20.59	2.58	1.43
-69.93	-19.45	8.81	1.43	-70.14	-19.81	-9.51	1.43	-70.00	-20.59	0.22	1.43
-70.00	-19.45	2.12	1.43	-70.07	-19.81	-10.26	1.43	-70.14	-20.52	-0.58	1.43
-70.14	-19.38	-8.09	1.43	-70.07	-19.88	-8.57	1.43	-70.07	-20.52	-5.67	1.43
-70.07	-19.38	-7.43	1.43	-70.00	-19.81	-13.09	1.43	-70.07	-20.59	0.45	1.43
-70.07	-19.45	-6.75	1.43	-69.93	-19.81	-5.26	1.43	-70.14	-20.59	3.46	1.43
-70.14	-19.45	-8.92	1.43	-69.93	-19.88	-4.38	1.43	-70.00	-20.66	2.81	1.45
-70.14	-19.52	-6.46	1.43	-70.00	-19.88	-8.44	1.42	-69.93	-20.66	5.66	1.44
-70.07	-19.52	-6.19	1.43	-70.00	-19.95	-8.31	1.43				
-70.07	-19.59	-10.15	1.43	-69.93	-19.95	-4.57	1.43				
-70.14	-19.59	-9.25	1.43	-69.93	-20.02	-8.32	1.43				

-70.00	-19.52	1.58	1.43	-70.00	-20.02	-9.60	1.43
-69.93	-19.52	4.27	1.43	-70.07	-19.95	-8.58	1.43

Table C.1: *Displacements of subsampled InSAR data in LOS of the satellite and errors as described in section 4.2.2 used for Sub-model I. The observations are not corrected for the linear ramp as this is part of the inversion.*

InSAR cell center coordinates		LOS Deformation [cm]	Error [mm]	InSAR cell center coordinates		LOS Deformation [cm]	Error [mm]	InSAR cell center coordinates		LOS Deformation [cm]	Error [mm]
Lon [°]	Lat [°]			Lon [°]	Lat [°]			Lon [°]	Lat [°]		
-70.25	-19.29	8.39	0.46	-70.01	-19.78	-36.40	0.43	-70.09	-20.34	36.05	0.45
-70.28	-19.29	15.56	0.47	-69.97	-19.84	-43.54	0.52	-70.05	-20.34	15.80	0.46
-70.20	-19.27	6.09	0.44	-69.97	-19.85	-44.00	0.53	-70.05	-20.37	12.55	0.46
-70.20	-19.33	5.70	0.43	-69.97	-19.87	-45.42	0.52	-70.09	-20.37	29.50	0.45
-70.26	-19.33	15.94	0.43	-70.01	-19.85	-35.99	0.43	-70.15	-20.34	79.66	0.46
-70.24	-19.37	15.86	0.53	-70.01	-19.91	-38.86	0.42	-70.12	-20.34	50.71	0.46
-70.24	-19.39	14.92	0.52	-69.96	-19.89	-45.69	0.46	-70.12	-20.37	51.75	0.45
-70.20	-19.40	5.81	0.43	-69.96	-19.93	-41.72	0.46	-70.16	-20.37	79.34	0.53
-70.20	-19.46	-1.79	0.43	-69.94	-19.97	-43.04	0.43	-70.14	-20.37	71.19	0.53
-70.13	-19.27	9.13	0.43	-70.01	-19.97	-35.43	0.42	-70.14	-20.38	80.39	0.52
-70.09	-19.29	0.83	0.52	-70.13	-19.91	-17.35	0.43	-70.16	-20.38	96.98	0.52
-70.09	-19.32	1.90	0.46	-70.07	-19.91	-26.24	0.42	-70.01	-20.29	-10.88	0.43
-70.09	-19.35	0.74	0.46	-70.07	-19.97	-22.48	0.42	-69.94	-20.29	-34.96	0.43
-70.13	-19.33	2.08	0.42	-70.12	-19.96	-15.05	0.45	-69.94	-20.36	-40.54	0.43
-70.13	-19.40	-0.12	0.43	-70.12	-19.99	-11.82	0.46	-70.02	-20.34	-2.04	0.46
-70.07	-19.40	-2.30	0.43	-70.12	-20.02	-6.60	0.45	-69.99	-20.34	-21.82	0.46
-70.07	-19.46	-6.87	0.43	-70.12	-20.05	-2.71	0.46	-69.99	-20.37	-23.69	0.45
-70.13	-19.46	-6.52	0.43	-70.07	-20.04	-14.73	0.42	-70.02	-20.37	-1.89	0.45
-70.13	-19.53	-4.50	0.43	-70.07	-20.10	-9.02	0.42	-70.02	-20.41	-5.43	0.46
-70.07	-19.53	-8.37	0.43	-70.12	-20.09	-4.40	0.46	-69.99	-20.41	-26.62	0.45
-70.07	-19.59	-17.48	0.43	-70.12	-20.12	1.13	0.46	-69.99	-20.44	-28.81	0.45
-70.13	-19.59	-8.06	0.43	-70.01	-20.04	-27.20	0.43	-70.02	-20.44	-11.73	0.46
-70.03	-19.57	-14.23	0.54	-69.94	-20.04	-44.71	0.43	-69.94	-20.42	-51.12	0.43
-70.03	-19.58	-14.91	0.53	-69.94	-20.10	-45.95	0.42	-69.96	-20.47	-52.41	0.46
-70.02	-19.61	-16.80	0.46	-70.01	-20.10	-25.33	0.43	-69.93	-20.47	-67.96	0.45
-70.02	-19.64	-18.23	0.46	-70.01	-20.17	-19.81	0.43	-69.93	-20.50	-77.96	0.45
-70.02	-19.67	-24.99	0.46	-69.94	-20.17	-38.51	0.43	-69.96	-20.50	-58.08	0.46
-70.01	-19.72	-30.08	0.43	-69.94	-20.23	-36.27	0.43	-70.02	-20.47	-18.54	0.45
-70.13	-19.65	-9.66	0.43	-70.01	-20.23	-16.96	0.43	-69.99	-20.47	-33.52	0.45
-70.07	-19.65	-20.43	0.43	-70.13	-20.17	16.64	0.43	-69.99	-20.50	-43.54	0.46
-70.07	-19.72	-27.96	0.43	-70.07	-20.17	-2.97	0.43	-70.02	-20.50	-29.85	0.45
-70.13	-19.72	-14.46	0.43	-70.07	-20.23	8.25	0.42	-70.15	-20.41	95.96	0.46
-70.20	-19.53	-4.69	0.43	-70.15	-20.21	45.37	0.46	-70.13	-20.40	69.09	0.53
-70.20	-19.59	-7.77	0.43	-70.12	-20.21	26.64	0.45	-70.11	-20.40	51.34	0.52
-70.18	-19.64	-5.70	0.46	-70.12	-20.25	36.73	0.45	-70.11	-20.41	60.67	0.53
-69.90	-20.13	-51.73	0.53	-70.14	-20.24	51.28	0.54	-70.13	-20.41	72.63	0.52

-69.90	-20.14	-50.34	0.53	-70.17	-20.35	98.97	0.59	-70.12	-20.44	64.01	0.45
-69.90	-20.16	-48.25	0.52	-70.17	-20.37	102.9	0.53	-70.15	-20.44	93.68	0.46
-69.89	-20.18	-48.45	0.46	-70.17	-20.38	104.9	0.54	-70.09	-20.41	33.15	0.45
-69.89	-20.21	-50.19	0.46	-70.12	-20.28	46.83	0.46	-70.05	-20.41	13.87	0.46
-69.89	-20.25	-50.81	0.46	-70.12	-20.31	53.03	0.46	-70.05	-20.44	12.00	0.46
-70.13	-19.78	-26.44	0.43	-70.09	-20.28	27.33	0.45	-70.09	-20.43	41.91	0.53
-70.07	-19.78	-32.97	0.42	-70.05	-20.28	9.18	0.45	-70.08	-20.43	22.76	0.52
-70.07	-19.85	-31.79	0.42	-70.05	-20.31	12.75	0.45	-70.08	-20.45	20.40	0.52
-70.13	-19.85	-21.57	0.43	-70.09	-20.31	32.33	0.46	-70.09	-20.45	37.24	0.52

InSAR cell center coordinates		LOS Deformation [cm]	Error [mm]
Lon [°]	Lat [°]		
-70.09	-20.47	23.97	0.46
-70.05	-20.47	1.24	0.45
-70.05	-20.50	-6.79	0.45
-70.09	-20.50	20.39	0.45
-70.15	-20.47	88.33	0.46
-70.13	-20.46	70.93	0.52
-70.11	-20.46	52.38	0.52
-70.11	-20.48	49.50	0.52
-70.13	-20.48	71.04	0.53
-70.12	-20.50	50.97	0.46
-70.15	-20.50	77.16	0.46
-70.12	-20.53	42.92	0.46
-70.12	-20.57	24.53	0.45
-70.09	-20.53	19.04	0.46
-70.05	-20.53	-11.54	0.46
-70.06	-20.56	-7.73	0.56
-70.05	-20.56	-26.94	0.53
-70.05	-20.57	-33.46	0.56
-70.06	-20.57	-13.14	0.57
-70.09	-20.57	5.17	0.46
-70.11	-20.59	10.36	0.61
-70.01	-20.55	-46.18	0.43
-69.96	-20.53	-68.58	0.46
-69.93	-20.53	-87.84	0.45
-69.97	-20.56	-71.77	0.58
-69.88	-20.29	-58.27	0.43
-69.88	-20.36	-64.18	0.42
-69.88	-20.42	-76.62	0.42
-69.84	-20.43	-88.39	0.53
-69.84	-20.45	-91.96	0.52
-69.83	-20.47	-101.41	0.46
-69.83	-20.50	-111.29	0.46
-69.88	-20.49	-89.72	0.42

-69.89	-20.53	-97.94	0.46
-69.86	-20.53	-111.26	0.47
-69.84	-20.53	-114.65	0.53
-69.82	-20.53	-117.01	0.55

Table C.2: *Displacements of subsampled InSAR data in LOS of the satellite and errors as described in section 4.2.2 used for Sub-model II. The observations are not corrected for the linear ramp as this is part of the inversion.*

InSAR cell center coordinates		LOS Deformation [cm]	Error [mm]	InSAR cell center coordinates		LOS Deformation [cm]	Error [mm]	InSAR cell center coordinates		LOS Deformation [cm]	Error [mm]
Lon [°]	Lat [°]			Lon [°]	Lat [°]			Lon [°]	Lat [°]		
-70.20	-19.27	-5.51	0.50	-70.20	-19.41	10.11	0.50	-70.05	-20.05	-2.93	0.50
-70.20	-19.30	-3.54	0.50	-70.20	-19.44	10.74	0.50	-70.05	-20.08	-9.07	0.50
-70.23	-19.30	-6.19	0.50	-70.20	-19.48	17.03	0.50	-70.09	-20.08	-4.22	0.50
-70.20	-19.34	-1.23	0.50	-70.20	-19.59	30.05	0.50	-70.02	-19.98	14.61	0.50
-70.23	-19.37	-1.05	0.50	-70.20	-19.62	27.99	0.50	-69.98	-19.98	13.53	0.50
-70.16	-19.27	-10.19	0.50	-70.12	-19.69	31.03	0.50	-69.98	-20.01	3.01	0.50
-70.12	-19.27	-8.63	0.50	-70.12	-19.73	30.18	0.50	-70.02	-20.01	2.91	0.50
-70.12	-19.30	-2.75	0.50	-70.09	-19.69	30.79	0.50	-69.95	-19.98	11.47	0.50
-70.16	-19.30	-6.74	0.50	-70.05	-19.69	32.44	0.50	-69.95	-20.01	-1.92	0.50
-70.09	-19.30	3.67	0.50	-70.05	-19.73	30.74	0.50	-69.95	-20.05	-12.04	0.50
-70.09	-19.34	12.58	0.50	-70.09	-19.73	30.97	0.50	-69.91	-20.08	-17.66	0.50
-70.09	-19.37	18.55	0.49	-70.09	-19.76	31.58	0.50	-69.95	-20.08	-15.46	0.50
-70.16	-19.34	1.95	0.49	-70.05	-19.76	23.53	0.50	-70.02	-20.05	-6.88	0.50
-70.12	-19.34	5.01	0.50	-70.05	-19.80	26.15	0.50	-69.98	-20.05	-8.26	0.50
-70.12	-19.37	11.61	0.50	-70.09	-19.80	29.67	0.50	-69.98	-20.08	-14.01	0.50
-70.16	-19.37	7.37	0.50	-70.12	-19.76	33.08	0.50	-70.02	-20.08	-14.70	0.50
-70.16	-19.41	13.29	0.50	-70.12	-19.80	36.47	0.50	-70.02	-20.12	-27.10	0.50
-70.12	-19.41	18.24	0.50	-70.02	-19.69	29.54	0.50	-69.98	-20.12	-27.95	0.50
-70.12	-19.44	18.72	0.50	-70.02	-19.73	25.23	0.50	-69.98	-20.16	-37.93	0.50
-70.16	-19.44	15.50	0.50	-70.02	-19.76	24.43	0.50	-70.02	-20.16	-37.36	0.50
-70.09	-19.41	24.72	0.50	-69.98	-19.80	23.82	0.50	-69.95	-20.12	-25.95	0.50
-70.09	-19.44	24.11	0.50	-70.02	-19.80	24.52	0.50	-69.91	-20.12	-28.45	0.50
-70.09	-19.48	21.00	0.50	-70.02	-19.84	23.68	0.50	-69.91	-20.16	-34.62	0.50
-70.05	-19.52	29.46	0.50	-69.98	-19.84	29.65	0.50	-69.95	-20.16	-35.98	0.50
-70.09	-19.52	20.80	0.50	-69.98	-19.87	31.70	0.49	-69.95	-20.19	-40.28	0.50
-70.16	-19.48	17.89	0.50	-70.02	-19.87	24.83	0.50	-69.91	-20.19	-39.55	0.50
-70.12	-19.48	19.18	0.49	-69.95	-19.94	21.21	0.50	-69.91	-20.23	-48.02	0.50
-70.16	-19.52	20.75	0.50	-70.02	-19.91	25.63	0.50	-69.95	-20.23	-50.71	0.50
-70.02	-19.62	29.99	0.50	-69.98	-19.91	26.02	0.50	-70.02	-20.19	-44.96	0.50
-70.02	-19.66	33.66	0.50	-69.98	-19.94	22.62	0.50	-69.98	-20.19	-39.67	0.49
-70.12	-19.55	22.35	0.50	-70.02	-19.94	22.42	0.50	-69.98	-20.23	-51.81	0.50
-70.12	-19.59	25.34	0.50	-70.12	-19.84	37.36	0.50	-70.02	-20.23	-53.40	0.49
-70.16	-19.59	28.03	0.50	-70.09	-19.84	33.49	0.50	-70.09	-20.12	-12.76	0.50
-70.09	-19.55	22.70	0.50	-70.05	-19.84	26.99	0.50	-70.05	-20.12	-20.64	0.50

-70.05	-19.55	31.35	0.49	-70.05	-19.87	25.28	0.50	-70.05	-20.16	-35.99	0.50
-70.05	-19.59	27.18	0.50	-70.09	-19.87	28.98	0.50	-70.09	-20.16	-23.33	0.50
-70.09	-19.59	26.42	0.50	-70.09	-19.91	31.80	0.50	-70.09	-20.19	-35.66	0.50
-70.09	-19.62	30.03	0.50	-70.05	-19.91	28.26	0.50	-70.05	-20.19	-45.68	0.50
-70.05	-19.62	31.07	0.50	-70.05	-19.94	27.20	0.50	-70.05	-20.23	-51.75	0.50
-70.05	-19.66	28.88	0.50	-70.09	-19.94	32.53	0.50	-70.05	-20.26	-59.91	0.50
-70.09	-19.66	29.87	0.50	-70.09	-19.98	28.74	0.50	-70.05	-20.30	-66.26	0.50
-70.16	-19.62	27.99	0.50	-70.05	-19.98	22.34	0.50	-70.09	-20.30	-65.78	0.50
-70.12	-19.62	27.37	0.50	-70.05	-20.01	9.54	0.50	-70.09	-20.33	-72.62	0.50
-70.12	-19.66	28.98	0.50	-70.09	-20.01	13.82	0.50	-70.05	-20.33	-75.90	0.50
-70.16	-19.66	29.27	0.50	-70.09	-20.05	4.82	0.50	-70.05	-20.37	-81.07	0.50

InSAR cell center coordinates		LOS Deformation [cm]	Error [mm]
Lon [°]	Lat [°]		
-70.09	-20.37	-80.91	0.50
-70.16	-20.37	-82.84	0.50
-70.02	-20.26	-61.87	0.50
-69.98	-20.26	-63.64	0.50
-69.98	-20.30	-74.18	0.50
-70.02	-20.30	-68.40	0.50
-69.95	-20.26	-58.37	0.49
-69.91	-20.26	-58.05	0.50
-69.91	-20.30	-65.55	0.50
-69.95	-20.30	-70.58	0.49
-69.95	-20.33	-71.91	0.50
-69.91	-20.33	-71.54	0.50
-69.91	-20.37	-74.47	0.50
-69.95	-20.37	-77.30	0.50
-70.02	-20.33	-78.77	0.49
-69.98	-20.33	-74.79	0.50
-69.98	-20.37	-79.81	0.50
-70.02	-20.37	-81.78	0.50
-70.02	-20.40	-86.35	0.50
-69.98	-20.40	-82.27	0.50
-69.98	-20.44	-84.03	0.50
-70.02	-20.44	-96.17	0.50
-69.95	-20.40	-79.18	0.50
-69.91	-20.40	-76.15	0.50
-69.91	-20.44	-78.59	0.50
-69.95	-20.44	-78.15	0.50
-69.95	-20.48	-78.47	0.50
-69.91	-20.48	-80.91	0.50
-69.91	-20.51	-84.10	0.50
-69.95	-20.51	-88.67	0.50
-70.02	-20.48	-108.87	0.50

-69.98	-20.48	-87.60	0.50
-69.98	-20.51	-106.71	0.50
-70.02	-20.51	-109.79	0.50
-70.12	-20.44	-100.57	0.50
-70.09	-20.40	-94.19	0.50
-70.05	-20.40	-87.63	0.50
-70.05	-20.44	-100.68	0.50

Table C.3: *Displacements of subsampled InSAR data in LOS of the satellite and errors as described in section 4.2.2 used for Sub-model III. The observations are not corrected for the linear ramp as this is part of the inversion.*

InSAR cell center coordinates		LOS Deformation [cm]	Error [mm]	InSAR cell center coordinates		LOS Deformation [cm]	Error [mm]	InSAR cell center coordinates		LOS Deformation [cm]	Error [mm]
Lon [°]	Lat [°]			Lon [°]	Lat [°]			Lon [°]	Lat [°]		
-70.29	-19.00	-42.15	0.55	-70.01	-19.35	-260.43	0.57	-69.86	-19.92	-385.37	0.58
-70.22	-19.00	-45.19	0.64	-70.15	-19.28	-251.84	0.58	-70.15	-19.71	-594.90	0.59
-70.22	-19.07	-89.89	0.65	-70.08	-19.28	-227.73	0.58	-70.08	-19.71	-550.23	0.56
-70.29	-19.07	-85.98	0.64	-70.08	-19.35	-284.82	0.57	-70.08	-19.78	-557.92	0.55
-70.22	-19.14	-142.73	0.55	-70.15	-19.35	-315.76	0.58	-70.15	-19.78	-593.78	0.55
-70.22	-19.21	-206.26	0.54	-70.15	-19.42	-388.86	0.58	-70.01	-19.71	-490.96	0.65
-70.22	-19.28	-268.50	0.58	-70.08	-19.42	-354.23	0.57	-69.94	-19.71	-426.60	0.64
-70.22	-19.35	-343.54	0.58	-70.08	-19.50	-415.64	0.65	-69.94	-19.78	-448.46	0.55
-70.01	-19.00	-34.00	0.55	-70.15	-19.50	-456.46	0.65	-70.01	-19.78	-501.98	0.55
-69.94	-19.07	-57.88	0.54	-70.01	-19.42	-315.36	0.64	-70.01	-19.85	-495.59	0.55
-70.01	-19.07	-66.11	0.55	-69.94	-19.42	-274.30	0.64	-69.94	-19.85	-446.01	0.64
-70.15	-19.00	-43.54	0.54	-69.94	-19.50	-318.69	0.55	-69.94	-19.92	-431.51	0.58
-70.08	-19.00	-38.78	0.54	-70.01	-19.50	-368.11	0.55	-70.01	-19.92	-475.03	0.58
-70.08	-19.07	-80.25	0.57	-70.01	-19.57	-417.27	0.55	-70.08	-19.85	-547.17	0.54
-70.15	-19.07	-90.12	0.58	-69.94	-19.57	-358.34	0.58	-70.08	-19.92	-515.16	0.55
-69.72	-19.07	-25.47	0.57	-69.94	-19.64	-395.73	0.58	-70.22	-19.42	-410.38	0.55
-69.79	-19.07	-35.58	0.58	-70.01	-19.64	-458.53	0.57	-69.58	-19.14	-12.50	0.55
-69.86	-19.07	-48.82	0.54	-70.15	-19.57	-520.91	0.57	-69.58	-19.21	-36.79	0.55
-69.86	-19.14	-78.78	0.54	-70.08	-19.57	-472.29	0.58	-70.08	-19.99	-468.11	0.55
-69.79	-19.14	-63.25	0.58	-70.08	-19.64	-516.31	0.57	-70.08	-20.06	-408.90	0.55
-69.79	-19.21	-86.18	0.58	-70.15	-19.64	-566.40	0.57	-70.01	-19.99	-441.53	0.55
-69.86	-19.21	-106.30	0.55	-69.86	-19.42	-226.64	0.58	-69.94	-19.99	-406.16	0.55
-69.72	-19.14	-46.57	0.55	-69.79	-19.42	-182.10	0.55	-69.94	-20.06	-375.99	0.66
-69.65	-19.14	-30.93	0.54	-69.79	-19.50	-218.40	0.58	-70.01	-20.06	-399.13	0.65
-69.65	-19.21	-51.19	0.55	-69.86	-19.50	-266.13	0.57	-70.01	-20.14	-351.88	0.58
-69.72	-19.21	-68.64	0.55	-69.72	-19.42	-142.70	0.57	-69.94	-20.14	-346.17	0.58
-69.72	-19.28	-92.65	0.55	-69.65	-19.42	-115.88	0.58	-69.94	-20.21	-306.72	0.58
-69.65	-19.28	-71.78	0.55	-69.65	-19.50	-145.56	0.57	-70.01	-20.21	-298.14	0.55
-69.65	-19.35	-89.68	0.55	-69.72	-19.50	-178.08	0.57	-70.08	-20.14	-344.21	0.55
-69.72	-19.35	-114.59	0.55	-69.72	-19.57	-207.38	0.58	-70.08	-20.21	-280.46	0.55
-69.86	-19.28	-145.87	0.55	-69.72	-19.64	-233.89	0.57	-69.86	-19.99	-373.26	0.55

-69.79	-19.28	-116.35	0.54	-69.86	-19.57	-309.20	0.58	-69.79	-19.99	-332.80	0.55
-69.79	-19.35	-144.60	0.58	-69.79	-19.57	-254.85	0.65	-69.79	-20.06	-325.31	0.55
-69.86	-19.35	-181.10	0.57	-69.79	-19.64	-287.59	0.64	-69.86	-20.06	-351.83	0.55
-70.15	-19.14	-142.12	0.57	-69.86	-19.64	-340.55	0.65	-69.86	-20.14	-327.40	0.58
-70.08	-19.14	-126.22	0.66	-69.86	-19.71	-368.44	0.64	-69.86	-20.21	-303.90	0.65
-70.08	-19.21	-180.78	0.71	-69.79	-19.71	-314.91	0.57	-69.86	-20.28	-273.13	0.65
-70.15	-19.21	-191.88	0.65	-69.79	-19.78	-333.29	0.58	-69.86	-20.35	-249.59	0.64
-70.01	-19.14	-106.69	0.66	-69.86	-19.78	-390.58	0.57	-70.08	-20.28	-228.41	0.58
-69.94	-19.14	-92.51	0.58	-69.72	-19.71	-261.37	0.58	-70.08	-20.35	-176.83	0.58
-69.94	-19.21	-132.81	0.58	-69.72	-19.78	-285.97	0.58	-70.15	-20.35	-145.71	0.58
-70.01	-19.21	-163.67	0.57	-69.72	-19.85	-303.39	0.65	-70.01	-20.28	-250.78	0.55
-70.01	-19.28	-204.22	0.57	-69.86	-19.85	-393.56	0.64	-69.94	-20.28	-268.83	0.54
-69.94	-19.28	-174.83	0.57	-69.79	-19.85	-345.87	0.64	-69.94	-20.35	-234.30	0.54
-69.94	-19.35	-221.60	0.58	-69.79	-19.92	-342.32	0.64	-70.01	-20.35	-208.55	0.55

InSAR cell center coordinates		LOS Deformation [cm]	Error [mm]
Lon [°]	Lat [°]		
-70.01	-20.42	-173.31	0.65
-69.94	-20.42	-199.28	0.68
-69.94	-20.49	-172.86	0.69
-70.01	-20.49	-141.89	0.58
-70.15	-20.42	-120.34	0.73
-70.08	-20.42	-140.51	0.55
-70.08	-20.49	-107.68	0.58
-70.15	-20.49	-98.44	0.57
-70.15	-20.56	-82.87	0.70
-70.08	-20.56	-92.09	0.55
-70.01	-20.56	-116.46	0.54
-69.94	-20.56	-145.43	0.54
-69.94	-20.63	-124.71	0.65
-70.01	-20.63	-106.22	0.64

Table C.4: *Displacements of subsampled InSAR data in LOS of the satellite and errors as described in section 4.2.2 used for Sub-model V. The observations are not corrected for the linear ramp as this is part of the inversion.*

InSAR cell center coordinates		LOS Deformation [cm]	Error [mm]	InSAR cell center coordinates		LOS Deformation [cm]	Error [mm]	InSAR cell center coordinates		LOS Deformation [cm]	Error [mm]
Lon [°]	Lat [°]			Lon [°]	Lat [°]			Lon [°]	Lat [°]		
-70.15	-18.93	-142.13	0.48	-69.94	-19.29	-50.50	0.56	-69.65	0.46	0.46	0.46
-70.22	-18.93	-149.59	0.48	-69.87	-19.29	-54.04	0.55	-69.79	0.46	0.46	0.46
-70.22	-19.00	-136.96	0.49	-69.87	-19.36	-41.05	0.48	-69.72	0.55	0.55	0.55
-70.15	-19.00	-130.91	0.46	-69.94	-19.36	-42.34	0.49	-69.72	0.56	0.56	0.56
-70.15	-19.07	-118.36	0.49	-70.08	-19.29	-53.76	0.48	-69.79	0.55	0.55	0.55
-70.22	-19.07	-124.73	0.48	-70.01	-19.29	-53.97	0.49	-70.08	0.46	0.46	0.46

-70.29	-19.00	-140.21	0.48	-70.01	-19.36	-45.96	0.49	-70.01	0.45	0.45	0.45
-70.22	-19.14	-107.86	0.49	-70.08	-19.36	-51.31	0.56	-70.01	0.49	0.49	0.49
-70.15	-19.14	-99.30	0.48	-70.08	-19.43	-38.63	0.55	-70.08	0.49	0.49	0.49
-70.15	-19.22	-72.91	0.48	-70.01	-19.43	-32.56	0.55	-69.94	0.46	0.46	0.46
-70.22	-19.22	-80.43	0.49	-70.01	-19.50	-19.00	0.55	-69.87	0.45	0.45	0.45
-70.22	-19.29	-67.58	0.48	-70.08	-19.50	-21.78	0.49	-69.87	0.46	0.46	0.46
-70.15	-19.29	-59.29	0.49	-69.94	-19.43	-28.22	0.48	-69.94	0.45	0.45	0.45
-70.15	-19.36	-58.00	0.56	-69.87	-19.43	-29.14	0.48	-69.94	0.45	0.45	0.45
-70.22	-19.36	-52.67	0.55	-69.87	-19.50	-21.69	0.48	-69.87	0.48	0.48	0.48
-70.01	-18.93	-111.66	0.56	-69.94	-19.50	-22.77	0.49	-69.87	0.49	0.49	0.49
-70.08	-18.93	-125.64	0.55	-69.94	-19.57	-16.68	0.55	-69.94	0.48	0.48	0.48
-69.94	-18.86	-115.14	0.48	-69.87	-19.57	-14.75	0.55	-70.08	0.49	0.49	0.49
-69.87	-18.86	-112.40	0.49	-69.87	-19.64	-16.59	0.55	-70.01	0.45	0.45	0.45
-69.87	-18.93	-98.53	0.48	-69.94	-19.64	-17.53	0.56	-70.01	0.45	0.45	0.45
-69.94	-18.93	-108.69	0.49	-70.08	-19.57	-19.25	0.49	-70.08	0.49	0.49	0.49
-69.94	-19.00	-98.97	0.49	-70.01	-19.57	-18.29	0.49	-70.22	0.49	0.49	0.49
-69.87	-19.00	-94.14	0.56	-70.01	-19.64	-18.10	0.49	-70.15	0.46	0.46	0.46
-69.87	-19.07	-77.61	0.55	-70.08	-19.64	-21.84	0.48	-70.15	0.46	0.46	0.46
-69.94	-19.07	-85.18	0.55	-69.79	-19.43	-23.37	0.49	-70.15	0.45	0.45	0.45
-70.08	-19.00	-117.48	0.55	-69.72	-19.43	-20.44	0.49	-70.15	0.46	0.46	0.46
-70.01	-19.00	-103.99	0.49	-69.72	-19.50	-17.87	0.59	-70.15	0.46	0.46	0.46
-70.01	-19.07	-99.19	0.48	-69.79	-19.50	-21.94	0.56	-70.15	0.46	0.46	0.46
-70.08	-19.07	-110.83	0.48	-69.65	-19.50	-18.32	0.59	-69.51	0.46	0.46	0.46
-69.79	-19.00	-86.04	0.48	-69.65	-19.57	-15.47	0.60	-69.51	0.46	0.46	0.46
-69.79	-19.07	-72.26	0.49	-69.65	-19.64	-20.23	0.49	-69.51	0.46	0.46	0.46
-69.79	-19.14	-63.15	0.55	-69.79	-19.57	-16.07	0.64	-69.51	0.46	0.46	0.46
-69.79	-19.22	-51.91	0.55	-69.72	-19.57	-14.08	0.46	-69.44	0.45	0.45	0.45
-69.79	-19.29	-47.56	0.55	-69.72	-19.64	-19.83	0.49	-69.51	0.49	0.49	0.49
-69.72	-19.29	-41.94	0.56	-69.79	-19.64	-15.13	0.48	-69.51	0.48	0.48	0.48
-69.72	-19.36	-29.02	0.49	-69.79	-19.71	-23.19	0.61	-69.44	0.48	0.48	0.48
-69.79	-19.36	-34.62	0.49	-69.72	-19.71	-26.75	0.46	-70.15	0.57	0.57	0.57
-70.08	-19.14	-95.83	0.49	-69.72	-19.78	-27.35	0.45	-70.15	0.62	0.62	0.62
-70.01	-19.14	-88.11	0.48	-69.79	-19.78	-29.64	0.45	-70.15	0.56	0.56	0.56
-70.01	-19.22	-69.69	0.49	-69.65	-19.71	-26.48	0.56	-70.08	0.57	0.57	0.57
-70.08	-19.22	-69.85	0.49	-69.58	-19.78	-33.31	0.55	-70.01	0.49	0.49	0.49
-69.94	-19.14	-72.92	0.59	-69.65	-19.78	-29.21	0.49	-70.01	0.49	0.49	0.49
-69.87	-19.14	-68.29	0.56	-69.65	-19.86	-40.70	0.49	-70.08	0.48	0.48	0.48
-69.87	-19.22	-62.09	0.59	-69.58	-19.86	-41.76	0.45	-69.94	0.48	0.48	0.48
-69.94	-19.22	-65.24	0.60	-69.58	-19.93	-61.66	0.49	-69.87	0.48	0.48	0.48

InSAR cell center coordinates		LOS Deformation [cm]	Error [mm]	InSAR cell center coordinates		LOS Deformation [cm]	Error [mm]
Lon [°]	Lat [°]			Lon [°]	Lat [°]		
-69.87	-20.07	-85.12	0.46	-69.94	-20.28	-118.80	0.49
-69.94	-20.07	-83.32	0.46	-69.87	-20.28	-134.87	0.50
-69.94	-20.14	-93.80	0.45	-69.87	-20.35	-150.76	0.47

-69.87	-20.14	-103.44	0.49
-69.87	-20.21	-119.55	0.48
-69.94	-20.21	-107.02	0.48
-70.08	-20.14	-31.89	0.57
-70.01	-20.14	-72.10	0.62
-70.01	-20.21	-83.06	0.56
-70.08	-20.21	-36.83	0.57
-69.79	-20.00	-68.61	0.49
-69.72	-20.00	-75.54	0.49
-69.72	-20.07	-92.30	0.48
-69.79	-20.07	-88.83	0.48
-69.65	-20.00	-76.71	0.48
-69.58	-20.00	-76.62	0.49
-69.58	-20.07	-82.07	0.48
-69.65	-20.07	-90.53	0.49
-69.65	-20.14	-107.15	0.49
-69.58	-20.14	-103.61	0.48
-69.58	-20.21	-121.38	0.49
-69.65	-20.21	-119.93	0.49
-69.79	-20.14	-110.11	0.48
-69.72	-20.14	-111.89	0.56
-69.72	-20.21	-123.76	0.56
-69.79	-20.21	-125.54	0.55
-69.79	-20.28	-136.32	0.55
-69.72	-20.28	-133.59	0.46
-69.72	-20.35	-151.59	0.46
-69.79	-20.35	-153.09	0.46
-69.65	-20.28	-135.63	0.49
-69.58	-20.28	-133.56	0.49
-69.58	-20.35	-147.99	0.48
-69.65	-20.35	-151.01	0.48
-69.65	-20.42	-167.08	0.49
-69.58	-20.42	-164.48	0.48
-69.65	-20.50	-177.44	0.48
-69.79	-20.42	-167.78	0.49
-69.72	-20.42	-170.40	0.46
-69.72	-20.50	-183.40	0.49
-69.79	-20.50	-180.53	0.48
-70.08	-20.28	-37.42	0.48
-70.01	-20.28	-88.04	0.49
-70.01	-20.35	-97.37	0.48
-70.08	-20.35	-41.52	0.48
-69.94	-20.35	-126.54	0.46
-69.94	-20.42	-139.42	0.46
-69.87	-20.42	-163.87	0.56
-69.87	-20.50	-174.13	0.55
-69.94	-20.50	-153.28	0.46
-70.08	-20.42	-50.85	0.46
-70.01	-20.42	-103.64	0.46
-70.01	-20.50	-113.75	0.55
-70.08	-20.50	-66.66	0.49
-70.08	-20.57	-88.52	0.49
-70.01	-20.57	-128.49	0.45
-69.94	-20.57	-154.53	0.46
-70.15	-20.57	-41.65	0.46

Table C.5: *Displacements of subsampled InSAR data in LOS of the satellite and errors as described in section 4.2.2 used for Sub-model VI. The observations are not corrected for the linear ramp as this is part of the inversion.*

GPS station	Data observation (total)			East error [mm]	North error [mm]	Up error [mm]
	East [mm]	North [mm]	Up [mm]			
aeda	-49.43	-5.40	-6.55	0.7	0.9	1.7
atjn	-52.67	-14.30	-26.30	0.7	0.9	1.4
cbaa	5.80	3.07	-0.25	0.7	0.9	1.4
chm2	-44.47	-7.72	5.15	0.7	0.9	1.4
cjnt	5.96	3.34	1.40	0.7	0.9	1.4
colc	-22.96	-6.03	-1.90	0.8	1.0	2.2
colo	4.43	4.72	1.10	0.7	0.9	1.4
crsc	-17.04	2.30	-4.25	0.7	0.9	1.4
iacr	-15.39	-17.83	-9.45	0.6	0.9	1.4
iqqe	-62.97	-7.97	-13.50	0.8	1.4	2.0
jrgn	6.97	0.35	-5.70	0.7	0.9	1.4
mcla	7.90	0.44	-4.05	0.7	0.9	1.4
mnmi	-46.06	-17.67	-4.05	0.8	1.0	2.3
pb01	-14.84	7.02	-7.75	0.7	0.9	1.5
pb02	-2.26	1.66	-1.35	0.7	0.9	1.4
pb03	5.78	0.99	-4.75	0.7	0.9	1.4
pb04	7.45	0.12	-1.55	0.7	0.9	1.4
pb05	7.56	0.26	-3.30	0.7	0.9	1.4
pb06	7.69	1.02	0.50	0.7	0.9	1.4
pb08	-39.39	-0.62	-1.30	0.7	0.9	1.4
pb11	-51.58	-12.41	-12.85	0.7	0.9	1.4
pccl	-17.91	-18.09	-8.90	0.6	0.9	1.4
pcha	-49.86	-8.83	-6.30	0.8	1.0	2.3
picc	-35.21	2.00	-3.10	0.8	0.9	1.7
pmej	9.22	2.59	-1.60	0.8	1.0	2.3
psga	-45.16	-14.55	-22.00	0.8	1.0	2.3
ptre	-10.60	-16.95	1.15	0.6	0.9	1.4
srgd	7.74	0.60	-1.85	0.7	0.9	1.4
tuzg	3.39	1.56	0.00	0.7	1.0	1.4
uape	-65.12	-10.48	-11.50	0.7	0.9	1.7
ucnf	7.72	0.80	4.50	0.8	1.0	2.2
urus	0.72	-0.78	0.10	0.7	1.4	1.7
utar	-17.15	-24.51	2.30	0.7	0.9	1.6
utur	3.77	3.66	-4.65	0.7	0.9	1.5
vlzl	7.65	-0.10	-1.15	0.7	0.9	1.4

Table C.6: *Static displacements of cGPS data in three components ENU in SOAM reference frame and errors as described in section 4.2.3 used for Sub-model I. The observations are corrected for the seasonal trend and antenna offsets.*

GPS station	Data observation (total)			East error [mm]	North error [mm]	Up error [mm]
	East [mm]	North [mm]	Up [mm]			
atjn	-81.09	-28.05	-32.90	0.7	0.9	1.4

cbaa	4.34	4.16	-4.15	0.7	0.9	1.4
cgtc	-218.26	-50.29	-21.00	0.7	0.9	1.4
chm2	-102.75	-38.04	-4.20	0.7	0.9	1.4
chmz	-103.35	-38.52	-2.40	0.7	0.9	1.4
cjnt	5.05	4.01	-2.60	0.7	0.9	1.4
colc	-50.03	-20.26	-7.30	0.8	1.0	2.2
colo	0.69	7.70	-1.20	0.7	0.9	1.4
crsc	-92.74	-21.61	-6.25	0.7	0.9	1.4
iacr	-25.07	-21.36	-5.55	0.6	0.9	1.4
jrgn	8.02	0.55	-5.35	0.7	0.9	1.4
lyar	-3.11	-8.43	1.75	0.8	0.9	2.1
mcla	9.45	-1.42	-6.05	0.7	0.9	1.4
mnmi	-76.95	-38.86	-12.90	0.8	1.0	2.3
pb01	-70.41	26.10	-24.40	0.7	0.9	1.5
pb02	-18.64	1.95	-13.40	0.7	0.9	1.4
pb03	4.57	0.00	-0.85	0.7	0.9	1.4
pb04	8.21	-2.79	-3.80	0.7	0.9	1.4
pb05	8.90	-1.20	-0.25	0.7	0.9	1.4
pb06	7.72	-0.24	-4.60	0.7	0.9	1.4
pb08	-130.15	-22.81	-18.30	0.7	0.9	1.4
pb11	-126.56	-61.28	-30.90	0.7	0.9	1.4
pccl	-25.94	-27.27	-17.75	0.6	0.9	1.4
pcha	-136.50	-54.34	-32.45	0.8	1.0	2.4
picc	-154.74	-0.53	-38.10	0.8	0.9	1.7
pmej	10.37	-0.75	-5.50	0.8	1.0	2.3
psga	-86.04	-33.59	-29.35	0.8	1.0	2.3
ptre	-17.68	-25.00	-4.65	0.6	0.9	1.4
srgd	8.14	0.28	-4.45	0.7	0.9	1.4
tuzg	4.35	0.69	-6.70	0.7	1.0	1.4
ucnf	12.17	0.05	-4.90	0.8	1.0	2.2
urus	-4.77	-5.06	-3.20	0.7	1.4	1.7
utar	-29.27	-31.10	5.75	0.7	0.9	1.6
utur	0.78	4.93	-2.75	0.7	0.9	1.5
vlzl	8.80	-1.22	-6.30	0.7	0.9	1.4

Table C.7: *Static displacements of cGPS data in three components ENU in SOAM reference frame and errors as described in section 4.2.3 used for Sub-model II. The observations are corrected for the seasonal trend and antenna offsets.*

GPS station	Data observation (total)			East error [mm]	North error [mm]	Up error [mm]
	East [mm]	North [mm]	Up [mm]			
atjn	-494.90	-280.18	-57.90	0.6	0.9	1.4
cbaa	38.56	12.66	0.90	0.7	0.9	1.4
cgtc	-363.05	76.79	-82.50	0.7	0.9	1.4
chmz	-190.65	-16.18	-17.90	0.7	0.9	1.5
cjnt	33.04	10.58	4.80	0.7	0.9	1.6
colc	-67.96	-15.68	4.50	0.8	1.0	2.2

colo	30.32	16.83	38.10	0.7	0.9	1.4
crsc	-23.28	-5.09	-12.30	0.7	0.9	1.4
iqqe	-435.88	14.56	13.40	0.8	1.2	2.0
jrgn	79.66	23.63	-8.70	0.7	0.9	1.4
mcla	64.98	16.94	4.00	0.7	0.9	1.4
mnmi	-212.06	-110.08	-24.00	0.7	1.0	2.2
pb01	23.01	30.77	5.00	0.7	0.9	1.5
pb02	56.96	18.69	-0.80	0.7	0.9	1.4
pb04	66.01	17.26	-0.40	0.7	0.9	1.4
pb06	56.72	11.06	2.20	0.7	0.9	1.4
pb07	63.98	14.89	2.30	0.7	0.9	1.4
pb08	-130.75	33.66	-5.30	0.7	0.9	1.4
pcha	-268.70	4.07	-20.20	0.8	1.0	2.3
picc	-76.32	50.82	-8.20	0.8	1.0	2.2
pmej	72.28	21.78	-4.00	0.8	1.0	2.4
ptre	-24.33	-41.35	-5.00	0.7	0.9	1.5
rado	41.98	12.77	-9.40	0.8	1.0	2.0
srgd	53.29	10.48	1.50	0.7	0.9	1.4
uape	-464.34	22.55	74.70	0.9	1.0	2.8
ucnf	71.30	18.92	4.30	0.9	1.1	2.3
urus	4.01	-1.63	-1.70	0.6	1.0	1.5
utar	-16.23	-64.99	-32.20	0.7	0.9	2.2
utur	27.94	12.24	6.70	0.7	0.9	1.5
vlzl	63.83	15.80	14.10	0.7	0.9	1.4

Table C.8: *Static displacements of cGPS data in three components ENU in SOAM reference frame and errors as described in section 4.2.3 used for Sub-model III. The observations are corrected for the seasonal trend and antenna offsets.*

GPS station	Data observation (total)			East error [mm]	North error [mm]	Up error [mm]
	East [mm]	North [mm]	Up [mm]			
atjn	-509.98	-290.85	-156.50	0.6	0.9	1.4
cbaa	47.70	14.37	-3.40	0.7	0.9	1.4
cgtc	-492.66	42.42	-69.30	0.7	0.9	1.4
chmz	-224.55	-38.06	-22.80	0.7	1.0	1.4
colo	34.44	19.78	37.30	0.7	1.0	1.4
crsc	-16.48	-5.39	-7.30	0.7	0.9	1.3
iqqe	-435.82	9.42	4.50	0.8	1.1	1.9
jrgn	96.91	27.97	-7.90	0.7	0.9	1.4
mcla	82.31	18.99	5.00	0.7	0.9	1.4
mnmi	-229.65	-128.86	-27.20	0.8	1.0	2.2
pb01	-20.05	52.07	-6.90	0.7	0.9	1.5
pb03	75.95	13.20	7.60	0.7	0.9	1.4
pb04	82.71	17.79	0.90	0.7	0.9	1.4
pb06	69.89	11.09	-0.90	0.7	0.9	1.4
pccl	-27.73	-73.04	-13.10	0.6	0.9	1.4

pcha	-344.83	-39.21	-54.60	0.8	1.0	2.2
picc	-184.02	50.70	-40.60	0.8	1.0	2.1
pmej	89.90	24.32	-5.80	0.8	1.0	2.4
psga	-792.45	-247.37	-264.70	0.8	1.0	2.2
rado	49.71	15.75	-10.30	0.8	1.0	2.0
srgd	66.66	12.20	2.30	0.7	0.9	1.4
uape	-465.91	20.79	86.10	0.9	1.0	2.8
ucnf	90.75	21.27	-0.80	0.9	1.1	2.2
urus	4.11	-2.48	-2.90	0.6	1.0	1.5
utar	-16.76	-72.63	-24.30	0.7	1.0	2.1
utur	33.56	15.93	11.00	0.7	1.0	1.5

Table C.9: *Static displacements of cGPS data in three components ENU in SOAM reference frame and errors as described in section 4.2.3 used for Sub-model V. The observations are corrected for the seasonal trend and antenna offsets.*

GPS station	Data observation (total)			East error [mm]	North error [mm]	Up error [mm]
	East [mm]	North [mm]	Up [mm]			
atjn	-597.61	-306.25	-182.15	0.7	0.9	1.5
cbaa	-2.19	5.62	-0.95	0.7	1.0	1.4
cgtc	-600.42	18.19	-95.20	0.7	0.9	1.4
chm2	-313.64	-65.52	-19.05	0.7	1.0	1.5
chmz	-314.15	-65.40	-18.00	0.7	1.0	1.5
cjnt	-2.07	3.83	-1.55	0.7	1.0	1.5
colc	-145.44	-42.92	-5.65	0.8	1.0	2.3
colo	-11.45	10.31	2.80	0.7	1.0	1.5
crsc	-106.54	-23.37	-20.50	0.7	0.9	1.4
iacr	-70.10	-80.33	-35.10	0.7	0.9	1.4
iqqe	-536.30	-9.23	0.40	0.8	1.4	2.2
jrgn	6.54	0.44	-2.00	0.8	0.9	1.4
mcla	4.90	-2.68	-5.10	0.7	0.9	1.4
pb01	-97.99	42.29	-24.25	0.7	1.0	1.5
pb02	-29.39	1.61	-17.35	0.7	0.9	1.4
pb03	-0.72	-1.03	-3.65	0.7	0.9	1.5
pb04	5.16	-4.84	-6.20	0.7	0.9	1.4
pb05	4.03	-3.39	-7.95	0.7	0.9	1.4
pb06	2.89	-0.94	-3.45	0.7	0.9	1.4
pb07	-4.70	-3.85	-12.30	0.7	0.9	1.4
pb08	-290.22	-1.61	-25.65	0.7	1.0	1.5
pb11	-562.24	-118.32	-110.95	0.7	0.9	1.4
pcha	-427.97	-60.58	-68.05	0.8	1.0	2.4
picc	-264.44	40.06	-43.50	0.8	1.0	1.9
pmej	6.16	-0.06	-6.30	0.9	1.0	2.3
psga	-871.83	-264.67	-277.30	0.8	1.0	2.3
ptre	-62.46	-70.85	-6.95	0.7	1.0	1.5
rado	-10.03	9.57	-1.40	0.8	1.0	1.8

srgd	2.45	0.08	-0.05	0.7	1.0	1.4
tuzg	-1.52	1.46	0.45	0.8	1.0	1.5
uape	-568.65	-1.38	63.45	0.8	1.0	2.3
ucnf	6.15	-1.17	-0.95	0.9	1.0	2.3
urus	-20.45	-10.60	8.45	0.8	1.5	1.9
utar	-73.45	-86.98	-33.75	0.8	1.0	2.3
utur	-9.76	7.20	0.70	0.7	1.0	1.6
vlzl	3.94	-1.08	2.00	0.8	1.0	1.5

Table C.10: *Static displacements of cGPS data in three components ENU in SOAM reference frame and errors as described in section 4.2.3 used for Sub-model VI. The observations are corrected for the seasonal trend and antenna offsets.*

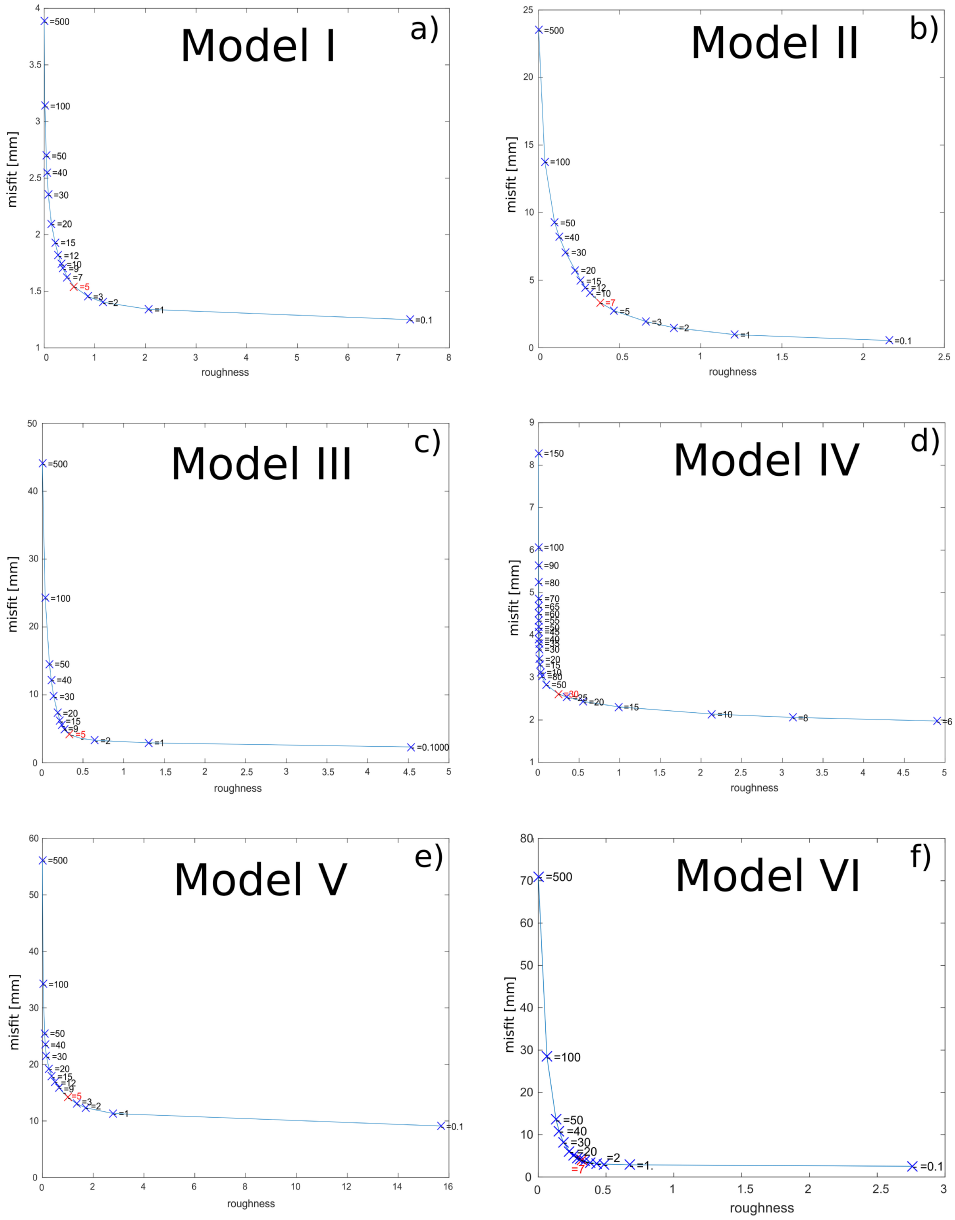

Figure C.3: *Trade-off curves of different models between roughness and misfit (in mm) using different smoothing values, the preferred one indicated in red. I used a smoothing of a) 5 b) 7 c) 5 d) 30 e) 5 f) 7.*

Misfit and roughness were calculated based on Menke (2012):

$$misfit = (G \cdot X) - data$$

, where G are the Greens functions and X is the modelled slip and

$$roughness = [DX]^T \cdot [DX]$$

, where D is the roughness matrix defined in Menke (2012).

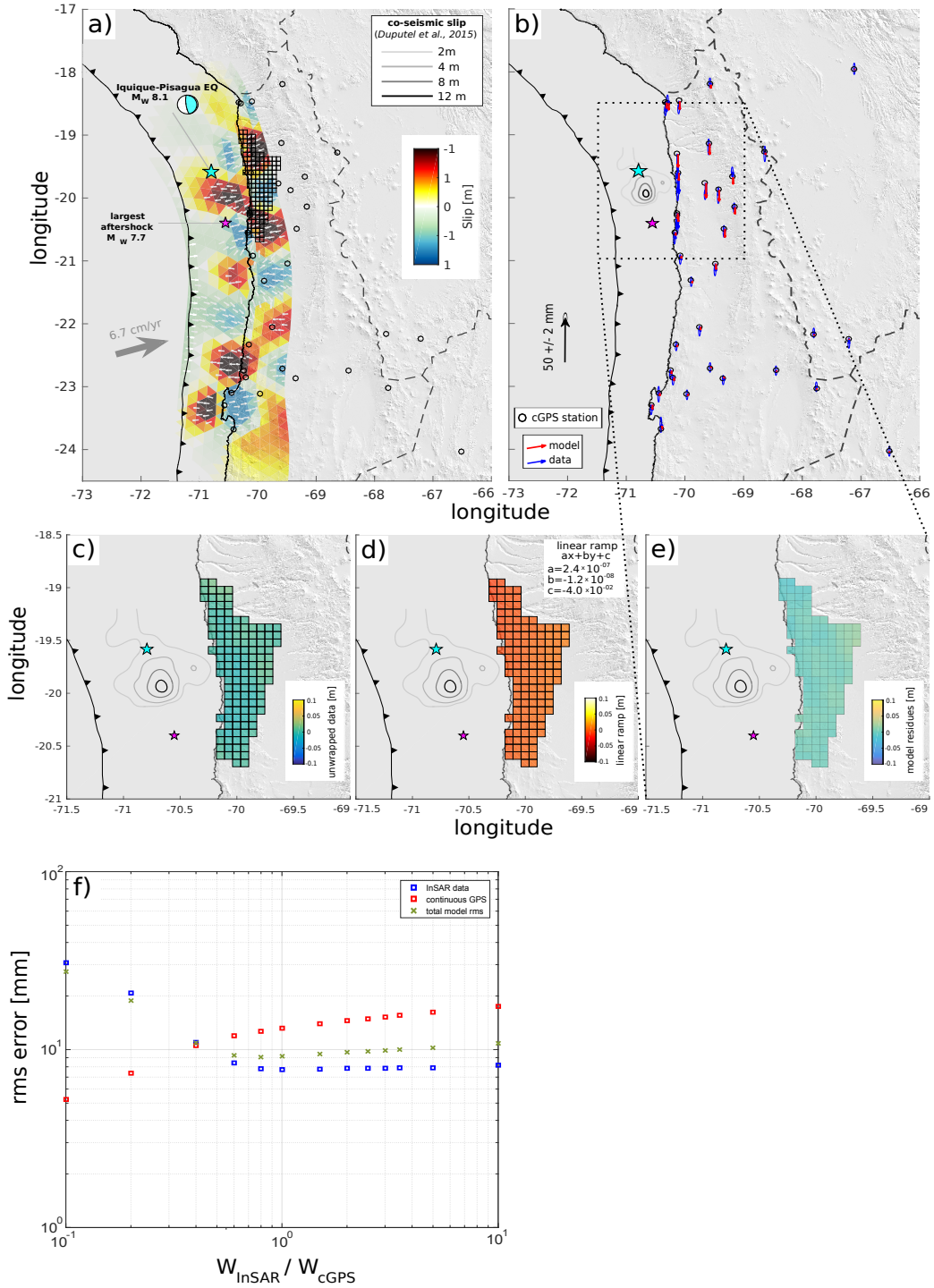

Figure C.4: *Auxiliary material for Sub-model I:*
a) The checkerboard test reveals resolution on the subducting plate interface. A slip of +/- 1 m on rectangular fault patches with ~80x80 km size was forward modelled and inverted. Input data are cGPS stations marked with black circles and subsampled InSAR data highlighted as black grid, b) modelled (red) and observed (blue) vertical cGPS displacements are displayed with 1-sigma uncertainties, c) the subsampled unwrapped InSAR data (desc. RS2 04042014-15062014), d) the linear ramp (ax+by+c) of the unwrapped InSAR data (desc. RS2 04042014-15062014) and e) the InSAR model residuals from the slip inversion of Model I, f) test of different weighting ratios w = w_{InSAR}/w_{cGPS}, where single cGPS rms error (red rectangles), single InSAR error (blue rectangles) and total error (green crosses) are plotted together. Least total rms error occurs at w = 0.75. For other features refer to Figure 4.11.

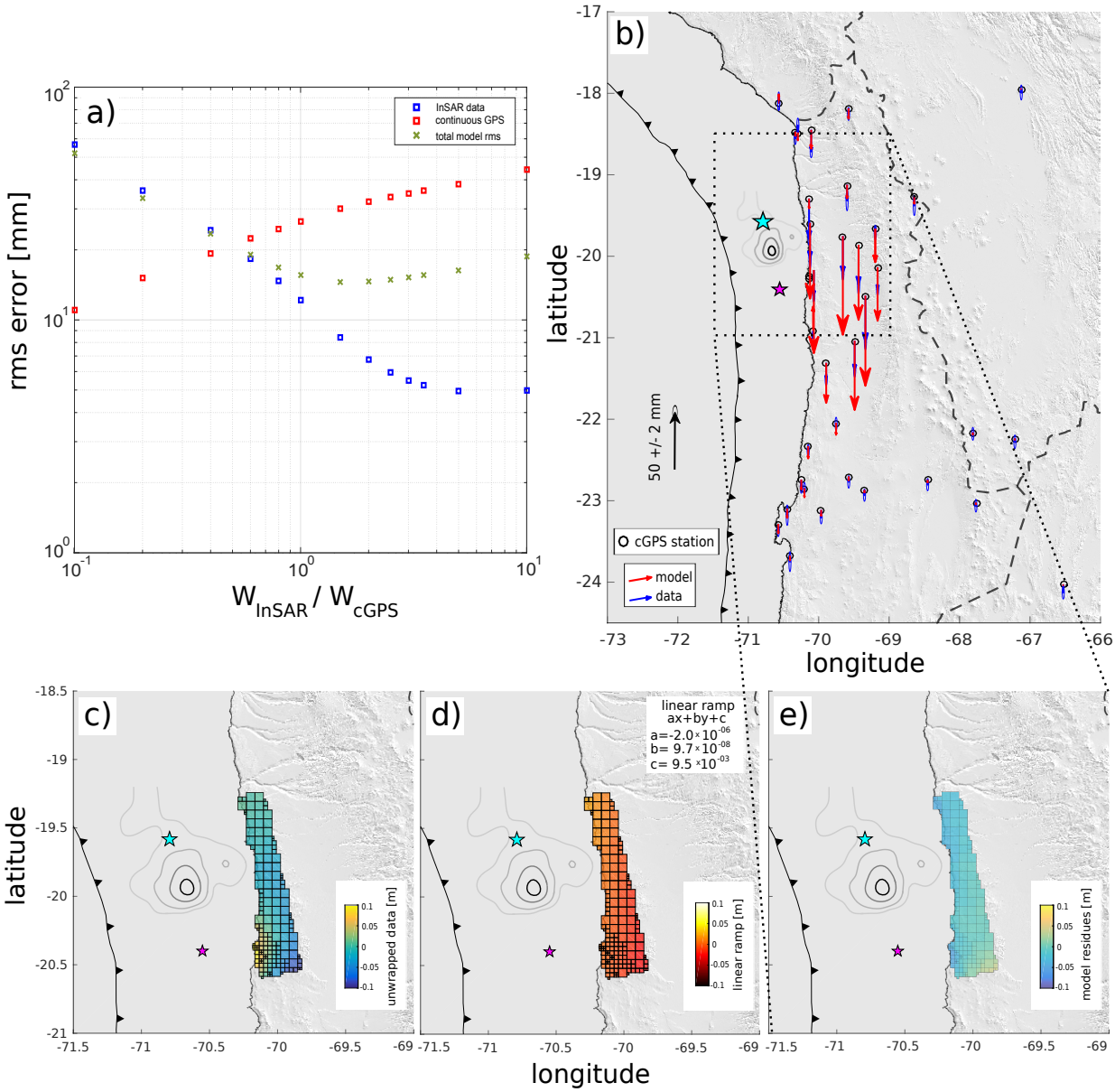

Figure C.5: *Auxiliary material for Sub-model II:*
a) Test of different weighting ratios w = w_{InSAR}/w_{cGPS}, where single cGPS rms error (red rectangles), single InSAR error (blue rectangles) and total error (green crosses) are plotted together. Least total rms error occurs at w = 1.5, b) Modelled (red) and observed (blue) vertical cGPS displacements are displayed with 1-sigma uncertainties, c) the subsampled unwrapped InSAR data (asc. TSX 02042014-18062014), d) the linear ramp (ax+by+c) of the unwrapped InSAR data (asc. TSX 02042014-18062014) and e) the InSAR model residuals from the slip inversion of Model II. For other features refer to Figure 4.11.

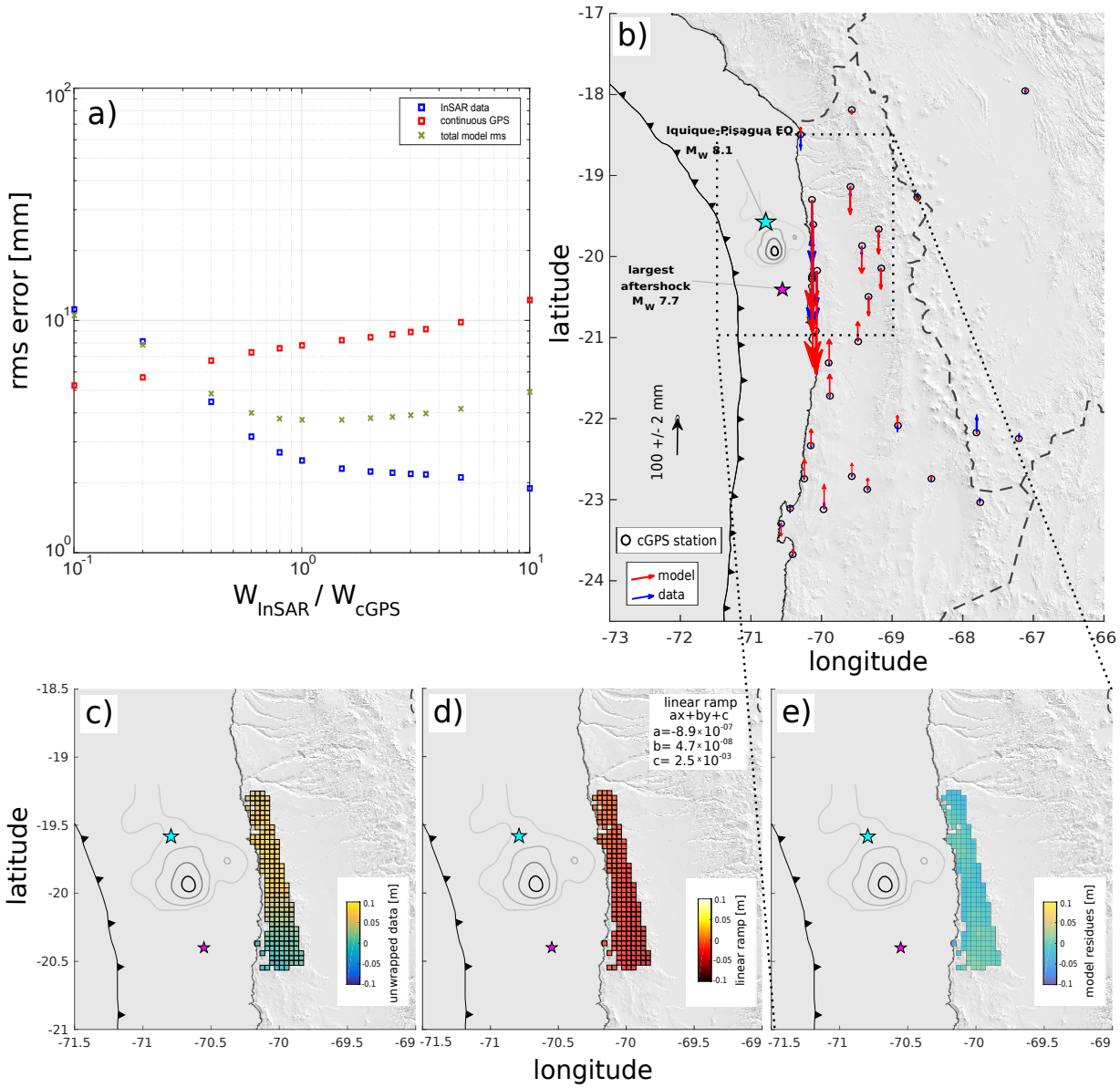

Figure C.6: *Auxiliary material for Sub-model III:*
a) Test of different weighting ratios w = w_{InSAR}/w_{cGPS}, where single cGPS rms error (red rectangles), single InSAR error (blue rectangles) and total error (green crosses) are plotted together. Least total rms error occurs at w = 1.25, b) Modelled (red) and observed (blue) vertical cGPS displacements are displayed with 1-sigma uncertainties, c) the subsampled unwrapped InSAR data (asc. TSX 18122011-02042014), d) the linear ramp (ax+by+c) of the unwrapped InSAR data (asc. TSX 18122011-02042014) and e) the InSAR model residuals from the slip inversion of Model III. For other features refer to Figure 4.11.

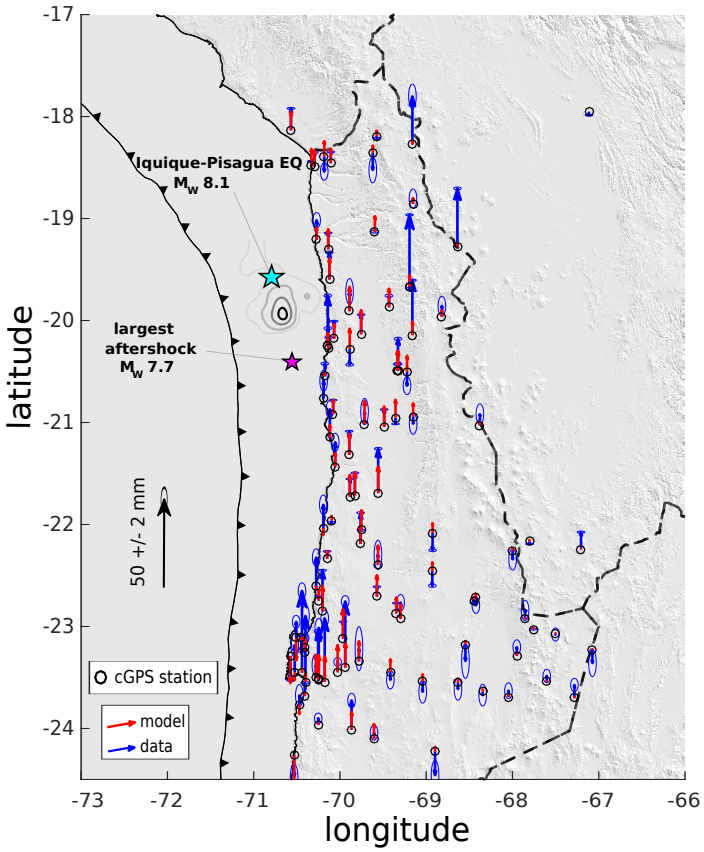

Figure C.7: *Auxiliary material for Sub-model IV:*
Modelled (red) and observed (blue) vertical cGPS displacements are displayed with 1-sigma uncertainties. For other features refer to Figure 4.11.

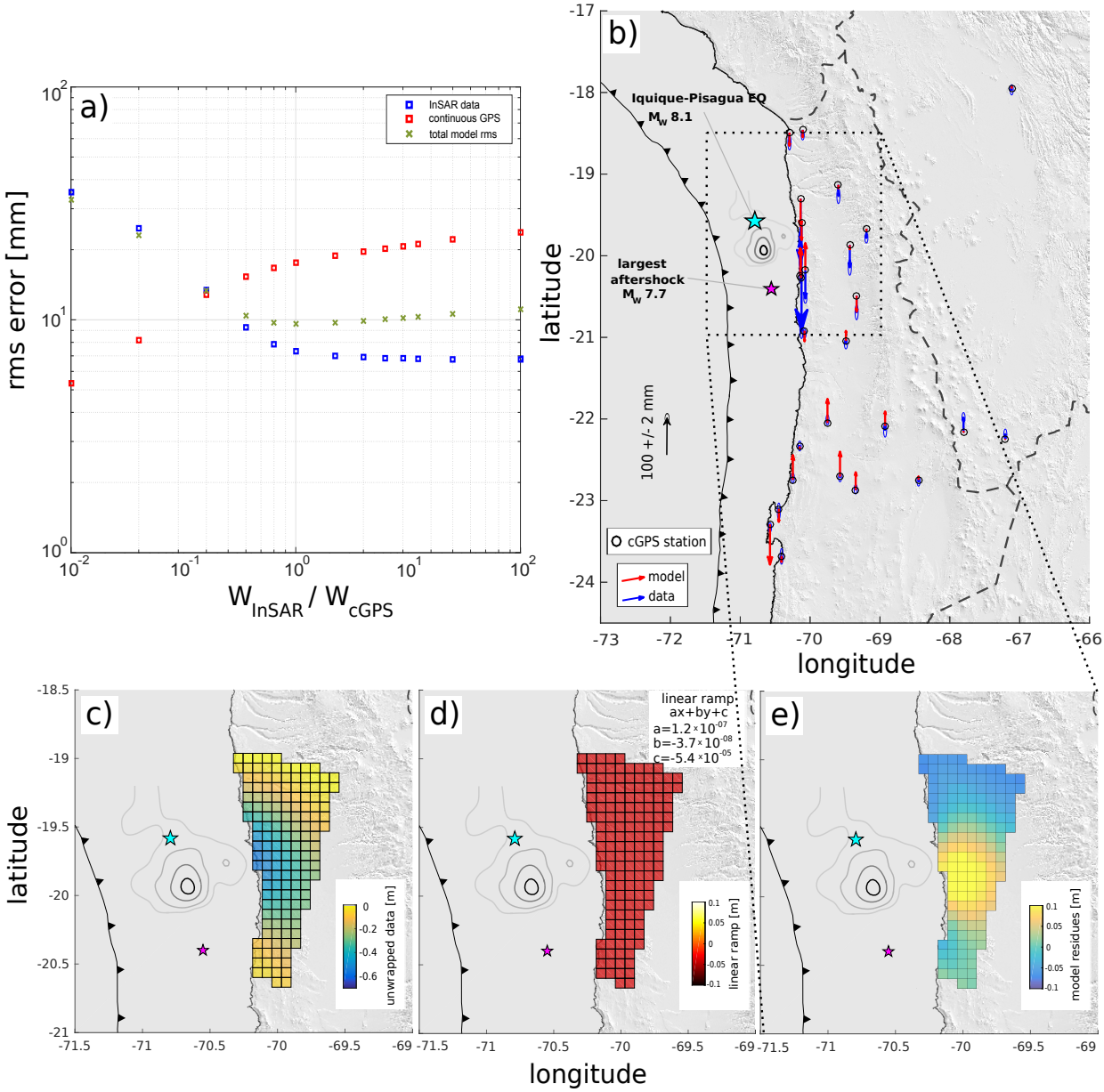

Figure C.8: *Auxiliary material for Sub-model V:*
a) Test of different weighting ratios w = w_{InSAR}/w_{cGPS}, where single cGPS rms error (red rectangles), single InSAR error (blue rectangles) and total error (green crosses) are plotted together. Least total rms error occurs at w = 1.25, b) Modelled (red) and observed (blue) vertical cGPS displacements are displayed with 1-sigma uncertainties, c) the subsampled unwrapped InSAR data (desc. RS2 01072011-04042014), d) the linear ramp (ax+by+c) of the unwrapped InSAR data (desc. RS2 01072011-04042014) and e) the InSAR model residuals from the slip inversion of Model V. For other features refer to Figure 4.11.

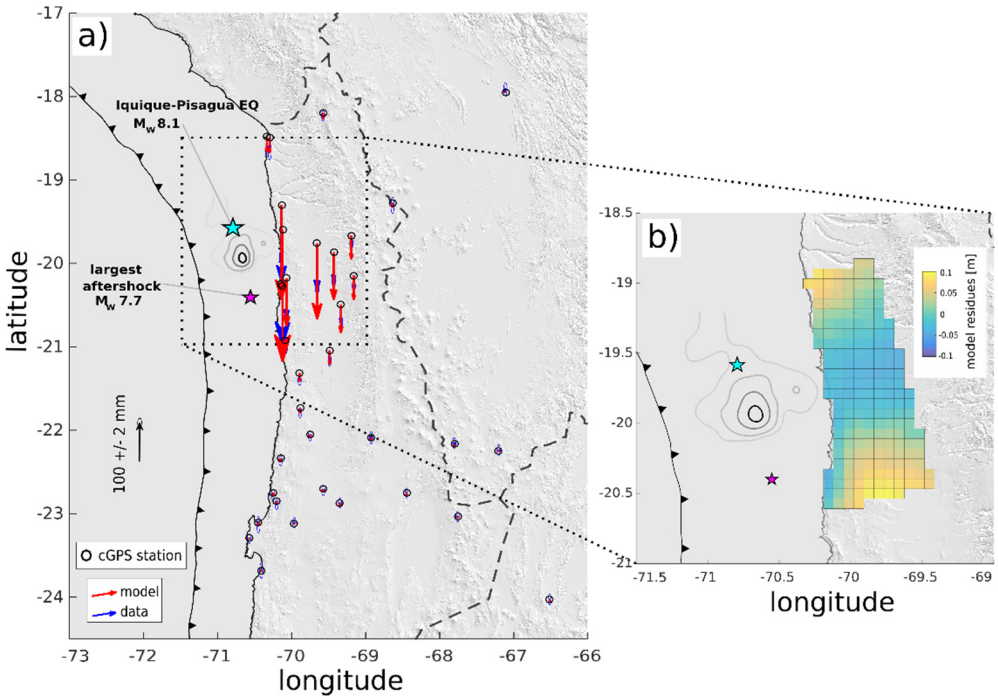

Figure C.9: *Auxiliary material for Sub-model VI:*
a) Modelled (red) and observed (blue) vertical cGPS displacements are displayed with 1-sigma uncertainties, b) the InSAR model residuals (asc. RS2 27032014-20042014) from the slip inversion of Sub-model VI. Unwrapped data and linear ramp is displayed in Figure 4.5, weighting of cGPS and InSAR is shown in Figure 4.6. For other features refer to Figure 4.11.

References

Aagaard, B., M. Knepley, and C.A. Williams (2013), A domain decomposition approach to implementing fault slip in finite-element models of quasi-static and dynamic crustal deformation, *J. Geophys. Res.* 118, 3059–3079, doi:10.1002/jgrb.50217.

Aki, K. (1979), Characterization of barriers on an earthquake fault. *Journal of Geophysical Research: Solid Earth*, *84*(B11), 6140-6148, doi: 10.1029/JB084iB11p06140.

Allmendinger, R.W., G. Gonzáles, J. Yu, G. Hoke, and B. Isacks (2005), Trench-parallel shortening in the Northern Chilean Forearc: Tectonic and climatic implications, *Geological Society of America Bulletin , 117 (1-2), 89-104*, doi: 10.1130/B25505.1

Allmendinger, R. W., and G. González (2010), Tectonophysics Invited review paper : Neogene to Quaternary tectonics of the coastal Cordillera , northern Chile, *Tectonophysics*, *495*(1–2), 93–110, doi:10.1016/j.tecto.2009.04.019.

Altamimi, Z., P. Rebischung, L. Métivier, and X. Collilieux (2016), ITRF2014: A new release of the International Terrestrial Reference Frame modeling nonlinear station motions, *J. Geophys. Res. Solid Earth*, *121*(8), 6109–6131, doi:10.1002/2016JB013098.

Amelung, F., S. Jónsson, H. Zebker, and P. Segall (2000), Widespread uplift and 'trapdoor' faulting on Galápagos volcanoes observed with radar interferometry, *Nature*, *407*(6807), 993, doi: 10.1038/35039604.

An, C., I. Sepúlveda, and P.L.F. Liu (2014), Tsunami source and its validation of the 2014 Iquique, Chile, earthquake, *Geophysical Research Letters*, *41*(11), 3988-3994, doi: 10.1002/2014GL060567.

Angermann, D., J. Klotz, and C. Reigber (1999), Space-geodetic estimation of the Nazca-South America Euler vector, *Earth Planet. Sci. Lett.*, *171*(3), 329–334, doi: 10.1016/S0012-821X(99)00173-9.

Asano, Y., T. Saito, Y. Ito, K. Shiomi, H. Hirose, T. Matsumoto, S.Aoi, S. Hori, and S. Sekiguchi (2011), Spatial distribution and focal mechanisms of aftershocks of the 2011 off the Pacific coast of Tohoku earthquake, *Earth Planets Space*, 63(7), 669–673.

Audet, P., and S. Schwartz (2013), Hydrologic control of forearc strength and seismicity in the Costa Rican subduction zone, *Nat. Geosci.*, 6, 852–855.

Beck, S., S. Barrientos, E. Kausel, and M. Reyes (1998), Source characteristics of historic earthquakes along the central Chile subduction zone, *J. South Am. Earth Sci.*, *11*, 115–129, doi:10.1016/S0895-9811(98)00005-4.

Bedford, J, M. Moreno, J.-C. Baez, D. Lange, F. Tilmann, M. Rosenau, O. Heidbach, O. Oncken, M. Bartsch, A. Rietbrock, A. Tassara, M. Bevis, and Christophe Vigny

(2013), A high-resolution, time-variable afterslip model for the 2010 Maule Mw = 8.8, Chile megathrust eäarthquake, *Earth Planet. Sci. Lett.*, *383*, 26–36, doi:10.1016/j.epsl.2013.09.020.

Bedford, J., M. Moreno, B. Schurr, M. Bartsch, and O. Oncken (2015), Investigating the final seismic swarm before the Iquique-Pisagua 2014 Mw 8.1 by comparison of continuous GPS and seismic foreshock data, *Geophysical Research Letters*, *42*(10), 3820-3828, doi: 10.1002/2015GL063953.

Bedford, J., M. Moreno, S. Li, O. Oncken, J.C. Baez, M. Bevis, O. Heidbach, and D. Lange (2016), Separating rapid relocking, afterslip, and viscoelastic relaxation: An application of the postseismic straightening method to the Maule 2010 cGPS, *Journal of Geophysical Research: Solid Earth*, *121*(10), 7618-7638, doi:10.1002/2016JB013093.

Béjar-Pizarro, M., A. Socquet, R. Armijo, D. Carrizo, J. Genrich, and M. Simons (2013), Andean structural control on interseismic coupling in the North Chile subduction zone, *Nature Geoscience*, *6*(6), 462-467, doi:10.1038/ngeo1802.

Bevis, M., and A. Brown (2014), Trajectory models and reference frames for crustal motion geodesy, *J. Geod.*, *88*(3), 283–311, doi:10.1007/s00190-013-0685-5.

Bevis, M., E. Kendrick, R. Smalley Jr., B. Brooks, R. Allmendinger, and B. Isacks (2001), On the strength of interplate coupling and the rate of back arc convergence in the central Andes: An analysis of the interseismic velocity field, *Geochemistry Geophys. Geosystems*, *2*(11), doi: 10.1029/2001GC000198.

Bilham, R. & N. Ambraseys (2005), Apparent himalayan slip deficit from the summation of seismic moments for himalayan earthquakes, 1500–2000, *Current Science*, 88(10), 1658–1663.

Bilham, R., R. Engdahl, N. Feldl, and S. Satyabala (2005), Partial and complete rupture of the indo-andaman plate boundary 1847-2004, *Seismological Research Letters*, 76(3), 299–311, doi:10.1785/gssrl.76.3.299.

Blewitt, G. (1997). Basics of the GPS technique: observation equations, *Geodetic applications of GPS*, 10-54.

Bloch, W., J. Kummerow, P. Salazar, P. Wigger, and S. A. Shapiro (2014), High-resolution image of the North Chilean subduction zone: Seismicity, reflectivity and fluids, *Geophys. J. Int.*, *197*(3), 1744–1749, doi:10.1093/gji/ggu084.

Boehm, J., J. Kouba, and H. Schuh (2009), Forecast Vienna Mapping Functions 1 for real-time analysis of space geodetic observations. *Journal of geodesy*, *83*(5), 397-401, doi: 10.1007/s00190-008-0216-y.

Bonafede, M., J. Strehlau, and A.R. Ritsema (1992), Geophysical and structural aspects of fault mechanics – a brief historical review, *Terra Nova,* 4(4), 458-463, doi:10.1111/j.1365-3121.1992.tb00581.x.

Bookhagen, B., and M.R. Strecker (2012), Spatiotemporal trends in erosion rates across a pronounced rainfall gradient: Examples from the southern Central Andes, *Earth and Planetary Science Letters*, *327*, 97-110, doi:10.1016/j.epsl.2012.02.005.

Boutelier, D., O. Oncken, and A.R. Cruden (2014), Trench-parallel shortening in the forearc caused by subduction along a seaward-concave plate boundary: Insights from analogue modelling experiments, *Tectonophysics*, *611*, 192-203.

Brodsky, E.E., & T. Lay (2014), Recognizing foreshocks from the 1 April 2014 Chile earthquake, *Science*, *344*(6185), 700-702, doi:10.1126/science.1255202.

Brooks, B.A., M. Bevis, K. Whipple, J.R. Arrowsmith, J. Foster , T. Zapata , E. Kendrick , E. Minaya , A. Echalar , M. Blanco , P. Euillades , M. Sandoval, and R.J. Smalley Jr (2011), Orogenic-wedge deformation and potential for great earthquakes in the central Andean backarc, *Nat. Geosci.*, *4*(6), 380–383, doi:10.1038/ngeo1143.

Brown, M., F. Diáz, and J. Grocott (1993), Displacement history of the Atacama fault system 25°00'S–27°00'S, northern Chile, *Geological Society of America Bulletin*, v. 105, p. 1,137–1,150, doi:10.1130/0016- 7606.

Bürgmann, R., P. A. Rosen, and E. J. Fielding (2000), Synthetic aperture radar interferometry to measure Earth's surface topography and its deformation, *Annu. Rev. Earth Planet. Sci.*, 28(1), 169–209, doi: 10.1146/annurev.earth.28.1.169.

Cahill, T., and B.L. Isacks (1992), Seismicity and shape of the subducted Nazca plate, *Journal of Geophysical Research: Solid Earth*, *97*(B12), 17503-17529, doi:10.1029/92JB00493.

Capitaine, N., P.T. Wallace, and J. Chapront (2005), Improvement of the IAU 2000 precession model, *Astronomy & Astrophysics*, *432*(1), 355-367, doi: 10.1051/0004-6361:20041908.

Carrapa, B., D. Adelmann, G.E. Hilley, E. Mortimer, E.R. Sobel, and M.R. Strecker (2005), Oligocene range uplift and development of plateau morphology in the southern central Andes, *Tectonics*, *24*(4), doi: 10.1029/2004TC001762.

Cavalié, O., M.P. Doin, C. Lasserre, and P. Briole (2007), Ground motion measurement in the Lake Mead area, Nevada, by differential synthetic aperture radar interferometry time series analysis: Probing the lithosphere rheological structure, *Journal of Geophysical Research: Solid Earth*, *112*(B3), doi: 10.1029/2006JB004344.

Cavalié, O., E. Pathier, M. Radiguet, M. Vergnolle, N. Cotte, A. Walpersdorf, V. Kostoglodov, and F. Cotton (2013), Slow slip event in the Mexican subduction zone: Evidence of shallower slip in the Guerrero seismic gap for the 2006 event revealed by the joint inversion of InSAR and GPS data, *Earth and Planetary Science Letters*, *367*, 52-60, doi: 10.1016/j.epsl.2013.02.020

Cembrano, J., A. Lavenu, G. Yañez, R. Riquelme, M. Garcia, G. González, and G. Hérail (2007), Neotectonics, In: Gibbons, W., and T. Moreno (Eds.), The Geology of Chile, *The Geological Society*, London, pp. 231-261.

Cesca, S., F. Grigoli, S. Heimann, T. Dahm, M. Kriegerowski, M. Sobiesiak, C. Tassara, and M. Olcay (2016), The Mw 8.1 2014 Iquique, Chile, seismic sequence: a tale of foreshocks and aftershocks, *Geophys. J. Int.*, 1766–1780, doi:10.1093/gji/ggv544.

Chen, C.W., and H.A. Zebker, H. A. (2001), Two-dimensional phase unwrapping with use of statistical models for cost functions in nonlinear optimization, *JOSA A*, *18*(2), 338-351, doi: 10.1364/JOSAA.18.000338.

Chilés, J.-P., and P. Delfiner (1999), Geostatistics - Modelling spatial uncertainties, Wiley series in probability and statistics, Applied probability and statistics section, *John Wiley & Sons. Inc.*, New York.

Chlieh, M., J.B. De Chabalier, J.C. Ruegg, R. Armijo, R. Dmowska, J. Campos, and K.L. Feigl (2004), Crustal deformation and fault slip during the seismic cycle in the North Chile subduction zone, from GPS and InSAR observations, *Geophysical Journal International*, *158*(2), 695-711, doi:10.1111/j.1365-246X.2004.02326.x.

Chlieh, M., H. Perfettini, H. Tavera, J. P. Avouac, D. Remy, J. M. Nocquet, F. Rolandone, F. Bondoux, G. Gabalda, and S. Bonvalot (2011), Interseismic coupling and seismic potential along the Central Andes subduction zone, *J. Geophys. Res. Solid Earth*, *116*(12), 1–21, doi: 10.1029/2010JB008166.

Christensen, N (1996), Poisson's ratio and crustal seismology, *J. Geophys. Res.* 101, 3139–3156, doi: 10.1029/95JB03446.

Clague, J.J., & P.T. Bobrowsky (1994), Tsunami deposits beneath tidal marshes on Vancouver island, British Columbia, *Geological Society of America Bulletin*, 106(10), 1293–1303, doi: 10.1130/0016-7606.

Coleman, T. F., and Y. Li (1996), A Reflective Newton Method for Minimizing a Quadratic Function Subject to Bounds on Some of the Variables, *SIAM J. Optim.*, *6*(4), 1040–1058, doi: 10.1137/S1052623494240456.

Comte, D., A. Eisenberg, E. Lorca, M. Pardo, L. Ponce, R. Saragoni, S. Singh, and G. Suarez (1986), The 1985 Central Chile earthquake: A repeat of previous great earthquakes in the region?, *Science*, *233*, 449–452, doi: 10.1126/science.233.4762.449.

Comte, D., and M. Pardo (1991), Reappraisal of great historical earthquakes in the northern Chile and southern Peru seismic gaps, *Nat. Hazards*, *4*(1), 23–44, doi: 10.1007/BF00126557.

Contreras-Reyes, E., J. Jara, I. Grevemeyer, S. Ruiz, and D. Carrizo (2012), Abrupt change in the dip of the subducting plate beneath north Chile, *Nature Geoscience*, 5:342–345. doi: 10.1038/ngeo1447.

Contreras-Reyes, E., J. A. Ruiz, J. Becerra, H. Kopp, C. Reichert, A. Maksymowicz, and C. Arriagada (2015), Structure and tectonics of the central Chilean margin (31° –33°S): Implications for subduction erosion and shallow crustal seismicity, *Geophys. J. Int.*, *203*, 776–791, doi:10.1093/gji/ggv309.

Costantini, M., and P.A. Rosen (1999), A generalized phase unwrapping approach for sparse data, *Proceedings of IGARSS'99*, Hamburg, 28 June-2 July, pp. 267-269.

Cubas, N., J.P. Avouac, P. Souloumiac, and Y. Leroy (2013), Megathrust friction determined from mechanical analysis of the forearc in the Maule earthquake area, *Earth and Planetary Science Letters*, *381*, 92-103, doi:10.1016/j.epsl.2013.07.037.

Curlander, J.C., and R.N. McDonough (1991), Synthetic aperture radar: systems and signal processing, *John Wiley & Sons*, New York, pp. 396.

Delacourt, C., P. Briole, and J.A. Achache (1998), Tropospheric corrections of SAR interferograms with strong topography, Application to Etna. *Geophysical Research Letters*, *25*(15), 2849-2852, doi: 10.1029/98GL02112.

Delouis, B., H. Philip, L. Dorbath, and A. Cisternas, (1998), Recent crustal deformation in the Antofagasta region (northern Chile) and the subduction process, *Geophysical Journal International,* 132(2), 302–338, doi: 10.1046/j.1365-246x.1998.00439.x.

Delouis, B., D. Giardini, P. Lundgren, and J. Salichon (2002), Joint Inversion of InSAR, GPS, Teleseismic, and Strong-Motion Data for the Spatial and Temporal Distribution of Earthquake Slip: Application to the 1999 Izmit Mainshock, *Bull. Seism. Soc. Am.*, 92(1), 278-299, doi: 10.1785/0120000806.

Delouis, B., and D. Legrand (2007), Mw 7.8 Tarapaca intermediate depth earthquake of 13 June 2005 (northern Chile): Fault plane identification and slip distribution by waveform inversion, *Geophysical Research Letters*, *34*(1), doi: 10.1029/2006GL028193.

Delouis, B., M. Pardo, D. Legrand, and T. Monfret (2009), The Mw 7.7 Tocopilla earthquake of 14 November 2007 at the southern edge of the northern Chile seismic gap: Rupture in the deep part of the coupled plate interface. *Bulletin of the Seismological Society of America*, *99*(1), 87-94, doi: 10.1785/0120080192.

Delouis, B., J.M. Nocquet, and M. Vallée (2010), Slip distribution of the February 27, 2010 Mw= 8.8 Maule earthquake, central Chile, from static and high-rate GPS, InSAR, and broadband teleseismic data. *Geophysical Research Letters*, *37*(17), doi: 10.1029/2010GL043899.

DeMets, C., R. G. Gordon, D. F. Argus, and S. Stein (1994), Effect of recent revisions to the geomagnetic reversal time scale on estimates of current plate motions, *Geophys. Res. Lett.*, *21*(20), 2191–2194, doi: 10.1029/94GL02118.

DeMets, C., R. G. Gordon, and D. F. Argus (2010), Geologically current plate motions, *Geophys. J. Int.*, *181*(1), 1–80, doi:10.1111/j.1365-246x.2009.04491.x.

Deng, Z., G. Gendt, and T. Schöne (2016), Status of the TIGA Tide Gauge Data Reprocessing at GFZ, In: Rizos, C, P. Willis (Eds.), IAG 150 Years: Proceedings of the IAG Scientific Assembly in Potsdam, Germany, 2013, (International

Association of Geodesy Symposia; 143), Springer International Publishing, pp. 33-40, doi: 10.1007/1345_2015_156.

Dixon, T. H. (1993), GPS measurement of relative motion of the Cocos and Caribbean Plates and strain accumulation across the Middle America Trench, *Geophys. Res. Lett*., 20(20), 2167–2170, doi: 10.1029/93GL02415.

Dong, D., P. Fang, Y. Bock, M. K. Cheng, and S. Miyazaki (2002), Anatomy of apparent seasonal variations from GPS-derived site position time series, *J. Geophys. Res.*, *107*(B4), 2075, doi: 10.1029/2001JB000573.

Dorbath, L., A. Cisternas, and C. Dorbath (1990), Quantitative assessment of great earthquakes in Peru, *Bull. Seism. Soc. Am.*, 80, 551–576

Du, Y., A. Aydin, and P. Segall (1992), Comparison of various inversion techniques as applied to the determination of a geophysical deformation model for the 1983 Borah Peak earthquake, *Bull. Seismol. Soc. Am.*, *82*(4), 1840–1866.

Duputel, Z., J. Jiang, R. Jolivet, M. Simons, L. Rivera, J.-P. Ampuero, B. Riel, S.E. Owen, A.W. Moore, S.V. Samsonov, F. Ortega Culaciati, and S.E. Minson (2015), The Iquique earthquake sequence of April 2014 : Bayesian modeling accounting for prediction uncertainty, *Geophys. Res. Lett.*, *42*(19), 7949–7957, doi: 10.1002/2015GL065402.

El-Rabbany, A. (2002). Introduction to GPS: the global positioning system, *Artech House*, Boston, pp.183.

Engdahl, E., R.D. van der Hilst, and R.P. Buland (1998), Global teleseismic earthquake relocation with improved travel times and procedures for depth determination, *Bul. Seismol. Soc. Am.*, *88*, 722–743.

Engdahl, E. R., and A. Villasenor (2002), Global Seismicity: 1900-1999, *Int. Geophys.*, *81*, 665–690, doi: 10.1016/S0074-6142(02)80244-3.

Farr, T., P. Rosen, E. Caro, E. Crippen, R. Duren, S. Hensley, M. Kobrick, M. Paller, E. Rodriguez, L. Roth, D. Seal, S. Shaffer, J. Shimada, J. Umland, M. Werner, M. Oskin, D. Burbank, and D. Alsdorf (2007), The Shuttle Radar Topography Mission, *Rev. Geophys.*, 45(RG2004).

Ferretti, A., C. Prati, and F. Rocca (2000), Nonlinear subsidence rate estimation using permanent scatterers in differential SAR interferometry, *IEEE Transactions on geoscience and remote sensing*, *38*(5), 2202-2212, doi:10.1109/36.868878.

Fialko, Y., and M. Simons (2000), Deformation and seismicity in the Coso geothermal area, Inyo County, California: Observations and modeling using satellite radar interferometry, *Journal of Geophysical Research: Solid Earth*, *105*(B9), 21781-21793, doi: 10.1029/2000JB900169.

Fowler, C.M.R. (1991), The Solid Earth - an Introduction to Global Geophysics, *Transactions American Geophysical Union*, *72*(40), 427-428, doi: 10.1029/90EO00309.

Gatelli, F., Monti Guarnieri, A., Parizzi, F., Pasquali, P., Prati, C., and Rocca, F. (1994). The wavenumber shift in SAR interferometry. IEEE Transactions on Geoscience and Remote Sensing, 32(4):855–865.

Geersen, J., C. R. Ranero, U. Barckhausen, and C. Reichert (2015), Subducting seamounts control interplate coupling and seismic rupture in the 2014 Iquique earthquake area, *Nat. Commun.*, *6*, 6–11, doi: 10.1038/ncomms9267.

Geirsson, H., T. Árnadóttir, C. Völksen, W. Jiang, E. Sturkell, T. Villemin, P. Einarsson, F. Sigmundsson, and R. Stefánsson (2006), Current plate movements across the Mid-Atlantic Ridge determined from 5 years of continuous GPS measurements in Iceland, *Journal of Geophysical Research: Solid Earth*, *111*(B9), doi: 10.1029/2005JB003717.

Geller, R. (2011), Shake-up time for Japanese seismology, *Nature 472*, 407-409, doi:10.1038/nature10105.

Gendt, G., Z. Deng, M. Ge, T. Nischan, M. Uhlemann, G. Beeskow, A. Brandt, and M. Bradke (2013), GFZ ANALYSIS CENTER OF IGS - Annual Report for 2013, 1–10.

Gephart, J.W. (1994), Topography and subduction geometry in the central Andes: Clues to the mechanics of a noncollisional orogen, *Journal of Geophysical Research: Solid Earth*, *99*(B6), 12279-12288, doi: 10.1029/94JB00129.

González, G., J. Cembrano, D. Carrizo, A. Macci, and H. Schneider (2003), The link between forearc tectonics and Pliocene–Quaternary deformation of the Coastal Cordillera, northern Chile, *Journal of South American Earth Sciences, 16(5), 321-342,* doi: 10.1016/S0895-9811(03)00100-7.

González, G., M. Gerbault, J. Martinod, J. Cembrano, R. Allmendinger, D. Carrizo, J. Espina (2008), Crack formation on top of propagating reverse faults of the Chuculay Fault System northern Chile: insights from field data and numerical modeling, *Journal of Structural Geology,* 30, 791–808. doi: 10.1016/j.jsg.2008.02.008.

González, G., P. Salazar, J. P. Loveless, R. W. Allmendinger, F. Aron, and M. Shrivastava (2015), Upper plate reverse fault reactivation and the unclamping of the megathrust during the 2014 northern Chile earthquake sequence, *Geology*, *43*(8), 1–4, doi:10.1130/G36703.1.

Goldstein, R.M., H. Engelhardt, B. Kamb, and R.M. Frolich (1993), Satellite radar interferometry for monitoring ice sheet motion: application to an Antarctic ice stream, *Science, 262(5139)*, 1525, doi: 10.1126/science.262.5139.1525.

Goldstein, R.M., and C.L. Werner (1998), Radar interferogram filtering for geophysical applications, *Geophysical Research Letters*, *25*(21), 4035-4038, doi: 10.1029/1998GL900033.

Goto, K., C. Chagué-Goff, S. Fujino, J. Goff, B. Jaffe, Y. Nishimura, B. Richmond, D. Sugawara, W. Szczucísnki, D.R. Tappin, R.C. Witter, and E. Yulianto (2011),

New insights of tsunami hazard from the 2011 Tohoku-oki event, *Marine Geology*, *290*(1-4), 46-50, doi: 10.1016/j.margeo.2011.10.004.

Hanssen, R.F. (2001), Radar Interferometry: Data Interpretation and Error Analysis, Vol. 2, *Kluwer Academic Publishers*, Dordrecht, pp. 308.

Hasegawa, A., K. Yoshida, Y. Asano, T. Okada, T. Iinuma, and Y. Ito (2012), Change in stress field after the 2011 great Tohoku-Oki earthquake, *Earth and Planetary Science Letters*, *355*, 231-243, doi: 10.1016/j.epsl.2012.08.042.

Hayes, G. P., D. J. Wald, and R. L. Johnson (2012), Slab1.0: A three-dimensional model of global subduction zone geometries, *J. Geophys. Res. Solid Earth*, *117*, doi: 10.1029/2011JB008524.

Hayes, G.P., M.W. Herman, W.D. Barnhart, K.P. Furlong, S. Riquelme, H.M. Benz, E. Bergman, S. Barrientos, P.S. Earle, and S. Samsonov (2014), Continuing megathrust earthquake potential in Chile after the 2014 Iquique earthquake, *Nature*, 512(7514), p. 295-298, doi: 10.1038/nature13677.

Heki, K. (2001), Seasonal modulation of interseismic strain buildup in northeastern Japan driven by snow loads, *Science*, *293*(5527), 89–92, doi: 10.1126/science.1061056.

Heki, K., and Y. Mitsui (2013), Accelerated pacific plate subduction following interplate thrust earthquakes at the Japan trench, *Earth Planet. Sci. Lett.*, *363*, 44–49, doi: 10.1016/j.epsl.2012.12.031.

Herman, M.W., K.P. Furlong, G.P. Hayes, and H.M. Benz (2016), Foreshock triggering of the 1 April 2014 Mw 8.2 Iquique, Chile, earthquake, *Earth and Planetary Science Letters*, *447*, 119-129, doi: 10.1016/j.epsl.2016.04.020.

Hertz, H. (1894), Untersuchungen Ueber Die Ausbreitung Der Elektrischen Kraft, Leipzig, *Johann Ambrosius Barth*, pp. 298.

Hirose, H., K. Hirahara, F. Kimata, N. Fujii, and S.I. Miyazaki (1999), A slow thrust slip event following the two 1996 Hyuganada earthquakes beneath the Bungo Channel, southwest Japan, *Geophysical Research Letters*, *26*(21), 3237-3240, doi: 10.1029/1999GL010999.

Hoffmann, F., S. Metzger, M. Moreno, Z. Deng, C. Sippl, F. Ortega-Culaciati, and O. Oncken (2018), Characterizing Afterslip and Ground Displacement Rate Increase Following the 2014 Iquique-Pisagua Mw 8.1 Earthquake, Northern Chile, *Journal of Geophysical Research: Solid Earth*, *123*(5), 4171-4192, doi: 10.1002/2017JB014970.

Hoffmann-Rothe, R., N. Kukowski, G. Dresen, H. Echtler, O. Oncken, J. Klotz, E. Scheuber, and A. Kellner (2006), Oblique Convergence along the Chilean Margin: Partitioning, Margin-Parallel Faulting and Force Interaction at the Plate Interface, In: Oncken et al.(Ed.): *The Andes: Active Subduction Orogeny,* Springer Berlin Heidelberg, pp. 125-146.

Hsu, Y.-J., M. Simons, J.-P. Avouac, J. Galetzka, K. Sieh, M. Chlieh, D. Natawidjaja, L. Prawirodirdjo, and Y. Bock (2006), Frictional Afterslip Following the 2005 Nias-Simeulue Earthquake, Sumatra, *Science*, *312*(5782), 1921–1926, doi: 10.1126/science.1126960.

Hughes, K.L.H., T. Masterlark, and W. Mooney (2010), Poroelastic stress-triggering of the 2005 M8 . 7 Nias earthquake by the 2004 M9 . 2 Sumatra – Andaman earthquake, Earth and Planetary Science Letters, 293 (3-4), p. 289-299, doi:10.1016/j.epsl.2010.02.043.

Husen, S., E. Kissling, and E.R. Flueh (2000), Local earthquake tomography of shallow subduction in north Chile: A combined onshore and offshore study, *Journal of Geophysical Research: Solid Earth*, *105*(B12), 28183-28198, doi: 10.1029/2000JB900229.

Huygens, C. (1690), Traité de la lumière, où sont expliquées les causes de ce qui luy arrive dans la reflexion, et dans la refraction: et particulierement dans l´étrange refraction du cristal d´Islande: avec un discours de la cause de la pesanteur, *Van der Aa*, Leiden.

Hyndman, R., K. Wang, and M. Yamano (1995), Thermal constraints on the seismogenic portion of the southwestern Japan subduction thrust, *J. Geophys. Res.*, 100 (B8), 15,373 –15,392, doi: 10.1029/95JB00153.

Isacks, B.L. (1988), Uplift of the central Andean plateau and bending of the Bolivian orocline, *Journal of Geophysical Research: Solid Earth*, *93*(B4), 3211-3231, doi: 10.1029/JB093iB04p03211.

Jaramillo, E., D. Melnick, J.C. Baez, H. Montecino, N.A. Lagos, E. Acuña, M. Manzano and P.A. Camus (2017), Calibrating coseismic coastal land-level changes during the 2014 Iquique (Mw= 8.2) earthquake (northern Chile) with leveling, GPS and intertidal biota, *PloS one*, *12*(3), e0174348, doi: 10.1371/journal.pone.0174348.

Jarrard, R.D. (1986), Terrane motion by strike-slip faulting of forearc slivers, Geology, 14, 780-783, doi:10.1130/0091-7613(1986)14<780:TMBSFO>2.0.CO;2.

Jónsson, S., H.A. Zebker, P. Segall, and F. Amelung (2002), Fault slip distribution of the 1999 Mw7.2 Hector Mine earthquake, California, estimated from satellite radar and GPS measurements, *Bull. Seism. Soc. Am.*, 92(4), 1377-1389, doi: 10.1785/0120130108.

Jónsson, S., P. Segall, R. Pedersen, and G. Björnsson (2003), Post-earthquake ground movements correlated to pore-pressure transients, *Nat. Geosci.*, *424*, 179–183, doi: 10.1038/nature0177.

Kanamori, H. (1973), Mode of strain release associated with major earthquakes in Japan, *Annual Review of Earth and Planetary Sciences*, *1*(1), 213-239, doi: 10.1146/annurev.ea.01.050173.001241.

Kanamori, H. (1977), The Energy Release in Great Earthquakes, *J. Geophys. Res.*, *82*(20), 2981–2987, doi: 10.1029/JB082i020p02981.

Kanamori, H. (1986). Rupture process of subduction-zone earthquakes, *Ann. Rev. Earth Planet. Sci.*, 14, 293–322, doi: 10.1146/annurev.ea.14.050186.001453.

Kaneko, Y., J.-P. Avouac, and N. Lapusta (2010), Towards inferring earthquake patterns from geodetic observations of interseismic coupling, *Nat. Geosci.*, *3*(5), 363–369, doi: 10.1038/ngeo843.

Kaplan, E., and C. Hegarty (Eds.) (2005), Understanding GPS: principles and applications, 2nd Ed., *Artech House Inc.,* Norwood, pp. 683, ISBN 1-58053-894-0.

Kato, A., K. Obara, T. Igarashi, H. Tsuruoka, S. Nakagawa, N. Hirata, (2012), Propagation of slow slip leading up to the 2011 Mw 9.0 Tohoku-Oki earthquake. Science 335, 705–708, doi: 10.1126/science.1215141.

Kato, A., and S. Nakagawa (2014), Multiple slow-slip events during a foreshock sequence of the 2014 Iquique, Chile Mw 8.1 earthquake, *Geophysical Research Letters*, *41*(15), 5420-5427, doi: 10.1002/2014GL061138.

Kato, A., J.I. Fukuda, T. Kumazawa, and S. Nakagawa (2016), Accelerated nucleation of the 2014 Iquique, Chile Mw 8.2 earthquake, *Scientific reports*, *6*, 24792, doi:10.1038/srep24792 (2016).

Kausel, E. (1986), Los terremotos de agosto de 1868 y mayo de 1877 que afectaron el sur del Perú y norte de Chile, *Boletín de la Academia Chilena de Ciencias*, *3*(1), 8-13.

Kelleher, J.A. (1972), Rupture zones of large South American earthquakes and some predictions, *J. Geophys. Res.*, *77*(11), 2087, doi: 10.1029/JB077i011p02087.

King, G.C.P., R.S. Stein, and J. Lin (1994), Static stress changes and the triggering of earthquakes, *Bull. Seismol. Soc. Am.*, *84*(3), 935–953.

Klein, E., L. Fleitout, C. Vigny, and J.D. Garaud (2016), Afterslip and viscoelastic relaxation model inferred from the large-scale post-seismic deformation following the 2010 Mw 8.8 Maule earthquake (Chile), *Geophysical Journal International*, *205*(3), 1455-1472, doi: 10.1093/gji/ggw086.

Klotz, J., D. Angermann, G.W. Michel, R. Porth, C. Reigber, J. Reinking, J. Viramonte, R. Perdomo, V.H. Rios, S. Barrientos, R. Barriga, O. Cifuentes (1999), GPS-derived Deformation of the Central Andes Including the 1995 Antofagasta Mw = 8.0 Earthquake, *Pure Appl. Geophys.*, *154*(3–4), 709–730, doi: 10.1007/s000240050249.

Klotz, J., G. Khazaradze, D. Angermann, C. Reigber, R. Perdomo, and O. Cifuentes (2001), Earthquake cycles dominates contemporary crustal deformation in Central and Southern Andes, *Earth Planet. Sci. Lett.*, *193*, 437–446, doi: 10.1016/S0012-821X(01)00532-5.

Lagler K, M. Schindelegger, J. Boehm, H. Krásná, and T. Nilsson T (2013), GPT2: Empirical slant delay model for radio space geodetic techniques. Geophys Res Lett 40:1069–1073, doi: 10.1002/grl.50288.

Lamb, S. (2000), Active deformation in the Bolivian Andes, South America, *J. Geophys. Res.*, *105*(B11), 25627–25653, doi: 10.1029/2000JB900187.

Lamb, S. (2006), Shear stresses on megathrusts: Implications for mountain building behind subduction zones, *Journal of Geophysical Research: Solid Earth*, *111*(B7), doi: 10.1029/2005JB003916.

Lange, D., F. Tilmann, S. E. Barrientos, E. Contreras-Reyes, P. Methe, M. Moreno, B. Heit, H. Agurto, P. Bernard, J.-P. Vilotte, and S. Beck (2012), Aftershock seismicity of the 27 February 2010 *Mw* 8.8 Maule earthquake rupture zone, *Earth Planet. Sci. Let.*, *317-318*, 413–425, doi:10.1016/j.epsl.2011.11.034.

Lay, T., and Bilek, S. (2007), Anomalous earthquake ruptures at shallow depths on subduction zone megathrusts, In: Dixon, T.H., and J.C. Moore (Ed), *The Seismogenic Zone of Subduction Thrust Faults*, Colombia Press, New York, 476-511.

Lee, S.-J., B.-S. Huang, M. Ando, H.-C. Chiu, and J.-H. Wang (2011), Evidence of large scale repeating slip during the 2011 Tohoku-Oki earthquake, *Geophys. Res. Lett.,* 38, L19306, doi: 10.1029/2011GL049580.

Leick, A., L. Rapoport, and D. Tatarnikov (2015), GPS Satellite Surveying, *4th Ed., John Wiley & Sons Inc.,* New Jersey, doi: 10.1002/9781119018612.

Lemoine, A., R. Madariaga, and J. Campos (2001), Evidence for earthquake interaction in central Chile: The July 1997–September 1998 sequence, *Geophys. Res. Lett.*, *28*(14), 2743–2746, doi:10.1029/2000GL012314.

León-ríos, S., S. Ruiz, A. Maksymowicz, and F. Leyton (2016), Diversity of the 2014 Iquique's foreshocks and aftershocks : clues about the complex rupture process of a M_w 8.1 earthquake, *J. Seismol.*, *1911*, 1059–1073, doi: 10.1007/s10950-016-9568-6.

Li, S., M. Moreno, J. Bedford, M. Rosenau, and O. Oncken (2015), Revisiting viscoelastic effects on interseismic deformation and locking degree: A case study of the Peru-North Chile subduction zone, *J. Geophys. Res. Solid Earth*, *120*(6), 4522–4538, doi: 10.1002/2015JB011903.

Li, S., M. Moreno, J. Bedford, M. Rosenau, O. Heidbach, D. Melnick, and O. Oncken (2017), Postseismic uplift of the Andes following the 2010 Maule earthquake: Implications for mantle rheology. *Geophysical Research Letters*, *44*(4), 1768-1776, doi: 10.1002/2016GL071995.

Lin, Y.N., A. Sladen, F. Ortega-Culaciati, M. Simons, J.-P. Avouac, E.J. Fielding, B.A. Brooks, M. Bevis, J. Genrich, A. Rietbrock, C. Vigny, R. Smalley, and A. Socquet (2013), Coseismic and postseismic slip associated with the 2010 Maule Earthquake, Chile: Characterizing the Arauco Peninsula barrier effect, Journal of

Geophysical Research: Solid Earth, 118 (6), pp. 3142-3159, doi:10.1002/jgrb.50207.

Lomnitz, C. (1970), Major earthquakes and tsunamis in Chile during the period 1535 to 1955, *Geologische Rundschau*, 59(3), pp.938-960.

Lomnitz, C., (2004), Major earthquakes of Chile: a historical survey, 1535– 1960, *Seismol. Res. Lett.*, 75(3), 368–378.

Loveless, J.P., R.W. Allmendinger, M.E. Pritchard, J.L. Garroway, and G.G. González (2009), Surface cracks record long-term seismic segmentation of the Andean margin, *Geology*, 37, 23–26, doi:10.1130/G25170A.1.

Loveless, J.P., C.P. Scott, R.W. Allmendinger, and G. González (2016), Slip distribution of the 2014 Mw= 8.1 Pisagua, northern Chile, earthquake sequence estimated from coseismic fore-arc surface cracks. *Geophysical Research Letters*, *43*(19), doi: 10.1002/2016GL070284.

Loveless, J. P. (2017), Super-interseismic periods: Redefining earthquake recurrence, *Geophys. Res. Lett.*, *44*(3), 1329–1332, doi: 10.1002/2017GL072525.

Lyard, F., F. Lefevre, T. Letellier, and O. Francis (2006), Modelling the global ocean tides: Modern insights from FES2004, *Ocean Dyn.*, *56*(5–6), 394–415, doi: 10.1007/s10236-006-0086-x.

Marone, C.J., C.H. Scholtz, and R. Bilham (1991), On the mechanics of earthquake afterslip, *J. Geophys. Res.*, *96*(B5), 8441, doi: 10.1029/91JB00275.

Massonnet, D., M. Rossi, C. Carmona, F. Adragna, G. Peltzer, K. Feigl, and T. Rabaute (1993), The displacement field of the Landers earthquake mapped by radar interferometry, *Nature, 364*(6433), 138-142, doi: 10.1038/364138a0.

Massonnet, D., and K.L. Feigl (1998), Radar interferometry and its application to changes in the Earth's surface, *Reviews of geophysics*, *36*(4), 441-500, doi: 10.1029/97RG03139.

Mazzotti, S., X. Le Pichon, P. Henry, and S.I. Miyazaki (2000), Full interseismic locking of the Nankai and Japan-west Kurile subduction zones: An analysis of uniform elastic strain accumulation in Japan constrained by permanent GPS, *Journal of Geophysical Research: Solid Earth*, *105*(B6), 13159-13177, doi: 10.1029/2000JB900060.

McCann, W., S. Nishenko, L. Sykes, and J. Krause (1979), Seismic gaps and plate tectonics: Seismic potential for major boundaries, Pure and Applied Geophysics, 117, 1082–1147, doi: 10.1007/BF00876211.

Melnick, D., B. Bookhagen, M.R. Strecker, and H.P. Echtler (2009), Segmentation of megathrust rupture zones from fore-arc deformation patterns over hundreds to millions of years, Arauco Peninsula, Chile, *Journal of Geophysical Research: Solid Earth (1978–2012)*, 114(B1), doi: 10.1029/2008JB005788.

Melnick, D. (2016), Rise of the central Andean coast by earthquakes straddling the Moho, *Nature Geoscience*, 9(5), 401-407, doi: 10.1038/ngeo2683.

Melnick, D., M. Moreno, J. Quinteros, J. C. Baez, Z. Deng, S. Li, and O. Oncken (2017), The super-interseismic phase of the megathrust earthquake cycle in Chile, *Geophys. Res. Lett.*, *44*(2), 784–791, doi: 10.1002/2016GL071845.

Meng, L., H. Huang, R. Bürgmann, J. P. Ampuero, and A. Strader (2015), Dual megathrust slip behaviors of the 2014 Iquique earthquake sequence, *Earth Planet. Sci. Lett.*, *411*, 177–187, doi: 10.1016/j.epsl.2014.11.041.

Menke, W. (2012). Geophysical Data Analysis: Discrete Inverse Theory: MATLAB edition, Third edition, *Columbia University Palisades*, New York*, pp. 57-59, 201,* ISBN: 978-0-12-397160-9.

Métois, M., A. Socquet, C. Vigny, D. Carrizo, S. Peyrat, A. Delorme, E. Maureira, M. C. Valderas-Bermejo, and I. Ortega (2013), Revisiting the North Chile seismic gap segmentation using GPS-derived interseismic coupling, *Geophys. J. Int.*, *194*(3), 1283–1294, doi:10.1093/gji/ggt183.

Métois, M., C. Vigny, A. Socquet, A. Delorme, S. Morvan, I. Ortega, and C.M. Valderas-Bermejo (2014), GPS-derived interseismic coupling on the subduction and seismic hazards in the Atacama region, Chile, *Geophys. J. Int.*, *196*(2), 644–655, doi: 10.1093/gji/ggt418.

Métois, M., C. Vigny, and A. Socquet (2016), Interseismic Coupling, Megathrust Earthquakes and Seismic Swarms Along the Chilean Subduction Zone (38°–18°S), *Pure Appl. Geophys.*, *173*(5), 1431–1449, doi: 10.1007/s00024-016-1280-5.

Metzger, S., S. Jónsson, G. Danielsen, S. Hreinsdóttir, F. Jouanne, D. Giardini and T. Villemin (2013), Present kinematics of the Tjörnes Fracture Zone, North Iceland, from campaign and continuous GPS measurements, *Geophys. J. Int.*, 192, 441-455, doi: 10.1093/gji/ggs032.

Miller, M.M., T. Melbourne, D.J. Johnson, and W.Q. Sumner (2002), Periodic slow earthquakes from the Cascadia subduction zone, *Science*, *295*(5564), 2423-2423, doi: 10.1126/science.1071193.

Mohr, J.J., N. Reeh, and S.N. Madsen (1998), Three-dimensional glacial flow and surface elevation measured with radar interferometry, *Nature*, *391*(6664), 273, doi: 10.1038/34635.

Moreno, M. S., Bolte, J., Klotz, J., and Melnick, D. (2009), Impact of megathrust geometry on inversion of coseismic slip from geodetic data: Application to the 1960 Chile earthquake, *Geophysical Research Letters*, *36*(16), doi: 10.1029/2009GL039276.

Moreno, M., M. Rosenau, and O. Oncken (2010), 2010 Maule earthquake slip correlates with pre-seismic locking of Andean subduction zone, *Nature*, *467*(7312), 198–202, doi: 10.1038/nature09349.

Moreno, M., D. Melnick, M. Rosenau, J. Bolte, J. Klotz, H. Echtler, J.C. Baez, K. Bataille, J. Chen, M. Bevis, H. Hase, and O. Oncken (2011), Heterogeneous plate locking in the South-Central Chile subduction zone: Building up the next great earthquake, *Earth Planet. Sci. Lett.*, *305*(3–4), 413–424, doi: 10.1016/j.epsl.2011.03.025.

Moreno, M., C. Haberland, O. Oncken, A. Rietbrock, S. Angiboust, and O. Heidbach (2014), Locking of the Chile subduction zone controlled by fluid pressure before the 2010 earthquake, *Nature Geoscience*, 292–296, doi:10.1038/ngeo2102.

Moreno, M, J. Bedford, J.-C. Baez, J. Klotz, F. Hoffmann, Z. Deng, I. Urrutia, C. Rojas, M. Shrivastava, F. Ortega-Culaciati, and E. Contreras-Reyes (2017), Survey Mode GPS data in the IPOC Region, Central Andes, Chile, GFZ Data Services, doi: 10.5880/GFZ.4.1.2017.003.

Mortimer, C., E. Farrar, and N. Saric (1974), K-Ar ages from Tertiary lavas of the northernmost Chilean Andes, *Geologische Rundschau*, *63*(2), 484-490.

Moscoso, E., I. Grevemeyer, E. Contreras-Reyes, E.R. Flueh, Y. Dzierma, W. Rabbel, and M. Thorwart (2011), Revealing the deep structure and rupture plane of the 2010 Maule, Chile earthquake (Mw= 8.8) using wide angle seismic data, *Earth and Planetary Science Letters*, *307*(1-2), 147-155, doi: 10.1016/j.epsl.2011.04.025.

Motagh, M., B. Schurr, J. Anderssohn, B. Cailleau, T. R. Walter, R. Wang, and J. P. Villotte (2010), Subduction earthquake deformation associated with 14 November 2007, Mw 7.8 Tocopilla earthquake in Chile: Results from InSAR and aftershocks, *Tectonophysics*, *490*(1), 60–68, doi: 10.1016/j.tecto.2010.04.033.

Mouslopoulou, V., D. Moraetis, and C. Fassoulas (2011), Identifying past earth- quakes on carbonate faults: Advances and limitations of the ‘rare earth element’ method based on analysis of the spili fault, Crete, Greece, *Earth and Planetary Science Letters*, 309(1), 45–55, doi: 10.1016/j.epsl.2011.06.015.

Mpodozis, C., and V.A. Ramos (1989), The Andes of Chile and Argentina, In: Ericksen et al. (Ed.), Geology of the Andes and its Relation to Hydrocarbon and Mineral Resources, *Circum-Pacific Council for Energy and Mineral Resources*, Houston, pp. 59–90.

Müller, R. D., M. Sdrolias, C. Gaina, and W. Roest (2008), Age, spreading rates, and spreading asymmetry of the world’s ocean crust, *Geochem. Geophys. Geosyst.*, *9*, Q0406, doi: 10.1029/2007GC001743.

Naylor, M., J. Greenhough, J. McCloskey, A. F. Bell, and I. G. Main (2009), Statistical evaluation of characteristic earthquakes in the frequency-magnitude distributions of Sumatra and other subduction zone regions, *Geophys. Res. Lett.*, *36*, L20303, doi: 10.1029/2009GL040460.

Nishenko, S. P. (1985), Seismic potential for large and great interplate earthquakes along the Chilean and Southern Peruvian Margins of South America: A

quantitative reappraisal, *J. Geophys. Res.*, *90*(B5), 3589–3615, doi: 10.1029/JB090iB05p03589.

Nocquet, J.M., P. Jarrin, M. Vallée, P.A. Mothes, R. Grandin, F. Rolandone, B. Delouis, H. Yepes, Y. Font, D. Fuentes, and M. Régnier (2017), Supercycle at the Ecuadorian subduction zone revealed after the 2016 Pedernales earthquake, *Nat. Geosci.*, 10(2), pp.145-149, doi: 10.1038/ngeo2864.

Noda, H., and N. Lapusta (2013), Stable creeping fault segments can become destructive as a result of dynamic weakening, *Nature*, 7433, 518–521.

Nocquet, J.M., P. Jarrin, M. Vallée, P.A. Mothes, R. Grandin, F. Rolandone, B. Delouis, H. Yepes, Y. Font, D. Fuentes, and M. Régnier (2017), Supercycle at the Ecuadorian subduction zone revealed after the 2016 Pedernales earthquake, *Nat. Geosci.*, 10(2), pp.145-149, doi: 10.1038/ngeo2864.

Norabuena, E., L. Leffler-Griffin, A. Mao, T. Dixon, S. Stein, I. Selwyn Sacks, L. Ocola, and M. Ellis (1998), Space geodetic observations of Nazca-South America convergence across the central Andes, *Science*, 279(5349), 358–362.

Norabuena, E.O., T.H. Dixon, S. Stein, and C.G. Harrison (1999), Decelerating Nazca-South America and Nazca-Pacific plate motions, *Geophysical Research Letters*, 26(22), 3405-3408, doi: 10.1029/1999GL005394.

Nur, A., and G. Mavko (1974), Postseismic viscoelastic rebound., *Science*, *183*(4121), 204–206, doi: 10.1126/science.183.4121.204.

Oleskevich, D.A., R.D. Hyndman, and K. Wang (1999), The updip and downdip limits to great subduction earthquakes: Thermal and structural models of Cascadia, south Alaska, SW Japan, and Chile, *Journal of Geophysical Research: Solid Earth*, *104*(B7), 14965-14991, doi: 10.1029/1999JB900060.

Okada, Y. (1992), Internal deformation due to shear and tensile faults in a half-space., *Bull. Seismol. Soc. Am.*, *82*(2), 1018–1040, doi: 10.1029/92JB00178.

Oncken, O., G. Asch, C. Haberland, J. Metchie, S. Sobolev, M. Stiller, X. Yuan H. Brasse, S. Buske , P. Giese, H.-J. Görze, S. Lueth, E. Scheuber, S. Shapiro, P. Wigger, M.-K. Yoon, P. Bravo, H. Vieytes, G. Chong, G. Gonzales, H.-G. Wilke, E. Lüschen, E. Martinez, R. Rössling, E. Ricaldi and A. Rietbrock (2003), Seismic imaging of a convergent continental margin and plateau in the central Andes (Andean Continental Research Project 1996 (ANCORP'96)), *Journal of Geophysical Research: Solid Earth*, *108*(B7), doi:10.1029/2002JB001771.

Oncken, O., D. Hindle, J. Kley, K. Elger, P. Victor and K. Schemmann (2006), Deformation of the central Andean upper plate system - Facts, fiction, and constraints for plateau models, In: *The Andes* (pp. 3-27), Springer, Berlin, Heidelberg.

Oncken, O., D. Boutelier, G. Dresen, and K. Schemmann (2012), Strain accumulation controls failure of a plate boundary zone: Linking deformation of the Central Andes and lithosphere mechanics, *Geochemistry, Geophysics, Geosystems*, *13*(12), doi: 10.1029/2012GC004280.

Ozawa, S., M. Murakami, S. Fujiwara, and M. Tobita (1997), Synthetic aperture radar interferogram of the 1995 Kobe earthquake and its geodetic inversion, *Geophysical Research Letters*, *24*(18), 2327-2330, doi: 10.1029/97GL02318.

Pacheco, J., and L. Sykes (1992), Seismic moment catalog for large shallow earthquakes from 1900 to 1989, *Bull. Seism. Soc.*, 82, 1306-1349.

Pardo-Casas, F., and P. Molnar (1987), Relative motion of the Nazca (Farallon) and South American plates since Late Cretaceous time, *Tectonics*, 6, 233–248, doi:10.1029/TC006i003p00233.

Pardo, M., D. Comte, and T. Monfret (2002), Seismotectonic and stress distribution in the central Chile subduction zone, *J. South Am. Earth Sci.*, *15*(1), 11–22, doi:10.1016/s0895-9811(02)00003-2.

Peltzer, G., P. Rosen, F. Rogez, and K. Hudnut (1996), Postseismic rebound in fault step-overs caused by pore fluid flow, *Science*, Vol. 237, No. 5279, pp. 1202-1204, doi: 10.1126/science.273.5279.1202.

Peltzer, G., P. Rosen, F. Rogez, and K. Hudnut (1998), Poroelastic rebound along the Landers 1992 earthquake surface rupture, *J. Geophys. Res.*, *103*(B12), 30,131-30,154, doi: 10.1029/98JB02302.

Perfettini, H., & J. P. Avouac (2007), Modeling afterslip and aftershocks following the 1992 Landers earthquake, *Journal of Geophysical Research: Solid Earth*, *112*(B7), doi: 10.1029/2006JB004399.

Perfettini, H., J.-P. Avouac , H. Tavera , A. Kositsky, J.-M. Nocquet , F. Bondoux, M. Chlieh, A. Sladen , L. Audin, D.L. Farber, and P. Soler (2010), Seismic and aseismic slip on the central Peru megathrust., *Nature*, *465*(7294), 78–81, doi: 10.1038/nature09062.

Petit, G, and B. Luzum (eds.) (2010), IERS Conventions (2010), IERS Technical Note No. 36, Verlag des Bundesamtes für Kartographie und Geodäsie, 179 pp., Frankfurt am Main 2010, ISBN 3-89888-989-6, (http://www.iers.org/TN36).

Pritchard, M. E., M. Simons, P. A. Rosen, S. Hensley, and F. H. Webb (2002), Co-seismic slip from the 1995 July 30 Mw= 8.1 Antofagasta, Chile, earthquake as constrained by InSAR and GPS observations, *Geophys. J. Int.*, 150(2), 362–376, doi: 10.1046/j.1365-246X.2002.01661.x.

Pritchard, M. E., C. Ji, and M. Simons (2006), Distribution of slip from 11Mw>6 earthquakes in the northern Chile subduction zone, *J. Geophys. Res.*, 111, B10302, doi: 10.1029/2005JB004013.

Rebischung, P., J. Ray, C. Benoist, L. Metivier, and Z. Altamimi (2015), Error Analysis of the IGS repro2 Station Position Time Series, *American Geophysical Union, Fall Meeting 2015*, p. 13, abstract #G23B-1065.

Reid, H.F. (1910), Mechanics of the earthquake, in: The California Earthquake of April 18, 1906, *Report of the State Investigation Commission*, Carnegie Institution of Washington, Washington DC.

Reid, H.F. (1913). Sudden earth movements in sumatra in 1892, *Seismological Society of America Bulletin*, 3(2), 72–79.

Reutter, K.-J., E. Scheuber, and P. Wigger (Eds.) (1994), Tectonics of the Southern Central Andes, Springer-Verlag, Heidelberg, pp.334, doi: 10.1007/978-3-642-77353-2.

Rietbrock, A., and F. Waldhauser (2004), A narrowly spaced double-seismic zone in the subducting Nazca plate, *Geophys. Res. Lett.*, *31*(10), doi: 10.1029/2004GL019610.

Rosen, P. A., C.W. Werner, and A. Hiramatsu (1994), Two-dimensional phase unwrapping of SAR interferograms by charge connection through neutral trees, *Proceedings of IGARSS'94*, Pasadena, 8-12 August, 1994.

Rosen, P., C. Werner, E. Fielding, S. Hensley, S. Buckley, and P. Vincent (1998), Aseismic creep along the San Andreas Fault northwest of Parkfield, CA measured by radar interferometry, *Geophysical Research Letters*, *25*(6), 825-828, doi: 10.1029/98GL50495.

Rosen, P.A., S. Hensley, I.R. Joughin, F.K. Li, S.N. Madsen, E. Rodriguez, and R.M. Goldstein (2000), Synthetic aperture radar interferometry, *Proceedings of the IEEE*, *88*(3), 333-382, doi: 10.1109/5.838084.

Ruegg, J.C. , J. Campos, R. Armijo, S. Barrientos, P. Briole, R. Thiele, M. Arancibia, J. Cañuta, T. Duquesnoy, M. Chang, D. Lazo, H. Lyon-Caen, L. Ortlieb, J.C. Rossignol, and L. Serrurier (1996), The Mw = 8.1 Antofagasta (North Chile) Earthquake of July 30,1995: First results from teleseismic and geodetic data, *Geophys. Res. Lett.*, *23*(9), 917–920, doi: 10.1029/96GL01026.

Ruegg, J. C., M. Olcay, and D. Lazo (2001), Co-, Post- and Pre(?)-seismic Displacements Associated with the Mw8.4 Southern Peru Earthquake of 23June 2001 from Continuous GPS Measurements, *Seismol. Res. Lett.*, *72*(6), 673–678, doi: 10.1785/gssrl.72.6.673.

Ruiz, S., M. Métois, A. Fuenzalida, J. Ruiz, F. Leyton, R. Grandin, C. Vigny, R. Madariaga, and J. Campos (2014), Intense foreshocks and a slow slip event preceded the 2014 Iquique Mw 8.1 earthquake., *Science*, *345*(6201), 1165–1169, doi: 10.1126/science.1256074.

Ruiz, S., and R. Madariaga (2018), Historical and recent large megathrust earthquakes in Chile, *Tectonophysics*, *733*, 37-56, doi: 10.1016/j.tecto.2018.01.015.

Saastamoinen, J. (1973), Contributions to the theory of atmospheric refraction, *Bulletin Géodésique (1946-1975)*, *107*(1), 13-34, doi: 10.1007/BF02522083.

Savage, J.C., & W.H. Prescott (1978), Asthenosphere readjustment and the earthquake cycle, *Journal of Geophysical Research: Solid Earth*, *83*(B7), 3369-3376, doi: 10.1029/JB083iB07p03369.

Savage, J.C. (1983), A dislocation model of strain accumulation and release at a subduction zone, *Journal of Geophysical Research: Solid Earth*, *88*(B6), 4984-4996, doi: 10.1029/JB088iB06p04984.

Schmid, R., P. Steigenberger, G. Gendt, M. Ge, and M. Rothacher (2007), Generation of a consistent absolute phase-center correction model for GPS receiver and satellite antennas, *J. Geod.*, *81*(12), 781–798, doi: 10.1007/s00190-007-0148-y.

Scholz, C. H. (1998), Earthquakes and friction laws, *Nature*, *391*(6662), 37–42, doi: 10.1038/34097.

Schurr, B., G. Asch , S. Hainzl, J. Bedford, A. Hoechner, M. Palo, R. Wang, M. Moreno, M. Bartsch, Y. Zhang, O. Oncken, F. Tilmann, T. Dahm, P. Victor, S. Barrientos, and J.-P. Vilotte (2014), Gradual unlocking of plate boundary controlled initiation of the 2014 Iquique earthquake, *Nature*, *512*(7514), 299–302, doi:10.1038/nature13681.

Scott, C. P., R. W. Allmendinger, G. González, and J. P. Loveless (2016), Coseismic extension from surface cracks reopened by the 2014 Pisagua, Northern Chile earthquake sequence, *Geology*, 44(5), 387–390, doi: 10.1130/G37662.1.

Shimazaki, K., and T. Nakata (1980), Time-predictable recurrence model for large earthquakes, *Geophys. Res. Lett.*, 7(4), 279–282, doi: 10.1029/ GL007i004p00279.

Simons, M., J.E. Galetzka, J.F. Genrich, F. Ortega, D. Comte, B. Glass, G. González, E. Norabuena, (2010), Central Andean Tectonic Observatory Geodetic Array, UNAVCO, GPS Data Set, doi: 10.7283/T50P0X37.

Sippl, C., ,B. Schurr, X. Yuan, J. Mechie, F. M. Schneider, M. Gadoev, S. Orunbaev, I. Oimahmadov, C. Haberland, U. Abdybachaev, V. Minaev, S. Negmatullaev, N. Radjabov (2013), Geometry of the Pamir-Hindu Kush intermediate-depth earthquake zone from local seismic data, *J. Geophys. Res. Solid Earth*, *118*(4), 1438–1457, doi: 10.1002/jgrb.50128.7.

Sippl, C., and B. Schurr (2017), Seismicity Structure of the Downgoing Nazca Slab in Northern Chile, Abstract T33B-0706, AGU Fall Meeting 2017, New Orleans, USA.

Sippl, C., B. Schurr, G. Asch, and J. Kummerow (2018), Seismicity structure of the northern Chile forearc from >100,000 double-difference relocated hypocenters, *Journal of Geophysical Research Solid Earth Solid Earth*, *123*, 4063-4087, doi:10.1002/2017JB015384.

Skolnik, M.I. (1962), Introduction to Radar Systems, *McGraw-Hill Kogakusha*, Ltd., Tokyo.

Smith, W. H. F., and D.T. Sandwell (1997), Global sea floor topography from satellite altimetry and ship depth soundings, *Science*, *277*, 1956–1962 doi: 10.1126/science.277.5334.1956.

Strecker, M.R., R.N. Alonso, B. Bookhagen, B. Carrapa, G.E. Hilley, E.R. Sobel, and M.H. Trauth (2007), Tectonics and climate of the southern central Andes, *Annu. Rev. Earth Planet. Sci.*, *35*, 747-787, doi:10.1146/annurev.earth.35.031306.140158.

Sudhaus, H., and J. Sigurjón (2009), Improved source modelling through combined use of InSAR and GPS under consideration of correlated data errors: application to the June 2000 Kleifarvatn earthquake, Iceland, *Geophysical Journal International*, *176*(2), 389-404, doi: 10.1111/j.1365-246X.2008.03989.x.

Tarayre, H., and D. Massonnet (1996), Atmospheric Propagation heterogeneities revealed by ERS-1 interferometry, *Geophysical Research Letters*, *23*(9), 989-992, doi: 10.1029/96GL00622.

Tassara, A. and A. Echaurren (2012), Anatomy of the Andean subduction zone: three-dimensional density model upgraded and compared against global-scale models, *Geophys. J. Int.* 189, 161–168, doi: 10.1111/j.1365-246X.2012.05397.x.

Tilmann, F., Y. Zhang, M. Moreno, J. Saul, F. Eckelmann, M. Palo, Z. Deng, A. Babeyko, K. Chen, J.-C. Baez, B. Schurr, R. Wang, and T. Dahm (2016), The 2015 Illapel earthquake, central Chile: A type case for a characteristic earthquake?. *Geophysical Research Letters*, *43*(2), 574-583, doi: 10.1002/2015GL066963.

Trubienko, O., L. Fleitout, J.D. Garaud, and C. Vigny (2013), Interpretation of interseismic deformations and the seismic cycle associated with large subduction earthquakes, *Tectonophysics*, *589*, 126-141, doi: 10.1016/j.tecto.2012.12.027.

Turcotte, D., and G. Schubert (2014), Geodynamics, 3rd ed., *Cambridge University Press*, pp. 612.

Van Dam, T., J. Wahr, P. C. D. Milly, A. B. Shmakin, G. Blewitt, D. Lavallée, and K. M. Larson (2001), Crustal displacements due to continental water loading, *Geophys. Res. Lett.*, *28*(4), 651–654, doi: 10.1029/2000GL012120.

von Huene, R., J. Corvalán, E. R. Flueh, K. Hinz, J. Korstgard, C. R. Ranero, W. Weinrebe, and C. Scientists (1997), Tectonic control of the subducting Juan Fernández Ridge on the Andean margin near Valparaiso, Chile, *Tectonics*, *16*(3), 474–488, doi:10.1029/96TC03703.

Victor, P., O. Oncken, and J. Glodny (2004), Uplift of the western Altiplano plateau: Evidence from the Precordillera between 20 and 21 S (northern Chile), *Tectonics*, *23*(4), doi: 10.1029/2003TC001519.

Vigny, C., , W.J.F. Simons , S. Abu, R. Bamphenyu, C. Satirapod, N. Choosakul, C. Subarya, A. Socquet, K. Omar , H.Z. Abidin, and B.A.C. Ambrosius (2005), In-

sight into the 2004 Sumatra-Andaman earthquake from GPS measurements in southeast Asia, *Nature*, *436*(7048), 201-206, doi: 10.1038/nature03937.

Vigny, C., A. Rudloff, J.C. Ruegg, R. Madariaga, J. Campos, and M. Alvarez (2009), Upper plate deformation measured by GPS in the Coquimbo Gap, Chile, *Physics of the Earth and Planetary Interiors*, *175*(1), 86-95, doi:10.1016/j.pepi.2008.02.013.

Wang, X., and P.L.F. Liu (2006), An analysis of 2004 Sumatra earthquake fault plane mechanisms and Indian Ocean tsunami, *Journal of Hydraulic Research*, *44*(2), 147-154, doi: 10.1080/00221686.2006.9521671.

Wang, K., and S. L. Bilek (2011), Do subducting seamounts generate or stop large earthquakes?, *Geology*, *39*(9), 819–822, doi: 10.1130/G31856.1.

Wang, K., Y. Hu, and J. He (2012), Deformation cycles of subduction earthquakes in a viscoelastic Earth, *Nature*, *484*(7394), 327–332, doi: 10.1038/nature11032.

Wegmüller, U., C. Werner, and T. Strozzi (1998), SAR interferometric and differential interferometric processing, *Proceedings of IGARS´98*, Seattle, 6-10 July, pp. 1106-1108.

Weiss, J. R., B.A. Brooks, J.H. Foster, M. Bevis, A. Echalar, D. Caccamise, J. Heck, E. Kendrick, K. Ahlgren, D. Raleigh, R. Smalley Jr., and G. Vergani (2016), Isolating active orogenic wedge deformation in the southern Subandes of Bolivia, *J. Geophys. Res. Solid Earth*, *121*(8), 6192–6218, doi: 10.1002/2016JB013070.

Werner C., U. Wegmüller, T. Strozzi, and A. Wiesmann (2000), Gamma SAR and Interferometric Processing Software, *Proceedings of ERS-ENVISAT Symposium*, Gothenburg, Sweden, 16-20 Oct. 2000.

Werner, C., U. Wegmüller, T. Strozzi, and A. Wiesmann (2002), Processing strategies for phase unwrapping for INSAR applications, *Proceedings EUSAR 2002*, Cologne, 4-6 June, 2002.

Wiley, C.A. (1954), Pulsed Doppler Radar Methods and Apparatus, *United States Patent*, No. 3196436.

Xu, Z.W., J. Wu, and Z.S. Wu (2004), A survey of ionospheric effects on space-based radar, *Waves in Random Media*, *14*(2), S189-S273, doi: 10.1088/0959-7174/14/2/008.

Yagi, Y., R. Okuwaki, B. Enescu, S. Hirano, Y. Yamagami, S. Endo, and T. Komoro (2014), Rupture process of the 2014 Iquique Chile earthquake in relation with the foreshock activity, *Geophysical Research Letters*, *41*(12), 4201-4206, doi: 10.1002/2014GL060274.

Yoon, M., S. Buske, S. A. Shapiro, and P. Wigger (2009), Reflection Image Spectroscopy across the Andean subduction zone, *Tectonophysics*, *472*(1), 51–61, doi: 10.1016/j.tecto.2008.03.014.

Zebker, H.A., and J. Villasenor (1992), Decorrelation in interferometric radar echoes, *IEEE Transactions on geoscience and remote sensing*, *30*(5), 950-959, doi: 10.1109/36.175330.

Zebker, H.A., P.A. Rosen, and S. Hensley (1997), Atmospheric effects in interferometric synthetic aperture radar surface deformation and topographic maps, *Journal of Geophysical Research: Solid Earth*, *102*(B4), 7547-7563, doi: 10.1029/96JB03804.

Curriculum Vitae

Der Lebenslauf ist in der Online-Version aus Gründen des Datenschutzes nicht enthalten.

Acknowledgements

I started my doctoral research at GFZ over five years ago in the section lithosphere dynamics. From the very first days in this section, my colleagues have been very helpful and any time open for scientific but also private discussions and for that I am sincerely grateful. I was very lucky to have had many colleagues that accompanied and supported me in all stages of the PhD. Special thanks go to our secretary and section head assistent Franziska Alberg for her support with all sorts of issues. Whenever I had a problem, I could go to her knowing for sure that she will solve it. Thanks also to Jon Bedford, with whom I had fruitful discussions about the Northern Chile subduction cycle. His door was always open whenever I had questions regarding modelling issues. He also constantly provided help with language issues and assisted in correcting grammarfor which I am really thankful.

I would also like to thank Prof. Onno Oncken and all members of the executive board of the GEOSIM scholarship for giving me the opportunity to research on a self-designed project in the context of geodynamic modelling at GFZ. I also acknowledge the DFG funding agency for funding the GEOSIM scholarship (BMBF, FKZ03G0809A). During the soft-skill and summer courses offered by the Helmholtz graduate reasearch school GeoSIM, I gained a lot of knowledge about career-related issues. I am very grateful to the former GeoSIM coordinator Karen Lever and the follower coordinator Sofia Kufner organising those events. Moreover both did a great job in managing the GeoSIM project and always supported their students as much as they can.

Furthermore I would like to thank the developpers of the Gamma software Charles Werner and Urs Wegmüller. Without this great software and the nice support of the developpers, it would have been so much harder to process my InSAR data.

I am grateful for the academic discussions that sharpened my scientific questions with Prof. Onno Oncken, Francisco Ortega Culaciati, Christian Sippl and all colleagues of section lithosphere dynamics at GFZ. Without the assistance in processing the GPS data from Zhiguo Deng, I would have no high quality GPS data to present, so I am very thankful to him for providing processed GPS solutions.

The biggest thank you goes to Sabrina Metzger and Marcos Moreno for their daily guidance, patience and kindness. I frequently received high quality feedback from both on my research and could benefit a lot from our fruitful academic discussions. Especially the patience of Sabrina Metzger who frequently discussed with me the basic concepts of modelling and also InSAR and GPS processing improved my work a lot. I want to give my special and deep thanks to both.

My final and warmest thanks go to my family. Dad, from my childhood on, you always have been my ideal and first source of inspiration. You have choosen the family as number one in your life and may gave up an extraordinary scientific career for us. You showed me how to perfectly balance life and what counts most! This thesis is also deidcated to you and your brilliancy! Mom, you have always been on my side, gave me so much love and supported me in all stages of my life and with all my decisions. I cannot imagine any better mother! Jakob, my big brother, it has been my dearest pleasure to spend my entire childhood together with you - we shared everything and always keep together until today. You ever kept your ear open for any strange issue I had. Thank you all three so much! Jule, my dear wife, this thesis would not have been feasible without your great support and also patience over more than five years! You always gave me the time to do research, even when there were many other things to do. It must have been my lucky day, when me met at a sunny September day in 2010. Two years ago, in June 2017, you gave birth to our biggest treasure, our daughter Lenja. It was so inspireing to have you two girls around me during the final stage of this thesis. Thank you so much!

Eidesstattliche Erklärung

Nach §7 (4) der Promotionsordnung des Fachbereichs Geowissenschaften der Freien Universität Berlin erkläre ich hiermit, dass ich diese Dissertation selbstständig ohne Hilfe Dritter und ohne Benutzung anderer als der angegebenen Quellen und Hilfsmittel verfasst habe. Alle den benutzten Quellen wörtlich oder sinngemäß entnommenen Stellen sind als solche einzeln kenntlich gemacht.

Diese Arbeit ist bislang keiner anderen Prüfungsbehörde vorgelegt worden.

Ich bin mir bewusst, dass eine falsche Erklärung rechtliche Folgen haben wird.

_____

Ort, Datum, Unterschrift